

The nature of Fermi-liquids, an optical perspective

STRICKER, Damien

Abstract

With the arrival of new experimental, numerical and theoretical techniques, the discovery of new materials and new processes has multiplied in recent decades. Condensed matter has diversified, but also became more intricate as the processes in some materials turned out to be quite entangled. The aim of this thesis is to show that beyond complex phenomena governing the single-layer ruthenate Sr_2RuO_4 and the mercury-based high-TC $\text{HgBa}_2\text{CuO}_{4+x}$, low-energy electronic properties can be universal. The Fermi-liquid theory is the finest example: its description and its application allow to create a background upon which deviations can be much better recognized.

Reference

STRICKER, Damien. *The nature of Fermi-liquids, an optical perspective*. Thèse de doctorat : Univ. Genève, 2015, no. Sc. 4873

URN : [urn:nbn:ch:unige-839918](http://nbn-resolving.org/urn:nbn:ch:unige-839918)

Available at:

<http://archive-ouverte.unige.ch/unige:83991>

Disclaimer: layout of this document may differ from the published version.



UNIVERSITÉ
DE GENÈVE

UNIVERSITÉ DE GENÈVE
Department of Quantum Matter Physics

FACULTÉ DES SCIENCES
Professeur Dirk van der Marel

The Nature of Fermi-liquids, an Optical Perspective

THÈSE

*présentée à la Faculté des Sciences de l'Université de Genève
pour obtenir le grade de docteur ès Sciences, mention Physique*

par

Damien Stricker

de

Herisau (Suisse)

Thèse n° 4873

GENÈVE
Imprimerie Harder
2015



**UNIVERSITÉ
DE GENÈVE**

FACULTÉ DES SCIENCES

***Doctorat ès sciences
Mention physique***

Thèse de *Monsieur Damien STRICKER*

Intitulée :

" The Nature of Fermi-liquids, an Optical Perspective "

La Faculté des sciences, sur le préavis de Monsieur D. VAN DER MAREL, professeur ordinaire et directeur de thèse (Department of Quantum Matter Physics), Monsieur F. BAUMBERGER, professeur ordinaire (Department of Quantum Matter Physics), Monsieur A. GEORGES, professeur (Collège de France, Institut de physique, Physique de la matière condensée, Paris, France), Monsieur R. LOBO, docteur (École supérieure de physique et de chimie industrielles de la ville de Paris, Laboratoire de Physique et d'Etude des Matériaux, Paris, France), et Monsieur A. VECCHIONE, docteur (Università degli Studi di Salerno, Dipartimento di Fisica « E. R. Caianiello », Fisciano, Italy), autorise l'impression de la présente thèse, sans exprimer d'opinion sur les propositions qui y sont énoncées.

Genève, le 17 décembre 2015

Thèse - 4873 -

Le Doyen

N.B. - La thèse doit porter la déclaration précédente et remplir les conditions énumérées dans les "Informations relatives aux thèses de doctorat à l'Université de Genève".

Ce travail est dédié à mes parents et à
Nadège pour leur soutien et leur amour.

Preface

Français: L'attrait qu'à toujours eu l'homme envers les métaux, surtout précieux, l'a poussé depuis bien longtemps d'essayer de les comprendre et de les décrire avec le plus de précision possible. Tout commença par les premiers alliages, mélanger du cuivre et de l'étain permettait non seulement de changer la couleur du métal mais lui donnait aussi un avantage non négligeable, il devenait plus résistant que le cuivre seul ou la pierre. Plus tard, il fut compris que l'ajout de petite quantité d'impuretés pouvait décupler la dureté du matériau ou le protéger en partie de l'oxydation. Mais la connaissance de la nature restait alors empirique, phénoménologique et macroscopique. Bien que les premières descriptions détaillées des phénomènes électriques débutèrent au XVIIIe siècle avec Fay et Coulomb, il fallu néanmoins attendre le milieu du XIXe siècle avec Richard Laming pour que la première notion microscopique classique de l'atome soit mise au point. S'en suit d'intenses efforts collectifs visant à décrire les premières propriétés des matériaux. Mais certaines de ces propriétés restaient mystérieuse et contre-intuitives, notamment la résistivité des métaux à basse température: devait-elle devenir nulle, se stabiliser ou finir par croître à nouveau? La découverte de la supraconductivité y est liée, mais devint un mystère supplémentaire. L'avènement de la mécanique quantique était providentielle mais tout en permettant d'expliquer nombre de phénomènes, la matière devenait une superposition d'état. Devait-elle devenir infiniment complexe ?

English: The attraction that man has always felt for metals, especially precious ones, has pushed since a long time to understand and describe them with the greatest possible precision. It all began with the first alloys. Mixing copper and tin not only allowed to change the color of the metal but also gave it a significant advantage: it was harder than copper or even stone. Later it turned out that adding a few impurities could improve the material properties, such as preventing its corrosion. Back then, the knowledge of nature was empirical, phenomenological and macroscopic. Although the first detailed descriptions of electric phenomena began in the eighteenth century with Fay and Coulomb, it nevertheless took until the mid-nineteenth century with Richard Laming before the first conventional microscopic concept of the atom was developed. What follows is an intense collective effort to understand properties of metals. Some

of these properties remained mysterious and counterintuitive, particularly the resistivity at low temperature: will it become zero, will it saturate or perhaps grow again? It was in answering this question that the superconductivity was discovered, only to present the researchers with another mystery. The advent of quantum mechanics brought a powerful new framework. But at the same time matter became a vast superposition of states: will its description be infinitely complex?

Abstract

Français: Avec l'avènement des nouvelles techniques expérimentales, numériques et théoriques la découverte de nouveaux matériaux et de nouveaux processus a été démultipliée ces dernières décennies: supraconducteurs à haute température critique, matériaux exfoliables et 2D (graphène, dichalcogénures), multiferroïques (manganites et ferries), semi-conducteurs organiques et hétérostructures quantiques. Ce bref aperçu des différents domaines de la matière condensée montre à quel point la recherche s'est diversifiée mais aussi complexifiée à mesure que les propriétés de certains matériaux devenaient, elles aussi, beaucoup plus inextricables. Le but de cette thèse est de montrer qu'au delà des phénomènes complexes qui régissent ces matériaux, les propriétés électronique à basse énergie peuvent être universelles. La théorie du liquide de Fermi en est le meilleur exemple; sa description et son application permettent, en outre, de former une base dans laquelle les déviations peuvent être beaucoup mieux décrites.

L'outil de travail est la spectroscopie optique. Le développement d'une nouvelle méthode de calibration a récemment permis d'augmenter considérablement la précision et la reproductibilité des résultats. La première partie de cette thèse introduit les concepts théoriques et expérimentaux de la spectroscopie optique mais aussi la théorie du liquide de Fermi. La deuxième partie présente une étude détaillée des supraconducteurs à haute température critique à base d'oxyde de cuivre (cuprates). Les résultats reposent sur la mesure de trois échantillons sous dopés de $\text{HgBa}_2\text{CuO}_{4+x}$. Cette famille de supraconducteur possède non seulement la plus haute température critique par rapport au nombre de couche d'oxyde de cuivre qui le compose, mais aussi la plus basse résistivité résiduelle. La motivation de cette étude provient du fait que dans la phase pseudogap il a récemment été démontré que ce matériau possédait une résistivité variant selon la prédiction du liquide de Fermi. Toujours dans la même phase, l'analyse optique révèle un taux de diffusion quadratique en température. Sa dépendance en énergie montre qu'en approchant la phase de Mott, le liquide de Fermi est graduellement affaibli par une augmentation des interactions et donc, du facteur de renormalisation. Une conclusion identique est obtenue en comparant directement la conductivité optique du modèle de liquide de Fermi aux résultats expérimentaux. De plus, l'analyse du poids spectral des

quasiparticules va dans le même sens et montre que celui est inversement proportionnel au dopage. L'extrapolation des données à zéro dopage montre l'état de Mott est obtenu. Malgré cet affaiblissement graduel le lien entre température et énergie est démontré par l'étude d'échelle du taux de diffusion, celle-ci montre en effet que le facteur liant les deux quantités, bien que différent des prédictions théoriques, est une valeur universelle pour tous les dopages ainsi que toutes les familles des cuprates. En continuation de ce résultat, la théorie de couplage fort Migdal-Eliashberg est utilisée et démontre que liquide de Fermi dans la phase pseudogap peut coexister en présence d'un fort couplage électron-boson apparaissant à plus haute énergie. La troisième partie démontre que le ruthénate de strontium Sr_2RuO_4 est le seul matériau connu à ce jour démontrant parfaitement les propriétés optiques de liquides de Fermi. Une analyse quantitative de son taux de diffusion montre que la valeur du paramètre d'échelle reliant la température et l'énergie est, contrairement aux cuprates, exactement celle prédite par la théorie. Motivé par ce résultat, le modèle de liquide de Fermi est appliqué aux mesures de transport et démontre qu'à l'aide de deux composantes la résistivité peut être décrite avec précision jusqu'à très haute température. Une étude numérique DFT et DMFT est présentée et démontre un excellent recouvrement avec l'expérience. Au regard de la conductivité optique, les deux techniques reproduisent parfaitement le modèle à basse énergie et basse température. Néanmoins un écart important apparaît avec le modèle à plus haute énergie ou température. En utilisant les capacités prédictives des calculs DMFT, l'excès de poids spectral est attribué à la présence de quasiparticules résilientes. Ces quasiparticules n'ont plus les mêmes propriétés que les paires électron-trou décrites par le liquide de Fermi, mais existent par le fait qu'à une certaine énergie le taux de diffusion est beaucoup plus faible qu'il devrait l'être, permettant ainsi aux quasiparticules d'exister suffisamment longtemps pour avoir un impact sur les propriétés électroniques du matériau. Finalement une analyse approfondie des phonons de l'axe isolant montre la complexité structurelle des échantillons de Sr_2RuO_4 .

English: With the arrival of new experimental, numerical and theoretical techniques, the discovery of new materials and new processes has multiplied in recent decades: high critical temperature superconductors, two-dimensional layered materials (graphene, dichalcogenides) multiferroics (manganites and ferrites), organic semiconductors, quantum heterostructures. Condensed matter has diversified, but also became more intricate as the processes in some materials turned out to be quite entangled. The aim of this thesis is to show that beyond complex phenomena governing these materials, low-energy electronic properties can be universal. Fermi liquid theory is the finest example: its description and its application allow to create a background upon which deviations can be much better recognized.

The tool of choice is optical spectroscopy. The development of a new method of calibration has recently significantly increased the accuracy and reproducibility of our experimental results. The thesis begins with a detailed introduction into the optical spectroscopy and the Fermi-liquid theory. The second part of this thesis presents a detailed analysis of high critical temperature

superconductors based on copper oxide (cuprates). The results are based on the measurement of three underdoped samples of $\text{HgBa}_2\text{CuO}_{4+x}$. This family of superconductors has not only the highest critical temperature with respect to the number of copper oxide layers, but it also has the lowest residual resistivity. The motivation for this study is the recent observation that in the pseudogap phase the resistivity follows the Fermi-liquid theory. In the same way, the optical analysis shows a quadratic temperature dependence of the scattering rate. The energy dependence of the scattering rate shows that approaching the Mott phase, the Fermi liquid is gradually weakened by an increase of interactions and mass renormalization. The same conclusion is obtained by directly comparing the optical conductivity of the Fermi-liquid model to the experimental results. Furthermore, analysis of the spectral weight of the quasiparticles points in the same direction and shows that the spectral weight is completely suppressed when going to the Mott state. Despite this gradual suppression, the link between temperature and energy is demonstrated by the scaling study of the scattering rate. The factor linking energy and temperature, while different from theoretical predictions, has a universal value for all cuprates. The strong coupling Migdal-Eliashberg theory shows that Fermi liquid in the pseudogap phase can coexist with the presence of a strongly coupled electron-boson modes appearing at higher energy.

The third part demonstrates that strontium ruthenate Sr_2RuO_4 is the only material known to date which perfectly exhibits the optical properties of a Fermi liquid. A quantitative analysis of its scattering rate indicates that the value of the scaling parameter between the temperature and the energy is, unlike the cuprates, *exactly* 2π , as predicted by theory. Motivated by this result, the Fermi liquid model is applied to transport measurement and demonstrates that, using two components, the resistivity can be accurately described up to very high temperatures. A numerical DFT and DMFT study is presented and shows excellent agreement with experiment. Regarding the optical conductivity, both techniques perfectly reproduce the low-energy and low-temperature Fermi-liquid model. However, a large discrepancy appears with respect to the model at higher energy, or high temperature. Using the predictive capabilities of DMFT calculations, excess spectral weight is attributed to the presence of resilient quasiparticles. These quasiparticles no longer have the same properties as the electron-hole pairs described by the Fermi liquid. This phenomenon is explained by the fact that at a definite energy the scattering rate becomes much lower than it should be, allowing the quasiparticles to exist long enough to have an impact on the electronic properties of the Sr_2RuO_4 . Finally, a detailed analysis of phonons along the insulating axis shows the structural complexity of the material.

Contents

List of Figures	vi
1 Optical Spectroscopy of metals	1
1.1 Electrodynamics	2
1.1.1 Maxwell equations in vacuum	2
1.1.2 Maxwell equations in matter	3
1.1.3 Fresnel equations	5
1.2 Optical models and functions	7
1.2.1 Drude model	7
1.2.1.1 The Drude model in optics	9
1.2.1.2 Sheet conductance	11
1.2.1.3 Hagen-Rubens regime	12
1.2.1.4 Relaxation regime	12
1.2.1.5 Transparent regime	14
1.2.2 Drude Lorentz model	14
1.2.2.1 Intraband and interband	15
1.2.3 Extended Drude model	16
1.2.3.1 Clausius Mossotti relation	18
1.2.4 Kramers-Kronig relations	18
1.2.4.1 Optical conductivity	20
1.2.4.2 Complex reflectivity	21
1.3 Kubo formula	22
1.3.1 Perturbation theory	23
1.3.2 Kubo formula in optics	26
1.3.3 Kubo formula in transport	29
1.4 Fermi-liquid	30
1.4.1 The Fermi-liquid in optics	30

CONTENTS

1.4.2	Energy ranges	32
1.4.2.1	Drude regime	32
1.4.2.2	Thermal regime	34
1.4.2.3	High energy regime	35
1.4.3	Understanding an optical spectrum	36
1.4.4	Bosonic spectral function models	36
1.4.4.1	Histogram representation	37
1.4.4.2	Power law and Fermi liquid representation	37
1.4.4.3	Double Fermi liquid and mixed model	39
1.4.4.4	An experimental cutoff	40
2	Experimental	41
2.1	Introduction	41
2.2	Infrared normal incidence reflectivity	43
2.2.1	Bruker IFS 113v	43
2.2.2	Polarizers	44
2.2.3	UHV Cryostat	46
2.2.4	Drift calibration	48
2.2.5	Visible normal incidence reflectivity	51
2.2.6	Ellipsometry	51
2.2.6.1	Basic principles	51
2.2.6.2	Equipment	51
2.2.6.3	Orthorhombic model	53
2.2.6.4	Cubic model	53
2.2.6.5	Tetragonal model	54
2.2.6.6	Window and focusing lens corrections	55
2.2.7	Raman spectroscopy	55
3	Fermi-liquid like properties in the pseudogap of the cuprates	57
3.1	Introduction	58
3.1.1	The complex phase diagram of the cuprates	58
3.1.2	Electronic structure	59
3.1.3	Superconductivity in the cuprates	61
3.1.4	Pseudogap	62
3.2	Samples	64
3.3	Transport measurements	65
3.4	Optical measurements	67
3.4.1	Sample preparation	67

3.4.2	Normal incidence reflectivity	68
3.4.2.1	In-plane measurement	68
3.4.2.2	c-axis measurement	71
3.4.3	Ellipsometry	72
3.4.4	High-energy spectral weight transfer	72
3.4.5	Drude-Lorentz analysis	75
3.4.6	Optical conductivity	77
3.4.7	Sheet conductance and spectral weight	80
3.4.8	Extended Drude analysis	82
3.5	Fermi liquid-like behavior in the underdoped cuprates	86
3.5.1	Scaling in the underdoped $\text{HgBa}_2\text{CuO}_{4+x}$	87
3.5.2	Scaling in the cuprates family	89
3.5.3	Discussion	91
3.5.4	Fermi-liquid optical conductivity	91
3.5.5	Strong Coupling Formalism	96
3.5.5.1	Histogram model	96
3.5.5.2	Fermi-liquid model	98
3.5.5.3	Discussion	100
3.5.6	Conclusions	100
4	Low energy optical response of Sr_2RuO_4	103
4.1	Introduction	104
4.1.1	The Ruddlesden-Popper family	104
4.1.2	Band structure	104
4.1.3	Unconventional superconductivity	107
4.2	Samples and crystal growth	109
4.3	Fermi-liquid in transport experiments	111
4.3.1	Experimental	111
4.3.2	Results	114
4.3.3	The anomalous transports of the c-axis	118
4.4	Universal Fermi-liquid scaling in optics	119
4.4.1	Sample preparation	119
4.4.1.1	In-plane measurement	119
4.4.1.2	c-axis measurements	119
4.4.2	Optical measurement	120
4.4.2.1	Normal incidence reflectivity	120
4.4.2.2	Ellipsometry	121
4.4.2.3	Drude-Lorentz analysis	123

CONTENTS

4.4.3	Optical conductivity	124
4.4.4	Thermal regime in the optical scattering rate	125
4.4.5	Thermal regime in the optical conductivity	130
4.5	Numerical calculations	131
4.5.1	DMFT + LDA	132
4.6	Resilient quasiparticles	132
4.6.1	Band velocities for the intraband conductivity	134
4.6.2	DFT+DMFT self-energies	135
4.6.3	Orbital dependence	137
4.6.4	Discussion	138
4.7	Phonon splitting in the c-axis spectra of Sr_2RuO_4	140
4.7.1	Optical phonon of the single layer ruthenate	140
4.7.2	Optical spectroscopy	141
4.7.2.1	Fano lineshape	141
4.7.2.2	Comparison with the literature	143
4.7.2.3	Phonon fitting	145
4.7.2.4	Raman spectroscopy	148
4.7.3	Characterization	152
4.7.3.1	Scanning electron microscope	152
4.7.3.2	Xray diffraction	153
4.7.3.3	Magnetometry	153
4.7.3.4	Discussion	157
4.8	Conclusions	158
Appendices		159
A Fermi-liquid like properties in the pseudogap phase of the cuprates		161
A.1	Fermi-liquid fit of the reflectivity	161
A.2	Fermi-liquid fit of the optical conductivity	162
B Optical phonon of the single layer ruthenate		167
Bibliography		169
Publication list		183
Acknowledgements		185
List of Figures		197

Optical Spectroscopy of metals

Among the different physical probes, optical spectroscopy can be described as a bulk contactless macroscopic technique. Unlike other spectroscopic techniques, such as STM/STS and ARPES, the penetration depth of the probe –here electromagnetic waves– into good metals is larger than 10 to 100 unit cells, which is enough to probe the bulk properties of any metal. Used since more than five decades, optical spectroscopy is still improving and advancing with the fast ongoing research. Together with the new emerging and upgraded instrumentation such as ARPES, ultra-high magnetic field transport experiments and X-ray techniques, these techniques allow both rough characterization of bulk materials as well as precise quantitative analysis of physical phenomena. Recent improvement focuses on high magnetic and electrical fields as well as time-resolved experiments. In this thesis, the special emphasis was placed on the low energy scale physics, which governs the charged particles in matter. In order to understand the physical phenomena, notably the Fermi-liquid theory, this chapter presents a gradual but non-exhaustive description of the underlying theory and concepts: from the macroscopic light and matter interaction to the microscopic Kubo formalism and Migdal-Eliashberg theory.

The first section introduces Maxwell equations, the optical functions and the different notations which are used through this work. The second section presents the phenomenological models such as the Drude model and the basic concepts of optical spectroscopy, the subsections present their different energy regimes and especially extract power law forms which are fingerprints of the underlying physics. The Kramers-Kronig relations are introduced and their importance to the experiment is discussed. Section 1.3 introduces the key formalism of this work, the microscopic link between experiment and theory, the Kubo formula is introduced, and its application to optics and transports experiment is discussed. section 1.4 introduces the Fermi-liquid theory which is developed and applied to optical conductivity through the Kubo formalism. A direct comparison with the Drude model is shown.

1.1 Electrodynamics

1.1.1 Maxwell equations in vacuum

In classical electrodynamics, Maxwell equations in vacuum Equation 1.1 are the starting point to describe the electrical $\mathbf{E}(\mathbf{r}, t)$ and magnetic $\mathbf{B}(\mathbf{r}, t)$ fields in the presence of free charges and (or) currents [1, 2]. They sum up previous integral laws such as the Gauss' law Equation 1.1a, Faraday's law Equation 1.1c and Ampère's law Equation 1.1d, by rewriting and extending them to a differential form. In vacuum these equations are

$$\nabla \cdot \mathbf{E}(\mathbf{r}, t) = 4\pi\rho(\mathbf{r}, t) \quad (1.1a)$$

$$\nabla \cdot \mathbf{B}(\mathbf{r}, t) = 0 \quad (1.1b)$$

$$\nabla \times \mathbf{E}(\mathbf{r}, t) = -\frac{1}{c} \frac{\partial \mathbf{B}(\mathbf{r}, t)}{\partial t} \quad (1.1c)$$

$$\nabla \times \mathbf{B}(\mathbf{r}, t) = \frac{1}{c} \frac{\partial \mathbf{E}(\mathbf{r}, t)}{\partial t} + \frac{4\pi}{c} \mathbf{J}(\mathbf{r}, t). \quad (1.1d)$$

Where c is the speed of light in free space, $\mathbf{J}(\mathbf{r}, t)$ and $\rho(\mathbf{r}, t)$ are respectively the current and charge distribution. Since most of spectroscopic community uses the CGS system rather than the SI, this study will keep the former notation, although the experimental results will be given in eV for comparison with other techniques. In SI units and 4π should be replaced by $1/\epsilon_0$ among other things. For convenience, the spatial and time notations are dropped when no ambiguity is present. \mathbf{E} and \mathbf{B} are respectively generated by a scalar Φ and vector potential \mathbf{A}

$$\mathbf{B} = \nabla \times \mathbf{A} \quad (1.2)$$

$$\mathbf{E} + \frac{1}{c} \frac{\partial \mathbf{A}}{\partial t} = -\nabla\Phi. \quad (1.3)$$

Two other important equations are respectively the force and the continuity equations

$$\mathbf{F} = q(\mathbf{E} + \mathbf{v} \times \mathbf{B}) \quad (1.4)$$

$$\nabla \cdot \mathbf{J} = -\frac{\partial \rho}{\partial t}. \quad (1.5)$$

With q the charge and \mathbf{v} the charge's speed. Maxwell equations tell how charges and currents produce fields while the force equation describes how charges are affected by the fields. In complete vacuum ($\mathbf{J} = 0$ and $\rho = 0$) the combination of Gauss' law Equation 1.1a, Faraday's

law Equation 1.1c, and Ampère's law Equation 1.1d give the electromagnetic wave equations

$$\nabla^2 \mathbf{E} - \frac{1}{c^2} \frac{\partial^2 \mathbf{E}}{\partial t^2} = 0 \quad (1.6a)$$

$$\nabla^2 \mathbf{B} - \frac{1}{c^2} \frac{\partial^2 \mathbf{B}}{\partial t^2} = 0. \quad (1.6b)$$

Whose simplest solutions are given by harmonic plane waves

$$\mathbf{E}(\mathbf{r}, t) = \mathbf{E}_0 e^{i(\mathbf{k}\cdot\mathbf{r} - \omega t)} \quad (1.7a)$$

$$\mathbf{B}(\mathbf{r}, t) = \mathbf{B}_0 e^{i(\mathbf{k}\cdot\mathbf{r} - \omega t)}. \quad (1.7b)$$

From Equation 1.1c and Equation 1.1d these two waves and the wave vector \mathbf{k} are perpendicular to one another. The oscillating frequency is defined by ω with the relation to the wavelength $\lambda = 2\pi/|\mathbf{k}|$. A more general solution is given by the Fourier transform

$$\mathbf{E}(\mathbf{r}, t) = \iint_{-\infty}^{\infty} \mathbf{E}(\mathbf{k}, \omega) e^{i(\mathbf{k}\cdot\mathbf{r} - \omega t)} d\omega d\mathbf{k} \quad (1.8a)$$

$$\mathbf{E}(\mathbf{k}, \omega) = \iint_{-\infty}^{\infty} \mathbf{E}(\mathbf{r}, t) e^{-i(\mathbf{k}\cdot\mathbf{r} - \omega t)} dt d\mathbf{r}. \quad (1.8b)$$

1.1.2 Maxwell equations in matter

Inside matter, the previous equations Equation 1.1 need to be adapted to take into account interactions of light with the medium. Microscopically the displacement of the electronic cloud from its neutral position, also-called the bound-charge ρ_b , creates a net electric polarization \mathbf{P} which in turn creates a polarization current \mathbf{J}_p ; equivalently the spin and the orbital motion of electron create a bound current \mathbf{J}_b from a net magnetization \mathbf{M} . By applying a potential difference on the medium, the Ohm's law applies and a net conduction current \mathbf{J}_c appears. The four source terms are

$$\rho_b = -\nabla \cdot \mathbf{P} \quad (1.9a)$$

$$\mathbf{J}_p = \frac{\partial \mathbf{P}}{\partial t} \quad (1.9b)$$

$$\mathbf{J}_b = c \nabla \times \mathbf{M} \quad (1.9c)$$

$$\mathbf{J}_c = \sigma_1 \mathbf{E}. \quad (1.9d)$$

Where σ_1 is the real part of the conductivity σ . An additional contribution is also added for free external electrons and current ρ_f and \mathbf{J}_f . The total charge and current inside the material

1. OPTICAL SPECTROSCOPY OF METALS

is

$$\rho_{\text{tot}} = \rho_f + \rho_p \quad (1.10a)$$

$$\mathbf{J}_{\text{tot}} = \mathbf{J}_f + \mathbf{J}_c + \mathbf{J}_p + \mathbf{J}_b. \quad (1.10b)$$

Putting these extra contributions into Maxwell equations (1.1), the Gauss' law Equation 1.1a becomes

$$\nabla \cdot \mathbf{E} = 4\pi(\rho_f - \nabla \cdot \mathbf{P}). \quad (1.11)$$

The comparison of the above terms with the vacuum formulation introduces the electric displacement $\mathbf{D}(\mathbf{r}, t)$. The same comparison applies to Ampère's law Equation 1.1d with the magnetic field strength $\mathbf{H}(\mathbf{r}, t)$:

$$\mathbf{D} = \epsilon_1 \mathbf{E} = (1 + 4\pi\chi_e)\mathbf{E} = \mathbf{E} + 4\pi\mathbf{P} \quad (1.12a)$$

$$\mathbf{B} = \mu_1 \mathbf{H} = (1 + 4\pi\chi_m)\mathbf{H} = \mathbf{H} + 4\pi\mathbf{M}. \quad (1.12b)$$

Here, ϵ_1 is the real part of the dielectric constant ϵ , μ_1 is the real part of the permeability μ , and χ_m and χ_e are the related susceptibilities. These quantities are real constants representing only half of the total complex dielectric constant or conductivity. In case of non-magnetic material, which is the case in this thesis, the permeability is set to unity. Consequently Equation 1.1 can be rewritten

$$\nabla \cdot \mathbf{D}(\mathbf{r}, t) = 4\pi\rho_f(\mathbf{r}, t) \quad (1.13a)$$

$$\nabla \cdot \mathbf{B}(\mathbf{r}, t) = 0 \quad (1.13b)$$

$$\nabla \times \mathbf{E}(\mathbf{r}, t) = -\frac{1}{c} \frac{\partial \mathbf{B}(\mathbf{r}, t)}{\partial t} \quad (1.13c)$$

$$\nabla \times \mathbf{H}(\mathbf{r}, t) = \frac{1}{c} \frac{\partial \mathbf{D}(\mathbf{r}, t)}{\partial t} + \frac{4\pi}{c} \mathbf{J}_c(\mathbf{r}, t). \quad (1.13d)$$

For convenience and without loss of generality the free current contribution is set to zero. Yet it is useful to write a more general form of the dielectric constant and conductivity and derive the relation between these two quantities. Assuming that the medium is homogeneous and isotropic

$$c\nabla \times \mathbf{H} = -i\epsilon_1 \mathbf{kE}_0 e^{i(\mathbf{k}\cdot\mathbf{r} - \omega t)} + 4\pi\sigma_1 \mathbf{E} = (-i\epsilon_1 \omega + 4\pi\sigma_1) \mathbf{E} = -i\omega\epsilon \mathbf{E} \quad (1.14)$$

and we can set

$$\epsilon = \epsilon_1 + i \frac{4\pi\sigma_1}{\omega} = \epsilon_1 + i\epsilon_2. \quad (1.15)$$

The conductivity can also be expressed as a complex quantity $\sigma = \sigma_1 + i\sigma_2$ which yields to a more general form of Ohm's law

$$\mathbf{J}_{\text{tot}} = \sigma \mathbf{E}. \quad (1.16)$$

The link between the dielectric constant and the conductivity is

$$\epsilon = 1 + \frac{4\pi i}{\omega} \sigma. \quad (1.17)$$

Both the dielectric constant and the conductivity are in fact –by generalization– response functions and the general way of expressing them is

$$\mathbf{D}(\mathbf{r}, t) = \iiint_{-\infty}^t \epsilon_1(\mathbf{r}, \mathbf{r}', t') \mathbf{E}(\mathbf{r}', t') dt' d\mathbf{r}' \quad (1.18a)$$

$$\mathbf{J}(\mathbf{r}, t) = \iiint_{-\infty}^t \sigma_1(\mathbf{r}, \mathbf{r}', t') \mathbf{E}(\mathbf{r}', t') dt' d\mathbf{r}'. \quad (1.18b)$$

Similarly to the propagation of plane waves into vacuum, the combination of Maxwell equations yields

$$\nabla^2 \mathbf{E} - \frac{\epsilon_1 \mu_1}{c^2} \frac{\partial^2 \mathbf{E}}{\partial t^2} - \frac{4\pi \mu_1 \sigma_1}{c^2} \frac{\partial \mathbf{E}}{\partial t} = 0 \quad (1.19a)$$

$$\nabla^2 \mathbf{H} - \frac{\epsilon_1 \mu_1}{c^2} \frac{\partial^2 \mathbf{H}}{\partial t^2} - \frac{4\pi \mu_1 \sigma_1}{c^2} \frac{\partial \mathbf{H}}{\partial t} = 0. \quad (1.19b)$$

A key difference is that \mathbf{H} can only have a transverse component but not the electrical field. Consequently \mathbf{k} and \mathbf{E} are perpendicular to \mathbf{H} but not necessarily between them. The dispersion relation becomes

$$\mathbf{k} = \frac{\omega}{c} \sqrt{\epsilon_1 \mu_1 + i \frac{4\pi \mu_1 \sigma_1}{\omega}} \mathbf{n}_k. \quad (1.20)$$

$\mathbf{n}_k = \mathbf{k}/|\mathbf{k}|$ is the unit vector along \mathbf{k} . This equation expresses that a wave propagation in a medium is attenuated.

1.1.3 Fresnel equations

When travelling through different semi-infinite materials with different index of refraction, the electromagnetic wave conserves its energy but gets a different velocity. This change happens right at the interface where the Fresnel equations set other important concepts such as the reflectivity R and transmission T . Part of the wave is transmitted, reflected, keeping $R + T = 1$. The absorption process takes place inside the medium. A schematic view of the interface of two different materials is shown in Figure 1.1. In view of usual reflectivity measurements the

1. OPTICAL SPECTROSCOPY OF METALS

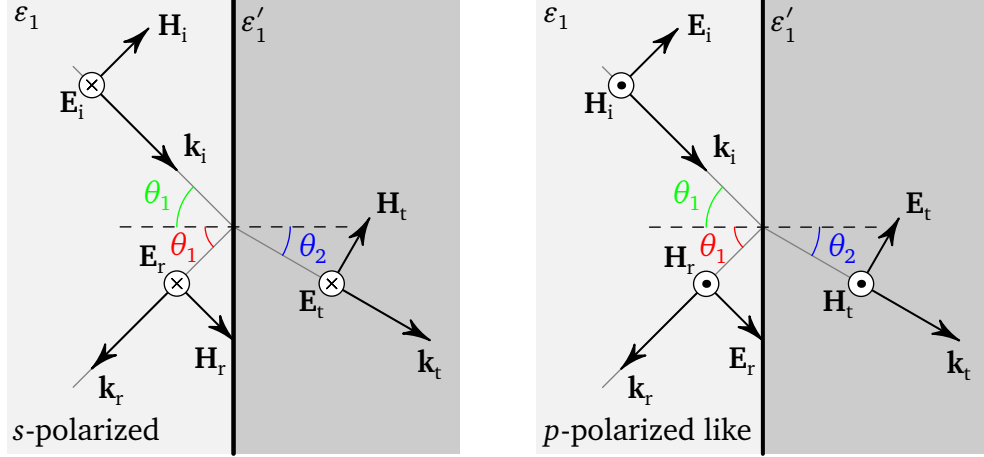


Figure 1.1: Schematic view of a right traveling wave through an interface between different materials. The wave vector \mathbf{k} gives the direction of the light propagation. The two subfigures indicates the electrical field either parallel (p -polarization) or perpendicular to the plane of incidence (s -polarization). The r and s subscript indicate the reflected and transmitted waves respectively.

first medium is considered to be the vacuum so that the wave equation can be written

$$\mathbf{E}_i = \mathbf{E}_{0i} e^{i(\mathbf{k}_i \cdot \mathbf{r} - \omega_i t)} \quad \mathbf{E}_r = \mathbf{E}_{0r} e^{i(\mathbf{k}_r \cdot \mathbf{r} - \omega_r t)} \quad \mathbf{E}_t = \mathbf{E}_{0t} e^{i(\mathbf{k}_t \cdot \mathbf{r} - \omega_t t)} \quad (1.21)$$

$$\mathbf{H}_i = \mathbf{n}_{\mathbf{k}_i} \times \mathbf{E}_i \quad \mathbf{H}_r = \mathbf{n}_{\mathbf{k}_r} \times \mathbf{E}_r \quad \mathbf{H}_t = \sqrt{\frac{\epsilon_1}{\mu_1}} \mathbf{n}_{\mathbf{k}_t} \times \mathbf{E}_t. \quad (1.22)$$

Introducing the complex index of refraction $N = n + i\kappa$ where

$$\epsilon = \frac{n^2 - \kappa^2}{\mu_1} + \frac{2ni\kappa}{\mu_1} \quad (1.23)$$

Snell's law is

$$N_i \sin \theta_i = N_t \sin \theta_t \quad (1.24)$$

The complex reflectance coefficient are obtained by using the different physical condition set at the interface of the two medium: The photon energy is always conserved and the continuity equation applies for normal component of the of \mathbf{D} and \mathbf{B} , and for the tangential component of \mathbf{E} and \mathbf{H} .

$$r_p = \frac{E_{Or}}{E_{Oi}} = \frac{N^2 \cos \theta_i - \mu_i \sqrt{N^2 - \sin^2 \theta_i}}{N^2 \cos \theta_i + \mu_i \sqrt{N^2 - \sin^2 \theta_i}} \quad (1.25a)$$

$$r_s = \frac{E_{Or}}{E_{Oi}} = \frac{\mu_1 \cos \theta_i - \sqrt{N^2 - \sin^2 \theta_i}}{\mu_1 \cos \theta_i + \sqrt{N^2 - \sin^2 \theta_i}}. \quad (1.25b)$$

At near normal incidence ($\theta_i \approx 0$) of a non magnetic material ($\mu_1 = 1$)

$$r_p = r_s = \frac{1 - N}{1 + N} = |r| e^{i\phi_r}. \quad (1.26)$$

Here, the phase of reflectivity ϕ_r and the reflectivity intensity are related to the index of refraction by

$$\phi_r = \arctan\left(\frac{-2\kappa}{1 - n^2 - \kappa^2}\right) \quad (1.27)$$

$$R = |r|^2 = \left|\frac{1 - N}{1 + N}\right|^2. \quad (1.28)$$

In the following, the reflectivity will directly refer to the intensity rather than the complex factor. The experimental normal incidence reflectivity is the ratio of power intensity reflected from the sample surface and the same surface covered by a perfect reference mirror.

$$R = \frac{I_{\text{sample}}}{I_{\text{reference}}}. \quad (1.29)$$

Below 1 eV gold has a nearly perfect reflecting surface and doesn't oxidize which makes it the perfect reference as can be seen in Figure 1.4. In the visible, silver or aluminum are preferred, having a lower but almost flat reflectivity which can be corrected with the knowledge of their respective reflectivity $R_{\text{reference}}$

$$R = \frac{I_{\text{sample}}}{I_{\text{reference}}} R_{\text{reference}}. \quad (1.30)$$

1.2 Optical models and functions

This section introduces the phenomenological optical models describing the low energy interactions in metals. The Drude model and the extended Drude model are derived. Optical functions and useful relations are also introduced, such as the Kramers-Kronig relations connecting the real and imaginary part of the optical functions.

1.2.1 Drude model

A phenomenological classical model describing the electric conduction in metals was proposed by Drude early in 1900 [3]. Depicted in Figure 1.2, the conduction process is described by the scattering of free (conduction) electrons on lattice impurities or imperfections. In the absence of electrical field electrons have a random motion and the whole electron cloud is static in average. The electrons start to move when an electrical field is applied. The average speed \mathbf{v}_d

1. OPTICAL SPECTROSCOPY OF METALS

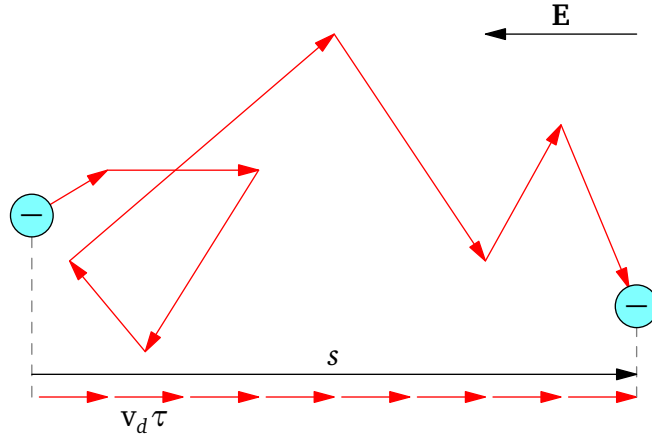


Figure 1.2: Classical representation of an electron motion in metal. When an electrical field is applied the average displacement of an electron between two collision with impurities is $v_d \tau$ giving rise to a net average current parallel to the field.

is calculated classically from the average time between two collisions τ

$$\mathbf{v}_d = \frac{e\mathbf{E}}{\tau m}. \quad (1.31)$$

τ is usually called relaxation time. In this model, the microscopical description of the interactions remains very simple; the scattering rate $\gamma = 1/\tau$ at which the interactions happen is given by random collisions of electrons with impurities, the lattice itself or its defects. In this framework $1/\tau$ is a constant term summing up independently all the contributions by virtue of Matthiessen's rule. At this stage, this model only considers a free gas of electrons so that no interaction between electrons is taken into account.

$$\frac{1}{\tau} = \frac{1}{\tau_{\text{impurities}}} + \frac{1}{\tau_{\text{phonons}}} + \frac{1}{\tau_{\text{defects}}}. \quad (1.32)$$

The current density is then

$$\mathbf{j}_d = ne\mathbf{v}_d = \frac{ne^2\tau}{m}\mathbf{E}. \quad (1.33)$$

n is the charge density, m the bare electron mass and e its charge. A direct comparison with Ohm's law Equation 1.9d allows to define the dc-conductivity

$$\sigma_{\text{dc}} = \frac{ne^2\tau}{m}. \quad (1.34)$$

1.2.1.1 The Drude model in optics

In optics, the dynamical equation for the momentum has the form of an harmonic oscillator

$$\frac{d\mathbf{p}_d}{dt} = -\frac{\mathbf{p}_d}{\tau} - e\mathbf{E}. \quad (1.35)$$

Using an harmonic field, such as Equation 1.7, its solution gives the equivalent energy dependent complex conductivity

$$\sigma(\omega) = \sigma_1(\omega) + i\sigma_2(\omega) = \frac{ne^2}{m} \frac{1}{1/\tau - i\omega} = \frac{\sigma_{dc}}{1 - i\omega\tau}. \quad (1.36)$$

In particular the dc-conductivity is recovered at zero energy. The integration along the energy axis is known as the Thomas-Reich-Kuhn or f-sum rule. It states that apart from constants, the area below the real part of the conductivity is proportional to the number of electrons. The sum rule is written

$$\int_0^\infty \sigma_1(\omega) d\omega = \frac{ne^2\tau}{m} \int_0^\infty \frac{1}{1 + \omega^2\tau^2} d\omega = \frac{\omega_p^2}{8} \quad (1.37)$$

with the plasma frequency defined as

$$\omega_p = \sqrt{\frac{4\pi ne^2}{m}}. \quad (1.38)$$

Simple metals can be fully described –at least at low energy– in terms of their plasma frequency ω_p and scattering rate γ

$$\sigma(\omega) = \frac{i}{4\pi} \frac{\omega_p^2}{i/\tau + \omega}. \quad (1.39)$$

The real and imaginary parts are given by

$$\sigma_1(\omega) = \frac{\omega_p^2\tau}{4\pi} \frac{1}{1 + \omega^2\tau^2} \quad \text{and} \quad \sigma_2(\omega) = \frac{\omega_p^2\tau}{4\pi} \frac{\omega\tau}{1 + \omega^2\tau^2}. \quad (1.40)$$

Optical spectroscopy is able to directly measure n/m whereas dc-transport needs to use the Hall effect. Figure 1.3 shows the principal parameter of the Drude model.

It is also possible to define a partial sum rule where the upper boundary of the integral is set at a certain cutoff. Unlike the f-sum rule which is independent of temperature by definition, the partial integration may be temperature dependent spectral weight transfer and thus may

1. OPTICAL SPECTROSCOPY OF METALS

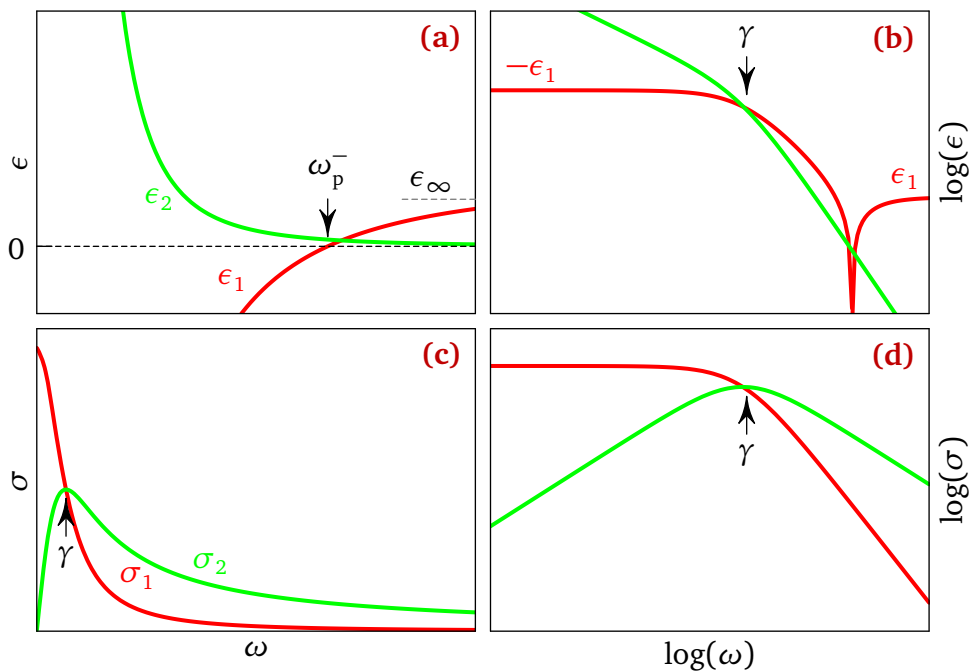


Figure 1.3: (a) and (b) Frequency dependent dielectric constant of the Drude model in linear and logarithmic scale. The dielectric constant is effectively independent of energy up to the scattering rate after which it increase and becomes positive at the plasma frequency. The imaginary part is always positive and only has a change of slopes at γ . (c) and (d) Frequency dependent optical conductivity in linear and logarithmic scale. The real part is nearly constant well below the scattering rate and correspond to the dc-conductivity. Above it falls as ω^{-2} . Whereas the imaginary part has a maximum at γ and then decrease as ω^{-1} . Arrangement from [4].

also vary with temperature

$$N_{\text{eff}}(\omega) = \frac{2mV}{\pi e^2} \int_0^\omega \sigma_1(\Omega) d\Omega \quad (1.41)$$

By integrating over the interband energies, the number of valence electron is recovered; at higher energy, usually above 100 eV, the core electron start to be integrated and the total number of electrons is recovered at infinite energy.

For a superconductor below T_c , the superfluid condensate can be described as a zero energy and zero scattering δ -peak which is experimentally impossible to measure. However the FGT sum rule [5] encounter the problem by using the conservation of spectral weight below and above T_c . The superconducting weight is recovered by subtracting the sum rule above and below T_c

$$\omega_{p,s} = 8 \int_{0^+}^{\infty} \sigma_1(\omega, T_c) - \sigma_1(\omega, T) d\omega \quad (1.42)$$

For a single isolated band around the Fermi level that can be approximated by a tight binding dispersion $\varepsilon_k = -t \cos(ka)$ where t is the hopping parameters and a the lattice constant. Using a low energy cutoff the sum rule also correspond to the kinetic energy of the charge carrier

$$\int_0^\omega \sigma_1(\Omega, T) d\Omega = -\frac{\pi e^2 a^2}{2\hbar^2 V} E_{\text{kin}}(T) \quad (1.43)$$

1.2.1.2 Sheet conductance

For quasi-2D copper oxides such as high- T_c superconductors, the sheet conductance is sometimes used in place of the optical conductivity in order to compare materials with different interlayer spacing $d_c = c/N_L$ (c the out-of-plane lattice spacing and N_L the number of CuO_2 layers per unit cell). This quantity is given in unit of the quantum conductance $G_0 = 2e^2/h$

$$G(\omega) = \frac{\pi K}{1/\tau - i\omega\tau} G_0 \quad (1.44)$$

The spectral weight factor K is defined in electronvolt as

$$\hbar\omega_p^2 = \frac{4\pi e^2}{d_c} K \quad (1.45)$$

The dielectric constant yields

$$\epsilon(\omega) = 1 - \frac{\omega_p^2}{\omega^2 - i\gamma\omega}. \quad (1.46)$$

The Drude model is a good representation of simple metals. The estimation of the density n

1. OPTICAL SPECTROSCOPY OF METALS

is done by multiplying the density of atoms by their valence. This is also called the free electron model and usually predicts plasma frequencies in the UV spectral range. As an example, the reflectivity of three typical metals is shown in Figure 1.4. On the negative side, the match with the experimental data in the UV spectral range is poor due to the onset of interband transitions appearing already in the NIR spectral range as depicted by the sharp rise of the DOS at the same energies. The sharp decrease of reflectivity of the material is usually wrongly attributed to the plasma frequency. As an example, the drop of reflectivity appearing for gold at 2.3 eV or silver at 4 eV is below their plasma frequency and is accounted for interband transition from the $3d$ to the $4s$ bands. An exception can be made for aluminum that has a nearly flat DOS which plasma frequency match very well, except a small dip at 1.5 eV occurring through two parallel bands. Above 5 eV most of the common metals have a poor reflection except aluminum [6]. This favors the use of the latter as mirrors for experiments working in the UV. In this thesis, gold is used as a reference below 1.2 eV, by virtue of a flat and the highest reflectivity. Above this energy and up to 2 eV silver is used instead aluminum principally due to the fact that the former is easily removable from the sample surface using adhesive tape.

1.2.1.3 Hagen-Rubens regime: ($\omega \ll 1/\tau$)

In optics, the Hagen-Rubens equation are extensively used to extrapolate the metallic behavior of samples when the low energy data is lacking (usually $\hbar\omega \leq 15$ meV). At very low energy, when the photon energy is much smaller than the scattering rate ($\omega \ll 1/\tau$), the optical conductivity becomes

$$\sigma_1(\omega) \approx \sigma_{dc} \qquad \sigma_2(\omega) \approx \sigma_{dc}\omega\tau \qquad (1.47)$$

$$\epsilon_1(\omega) \approx 1 - \omega_p^2\tau^2 \qquad \epsilon_2(\omega) \approx \frac{\pi\sigma_{dc}}{2\omega}. \qquad (1.48)$$

Although the imaginary part is much smaller and scales linearly down to zero, the real part of the optical conductivity is nearly constant. On the other hand, the real part of dielectric constant is large and negative, while its imaginary part diverges to large and positive values. The reflectivity can be thus rewritten

$$R(\omega) = \frac{1 - \sqrt{\epsilon}}{1 + \sqrt{\epsilon}} \approx 1 - \sqrt{\frac{2\omega}{\pi\sigma_{dc}}}. \qquad (1.49)$$

1.2.1.4 Relaxation regime: ($\omega = 1/\tau$)

The crossing between real part and imaginary part of both optical conductivity and dielectric constant ($\sigma_1 = \sigma_2$ or $|\epsilon_1| = \epsilon_2$) defines the onset of the relaxation regime. In fact it happens

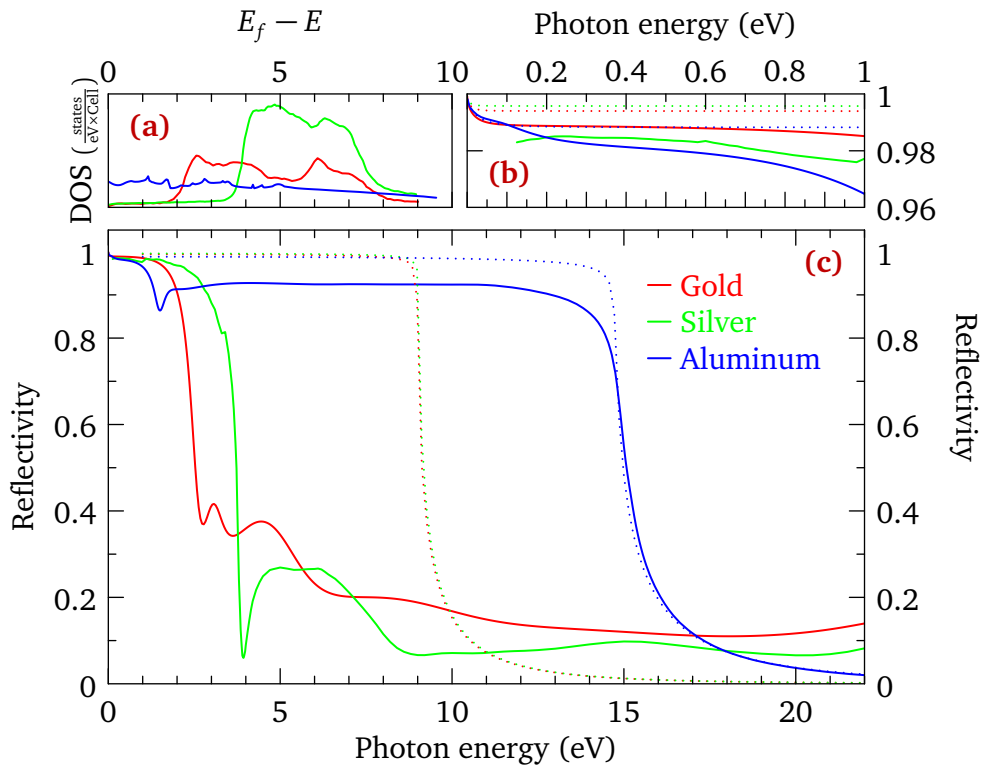


Figure 1.4: (a) Density of states of the three metals. The x-axis matches with panel (c) indicating that the onset of the rise of the DOS correspond to the sharp decrease of reflectivity. The gold DOS is from [7] and for silver [8]. The aluminum DOS was obtained by LDA calculations [9]. The DOS amplitude have been approximately scaled to match LDA calculations. (b) Low energy experimental reflectivity (full line). The aluminum data is reproduced from [10–12], gold and silver [13–15]. The Drude free electron model (dashed lines) was computed from dc-transport and an estimation of the electron density. The model parameters are [13] : gold ($\hbar\omega_p = 8.99$ eV, $\hbar\gamma = 27$ meV), silver ($\hbar\omega_p = 9.02$ eV, $\hbar\gamma = 19$ meV) and aluminum ($\hbar\omega_p = 14.75$ eV, $\hbar\gamma = 87$ meV). (c) Experimental reflectivity (straight line) and model (dashed lines).

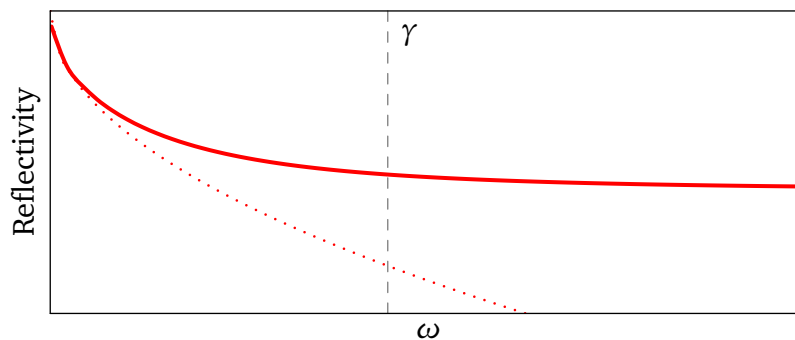


Figure 1.5: Hagen-Rubens fit to the low energy reflectivity. This regime works well for energies below the scattering rate, when the real part of the conductivity is nearly constant.

1. OPTICAL SPECTROSCOPY OF METALS

when $\omega = 1/\tau$ shown in Figure 1.3. For energies $\omega \gg 1/\tau$ but still below ω_p the optical function are well described by

$$\sigma_1(\omega) \approx \frac{\sigma_{dc}}{(\omega\tau)^2} \quad \sigma_2(\omega) \approx \frac{\sigma_{dc}}{\omega\tau} \quad (1.50)$$

$$\epsilon_1(\omega) \approx 1 - \frac{\omega_p^2}{\omega^2} \quad \epsilon_2(\omega) \approx \frac{\omega_p^2}{\omega^3\tau}. \quad (1.51)$$

At higher energy or above $\omega = \gamma$, the system moves from a dissipative to an inductive regime where $\sigma_1(\omega) \gg \sigma_2(\omega)$. The zero-crossing of $\epsilon_1(\omega)$ in Figure 1.3 appears at $\omega_p^- = [\omega_p^2 - (1/\tau)^2]^{1/2}$. In the case of good metal $1/\tau \ll \omega_p$ the crossing appears at the plasma frequency.

1.2.1.5 Transparent regime ($\omega > \omega_p$)

As shown in Figure 1.3, the reflectivity drops above the plasma frequency ($\omega > \omega_p$) and the material becomes transparent. Both the real part and imaginary part of the optical conductivity decreases although with different power law behavior : $\sigma_1(\omega) \propto \omega^{-2}$ and $\sigma_2(\omega) \propto \omega^{-1}$. In addition

$$\epsilon_1(\omega) \approx 1 - \left(\frac{\omega_p}{\omega}\right)^2, \quad (1.52)$$

in the limit $\omega\tau \gg 1$ where $\epsilon_1 \rightarrow 1$. Note that this single component approach is for sure not describing real material at high energy, where the interband transitions are always taking place.

1.2.2 Drude Lorentz model

The Drude formalism can be generalized to describe finite energy modes such as phonons, magnons and other collectives modes. An example of the different collective modes is shown in Figure 2.1. It is possible to start from a quantum model taking into account electronic transitions [2] but for the sake of the simplicity an equivalent classical model is explained. The idea is to describe collective modes as a classical harmonic oscillators. Starting from Equation 1.35 with an additional restoring forces constant K gives

$$\frac{d^2\mathbf{r}}{dt^2} + \frac{1}{\tau} \frac{d\mathbf{r}}{dt} + \omega_0^2 \mathbf{r} = -\frac{e}{m} \mathbf{E}(t). \quad (1.53)$$

$\omega_0 = (K/m)^{1/2}$ is the mode energy. Similarly considering oscillating fields Equation 1.6 the solution leads to the dipole moment $\mathbf{p}(\omega)$ in the energy domain

$$\mathbf{p}(\omega) = -e\mathbf{r}\omega = \frac{e^2\mathbf{E}/m}{(\omega_0^2 - \omega^2) - i\gamma\omega}. \quad (1.54)$$

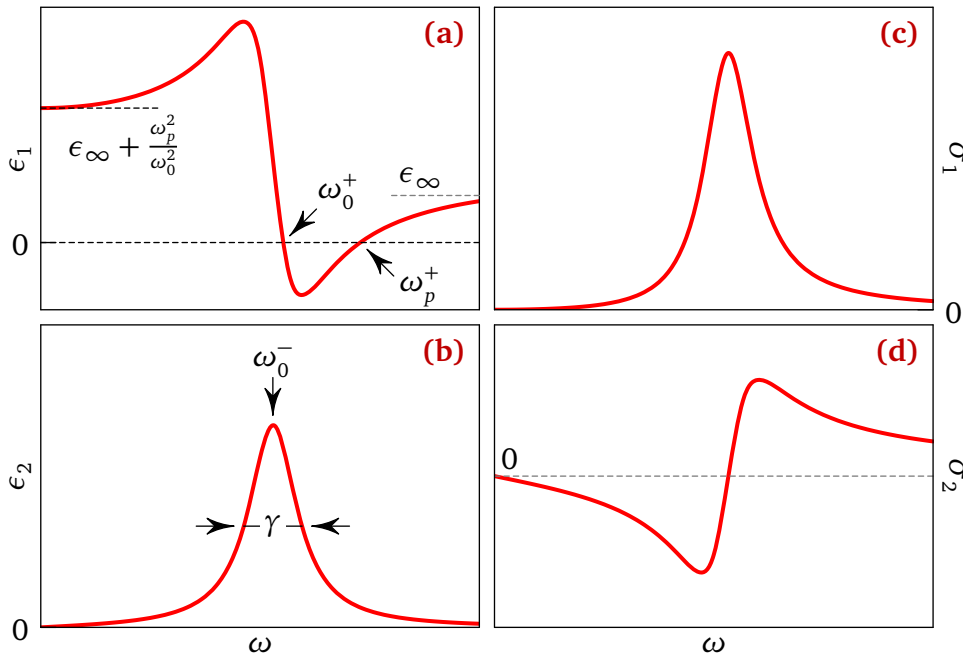


Figure 1.6: Drude-Lorentz model. **(a)** and **(b)** Real and imaginary part of the dielectric constant. The limits are shown on the graph with dashed lines. The indices +/- are used to indicate that the variable is either approaching the constant from the right (+) or from the left (-). **(c)** and **(d)** Real and imaginary part of the optical conductivity.

Identifying the susceptibility and thus the dielectric constant in the total polarization $\mathbf{P} = N\langle\mathbf{p}\rangle = \chi_e\mathbf{E}$ one reads

$$\epsilon(\omega) = 1 + \frac{\omega_p^2}{(\omega_0^2 - \omega^2) - i\gamma\omega} \quad (1.55)$$

$$\sigma(\omega) = \frac{Ne^2}{m} \frac{\omega}{i(\omega_0^2 - \omega^2) + \gamma\omega}. \quad (1.56)$$

Plotting these functions in Figure 1.6 allows to easily recognize the mode energy ω_0 , its broadening $\gamma = 1/\tau$ and its strength ω_p . Depending on the values used in the model, the energy where ϵ_1 crosses zero is approaching the mode energy. The indices used in the figure indicate if the value is respectively approached from lower (-) or higher energies (+). The zero energy mode $\omega_0 = 0$ is indeed the Drude model.

1.2.2.1 Intraband and interband

In real materials, several Drude-Lorentz oscillators are usually needed for a complete description of the optical functions. When the high energy data is not accessible by experiment, it can be described through the ϵ_∞ constant. The total dielectric function is a sum of Drude-Lorentz

1. OPTICAL SPECTROSCOPY OF METALS

oscillators $\epsilon(\omega)$:

$$\epsilon(\omega) = \epsilon_\infty + \sum_{j=1}^n \frac{\omega_{p,j}^2}{(\omega_{0,j}^2 - \omega^2) - i\gamma_j \omega}. \quad (1.57)$$

This model is displayed in Figure 3.13. This description has the advantage of considering all the modes separately. Intraband excitations (mobile charge carriers) of the solid can be easily decoupled from interband (bound charge carrier) provided that they are well separated and a careful fitting is done.

$$\epsilon(\omega) = \epsilon_{\text{cond}} + \epsilon_b + \epsilon_\infty \quad (1.58)$$

The data was fitted using the Drude-Lorentz model using RefFIT software [16]. The total intraband plasma frequency including the Drude peak ($\omega_0 = 0$) is given by

$$\omega_p^2 \equiv \sum_{j=0}^{n_{\text{intra}}} \omega_{p,j}^2. \quad (1.59)$$

where n is the number of intraband oscillators.

The other advantage of having two well separated response is that the high-energy bound-charge dielectric constant can be considered as constant when looking at the low energy conduction response of the solid

$$\epsilon_{\text{bound}}(\omega) = \epsilon_\infty + \sum_{j=n_{\text{intra}}}^n \frac{\omega_{p,j}^2}{\omega_j^2 - \omega(\omega + i\gamma_j)} \quad (1.60)$$

$$\approx \epsilon_\infty + \sum_{j=n_{\text{intra}}}^n \frac{\omega_{p,j}^2}{\omega_j^2} \quad (1.61)$$

This assumption is displayed in Figure 3.14.

1.2.3 Extended Drude model

It is already remarkable how far the Drude model is able to summarize most of the low energy physics of simple metals with only two constant parameters ($1/\tau$, ω_p). However in the presence of strong disorder or strong interactions this model usually breaks down. The typical example is when the typical energy scale describing the strength of interaction is comparable to the kinetic energy of the electrons [2]. The highly correlated systems usually have a more complicated conductivity which can markedly deviate from the Drude model. This is the result of complex electrons or electrons-bosons correlations, which cannot be described by an energy independent scattering rate. The simplest example is a material with an optical conductivity made of a coherent and an incoherent (broader) peak; later one intraband will refer to the process involving the free carrier (coherent + incoherent) response only

The Drude formalism is extended by taking an energy dependent and complex scattering rate [17] which can be derived through specific microscopic models such as the Fermi-liquid model. The Drude optical conductivity is extended by replacing the constant scattering rate by an optical self-energy following Ref. [17], also-called the memory function $M(\omega) = M_1(\omega) + iM_2(\omega)$. By introducing it in place of the constant scattering rate, the optical conductivity becomes

$$\begin{aligned}\sigma(\omega) &= \frac{i}{4\pi} \frac{\omega_p^2}{M(\omega) + \omega} = \frac{i}{4\pi} \frac{\omega_p^2}{M_1(\omega) + iM_2(\omega) + \omega} \\ &= \frac{i}{4\pi} \frac{\omega_p^2}{iM_2(\omega) + \omega(M_1(\omega)/\omega + 1)} = \frac{i}{4\pi} \frac{\omega_p^2}{iM_2(\omega) + \omega(M_1(\omega)/\omega + 1)} \\ &= \frac{i}{4\pi} \frac{\omega_p^2}{i/\tau(\omega) + \omega m^*(\omega)/m}.\end{aligned}\tag{1.62}$$

Comparing with Equation 1.39 gives

$$M_1(\omega) = \omega \left(\frac{m^*(\omega)}{m} - 1 \right)\tag{1.63a}$$

$$M_2(\omega) = 1/\tau(\omega).\tag{1.63b}$$

By causality, the energy-dependent scattering rate is linked to the dynamical mass renormalization factor m^*/m . Different notations are used in the literature [17–19]. Equation 1.62 is rewritten

$$\sigma(\omega) = \frac{i}{4\pi} \frac{\omega_p^{*2}}{i/\tau^*(\omega) + \omega}\tag{1.64}$$

The optical scattering rate $1/\tau^*$ is renormalized by the effective mass and is replaced by $1/\tau^*(\omega) \equiv \frac{m^*(\omega)}{m} 1/\tau(\omega)$. The optical resistivity $\rho(\omega) = \sigma_1^{-1}(\omega)$ is also widely used and a quick comparison gives¹

$$M_2(\omega) \equiv 1/\tau_{\text{opt}}(\omega) \equiv 1/\tau(\omega) = \frac{\omega_p^2}{4\pi} \rho(\omega) = \frac{m^*}{m} 1/\tau^*(\omega)\tag{1.65}$$

Even if the extended Drude model is able to describe the complex variation of the low energy scattering rate it remain a single component model which make it unable to describe interband transitions. In such a case, the high energy modes are subtracted from the optical conductivity prior to the conversion to the memory function. Hopefully for both cuprates and the single layer ruthenate intraband transitions are well separated from the interband response [20]; the extension of the Lorentz modes is assumed to be negligible at low energy and are thus replaced

¹Since the resistivity is usually expressed in $\Omega \text{ cm}$ it is necessary to use conversion factor to get the scattering rate expressed in eV : $\hbar/\tau = \frac{\rho(\hbar\omega_p)^2}{4\pi\hbar} = \rho(\hbar\omega_p)^2 * 134.51715$ with ρ in $\Omega \text{ cm}$ and $\hbar\omega_p$ in eV. $\hbar = 6.5822 \times 10^{-16} \text{ eV s}$ and $1 \Omega \text{ cm} = 1.11265006 \times 10^{-12} \text{ s}$.

1. OPTICAL SPECTROSCOPY OF METALS

by constant dielectric functions. At least part of the lowest energy interband transitions are accessible by experiment and can be fitted by assuming that they follow the Drude-Lorentz model. Additionally, the higher energy modes that cannot be measured in the experiment have a simple constant impact on the low-energy data so that they summarized into the constant ϵ_∞ . Adding all the transition together leads to

$$\epsilon_b = \epsilon_\infty + \sum_{i=1}^n \frac{\omega_{p,i}^2}{\omega_{0,i}^2}. \quad (1.66)$$

which can later be removed from the main component.

$$M_1(\omega) = \frac{\omega_p^2}{\omega} \frac{\epsilon_b - \epsilon_1(\omega)}{(\epsilon_b - \epsilon_1(\omega))^2 + \epsilon_2^2(\omega)} - \omega \quad (1.67a)$$

$$M_2(\omega) = \frac{\omega_p^2}{\omega} \frac{\epsilon_2(\omega)}{(\epsilon_b - \epsilon_1(\omega))^2 + \epsilon_2^2(\omega)}. \quad (1.67b)$$

1.2.3.1 Clausius Mossotti relation

The polarizability at low energy from interband transitions can be approximately by retrieved using the Clausius-Mossotti relation [21], which supposes a simple homogeneous cubic structure

$$\frac{\epsilon - 1}{\epsilon + 2} = \frac{4\pi}{3} n\alpha. \quad (1.68)$$

The dielectric constant is

$$\epsilon = 1 + \frac{4\pi n\alpha}{1 - 4\pi n\alpha/3}. \quad (1.69)$$

where α is the ionic polarizability, $n = N/V$ the density of atoms per unit cell. In this thesis, both the oxygen of cuprates and ruthenate have the highest polarizability compared to other atoms in the structures [22]. It is therefore possible to count only for the contribution of O^{2-} where $\alpha = 3.88 \times 10^{-24} \text{ cm}^3$ [23] For $\text{HgBa}_2\text{CuO}_{4+x}$ the cell parameters are $a = b = 3.85 \text{ \AA}$, $c = 9.5 \text{ \AA}$ and contain 4 oxygen atoms per unit cell which leads to $\epsilon_b = 3.57$. For Sr_2RuO_4 $a = b = 3.8730(3) \text{ \AA}$, $c = 12.7323(9) \text{ \AA}$ [24] and contain also 4 oxygen atoms which gives $\epsilon_b = 2.55$. Taking into account all the contribution gives 2.82 which indicate the importance of the oxygen cation in these material [25].

1.2.4 Kramers-Kronig relations

The Kramers-Kronig relations relates the real and imaginary part of any causal response function by the principle that the stimulus always comes before any response. From the linear response

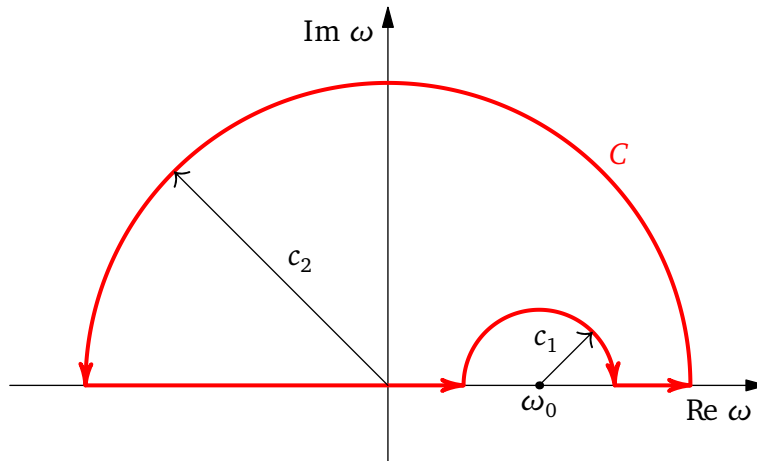


Figure 1.7: Contour integral over the real and imaginary energy axis.

theory, the differential equation representing the response to an external perturbation $j(\mathbf{r}, t)$ is

$$D\varphi(\mathbf{r}, t) = j(\mathbf{r}, t), \quad (1.70)$$

with D , the differential operator. The response $\varphi(\mathbf{r}, t)$ is given by the convolution of the response –a Green’s function– with the perturbation itself

$$\varphi(\mathbf{r}, t) = \iint_{-\infty}^{\infty} G(\mathbf{r}, \mathbf{r}', t, t') j(\mathbf{r}', t') d\mathbf{r}' dt'. \quad (1.71)$$

The main argument is that the system is causal and the origin of time is not essential

$$G(t - t') = 0 \quad t < t'. \quad (1.72)$$

In addition the medium is homogeneous and isotropic so that the response reduces to

$$\varphi(t) = \int_{-\infty}^t G(t - t') j(t') dt'. \quad (1.73)$$

In Fourier space the convolution is simply the product

$$\varphi(\omega) = G(\omega) j(\omega). \quad (1.74)$$

Further assuming that the energy is complex $\omega = \omega_1 + i\omega_2$ the Fourier transform of $G(t - t')$ is therefor

$$G(\omega) = \int G(t - t') e^{i\omega_1(t-t')} e^{-\omega_2(t-t')} dt. \quad (1.75)$$

$e^{-\omega_2(t-t')}$ is bounded in the upper half of the complex plane for $t - t' > 0$ and in the lower half

1. OPTICAL SPECTROSCOPY OF METALS

for $t - t' < 0$. By virtue of Equation 1.72, the integral is thus limited in the upper half plane. The contour C is represented by Figure 1.7 with a small diameter $c_2 \rightarrow 0$ and a large circle $c_1 \rightarrow \infty$. All the poles happen on the real axis so that the Cauchy theorem over C gives

$$\oint_C \frac{G(\omega')}{\omega' - \omega_0} d\omega' = 0. \quad (1.76)$$

Since $G(\omega' \rightarrow \infty) \rightarrow 0$ the integration over the large radius gives zero contribution. The remaining contribution can be achieved through Dirac identities, the small circle can be parametrized using $\omega' = \omega_0 - c_2 e^{i\theta}$ and in the limit where c_2 tends to zero and gives the imaginary part of the identity. The contribution from the remaining real axis gives its principle part \mathcal{P}

$$\mathcal{P} \int_{-\infty}^{\infty} \frac{G(\omega')}{\omega' - \omega_0} d\omega' - i\pi G(\omega_0) = 0. \quad (1.77)$$

By redefining $\omega_0 = \omega$ the Kramers-Kronig relations are obtained.

$$\begin{aligned} G_1(\omega) &= \frac{1}{\pi} \mathcal{P} \int_{-\infty}^{\infty} \frac{G_2(\omega')}{\omega' - \omega} d\omega' \\ G_2(\omega) &= -\frac{1}{\pi} \mathcal{P} \int_{-\infty}^{\infty} \frac{G_1(\omega')}{\omega' - \omega} d\omega'. \end{aligned} \quad (1.78)$$

By virtue of the causality principle, this equation permits to recover either the real or imaginary part if a full knowledge of the energy dependence of the opposite part is known. As an example, the KKR are deduced in the following sections for the optical conductivity and reflectivity. The other relations for the dielectric constant and index of refraction can be found in [2].

1.2.4.1 Optical conductivity

Looking at Ohm's law Equation 1.9d, one can see that the complex optical conductivity $\sigma(\omega)$ is the response function of the current density. Since the energy axis in optic is positive, one can use the fact that σ_1 is an even function ($\sigma_1(-\omega) = \sigma_1(\omega)$) and σ_2 is odd ($\sigma_2(\omega) = -\sigma_2(\omega)$) to restrict the integration to the positive part of the energy axis.

$$\begin{aligned} \sigma_1(\omega) &= \frac{2}{\pi} \mathcal{P} \int_0^{\infty} \frac{\omega' \sigma_2(\omega')}{\omega'^2 - \omega^2} d\omega' \\ \sigma_2(\omega) &= \frac{2\omega}{\pi} \mathcal{P} \int_0^{\infty} \frac{\sigma_2(\omega')}{\omega'^2 - \omega^2} d\omega'. \end{aligned} \quad (1.79)$$

For the reflectivity, it is more complicated. In particular one has to study thoroughly the analytical structure of the final equation. For s -polarized light and p -polarized light with

an angle of incidence less than 45° with the surface normal one can once again formulate Kramers-Kronig relations for the phase and the logarithm of the reflectivity amplitude

$$r = \frac{1 - \sqrt{\epsilon}}{1 + \sqrt{\epsilon}} = \sqrt{R}e^{i\phi_r}. \quad (1.80)$$

The KKR can be written using $\ln(r) = \ln \sqrt{R(\omega)} + i\phi_r(\omega)$ to recover the phase information from the reflected power (reflectivity)

$$\phi_r(\omega) = -\frac{2\omega}{\pi} \mathcal{P} \int_0^\infty \frac{\ln \sqrt{R(\omega')}}{\omega'^2 - \omega^2} d\omega' + \phi_r(0). \quad (1.81)$$

1.2.4.2 Complex reflectivity

The typical experimental apparatus used in this thesis covers a wide energy range spreading from 0.003 eV to 6 eV (x-FIR to UV). Nonetheless the integration of Equation 1.81 spans energies from zero to infinity which mean that the missing information beyond the boundaries may strongly affect the calculated optical function within that range. Consequently, careful extrapolation are essential to guarantee the optical functions data at least at energies far inside the experimental spectral range. Many strategies exist and a comparison of the techniques is shown in Figure 1.8.

The low-energy window of metals-like material (0 meV to 8 meV) is usually extrapolated by the Hagen-Rubens Equation 1.49. A different approaches consists of a Drude fit, a double Drude or a sum of Drude and Lorentzian oscillators. Whatever the method used, the fit is then mapped onto energies down to zero and stitched to the experimental data. In this thesis, both approaches are used and give almost similar results. For insulating materials, the optical parameters are simply extrapolated using the Drude-Lorentz model.

The traditional way of extrapolating the data at high energy is based on the assumptions of remaining interband transitions and also on the free electron model [26, 27]. Between $\omega_{\text{HF}} = 5$ eV and 50 eV interband transitions (see Figure 2.1) continue to occur and contribute to the reflectivity, the data is usually extrapolated with a power-law function and the lack of knowledge of the interband processes is determined by adjusting the power s (usually between 0.5 and 3) in order to match the slope of the data

$$R(\omega) = R(\omega_{\text{HF}}) \left(\frac{\omega_{\text{HF}}}{\omega} \right)^s. \quad (1.82)$$

Beyond 100 eV the free-electron asymptotic limit is used with $s = 4$ in Equation 1.82.

The method used in this thesis is rather different and use of Drude-Lorentz fit for both the reflectivity data and the ellipsometric complex function. In this respect, the Kramers-Kronig relations are anchored and an extrapolation up to 150 eV allows the Kramers-Kronig transformed reflectivity to closely match up to the maximum energy of the data (See Figure 1.8).

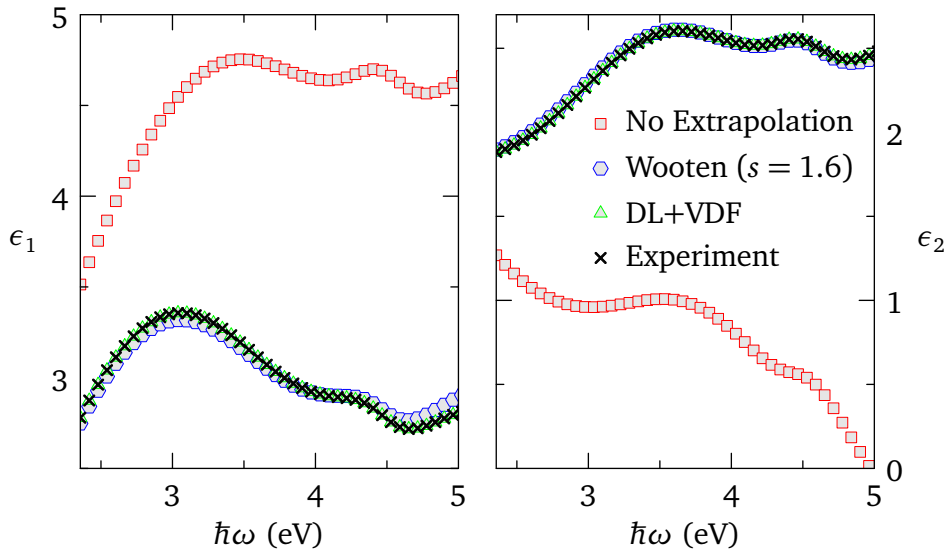


Figure 1.8: In-plane dielectric function of Sr_2RuO_4 from the ellipsometric measurement compared to Kramers-Kronig transformation of the data with and without extrapolations. In the case of the Wooten extrapolation, a good match is obtained with $s = 1.6$. The Drude-Lorentz (DL) and variable dielectric function (VDF) [28] extrapolation give an imperceptible difference with the experiment, here ellipsometry.

Another approach and an extensive comparison for different value of the parameter s is shown by Tanner *et al.* [29]. This method uses x-ray atomic scattering functions presented by Henkel *et al.* [30] on the assumption that the solid is a linear combination of its atomic constituents.

1.3 Kubo formula

The previous models are phenomenological, which directly relate classical or semi-classical effects to optical functions. On the other hand, the Kubo formula, which is also known as the fluctuation-dissipation theorem, relates the linear response of an observable –such as the optical conductivity– to a time-dependent perturbation. The resistivity is computed from the dc current-current correlation function. This framework has the advantage of being a bridge from the microscopic model and the optical functions. It allows to separately define the correlation between the constituent of the matter and include them later on a self-energy term or spectral function.

This framework use a large variety of theoretical concepts, in this thesis the general Kubo formula derivation follows the course textbook by Berthod [31] but many alternatives exist in the literature and textbooks [2, 32–35]. This section is mostly theoretical but is important for completeness of the underlying Fermi-liquid model introduced in section 1.4. The reader may refer to the small cartoon shown in Figure 1.9 in order to understand at least superficially

the physical processes and the meaning of the different functions and operators behind this considerable theory.

1.3.1 Perturbation theory

As a starting point we first define the concept of perturbation theory for the particle-current density operator \mathbf{j} and rewrite the Ohm's law Equation 1.9d in a form that allows the identification of the optical conductivity.

The first-order variation of the property A induced by a field F which couples to the property B is proportional to the retarded correlation function of operators A and B , evaluated in absence of field

$$\langle A(t) \rangle_V^{1^{\text{st}}\text{order}} = \int \chi_{AB}(t-t_1) * F(t_1) dt_1. \quad (1.83)$$

The retarded correlation function is defined as

$$\chi(t) = -\frac{i}{\hbar} \theta(t) \langle [A(t), B(0)] \rangle = C_{AB}^R(t). \quad (1.84)$$

For non-interacting independent particles the derivation is straightforward from the single-particles energies, and works in principle at zero temperature. For interacting particles, the imaginary-time formalism [31] is needed and the correlation function becomes

$$\chi(t) = -\langle T_\tau A(\tau) B(0) \rangle = \mathcal{C}_{AB}(\tau) \quad (1.85)$$

where T_τ is the τ -ordering operator. Using Equation 1.83

$$\langle A(t) \rangle_V^{1^{\text{st}}\text{order}} = \int \frac{d\omega}{2\pi} e^{-i\omega t} \mathcal{C}_{AB}(i\nu_n \rightarrow \omega + i0^+) * F(\omega). \quad (1.86)$$

$i\nu_n \rightarrow \omega + i0^+$ is used for recovering back the usual energy axis from the imaginary time formalism. The next step is to use the particle-current density operator which is split into a paramagnetic and diamagnetic part $\mathbf{j}(\mathbf{r}, t) = \mathbf{j}^p(\mathbf{r}, t) + \mathbf{j}^d(\mathbf{r}, t)$

$$\mathbf{j}^p(\mathbf{r}) = \frac{i\hbar}{2m} \sum_\zeta [(\nabla_{\mathbf{r}} a_{\mathbf{r}\zeta}^\dagger) a_{\mathbf{r}\zeta} - a_{\mathbf{r}\zeta}^\dagger (\nabla_{\mathbf{r}} a_{\mathbf{r}\zeta})] \quad (1.87a)$$

$$\mathbf{j}^d(\mathbf{r}) = -\frac{e}{m} \sum_\zeta \mathbf{A}(\mathbf{r}) a_{\mathbf{r}\zeta}^\dagger a_{\mathbf{r}\zeta}. \quad (1.87b)$$

$a_{\mathbf{r}\zeta}^\dagger$ and $a_{\mathbf{r}\zeta}$ are respectively the creation and destruction operator of a particle at a position \mathbf{r} with spin ζ . Then, the particle-current operator averaged over the volume V is written as

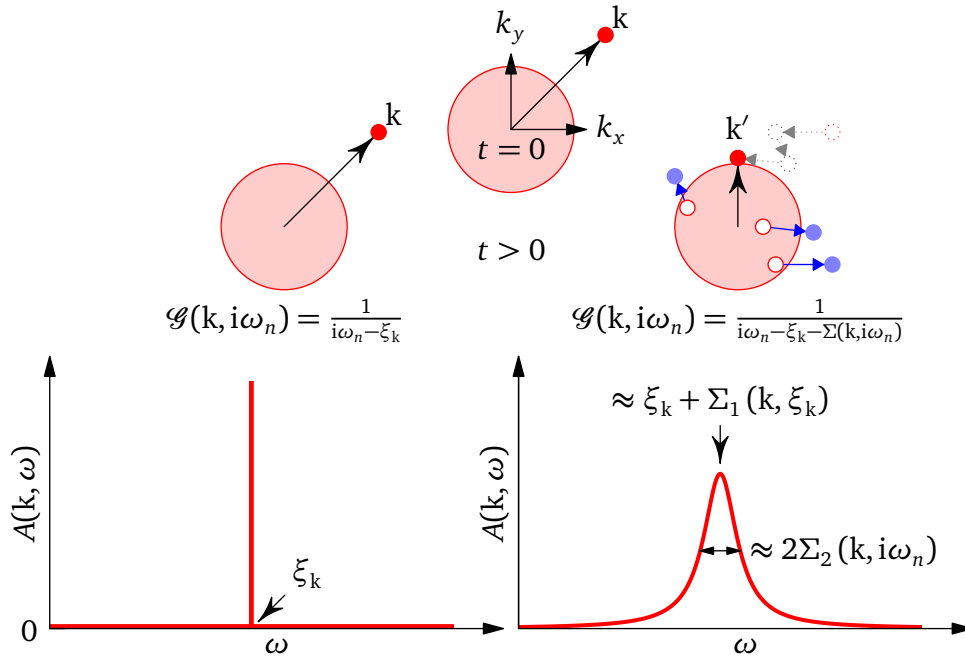


Figure 1.9: Representation of the Green's and spectral functions of an interacting and non-interacting Fermi gas. An electron with momentum \mathbf{k} is added at time $t = 0$. After an elapsed time $t > 0$ the non-interacting electron is unchanged while the other had time to interact with the electrons below the Fermi surface losing its energy and changing its momentum by leaving a bunch of electron-hole pairs. The resulting Green's function of the interacting gas has self-energy $\Sigma(\mathbf{k}, i\omega_n)$.

Matsubara energies. \mathcal{G} is the Green's function defined as

$$\mathcal{G}(\mathbf{k}, i\omega_n) = \frac{1}{i\omega_n - \xi_{\mathbf{k}} - \Sigma(\mathbf{k}, i\omega_n)} \quad (1.95)$$

With the self-energy $\Sigma(\mathbf{k}, i\omega_n) = \Sigma_1 + i\Sigma_2$ and $\xi_{\mathbf{k}} = E_{\mathbf{k}-\mu}$ and μ is the chemical potential. Σ_2 is usually called the quasiparticle scattering rate, which is different from the optical scattering rate. On the other side Σ_1 take into account the renormalization due to the interactions. Without vertex corrections, the electron-hole interactions are nonexistent and the particles evolve independently implying a product of two single particle Green's functions. From Migdal theorem the vertex corrections are assumed small [36] so that by using Equation 1.94 in Equation 1.92 with the Green function of Equation 1.95 gives

$$\begin{aligned} \sigma_{\mu\nu}(\mathbf{q}, \omega) \approx & \frac{ie^2\hbar}{\omega} \left[\frac{1}{\mathcal{V}} \sum_{\mathbf{k}\sigma} \left(\mathbf{k}_\mu + \frac{\mathbf{q}_\mu}{2} \right) \left(\mathbf{k}_\nu + \frac{\mathbf{q}_\nu}{2} \right) \int d\varepsilon_1 d\varepsilon_2 A(\mathbf{k}, \varepsilon_1) A(\mathbf{k}, \varepsilon_2) \right. \\ & \left. \times \frac{f(\varepsilon_1) - f(\varepsilon_2)}{\Omega_n + \varepsilon_1 - \varepsilon_2} + \delta_{\mu\nu} \frac{\langle n \rangle}{m} \right] + \text{vertex corrections.} \end{aligned} \quad (1.96)$$

$A(\mathbf{k}, \varepsilon) = -\text{Im } \mathcal{G}(\mathbf{k}, \varepsilon)$ is the one-electron spectral function.

1.3.2 Kubo formula in optics

For a local model, the vertex corrections of Equation 1.96 vanish by symmetry due to the fact that the self-energy is momentum independent [37]. The link with the spectral function $A(\mathbf{k}, \omega)$ is therefore given by

$$A(\mathbf{k}, \omega) = -\frac{1}{\pi} \text{Im} \mathcal{G}(\mathbf{k}, i\nu_n \rightarrow \omega + i0^+) = \frac{-\Sigma_2(\omega)/\pi}{[\omega - \xi_{\mathbf{k}} - \Sigma_1(\omega)]^2 + [\Sigma_2(\omega)]^2}. \quad (1.97)$$

In optics transfer of momentum is usually negligible so that $q = 0$ and the final Kubo formula for the conductivity is written

$$\begin{aligned} \text{Re } \sigma_{\mu\nu}(\mathbf{q} = 0, \omega) &= -\frac{e^2 \hbar}{\omega} \frac{1}{\mathcal{V}} \text{Im} \chi_{jj}^{\mu\nu}(\mathbf{0}, i\Omega_n \rightarrow \omega + i0^+) \\ &= \frac{\pi e^2 \hbar^3}{m^2 \omega} \frac{1}{\mathcal{V}} \sum_{\mathbf{k}\sigma} \mathbf{k}_\mu \mathbf{k}_\nu \int d\varepsilon A(\mathbf{k}, \varepsilon) A(\mathbf{k}, \varepsilon + \omega) [f(\varepsilon) - f(\varepsilon + \omega)] \end{aligned} \quad (1.98)$$

By introducing the group velocity $\mathbf{v}_{\mathbf{k}} = 1/\hbar \nabla \mathbf{E}_{\mathbf{k}}$ and inserting Equation 1.97 in Equation 1.98 The real part of the isotropic optical conductivity is

$$\sigma_1(\omega) = \frac{\pi}{\omega} \int_{-\infty}^{\infty} d\varepsilon [f(\varepsilon) - f(\varepsilon + \omega)] \int_{-\infty}^{\infty} d\xi \Phi(\xi) A(\xi, \varepsilon) A(\xi, \varepsilon + \omega). \quad (1.99)$$

The transport function is defined as

$$\Phi(\xi) = \frac{2e^2}{dL^d} \sum_{\mathbf{k}} \mathbf{v}_{\mathbf{k}}^2 \delta(\xi - \xi_{\mathbf{k}}) \quad (1.100)$$

with d the dimensionality ($\mathcal{V} = L^d$). Whereas the spectral function is peaked at $\varepsilon \approx \xi$ the transport function $\Phi(\xi)$ (proportional to the average of the group velocity at energy ξ), is usually a slow function of its argument so that it can be approximated as a constant value set a zero energy. Finally Equation 1.99 further reduces to the Allen formula

$$\sigma(\omega) = \frac{i\Phi(0)}{\omega} \int_{-\infty}^{\infty} d\varepsilon \frac{f(\varepsilon) - f(\varepsilon + \omega)}{\omega + \Sigma^*(\varepsilon) - \Sigma(\varepsilon + \omega)}. \quad (1.101)$$

Where $f(\varepsilon) = [\exp\{\varepsilon/(k_B T)\} + 1]^{-1}$ is the Fermi-Dirac function, $b(\varepsilon) = [\exp\{\varepsilon/(k_B T)\} - 1]^{-1}$ is the Bose-Einstein function and Σ^* is the complex conjugate of the selfenergy. It is interesting to see that if the self-energy of independent particles is taken as a constant scattering term $\Sigma(\varepsilon) = -i\hbar/(2\tau_D)$ (in the three dimensional electron gas framework) the Drude model $\rho = m/(ne^2\tau)$ is recovered by identifying $\Phi(0)$ to the intraband spectral weight $\Phi(0) = \omega_p/4\pi = ne^2/m$. In

term of the extended Drude model, the Allen formula becomes

$$M(\omega) = \omega \left\{ \int_{-\infty}^{\infty} \frac{f(\xi) - f(\xi + \omega)}{\omega + \Sigma^*(\xi) - \Sigma(\xi + \omega) + i\Gamma_{\text{imp}}} d\xi \right\}^{-1} - \omega. \quad (1.102)$$

Here the constant impurity scattering rate Γ_{imp} has been pulled out of from the self-energy. The Allen formula is the key ingredient between the microscopic theory of a conventional metal and the experiment. The self-energy is computed for electrons coupled to a local collective mode. This general form derived in [38] allows to even further simplify the model by the product of a coupling function to the imaginary part of a momentum averaged susceptibility (assumed to be momentum independent): $\alpha^2 \chi_2(\omega)$

$$\begin{aligned} \Sigma(\omega) &= \Sigma_1(\omega) + i\Sigma_2(\omega) = \frac{1}{\pi} \int_{-\infty}^{\infty} d\Omega \alpha^2 \chi_2(\Omega) \int_{-\infty}^{\infty} d\varepsilon N(\varepsilon) \frac{f(-\varepsilon) + b(\Omega)}{\omega - \Omega - \varepsilon + i0^+} \\ &= \frac{N(0)}{\pi} \int_0^{\infty} d\Omega \alpha^2 \chi_2(\Omega) \int_{-D}^D d\varepsilon \left[\frac{f(-\varepsilon) + b(\Omega)}{\omega - \Omega - \varepsilon + i0^+} + \frac{f(\varepsilon) + b(\Omega)}{\omega + \Omega - \varepsilon + i0^+} \right]. \end{aligned} \quad (1.103)$$

In other words $\chi_2(\omega)$ can be seen as the boson density of states. $N(\varepsilon)$ is the electron DOS (per spin). The scattering process can be understood as follows: an electron relaxes by emitting a boson. The initial state has an electron at energy ω and no boson, the final state has an electron at energy $\varepsilon = \omega - \Omega$ and a boson at energy Ω . The process is possible if the final state exists (factors $\chi_2(\Omega)$ and $N(\varepsilon)$) and is available (empty final state for the electron, factor $f(-\varepsilon)$)², and the enhancement term $b(\Omega)$ is the stimulated emission. At the second line, we have assumed a constant electronic DOS $N(\varepsilon) = N_0$ over the bandwidth $[-D, +D]$, used the fact that the function $\alpha^2 \chi_2(\Omega)$ is odd in Ω , and used the relations $f(-\varepsilon) = 1 - f(\varepsilon)$ and $b(-\Omega) = -1 - b(\Omega)$.

Different notations are used in the literature [2, 38–40], in this thesis $\alpha^2 \chi_2(\Omega)$ is used in the theory while experimental and phenomenological models use the so-called glue function defined as $\Pi(\Omega) = \frac{N_0}{\pi} \alpha^2 \chi_2(\Omega)$. We also define the kernel function [42]

$$L(\omega, \Omega) = \int_{-D}^D d\varepsilon \left[\frac{f(-\varepsilon) + b(\Omega)}{\omega - \Omega - \varepsilon + i0^+} + \frac{f(\varepsilon) + b(\Omega)}{\omega + \Omega - \varepsilon + i0^+} \right]. \quad (1.104)$$

The integration over the bandwidth D gives

$$\begin{aligned} L(\omega, \Omega) &= -i\pi \coth\left(\frac{\Omega}{2k_B T}\right) + \psi\left(\frac{1}{2} + i\frac{\Omega - \omega}{2\pi k_B T}\right) \\ &\quad - \psi\left(\frac{1}{2} - i\frac{\Omega + \omega}{2\pi k_B T}\right) + b(\Omega) \ln \left| \frac{(D + \omega)^2 - \Omega^2}{(D - \omega)^2 - \Omega^2} \right|. \end{aligned} \quad (1.105)$$

²There is no such factor for the boson because the final state of the boson does not needs be empty

1. OPTICAL SPECTROSCOPY OF METALS

ψ is the digamma function defined as

$$\psi(z) = \lim_{M \rightarrow \infty} \left[\ln M - \sum_{n=0}^M \frac{1}{(n+z)} \right]. \quad (1.106)$$

The last term of Equation 1.105 vanishes for $D \rightarrow \infty$, but only if $|\omega| < D$ and $|\Omega| < D$ [43]. This means that, if the kernel is used in an integral on ω and/or Ω , and if the behavior at $|\omega| \rightarrow \infty$ and/or $|\Omega| \rightarrow \infty$ is controlled by the kernel, it is not allowed to discard this term. The integral must be performed with it and D is sent to infinity after. Allen took the problem differently by sending the bandwidth to infinity and used explicit Debye-like cutoff introduced on the Ω integral [44]. Anyway as shown in section 1.4.4.2, the Fermi liquid, for which $\alpha^2 \chi_2(\Omega) \propto \Omega$ without high-energy cutoff has no problem with the imaginary part. The self-energy can be written in a more compact form

$$\Sigma(\omega) = \int_0^\infty \Pi(\Omega) L(\omega, \Omega) d\Omega. \quad (1.107)$$

The mass renormalization factor is related by

$$\lambda = 2 \int_0^\infty \frac{\Pi(\omega)}{\omega} d\omega \quad (1.108)$$

and

$$\frac{m^*}{m} = 1 + \lambda \quad (1.109)$$

One of the major unanswered question of high- T_c superconductivity is its microscopical mechanism. For standard superconductor the BCS theory clearly explains that it shows up through the condensation of Cooper pairs into a boson-like state and that *glue* overcoming the Coulomb repulsion comes from the lattice and is called the electron-phonon coupling $\alpha^2 F(\omega)$. The evidence of this mechanism was linked with underlying lattice by Maxwell [45] and Reynolds et al. [46] and is know as the isotope effect: they showed that T_c was scaling with the mass of the lattice ions as the Debye energy was. That lead Bardeen Cooper and Schrieffer to their theory [47]. When electron-phonon interactions are small the BCS equation is

$$k_B T = 1.14 \hbar \omega e^{-\frac{1}{N(0)U}} \quad (1.110)$$

Where the mass dependence is in the pre-factor, $N(0)$ is the density of states at the Fermi surface and U is the interaction potential. In the case of high- T_c , the precise mechanism is still not known and the *glue* or bosonic spectral function must remain a generic function $\Pi(\omega)$. It could be composed by phonons, spin and charge fluctuations and other modes to couple to. The

starting point is at least the assumption that the unperturbed state is a Fermi-liquid [48].

1.3.3 Kubo formula in transport

It is also possible to define the zero energy Kubo resistivity [38]

$$\rho_K(T) = \frac{2}{\hbar\Phi(0)} \left[\int_{-\infty}^{\infty} d\varepsilon \frac{f'(\varepsilon)}{\Sigma_2(\varepsilon)} \right]^{-1}. \quad (1.111)$$

Here $f'(\varepsilon)$ is the derivative of the Fermi function. Equation 1.111 measures the inverse of the thermally-averaged inverse electronic scattering for electrons ($\Sigma_2(\varepsilon)$) within a few $k_B T$ of the Fermi surface. The imaginary part of the self-energy is

$$-\Sigma_2(\varepsilon) = N(0) \int_0^{\infty} d\Omega \alpha^2 \chi_2(\Omega) \times [f(\Omega - \varepsilon) + f(\Omega + \varepsilon) + 2b(\Omega)]. \quad (1.112)$$

Depending on the form of the self-energy, this equation may require numerical integration. With special forms of $\alpha^2 \chi_2(\Omega)$ such as the Fermi-liquid model, this formalism is new and specially developed to fit the dc-transport of Sr_2RuO_4 in section 4.3.2.

It is possible to approach it analytically by taking the multiplicative inverse directly to the integrand and thus the thermally averaged scattering rate, which leads to

$$\rho_Z(T) = \frac{2}{\hbar\Phi(0)} \int_{-\infty}^{\infty} d\varepsilon f'(\varepsilon) \Sigma_2(\varepsilon). \quad (1.113)$$

Introducing Equation 1.112 into Equation 1.113 and after some algebra

$$\rho_Z = \frac{4N(0)}{\hbar\Phi(0)} \frac{1}{k_B T} \int_0^{\infty} d\Omega \alpha^2 \chi_2(\Omega) \Omega b(\Omega) [b(\Omega) + 1]. \quad (1.114)$$

In the literature, this formula is equivalent to the Ziman formula [40] used by Allen in [39].

$$\rho(T) = \frac{4\pi m \hbar}{k_B T n e^2} \int_0^{\infty} d\omega \alpha^2 \chi_2(\omega) \omega b(\omega) [b(\omega) + 1] d\omega. \quad (1.115)$$

Which could also be rewritten in term of the plasma frequency and simplified by expanding the Bose-Einstein function

$$\rho(T) = \frac{\hbar}{k_B T} \frac{1}{2\omega_p^2} \int_0^{\infty} \frac{\omega \Pi(\omega)}{\cosh\left(\frac{\omega}{k_B T}\right) - 1} d\omega \quad (1.116)$$

1.4 Fermi-liquid

The Fermi-liquid model is a description of the electronic interactions in metals. The solution came from Landau [49] starting with a non-interacting gas of particles, the so-called Fermi gas. By Pauli's exclusion principle and energy conservation, the ground state of electron gas is a sum of all different momenta piling up to the Fermi momentum. In this framework, the lattice is playing no role and the gas is following the Fermi statistics. By slowly turning on interactions the ground state is adiabatically transformed into the ground state of the interacting system. It is possible to produce excitations or quasiparticles (particle-hole) which are responsible for the material properties such as the classical Drude-conduction electrons. This gas thus becomes a Fermi-liquid. The impact of the interaction leads to a renormalization of the mass, magnetic moment and other dynamical properties of the quasiparticles although keeping the spin, the charge, and the momentum unaffected. This renormalization can be extremely high such as in heavy fermions where effective mass can be up to three order of magnitude the bare electron mass [50]. Close to the Fermi energy the quasiparticles excitations are long lived with a lifetime τ much larger than the Fermi energy ($1/\tau \ll \varepsilon_F$). The advantage of that model is that the interactions are embedded in the effective mass, keeping a direct correspondence with the previous semi-classical formula such as the Drude model explaining the fact why this classical formula is working for simple metals.

1.4.1 The Fermi-liquid in optics

In this section the fundamental optical properties of Fermi-liquids will be presented. It will be shown that at low energy, the Fermi-liquid is mostly mapped onto the Drude model, but deviations appear at higher energy, which are the main fingerprint of this model.

The derivation is a continuation of the previous section 1.4.4.2. First by assuming that the coupling $\alpha^2 \chi_2(\omega)$ is valid to the infinity [39], the self energy becomes a function depending only on the square energy and temperature plus three parameters defining the material properties. That is the power of this formalism, and it basically tells that the energy and temperature are playing the same role in the scattering phenomenon of these materials. The equations follows

$$\Sigma(\varepsilon, T) = \left(1 - \frac{1}{Z}\right) \varepsilon - \frac{i}{Z \pi k_B T_0} [\varepsilon^2 + (\pi k_B T)^2]. \quad (1.117)$$

$Z = m/m^*$ is the quasiparticle spectral weight, as it has already been shown in section 1.2.3 this renormalization affects the dynamical parameters such as the Fermi velocity $\mathbf{v}_F^* = Z \mathbf{v}_F$. T_0 is the Fermi-liquid temperature scale. In addition, Luttinger demonstrated that higher order diagrams do not change the quadratic temperature and energy behavior [51]. This self-energy can be introduced back into the spectral function Equation 1.97. In the low energy $\varepsilon \ll k_B T$ limit the

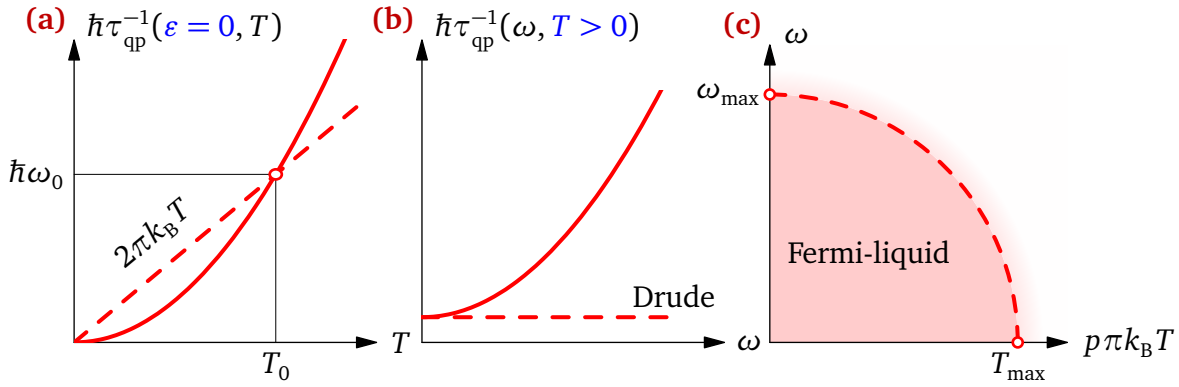


Figure 1.10: Fermi liquid quasiparticle scattering rate. **(a)** At zero energy $\hbar\tau_{\text{qp}}^{-1}$ scales quadratically with the temperature. The intercept with the thermal function $2\pi k_B T$ is defining both T_0 and ω_0 . **(b)** At a non zero but constant temperature, the scattering rate deviates quadratically from the Drude model (constant scattering rate). **(c)** Temperature and energy relation for the experimental optical scattering rate. The experimental maximum energy scale ξ_{max} is shown by the red dashed line. At zero energy the Fermi-liquid is seen up to T_{max} , whereas at zero temperature it corresponds to $\omega_{\text{max}} = p\pi k_B T_{\text{max}}$ with $p = 2$.

imaginary part of the spectral function thus reproduces a Lorentzian like shape centered at $\varepsilon = Z\xi_k$ (See Figure 1.9). Its width –the quasiparticle peak– correspond approximately to half the life time. In the $\omega \rightarrow 0$ limit it becomes even smaller than the energy by virtue of the ω^2 dependence of Σ_2 . At zero energy the inverse quasiparticle life-time, is thus

$$\frac{\hbar}{\tau_{\text{qp}}} \equiv 2Z |\Sigma_2(\varepsilon = 0, T)| = 2\pi \frac{(k_B T)^2}{k_B T_0}. \quad (1.118)$$

A comparison with a simple constant scattering is shown in Figure 1.10. The Fermi energy scale $k_B T_0$ sets the interaction strength and correspond to temperature where $\hbar/\tau_{\text{qp}} = 2\pi k_B T$ (See Figure 1.10). A small T_0 correspond to a large Σ_1 thus strong electron-electron interaction and scattering. DMFT calculations have shown T_0 to be about one order of magnitude larger than the Fermi-liquid temperature T_{FL} [38]. In typical systems T_{FL} is in the range 20 K to 25 K [52] which lead to T_0 of the order or slightly smaller than room temperature. T_0 is also one order of magnitude smaller than the typical Mott-Ioffe-Regel limit [53–55].

In order to compute the macroscopic optical conductivity equation, the self-energy Equation 1.117 is inserted into the Kubo Equation 1.101 which is summarized in a scaling function depending on the energy-temperature ratio and on the product $\omega\tau_{\text{qp}}$

$$\sigma(\omega) = \sigma_{\text{dc}} \mathcal{S} \left(\frac{\hbar\omega}{2\pi k_B T}, \omega\tau_{\text{qp}} \right). \quad (1.119)$$

1. OPTICAL SPECTROSCOPY OF METALS

σ_{dc} the dc-conductivity and the scaling function are defined by

$$\sigma_{\text{dc}} = \frac{\pi^2}{12} Z \Phi(0) \tau_{\text{qp}} \quad (1.120)$$

$$\mathcal{S}(x, y) = \frac{6i}{\pi^2} \frac{\psi\left(\frac{1}{2}[1 + r(x, y) - ix]\right) - \psi\left(\frac{1}{2}[1 + r(x, y) + ix]\right)}{x r(x, y)}, \quad (1.121)$$

with $r(x, y) = \sqrt{1 + x^2 - iy}$ and ψ , the digamma function.

The non-universal dc-conductivity depends on the quasiparticle residue Z , and on the transport function $\Phi(0)$ proportional to the average squared velocity on the Fermi surface. In the dc conductivity, these two quantities enter as the product $Z\Phi(0)$. This product also coincides with the weight of the Drude peak. The Fermi-liquid model can be generalized to include impurity scattering in the form of a constant scattering rate Γ_{imp} , entering the optical conductivity as the product $Z\Gamma$. Thus the low-energy optical conductivity of a local Fermi-liquid can be represented by the three parameters T_0 , $Z\Phi(0)$, and $Z\Gamma_{\text{imp}}$. The temperature scale T_0 is a relatively large scale, typically ten times larger than T_{FL} , below which the universal Fermi-liquid behavior is generally observed [38].

1.4.2 Energy ranges

The characteristic features of the Fermi-liquid conductivity are drawn in Figure 1.11 (a) both at low ($T = 0.1T_0$) and high temperature ($T = 0.6T_0$). At low temperature the real part of the optical conductivity displays a shoulder in log-scale plot. Unlike the Drude model that indicate only one crossing of the real and imaginary part (See Figure 1.3). The Fermi-liquid model has two crossing where the optical conductivity behave successively from a dissipative ($\sigma_1 > \sigma_2$), inductive ($\sigma_1 < \sigma_2$) and again a dissipative behavior. It is therefore possible to describe three different energy regimes.

1.4.2.1 Drude regime

The low energy regime $\omega \lesssim \omega_L < 2\pi k_B T / \hbar$ is comparable to the Drude model represented with dashed lines in Figure 1.11 and Equation 1.101 in the limit $\hbar\omega / (2\pi k_B T) \rightarrow 0$ becomes comparable to the Drude Equation 1.36

$$\frac{\sigma(\omega)}{\sigma_{\text{dc}}} \approx \frac{6}{\pi^2} \frac{\psi'\left(\frac{1}{2}\left[1 + \sqrt{1 - i\omega\tau_{\text{qp}}}\right]\right)}{\sqrt{1 - i\omega\tau_{\text{qp}}}}. \quad (1.122)$$

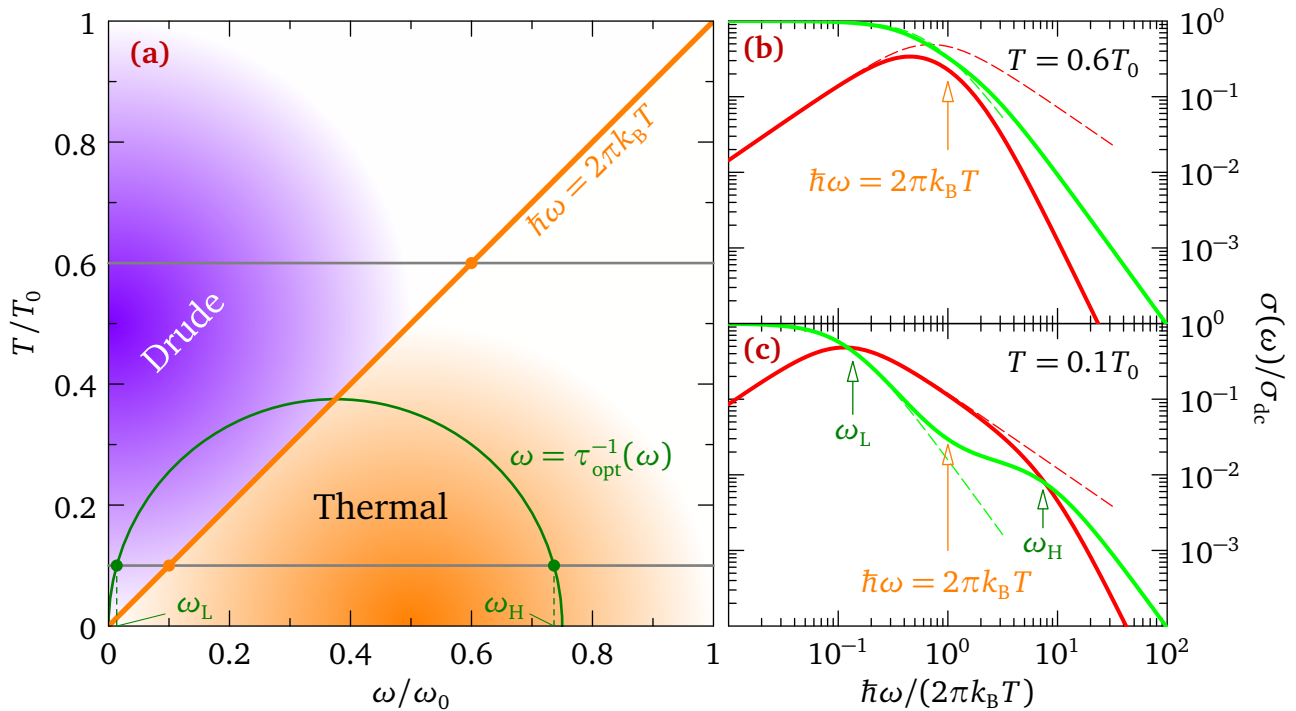


Figure 1.11: (a) Fermi liquid temperature and energy regimes. The Drude regime applies for $\hbar\omega < 2\pi k_B T$ while the thermal regime start at $\hbar\omega \gtrsim 2\pi k_B T$. The two gray lines indicate the regime at $T = 0.1T_0$ and $T = 0.6T_0$. (b-c) Optical conductivity of a Fermi-liquid and of the classical Drude model for the two temperature shown in (a). The axis are rescaled to allow a comparison between the two regimes. At low temperature the crossing of the real part and imaginary part that separate the dissipative ($\sigma_1 > \sigma_2$) and the inductive ($\sigma_1 < \sigma_2$) regimes happen at ω_L and ω_H shown in (a) as when the photo energy is equivalent to the optical scattering rate. At high temperature no crossing is predicted by the model and real part of the optical conductivity is almost equal the Drude model. Adapted form [38]

1. OPTICAL SPECTROSCOPY OF METALS

1.4.2.2 Thermal regime

The intermediate regime is the thermal regime where the energy is approaching the temperature $\omega \gtrsim 2\pi k_B T$ and $\omega\tau_{qp} \gg 1$. Figure 1.11 clearly indicates a deviation from the low energy Drude model. In Figure 1.11, this archetypal shoulder is the fingerprint of the Fermi-liquid in optical conductivity. The extended Drude model Equation 1.64 is recovered

$$\sigma(\omega) \approx \frac{Z\Phi(0)}{-i\omega + 1/\tau^*(\omega)}. \quad (1.123)$$

The self-energy Equation 1.117 is not including any impurity scattering. This form of scattering is further introduced directly into the memory function by introducing a constant scattering term Γ_{imp} which gives

$$M(\omega) \approx \left(\frac{1}{\tilde{Z}} - 1\right)\omega + \frac{2i}{\hbar\tilde{Z}} \left[\frac{(\hbar\omega)^2 + (2\pi k_B T)^2}{3\pi k_B T_0} + Z\Gamma_{imp} \right]. \quad (1.124)$$

Scaling parameter p is equal to two in this framework. It is also possible to compute the renormalized optical scattering rate

$$\frac{\hbar}{\tau^*(\omega)} = \frac{2}{3\pi k_B T_0} [(\hbar\omega)^2 + (p\pi k_B T)^2] + 2Z\Gamma_{imp}. \quad (1.125)$$

Although the one-particle self-energy and thus the quasiparticle scattering rate is proportional to $(\hbar\omega)^2 + (\pi k_B T)^2$ the optical conductivity imply a two-particle correlation function and the optical scattering rate has an extra 2 factor [56]. Equation 1.125 demonstrate the well known T^2 dependence of the resistivity $\rho(T) = AT^2 + \rho_0$ with $A = 8\pi/(3k_B T_0 Z \phi_0)$. The determination of the T^2 prefactor A allows, as an example, to plot and show a certain class of universality among correlated systems. The Rice-Kadowaki-Woods ratio –here rescaled following Hussey *et al.* and Jacko *et al.* papers [57, 58]– and presented in Figure 1.12 is defined as

$$\frac{A f_{dx(n)}}{\gamma^2} = \frac{81}{4\pi\hbar k_B^2 e^2}. \quad (1.126)$$

f_{dx} has been added to take into account dimensionality, unit cell dimension, density of charge and multi-band systems. The red shaded area in Figure 1.12 indicates the materials whose reflectivity may exceed 99.5% and could complicate the experimental measurements using optical spectroscopy. As an example, Sr_2RuO_4 is an excellent metal with a very good in-plane conductivity, its resistivity factor A is very small and thus the material is expected to have a reflectivity above 99.5% below 1 meV and at about 20 K, which means that a conventional study in the FIR is still technically doable. Note that the reflectivity threshold at 99.5% is linked to the usual 0.5% incertitude in the reproducibility of FTIR experiments.

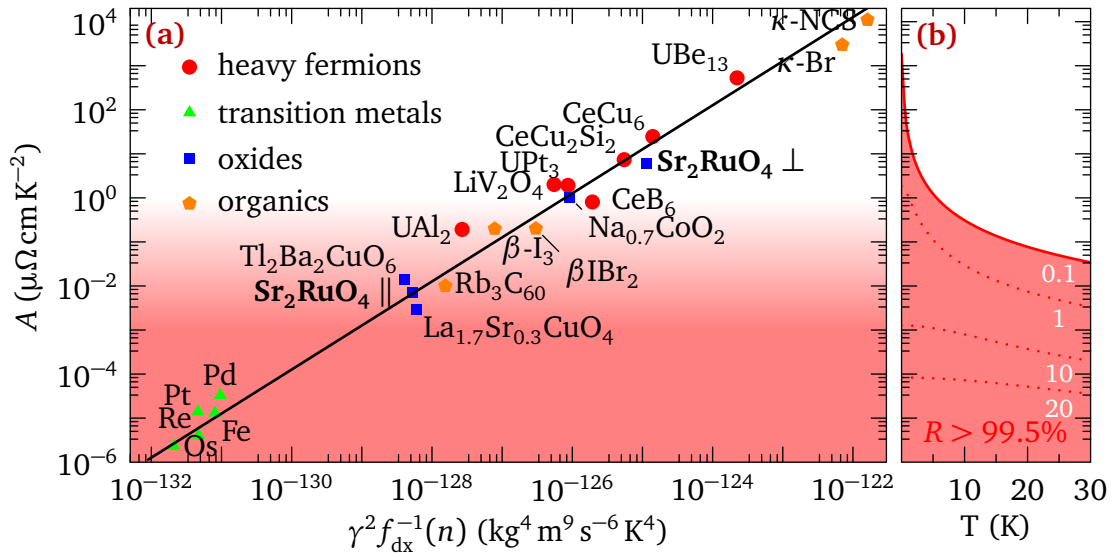


Figure 1.12: (left) Rescaled Rice-Kadowaki-Woods ratio adapted from [58]. The red shaded area indicates the experimental difficult spectral range for optical spectroscopy. (right) Area where the reflectivity is above 99.5% at selected photon energies (0.1 meV to 10 meV). The area is a rough estimation based on the Hagen-Rubens equation presented in section 1.2.1.3 and the optical conductivity computed from Equation 1.125

The drawback of working with the memory function it is not the bare output quantity from spectrometers. In order to avoid fitting routines and assumption underneath the extended Drude model one can directly extract the theoretical scaling formula from the reflectivity in the thermal regime, $\hbar\omega \sim 2\pi k_B T$. So that the definition of the memory function is substituted in Equation 1.80, and expanded in powers of $M_2/(\omega + M_1)$

$$1 - R(\omega) \approx \sqrt{\frac{8\epsilon_0\omega}{Z\Phi(0)} \left(M_2 + \sqrt{(\omega + M_1)^2 + M_2^2} \right)} = 2\sqrt{\frac{\epsilon_0}{Z\Phi(0)} \frac{M_2}{\omega + M_1}} + O\left(\left[\frac{M_2}{\omega + M_1}\right]^2\right). \quad (1.127)$$

Substituting Equation 1.124 for $M(\omega)$ we find that, in the thermal regime, $1 - R(\omega)$ behaves like $M_2(\omega)$

$$1 - R(\omega) = \frac{4}{\hbar} \sqrt{\frac{\epsilon_0}{Z\Phi(0)}} \left[\frac{(\hbar\omega)^2 + (2\pi k_B T)^2}{3\pi k_B T_0} + Z\Gamma \right]. \quad (1.128)$$

1.4.2.3 High energy regime

At high energy σ_1 recover the Drude like $1/\omega^2$ decay although σ_2 goes like $1/\omega^3$ which is caused by the unsaturated self-energy ω^2 behavior and is not physically relevant.

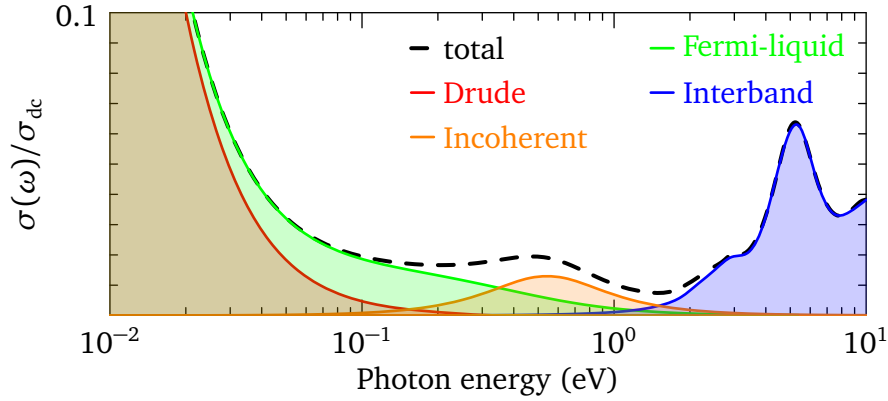


Figure 1.13: Schematic view of the different electronic components forming the total conductivity of a single band strongly correlated metal (cuprates, single layer ruthenate)

1.4.3 Understanding an optical spectrum

With the different models presented in the previous section, it could be difficult to disentangle the physical phenomena present in typical optical spectra. For that purpose, such a spectrum is shown in Figure 1.13. The black dashed curve represents the total experimental conductivity. The Drude model is also seen as the coherent quasiparticle peak while the Fermi-liquid is a specific extension of the Drude model: at low-energy they are almost exactly the same, but at the thermal energy an excess spectral weight is seen. Still below the interband transition, the intraband incoherent conductivity (σ_{MIR}) is represented in orange. In the Fermi-liquid model, $Z\Phi(0)$ correspond to the spectral weight of the Drude component only (without the thermal part). In comparison, the total intraband response ω_p of the extended Drude model Equation 1.64 is the spectral weight of the Fermi-liquid and the incoherent conductivity. Finally, the interband conductivity is usually sufficiently separated to be safely distinguished from the low-energy intraband.

1.4.4 Bosonic spectral function models

This section introduces the different bosonic spectral models used in this work. The histogram model is a generic way of representing the bosonic spectral function using numerous step functions (histograms). The other model is the Fermi-liquid electron-electron correlations model. A model mixing the both approaches is also presented. Note that in order to keep a link with the previous works, the optical data is uses $\Pi(\omega)$ while transport measurement directly uses the $\alpha\chi_2(\omega)$.

1.4.4.1 Histogram representation

The histogram model was developed in previous works [2, 22, 35, 59]. This method aims to simplify the extraction of the bosonic spectral function from the two integrals (1.102) and (1.107), for which no analytical inversion exist. Assuming a minimal model for $\Pi(\omega)$ allows to fit the data (e.g. the memory function) and extract the model dependent information on what "glues" the electron together. In this respect several models exist such as the Fermi-liquid, the marginal Fermi liquid [60] or the MMP model [61]. Here the bosonic spectral function as a sum of blocks is depicted in Figure 1.14 (a). Over a fixed energy range, the position width and position of the blocks are fixed and their height is a free parameter. Mathematically they are represented by an addition of two Heaviside step function $\theta(\omega_i)$ with i the block index.

$$\Pi(\omega) = \sum_{i=1}^n h_i [\theta(\omega_i) - \theta(\omega_{i+1})]. \quad (1.129)$$

That output self-energy is a sum over a set of functions that need to be evaluated numerically

$$\begin{aligned} \Sigma(\omega) = \sum_{i=1}^n h_i \left\{ -2\pi i T \ln \left(\sinh \left(\frac{\omega'}{2T} \right) \right) \Big|_{\omega'_i}^{\omega'_{i+1}} \right. \\ \left. + \ln \Gamma \left(\frac{1}{2} + i \frac{\omega' - \omega}{2\pi T} \right) \Big|_{\omega'_i}^{\omega'_{i+1}} \right. \\ \left. + \ln \Gamma \left(\frac{1}{2} - i \frac{\omega' + \omega}{2\pi T} \right) \Big|_{\omega'_i}^{\omega'_{i+1}} \right\}. \end{aligned} \quad (1.130)$$

In [2], it has been shown that this method is less prone to be stuck in local minimum during the fitting process. This is a major advantage over the previous algorithm used in previous works. In [22, 59] the histograms are limited to 6 blocks with their width as free parameters.

1.4.4.2 Power law and Fermi liquid representation

This model is the step preceding the derivation of the self energy Equation 1.117. For a three dimension momentum independent Fermi-liquid, the absorptive part of the particle-hole susceptibility is proportional to energy up to the Fermi energy ($\chi_2(\omega) \propto \omega$) [31, 38, 49, 62–64]. Namely this dependence is the key element responsible for both, the temperature and energy dependence, of the self-energy and thus the optical functions. More generally the different interactions can be represented by a power law function

$$\alpha^2 \chi_2(\omega) = \alpha^2 \chi_2(\omega_c) \left(\frac{\omega}{\omega_c} \right)^\eta \theta(\omega_c - \omega), \quad (1.131)$$

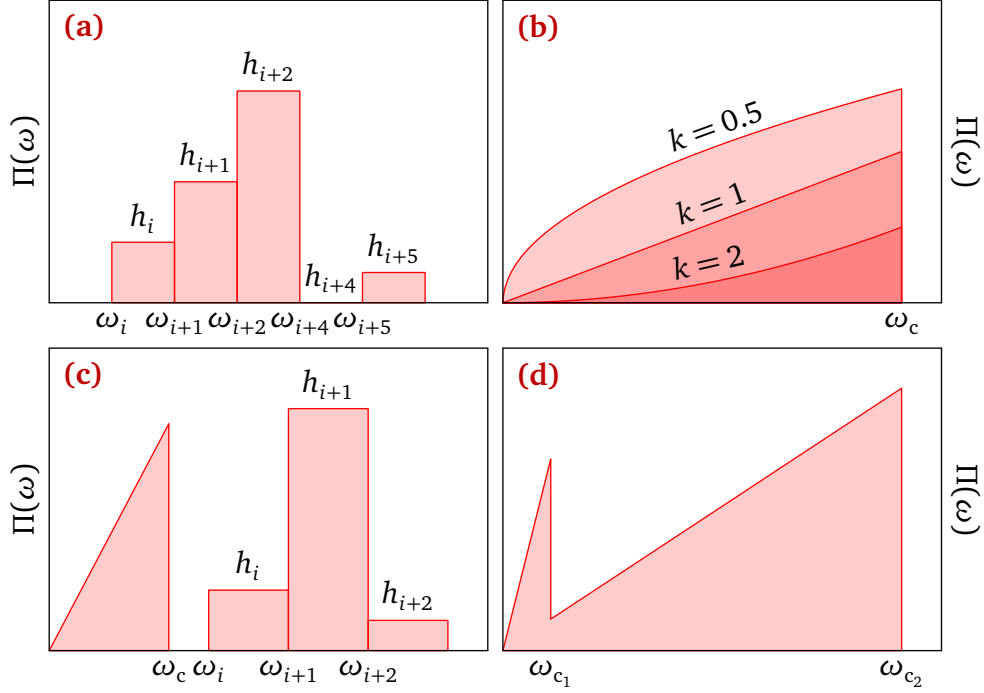


Figure 1.14: Glue function $\Pi(\omega)$ represented for different models. **(a)** histogram (block) representation, **(b)** power law representation. The Fermi-liquid model states $k = 1$ Fermi-liquid (triangle representation). Phonon interaction in 3D are represented through $k = 2$. **(c)** Fermi-liquid with additional bosonic modes. **(d)** Double Fermi-liquid representation.

where ω_c defines the cutoff energy which –depending on the model– could represent the Fermi energy, the width of the band or more phenomenologically, the experimental range of validity of the model. A schematic view of the model is shown in Figure 1.14 (b). The 3D Fermi-liquid is recovered with $\eta = 1$. While other modes, like acoustic phonon interaction would be represented with $\eta = 2$. In the case of the histogram model a small Fermi-liquid regime is introduced in order to assure the convergence of Equation 1.103 at zero energy. Introducing Equation 1.131 into Equation 1.112 gives

$$-\Sigma_2(\varepsilon) = N(0)\omega_c\alpha^2\chi_2(\omega_c)\left(\frac{k_B T}{\omega_c}\right)^{\eta+1} S_\eta\left(\frac{k_B T}{\omega_c}, \frac{\varepsilon}{k_B T}\right) \quad (1.132a)$$

$$S_\eta(x, y) = \int_0^{\frac{1}{x}} du u^\eta \left(\frac{1}{e^{u-y} + 1} + \frac{1}{e^{u+y} + 1} + \frac{2}{e^u - 1} \right). \quad (1.132b)$$

For integer values of η the scaling function S_η can be evaluated explicitly. The Kubo resistivity Equation 1.111 can be rewritten

$$\rho(T) = A_\eta \left(\frac{k_B T}{\omega_c} \right)^{\eta+1} F_\eta \left(\frac{k_B T}{\omega_c} \right). \quad (1.133)$$

With $A_\eta = 2c_\eta N(0)\omega_c \alpha^2 \chi_2(\omega_c)/[\hbar\Phi(0)]$ a constant term and

$$F_\eta(x) = \frac{1}{c_\eta} \left[\int_{-\infty}^{\infty} d\nu \frac{e^\nu}{(e^\nu + 1)^2} \frac{1}{S_\eta(x, \nu)} \right]^{-1}. \quad (1.134)$$

The normalization constant c_η is defined such that $F_\eta = 1$. When $\omega \ll \omega_c$ or $\omega_c \rightarrow \infty$, the well known energy and temperature dependence of a Fermi-liquid [38] is obtained

$$\Sigma_2(\omega) \propto -\frac{\pi}{2} [\omega^2 + (\pi k_B T)^2]. \quad (1.135)$$

Likewise the resistivity behavior is $\rho \propto T^{\eta+1}$. While Equation 1.133 has to be evaluated numerically, it is also possible to use the Ziman approximation Equation 1.114 which result in

$$\tilde{\rho}(T) = \tilde{A}_\eta \left(\frac{k_B T}{\omega_c} \right)^{\eta+1} \tilde{F}_\eta \left(\frac{k_B T}{\omega_c} \right) \quad (1.136a)$$

$$\tilde{F}_\eta(x) = \frac{1}{\tilde{c}_\eta} \int_0^{\frac{1}{x}} du \frac{u^{\eta+1}}{4 \sinh^2(u/2)} \quad (1.136b)$$

$$\tilde{A}_\eta = 4\tilde{c}_\eta \frac{N(0)\omega_c \alpha^2 \chi_2(\omega_c)}{\hbar\Phi(0)}. \quad (1.136c)$$

The calculation for the Fermi-liquid $\eta = 1$ gives

$$\tilde{F}_1(x) = \frac{3}{\pi^2} \left[2\text{Li}_2(1 - e^{-1/x}) + \frac{x^{-2}}{1 - e^{1/x}} \right] \quad (1.137)$$

Thus

$$\tilde{\rho}(T) = \frac{a\pi}{\hbar\omega_p^2} (k_B T)^2 \times \left[2\text{Li}_2(1 - e^{-1/x}) + \frac{x^{-2}}{1 - e^{1/x}} \right]. \quad (1.138)$$

$\text{Li}_n(x)$ is the polylogarithm function of order n . At low temperature or in the $k_B T/\omega_c \rightarrow 0$ limit $\tilde{F}(x)$ goes to a constant value and the resistivity is indeed proportional to T^2 . Note that for $x \neq 0$ the function is not analytic. Whereas for $k_B T \gg \omega_c$, $\tilde{F}(x) \propto 3/(\pi^2 x)$ which gives a linear regime in temperature for the resistivity. This simple model is thus able to reproduce the different temperature dependences seen for the underdoped cuprates. The slope of the susceptibility is defined as $a = \alpha^2 \chi_2(\omega_c)/\omega_c$.

1.4.4.3 Double Fermi liquid and mixed model

A composition of the different models is needed when: 1) both electron-electron and electron-boson interactions are present in a single band system. 2) the different scattering mechanisms are considered independent in a multi-band system. The former assumption will be used for Sr_2RuO_4 in chapter 4 and the later for $\text{HgBa}_2\text{CuO}_{4+x}$ in chapter 3. The mixed model is presented

1. OPTICAL SPECTROSCOPY OF METALS

in Figure 1.14 (c), the double Fermi-liquid model in inset (d) with the two respective cutoffs ω_{c_1} and ω_{c_2} .

1.4.4.4 An experimental cutoff

Understanding the physical meaning of the Fermi-liquid cutoff is a ground level question. In the optical spectra, it is very difficult to experimentally disentangle if the Fermi-liquid disappears due to the onset of a bosonic mode or by the fact that the coupling is suppressed above ω_c . And this is indeed without considering any complex interplay with the interband transitions, excitons and so on [65, 66]. By considering a simple metal with only the Fermi-liquid triangle model, the Fermi-liquid energy parameter $\xi^2 = [(\omega)^2 + (p\pi k_B T)^2]$ is also bounded to the energy cutoff ω_c so that $\xi(\omega_c, T = 0)^2 = \omega_c = \xi_{\max}$ and by construction in the dc limit, $T_{\max} = \omega_c / (p\pi)$ (T_{\max} is preferred to T_c , which avoids confusion with the superconducting critical temperature). This reasoning is summarized in Figure 1.10 (c), which shows a "phase diagram" of the range of validity of the Fermi-liquid.

Experimental

This chapter highlight the experimental apparatus and techniques common to the main chapter of this work; the specific techniques are introduced in the respective chapters.

In order to situate the place of FTIR spectroscopy among the different optical techniques the first section introduce the different energy scales as well as their respective experimental techniques. The second section focus on FTIR spectroscopy and the equipment linked to it. The last section introduces the ellipsometric technique and very briefly the Raman spectroscopy setup.

2.1 Introduction

Measuring the optical constant of correlated electrons can be achieved by numerous of techniques. Each of them is well adapted for a precise spectral range. In most of the cases, these techniques overlap over a broad energy range, which allows cross checking and stitching the different spectra together. Figure 2.1 is a brief overview of the typical energy scale of some common condensed matter features. The common names used for describing the energy ranges is usually shared among the different field of research; it is shown in grayscale in the figure. However, at least four different systems of units are used to describe the energy: meter, Hertz, electronvolt, and wavenumber. In this work, all the units have been harmonized in electronvolt.

Starting with dc transport the kHz and MHz (\approx neV) is obtained by the use of microwave cavity perturbation technique, the sample is contacted into a metallic cavity and measured with radio frequency fields using lock-in amplifiers or impedance analyzers. A typical example comes from the work of Slater *et al.* [69]. Above these energies, contact-free techniques are needed. In the MHz to GHz range (typical radio-frequency (RF) techniques are used. In this range two typical technologies are used: the cavity perturbation technique and Corbino spectrometers. The former is widely used since the late sixties thanks to its high sensitivity but suffers from the fact that it can measure single energies depending on their size/geometry. The later has

2. EXPERIMENTAL

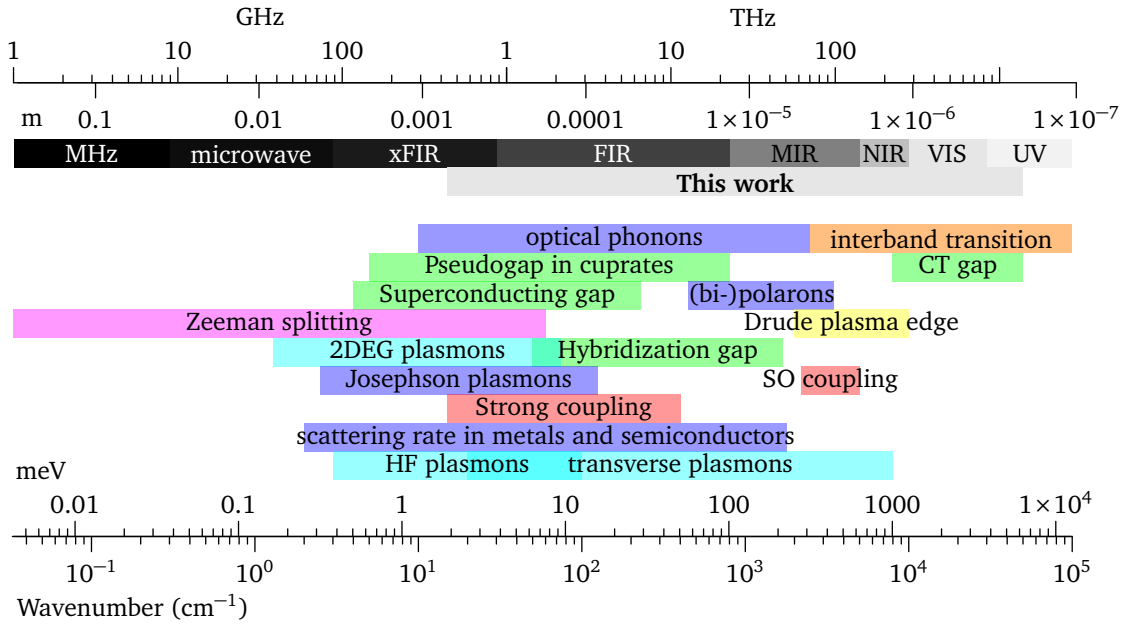


Figure 2.1: Typical energy scales found in condensed matter experiments. The color pattern group physical phenomenon by class. The common name for the different energy ranges is in gray shade. The energy range measured during this work is shown in light gray. The abbreviations are Charge transfer gap (CT), spin-orbit coupling (SO), 2D electron gas (2DEG), heavy-fermion plasmons (HF). Energy ranges taken from [67, 68]

the advantage of probing a broader energy range but need extensive calibration. A typical example is the experiment by Scheffler *et al.* [70], the Corbino spectrometer with energies ranging from 10^{-7} eV to 10^{-4} eV allowed the authors to measure the very low energy relaxation rate of electrons in UPd_2Al_3 . In the GHz regime several techniques compete : Martin-Puplett interferometer (0.25 eV to 25 eV) [71], THz-time domain spectrometers (0.12 meV to 25 meV) and the common Fourier transform infrared (FTIR) spectrometer (0.6 meV to 3300 meV). Starting as well in the FIR region, ellipsometry is a very convenient tool to probe the thin layers and other surface defects of e.g. silicon wafer in the industry. It is used up to several eV and is combined with a grating monochromator to select the desired wavelength. Since many years, several of these technologies tends to merge leading to novel probes such as THz-time domain ellipsometer or pump-probe experiments.

In this study, for samples larger than 0.5 mm, the total energy range used is shown in light gray in Figure 2.1. From 2.3 meV to 1.2 eV a Bruker IFS 113v FTIR spectrometer was used. The energy range was extended to the visible light (3 eV) using a Bruker IFS 66v/S FTIR. The measurement of sample with a smaller surface, usually of the order $100 \mu\text{m} \times 100 \mu\text{m}$, was done on a Bruker 70v attached to a IR-microscope. Finally the high energy (UV) was extended up to 6.2 meV with a Woolam VASE ellipsometer.

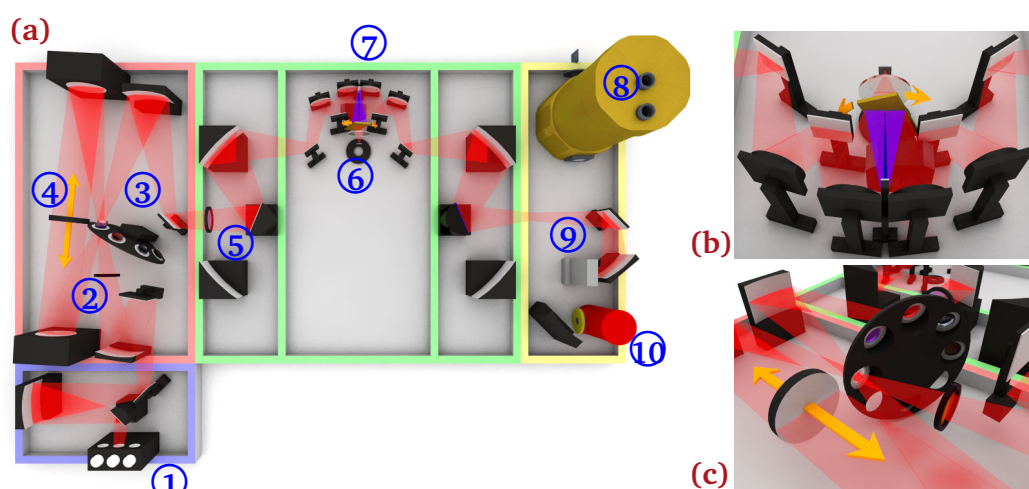


Figure 2.2: (a) Schematic view of the Bruker FTIR spectrometer used for most of the results of this study. The system is made of four compartments, the sources (blue), the interferometer (red), the samples compartment (green) and the detectors (yellow). The blue numbers represents : ① Hg-arc, globar and tungsten lamps, ② UV filters, ③ beam splitter wheel, ④ interferometer scanning mirror, ⑤ polarizer and channel selector, ⑥ cryostat fitting base, ⑦ reference mirror ⑧ bolometer (bolo4K, bolo MIR, bolo2K), ⑨ DTGS and ⑩ MCT detectors. (b) Close view of the beam splitter wheel and the scanner mobile mirror. (c) Reference mirror and the reference light path (in blue).

2.2 Infrared normal incidence reflectivity

2.2.1 Bruker IFS 113v

The Bruker IFS 113v is a common spectrometer used to measure the near normal incidence reflectivity (angle of incidence $\approx 7^\circ$). A schematic view of the apparatus is shown in Figure 2.2. The system is made out of four compartments highlighted in color on the figure. The whole system is kept under vacuum in order to protect the hygroscopic optical components and to avoid fluctuation of intensity due to various absorption of gas. The usual residual pressure is about 9 mbar due to the fact that the motion of the interferometer mirror is done with nitrogen bearing. The sources compartment (blue) is composed by a tungsten light bulb (NIR to visible), a SiC Globar and mercury arc lamp (FIR, and xFIR). The emittance spectrum of these sources is drawn in Figure 2.3 (a). The interferometer (red) uses a Genzel geometry [72] which has many advantages over the standard Michelson arrangement. As an example, the beam is focused on small beam splitters mounted on an automatic wheel (subfigure c) allowing the user to change the spectral range during the experiment without breaking the vacuum of the whole system. The light output is nearly unpolarized allowing the use of a polarizer to set the desired linear polarization of output light. The sample compartment is shown in green. Finally the detector (yellow) depends on the energy range needed for the measurement; the typical combination of beam splitter / detector is summarized in Table 2.1. The bolometers have different spectral filters which allows to select the energy range with the highest signal to

2. EXPERIMENTAL

noise ratio. The resulting spectra, using different filters (F1 to F3) are shown in Figure 2.3 (b).

Table 2.1: Typical combination of sources, beam splitters and detectors used in this work.

Range (meV)	2 to 10	6 to 80	55 to 200	120 to 750	430 to 1200
Source	Hg	Hg/Globalar	Globalar	Globalar	Tungsten
Beam splitter	Si10	Ge/Mylar	Ge/KBr	Ge/KBr	Si/CaF
Detector	Bolo 1.6K	Bolo 4K	Bolo MIR	MCT	MCT
Polarizer	PE	Gold	KrS-5	KrS-5/MIR	MIR/NIR

2.2.2 Polarizers

Polarized light can be used to probe specific optical response of anisotropic samples. It is also useful to suppress unwanted spectral features coming from miscut, misalignment or crystallographic defects/domains of samples.

As an example, the crystals used in this study are all member of the tetragonal family. The in-plane (ab -plane) component of the conductivity is showing a metallic behavior, although the out of plane (c -axis) component is insulating. For each of these samples the reflectivity can be measured with three different geometries, the a -axis reflectivity (or ab -plane reflectivity) measured from the ab -plane face, the a -axis reflectivity measured from the ac -plane and finally the c -axis reflectivity from the ac -plane. These geometries are shown in Figure 2.4. As an example the radical change of reflectivity of an ac -plane Sr_2RuO_4 crystal is shown in Figure 2.4 (c) and (d); the reflectivity goes almost from an insulating behavior to a good metal. In that sense it is usually advised to measure the ab -plane component of the reflectivity from the ab -plane surface and the c -axis from the ac -plane.

If the sample shows no sign of defects or miscuts, the ab -plane reflectivity can in principle be measured with unpolarized light. However, the light propagation is never exactly perpendicular to the ab -plane. This problem is due to the size of the optical mirrors which doesn't allow a perfect normal incidence and is about 8° in the Bruker IFS 113v setup. The typical drawback of these measurements is the mix of 5 % to 15 % of c -axis features such as c -axis phonons peaks or an overall change of reflectivity. This case is presented in the left panel of Figure 2.4. It shows the presence of a c -axis phonon of $\text{HgBa}_2\text{CuO}_{4+x}$ at 82.75 meV. This example indicates that polarized measurement will be necessary. When the polarization is changed from 0° to 176° the feature is gradually suppressed at about 120° , this can easily be seen in the top subfigure that plots the reflectivity versus polarization. Fitting these points using a simple cosine allows to find the precise angle at which the measurement can be done.

It is important to note that, like other optical components, the use of polarizers can reduce up to 50 % of the overall light intensity. In particular the use of a polarizer for the small

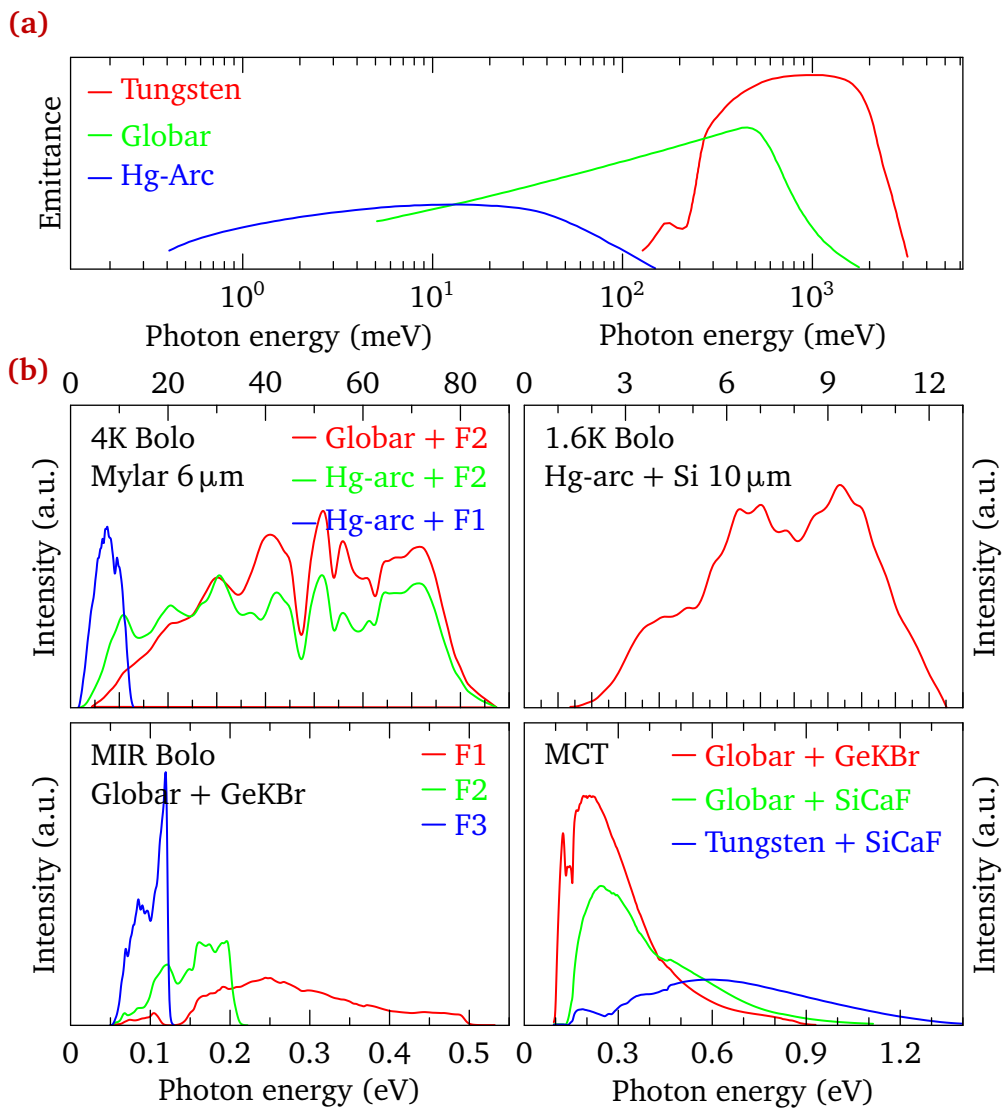


Figure 2.3: (a) Emittance spectrum of the commercial Bruker Optics light sources [73]. (b) Experimental parameters of standard reflectivity Bruker IFS 113v experiments. The different bolometer filters are indicated as F1, F2 and F3.

2. EXPERIMENTAL

HgBa₂CuO_{4+x} crystal required longer measurement time or the averaging of many measurement spectra. The useable bandwidth of polarizers is generally spreading over one decade of energy, so that it is necessary to use several polarizer to cover the entire spectral range. The selection of the right polarization from one polarizer to an other was done using their spectral range overlap. The procedure is done as follows: The sample reflectivity is measured in the FIR region as a function of polarizer angle and is then analyzed at the *c*-axis phonon energies. If no angle dependence is found the sample is measured without polarizer. If there is angle dependence, the MIR and NIR polarizers are calibrated by tracking the angle dependence of transmission in the overlap region with the FIR polarizer. This calibration is done for the reflectivity from the xFIR to the VIS.

2.2.3 UHV Cryostat

The UHV continuous flow cryostat used in this study has been specially designed to reduce the thermal contractions of the copper cold finger which ensure an excellent reproducibility of the measurement during the thermal cycling. A rough calculation suggests that a tilt of 0.06° of the sample could move the spot out of the detector. In order to reach the required stability, the sample holder sits on a thermally insulated base and is flexibly coupled from the top to the cold finger through copper ribbons. As a result, this design fulfills the stability requirement but slightly reduce the cooling power which allows sample's temperature typically ranging from 8 K to 400 K. A 50 Ω resistor and a Lakeshore diode are mounted on the sample holder and connected to a closed loop PID temperature controlling unit (ITC503, Keithley) assuring a smooth and continuous monitoring of the temperature. The cryostat has a built-in turbo molecular pump with a typical working pressure of around 8×10^{-8} mbar. The pressure is monitored through a Pirani detector (primary) and an ion gauge (secondary). The vacuum can be improved beyond 10^{-9} mbar (UHV) by baking the cryostat for 24 h at 150 °C, using OFC copper o-rings and the built-in ionic pump. The front window has a clear aperture of 25 mm and can be changed to a different material to fit the energy range needed although due to the very good transmittance of diamond only one window was used over the entire energy range (2 meV to 1200 meV). The reference measurement is done in-situ through two evaporators. A small piece of the material to evaporate (typically gold) is wrapped around a tungsten 0.5 mm wire connected to the current feed through with a home-made copper connector. At full power, 32 W (8 A and 4 V) are injected through the wire for about 20 s to evaporate the metal on the sample surface.

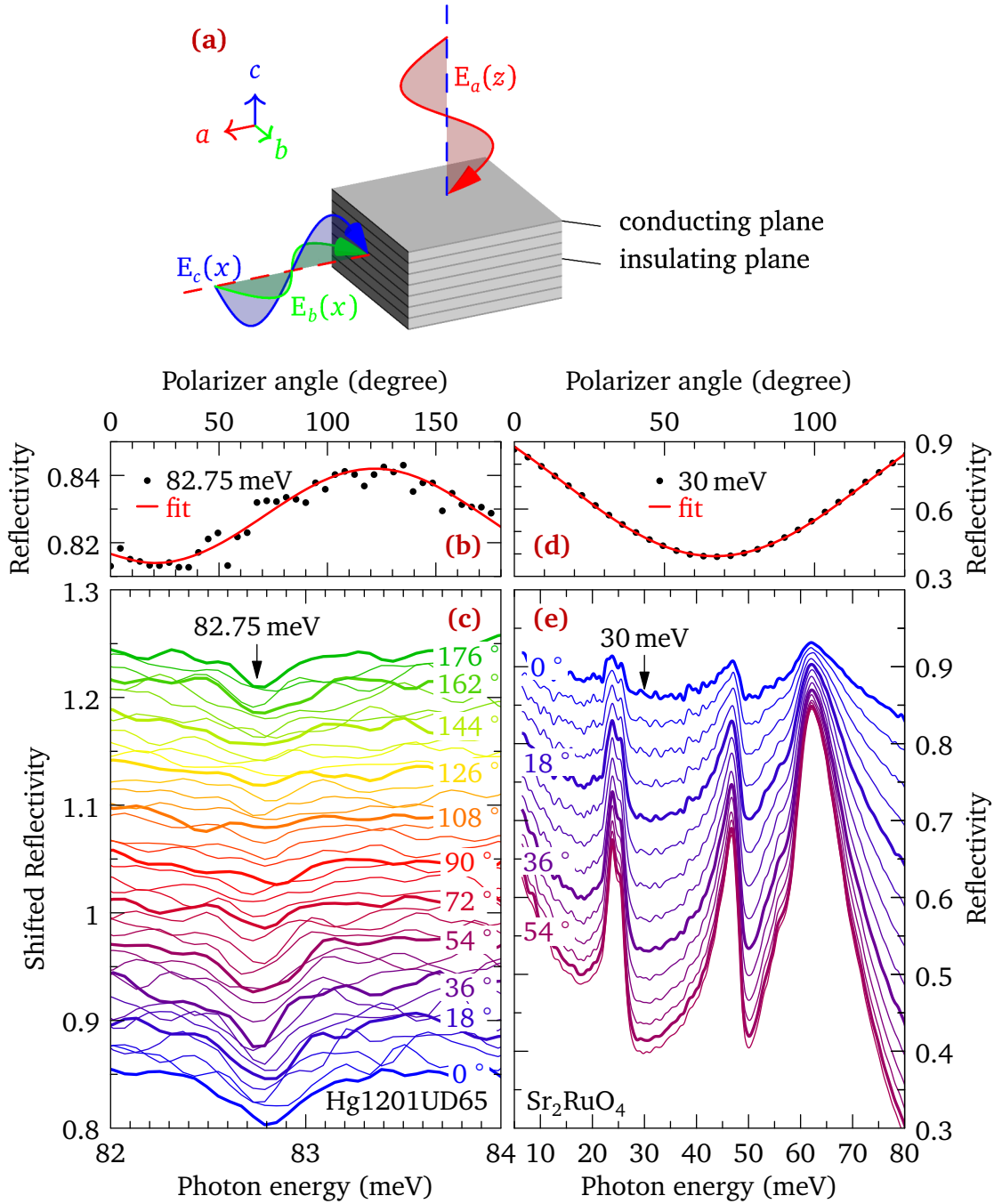


Figure 2.4: (a) Typical geometry using polarized light for measuring the reflectivity in the three space directions. In that thesis, the crystal structure of Sr_2RuO_4 or $\text{HgBa}_2\text{CuO}_{4+x}$ is tetragonal which implies that the lattice parameters $a = b$ so that $E_a(z) = E_b(x)$. (b) in-plane polarization dependent reflectivity of $\text{HgBa}_2\text{CuO}_{4+x}$ at 87.75 meV. The fit to the data is shown by the plain red line (c) in-plane polarization dependent reflectivity of $\text{HgBa}_2\text{CuO}_{4+x}$. The spurious c -axis phonon peaks are shown by the black arrow. ((d-e)) ac -plane reflectivity of Sr_2RuO_4 . The ab -plane is selected when the reflectivity is the highest (not shown here) while the pure c -axis shows strong phonon peaks at about 24 meV, 45 meV and 62 meV.

2. EXPERIMENTAL

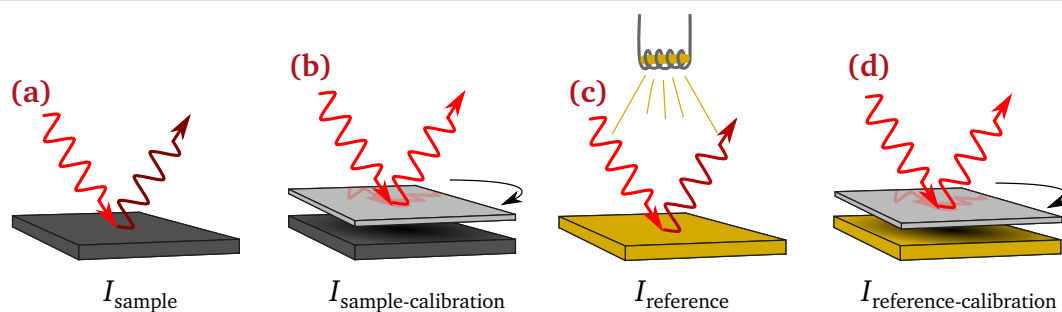


Figure 2.5: Evaporation and drift calibration procedure. (a) The reflectivity power is measured from the sample surface. (b) The reference mirror is placed in front of the sample and the reference is measured. (c) Gold is evaporated from a melted pure gold wire. The gold reference is then measured. (d) The reference mirror is again flipped and the measurement is done. This closes the calibration procedure.

2.2.4 Drift calibration

Due to small sample size and the required temperature resolution of the data, the typical experiment duration was about 8 h to 16 h. With that time scale, the overall drift of the signal intensity is non-negligible. The drift is usually assessed to two different time scales: the rapid shift or intensity jumps and long intensity drift.

The intensity jumps are usually due to unexpected problems with the sources, the interferometer, the cryostat or the detector. Unfortunately, they are usually difficult to correct afterward but are typically avoidable by a careful setup of the experiment. The typical problems are due to abrupt changes in the sensitivity of the detector that is usually due to the total depletion of cryogenic liquids of the detectors (bad filling or poor vacuum shield) or of electrical power (bias batteries). Additionally the interferometer may also run out of the working gas (nitrogen), the cryostat may release internal stress at specific temperatures or simply by a nonreproducible change of measurement parameters (beam splitter, aperture, mirror alignment) or mechanical shock of the spectrometer. Other non-predictable problems happen time to time during the experiments, mostly due to connection/error with the controlling computer or temperature unit but also electronic problems on the board of the spectrometer (ADC, interferometer control unit) or in the detector (Bolometer bias battery, cold module, and pre-amplifier electronics). Finally, the interferometer may also lose the white light self-position or laser threshold. Finally, the spectrometer is very sensitive to over voltage spikes that may happen during lightning.

The long timescale drift is happening on the sources, the detector or the interferometer. It is typically due to the slow depletion of the cryogenic liquid but also to the battery power loss in the detectors that change their characteristic sensitivity or a drift of the sources temperature. Other effects of the temperature drift of the room during the day or a change in pressure in the interferometer were also observed.

The calibration is done by measuring the direct output spectrum of the sources and is done by deviating the light from the sample. The procedure is shown in Figure 2.5 and starts by

2.2 Infrared normal incidence reflectivity

measuring the sample as normal and is then followed by a measurement of the direct output; the procedure is then repeated during the reference measurement. The reflectivity Equation 1.29 then becomes

$$R = \frac{I_{\text{sample}}}{I_{\text{reference}}} \frac{I_{\text{reference-calibration}}}{I_{\text{sample-calibration}}}. \quad (2.1)$$

The former procedure was using the second measuring channel of the IFS 113 spectrometer modifying the beam path by turning two mirrors. This procedure was simple but had proven to be nonreproducible since moving parts were lacking precision. The usual way is to use a reference mirror to deviate the beam as close as possible from the sample, enabling a very good calibration of most of the drift without affecting the reproducibility of the sample measurement (See Figure 2.2). The mirror is mounted onto a closed loop precise piezo motor rotation stage (Agilis Conex PR100P). When a reference scan is needed the mirror is moved up and the beam is reflected back onto a fixed mirror reproducing the inverted sample position. The beam is then reflected again onto the sliding mirror and recovers the usual beam path to the detector. Such a design has advantages over the technique that fixes the mirror onto the cold finger. As an example, the whole cryostat doesn't need to be rotated or displaced during the measurement, the mirror is put as close as possible to the cryostat and allows to calibrate most of the spectrometer, except the cryostat itself, which is the only drawback. Typically the calibration measurement is done three times every twenty measurement scans. Additionally, the consistency of the calibration can be assessed by plotting the reflected intensity during the cooldown and the warmup of the sample. Figure 2.6 displays a typical successful calibration for a large drift of the 4 K FIR bolometer. The intensity drift is defined as $I_{\text{mirror}}(t)/I_{\text{mirror}}(0)$ and is shown in Figure 2.6 (a) as a function of time, starting two hours after the coolant filling. The data is taken at 28 meV. The bolometer is first stable for more than 8 hours but then gradually loses sensitivity. This phenomenon is usually seen for all the different bolometers and is coming from the light sources or the interferometer. Every twenty minutes the mirror is flipped up and three spectra are taken (red line). The spread of this line around the averaged black point is a good indication of measurement noise, here about 0.2%. Panel (b) shows the same drift ratio but as a function of energy and for selected elapsed time. Panel (c) represents the intensity measurement on the sample surface, at the same energy, as a function of temperature. The red line is the measurement on the sample surface while the blue line is after the reference evaporation. The sample was cooled down and warmed up, as shown by the arrows. The dotted curves represent that calibrated data and indicate that after the calibration, the cooldown and warmup measurements are nearly indistinguishable. The difference between the cooldown and warmup data is represented in the last figure (d). This plot was always used as a quality check of the measurement, if the remaining drift exceeded the requirement, usually within 0.5% for the bolometers, the total measurement was discarded.

2. EXPERIMENTAL

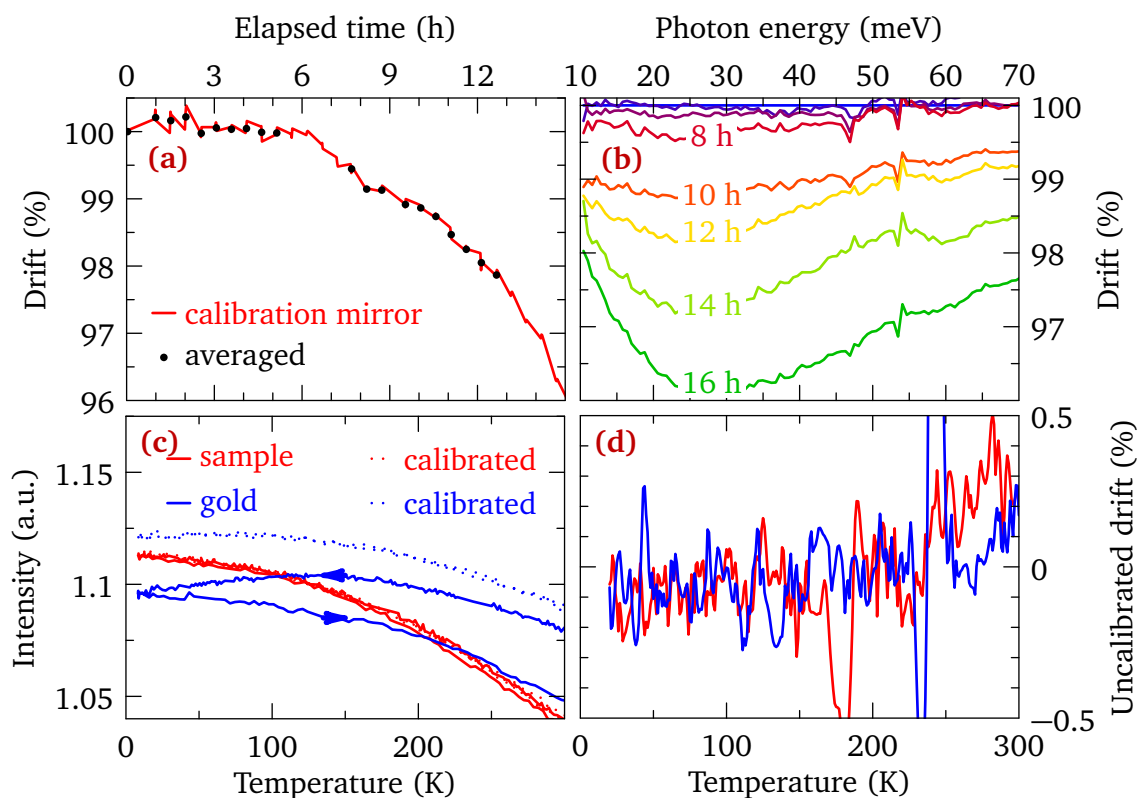


Figure 2.6: Typical drift analysis taken during the measurement of the Sr_2RuO_4 sample. The data indicate the usual drift of the FIR bolometer and the Hg-arc source that are correctly calibrated. The temperature or time panel show data at 28 meV. **(a)** The drift is measured for three consecutive spectra (red line) every 20 minutes and then averaged (black points). **(b)** In correspondence with the trace at 50 meV the full spectrum illustrates the fact that the drift is energy dependent and clearly appears when the liquid helium starts to deplete. **(c)** Intensity of light reflected from the sample and after the gold evaporation (continuous lines) measured while cooling down and warming up the sample (arrows). After calibration (dotted lines) these curves fall on each other. **(d)** Residual drift after calibration calculated from the difference of intensity between the cool down and warm up cycle of the sample.

Measuring the sample reflected intensity allows to check the calibration consistency since there should be no hysteresis in the temperature trace. The difference of intensity between the cool down and the warm up of the sample is shown in panel (d). This curves indicates the high quality of the correction and allow evaluating the systematic error on the absolute reflectivity. Between the lowest temperature and 230 K there is no systematic error. At higher temperature, it is possible to explain the small hysteresis from the remaining thermal contraction of the cold finger affecting the sample holder. In this example, the error remains below 0.5% showing the quality of the data. The calibration mirror is thus a very good tool if the drift time scale is much longer than the sampling interval (about 20 min).

2.2.5 Visible normal incidence reflectivity

Above 1.2 eV a Bruker IFS 66v/S spectrometer upgraded for the VIS range was used. In addition of a diode detector, all the reflecting mirror are coated with aluminum, the light source is a tungsten bulb. A smaller home-made HV cryostat was used and the reference was made using silver in place of gold.

2.2.6 Ellipsometry

2.2.6.1 Basic principles

Ellipsometry is an optical technique that uses the light polarization to achieve a very sensitive characterization of numerous parameters of the surface of the sample. Unlike FTIR spectrometers, which require evaporation of a reference metallic layer or calibration with mirrors, this technique allows the simultaneous measurement of the two component of light (real and imaginary part). As a direct consequence, the Kramers-Kronig relations are not needed. As an example, by measuring the change in polarization before and after the reflection on the sample, it is possible to determine the surface roughness, thickness (for thin films) and the complex dielectric constant of the material. As a consequence, only a small ultra-thin oxide or condensed water layer may disrupt the measurement. This drawback, but also the different models and analysis method used to extract the in-plane optical parameters of anisotropic materials, will be discussed in the following sections.

2.2.6.2 Equipment

In this study, a J.A. Woollam VASE ellipsometer was used to measure the optical response of the different samples in the 0.47 eV to 6.2 eV range. The whole NIR to UV spectrum is generated by a Xenon lamp and the energy is selected through a monochromator. The light is guided to the optical board through special NIR-VIS or VIS-UV optical fibers. The samples are mounted

2. EXPERIMENTAL

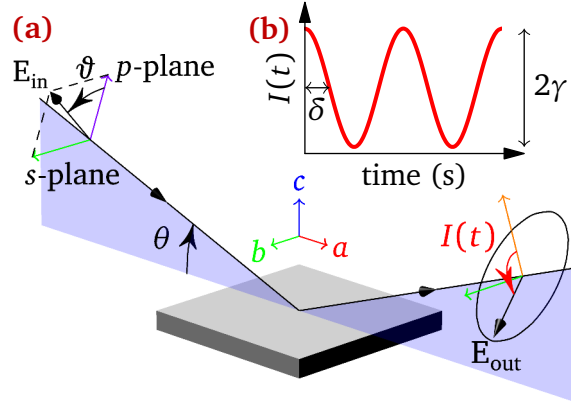


Figure 2.7: (a) Typical ellipsometry configuration. The incoming linearly polarized light has both s and p components. The blue shaded area represents the plane of incidence. After reflecting onto the sample surface with an incident angle $\theta = \pi/2 - \phi$ both incoming components undergo amplitude and phase changes which turns the light into an elliptical polarization. (b) Intensity recorder from the rotation of the analyzer. The phase shift δ and amplitude 2γ are directly related to Equation 2.2

into an UHV cryostat with an adapted design. The light is first linearly polarized through the input polarizer mounted on a rotating arm allowing to set both the incident angle θ and the linear polarization ϑ and (See Figure 2.7). The light is then reflected onto the sample and collected on the second rotating arm which support both the analyzer and the detector.

Unlike grazing incidence reflectometry [2] which measures the complex reflective coefficients r_s and r_p independently, the ellipsometry measures directly their ratio

$$\varrho = \frac{r_p}{r_s} = \left| \frac{r_p}{r_s} \right|^2 e^{i(\phi_p - \phi_s)} = \tan(\psi) e^{i\Delta}. \quad (2.2)$$

Ψ and $\Delta = \phi_p - \phi_s$ represent respectively the amplitude ratio and the difference of the phase shifts (ϕ_s and ϕ_p). In fact these parameters are not measured directly but at desired photon energy, the polarizer angle ϑ is fixed while the analyzer is rotating. The detector voltage is recorded using a lock-in technique and plotted versus the analyzer angle (See Figure 2.7).

$$I(t) = I_0 + A \sin(2\omega t) + B \cos(2\omega t). \quad (2.3)$$

This technique allows to directly extract the two Fourier components from the previous equation leading to [74]

$$\alpha = \frac{A}{I_0} = \frac{\tan^2 \Psi - \tan^2 P}{\tan^2 \Psi + \tan^2 P} \quad (2.4a)$$

$$\beta = \frac{B}{I_0} = \frac{2 \tan \Psi \cos \Delta \tan P}{\tan^2 \Psi + \tan^2 P}. \quad (2.4b)$$

Which allows to directly link to the Ψ and Δ of Equation 2.2

$$\tan \Psi = \sqrt{\frac{1 + \alpha}{1 - \alpha}} |\tan P| \quad (2.5a)$$

$$\cos \Delta = \frac{\beta}{\sqrt{1 - \alpha^2}} \frac{\tan P}{|\tan P|}. \quad (2.5b)$$

2.2.6.3 Orthorhombic model

Beside the advantages of ellipsometry, ellipsometry data relies on model assumption of the material crystal parameters and the assumption of very high surface quality (very low roughness, no oxide layer). This study considers an orthorhombic material and follows the notations shown in Figure 2.7. The Equation 1.25 for the s -polarization and p -polarization can be generalized for the orthorhombic case ($a \neq b \neq c$).

$$r_p = \frac{n_c n_b \cos \theta - \sqrt{n_c^2 - \sin^2 \theta}}{n_c n_b \cos \theta_i + \sqrt{n_c^2 - \sin^2 \theta}} \quad (2.6a)$$

$$r_s = \frac{\cos \theta - \sqrt{n_a^2 - \sin^2 \theta}}{\cos \theta_i + \sqrt{n_a^2 - \sin^2 \theta}} \quad (2.6b)$$

with n_a, n_b and n_c the three components of the anisotropic index of refraction. In order to obtain the dielectric constant of the orthorhombic model it is necessary to invert the following equation

$$\frac{n_c n_b \cos \theta - \sqrt{n_c^2 - \sin^2 \theta}}{n_c n_b \cos \theta_i + \sqrt{n_c^2 - \sin^2 \theta}} \frac{\cos \theta_i + \sqrt{n_a^2 - \sin^2 \theta}}{\cos \theta - \sqrt{n_a^2 - \sin^2 \theta}} = \tan(\psi) e^{i\Delta}. \quad (2.7)$$

Which is not possible without additional assumptions, or without different measurements from different sides of the samples [75].

2.2.6.4 Cubic model

In a fully isotropic medium $\epsilon_a = \epsilon_b = \epsilon_c$ Equation 2.7 can easily be inverted

$$\epsilon(\omega) = \sin^2 \theta \left[1 + \tan^2 \theta \left(\frac{1 - \rho}{1 + \rho} \right)^2 \right] \quad (2.8)$$

2. EXPERIMENTAL

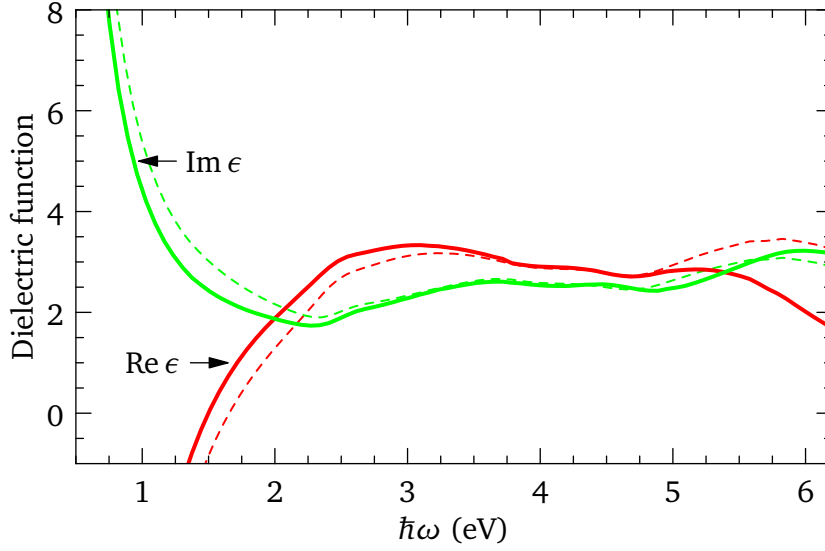


Figure 2.8: Dielectric function of Sr_2RuO_4 . The pseudo dielectric function (dashed curve) is the actual ellipsometer output although the full line represent ab -plane true dielectric function calculated from the c -axis dielectric function of [77].

Which leads to

$$\epsilon_1 = \sin^2(\theta) \left[1 + \frac{\tan^2(\theta) (\cos^2(2\psi) - \sin^2(\Delta) \sin^2(2\psi))}{(1 + \sin(2\psi) \cos(\Delta))^2} \right] \quad (2.9a)$$

$$\epsilon_2 = \sin^2(\theta) \frac{\tan^2(\theta) \sin(4\psi) \sin(\Delta)}{[1 + \sin(2\psi) \cos(\Delta)]^2}. \quad (2.9b)$$

2.2.6.5 Tetragonal model

In this study both Sr_2RuO_4 and $\text{HgBa}_2\text{CuO}_{4+x}$ have a tetragonal crystal structure so that $\epsilon_a = \epsilon_b \neq \epsilon_c$. The inversion can be done in several steps. First Ψ and Δ are inverted using the cubic model, Equation 2.9, to get the so called pseudo dielectric function ϵ_{pd} [22, 76] which is a mix of the ab -plane and c -axis. Then the c -axis dielectric function –for example from Kramers-Kronig analysis analysis taken from reflectance data– is used to invert Equation 2.7

$$\epsilon_{\text{pd}} = \sin^2\theta + \sin^4\theta \times \left(\frac{\sqrt{\epsilon - \sin^2\theta} \sqrt{\epsilon} - \sqrt{1 - \epsilon_c^{-1} \sin^2\theta}}{\sqrt{\epsilon - \sin^2\theta} \sqrt{1 - \epsilon_c^{-1} \sin^2\theta} - \sqrt{\epsilon} \cos^2\theta} \right)^2. \quad (2.10)$$

The resulting in-plane dielectric function is shown in Figure 2.8 along with the pseudo dielectric function

2.2.6.6 Window and focusing lens corrections

By using a cryostat and focusing lenses the light travels through two additional mediums, which affects its polarization. It is possible to remove these components by measuring the optical function of the optical equipment afterwards. At room temperature the sample is measured inside the cryostat with the focusing lenses, then it is measured in air without any lenses. The comparison of the two measurements allows deducing the impact of both the lenses and cryostat windows

$$\tan \psi_{\text{win}} = \frac{\tan \psi_{\text{cryo}}}{\tan \psi_{\text{free}}} \quad (2.11a)$$

$$\Delta_{\text{win}} = \Delta_{\text{cryo}} - \Delta_{\text{free}}. \quad (2.11b)$$

Using the fact that the windows and lenses are not affected by the change of temperature of the sample inside the cryostat, it is possible to perform the correction at any temperature

$$\tan \psi(T) = \frac{\tan \psi_{\text{cryo}}(T)}{\tan \psi_{\text{free}}} \quad (2.12a)$$

$$\Delta(T) = \Delta_{\text{cryo}}(T) - \Delta_{\text{free}}. \quad (2.12b)$$

Provided that the window calibration is correct and that no oxide/water layer is present on the sample surface, this procedure allows to have a precise anchor of both the phase and the intensity of the reflectivity which greatly helps the fitting and the KKR of the data at high energy.

2.2.7 Raman spectroscopy

The Raman spectra are measured at room temperature with polarizers using a homemade micro-Raman spectrometer equipped with an argon laser with a wavelength of 514.5 nm, a 5x,20x,50x and 100x lenses, a half-meter monochromator, and a liquid nitrogen-cooled charge-coupled-device (CCD) detector. The spectral resolution is 0.12 meV and the laser power is kept low to prevent any damage to the sample surface.

2. EXPERIMENTAL

Fermi-liquid like properties in the pseudogap phase of the cuprates

Cuprates high- T_c superconductors exhibit enigmatic behavior in the non-superconducting state. For carrier concentrations near optimal doping, the transport and spectroscopic properties are unlike those of a Landau-Fermi liquid. Overdoped cuprates behave like conventional Fermi-liquid metals [78–80]. Recently the idea of Fermi-liquid properties on the underdoped side had a growing impact in the literature and these properties remained elusive for a long period mostly due to the difficulty to grow high quality underdoped crystals of large size. Thanks to a recent breakthrough in crystal growth, very clean samples of the $\text{HgBa}_2\text{Ca}_{n+1}\text{Cu}_n\text{O}_{2n+2}$ family were produced [81]. $\text{HgBa}_2\text{CuO}_{4+x}$ is the simplest member of the family but also has, to date, the highest critical temperature among the single layers cuprates, with $T_c = 97\text{ K}$.

The study presented here shines light on the pseudogap phase of the cuprates. It will point out three important phenomena: 1) The near-nodal excitations of underdoped cuprates obey Fermi-liquid like behavior. Data from previous studies and from the literature point to the same conclusion, which indicates a class of universality among the cuprates. 2) In the normal state, coexistence of strong coupling to bosonic modes and Fermi-liquid correlations is possible. 3) By going toward the Mott-insulating state optical spectral weight of the coherent quasiparticle peak is suppressed. A direct link is made to the gradual decrease of the Fermi surface and thus the proximity of the Mott state.

The first part of this chapter summarizes the key features of the underdoped cuprates. The second part focuses on $\text{HgBa}_2\text{CuO}_{4+x}$, describing the samples and their characterization. The third section presents the optical measurements for three different underdoped samples and a comparison with the data of an optimally doped sample measured in a previous study. In the fourth section the Fermi-liquid energy and temperature dependence of optical scattering rate are established. The analysis is done on the $\text{HgBa}_2\text{CuO}_{4+x}$ samples but also on data of other cuprates families taken from the literature. Conclusions are drawn on the universality

3. FERMI-LIQUID LIKE PROPERTIES IN THE PSEUDOGAP OF THE CUPRATES

of the temperature and energy scaling parameter p . In the fifth section, the strong coupling formalism is used to show that within the complex electron correlations, a scenario including a Fermi-liquid correlation plus higher energy coupling modes is able to describe the data in the pseudogap state.

3.1 Introduction

With almost thirty years of extensive research and 200 000 papers published since the discovery of their superconducting properties by Bednorz and Müller [82], the cuprate literature has now a numerous of excellent reviews. For a detailed overview of the efforts done within these years, the reader may refer to Refs. [67, 83–85]. In this section, the common features of the cuprates important for the understanding of this study are discussed.

3.1.1 The complex phase diagram of the cuprates

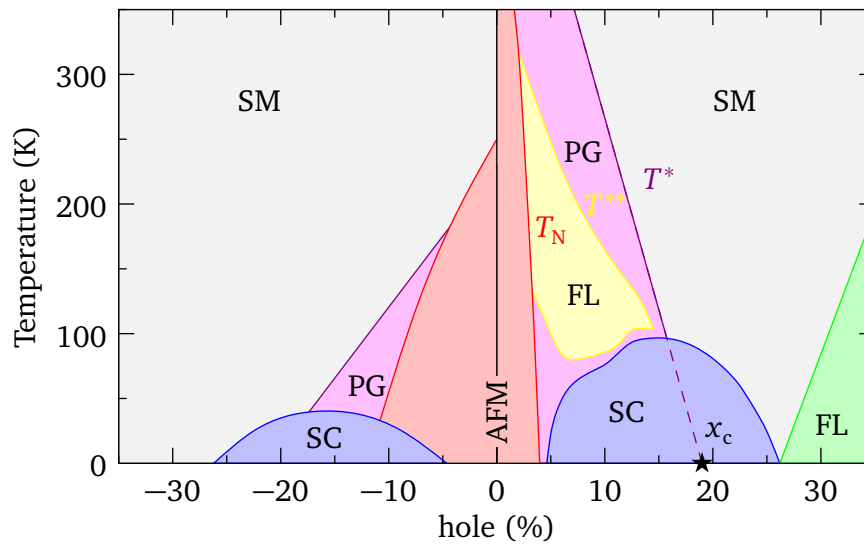


Figure 3.1: Schematic phase diagram of the cuprates. The notation stands for: the superconductivity dome (SC), the insulating antiferromagnetic (AFM), the pseudogap (PG), the strange metal regime (SM) but also a crossover area where the Fermi-liquid (FL) properties are observed. The Néel (T_N) temperature, the T^2 resistivity regime temperature (crossover) and the pseudogap temperature T^* and the critical doping x_c at 19% are also indicated. The temperature boundary (shown as thick lines) of the pseudogap, the underdoped and overdoped Fermi-liquid represent crossover temperatures.

The phase diagram of the high- T_c cuprate superconductors is usually shown as a doping-temperature graph divided into hole and electron doping. Their common feature is an alternating multi-layer of CuO_2 . The hole doped part (see Figure 3.1) is formed by hundred of different compounds which are usually grouped in families named after the first element of their chemical

formula: bismuth ($\text{Bi}_2\text{Sr}_2\text{Ca}_{n-1}\text{Cu}_n\text{O}_{4+2n+x}$, $n = 1$ and 2.3), thallium ($\text{TlBa}_2\text{Ca}_{n-1}\text{Cu}_n\text{O}_{2n+3}$), mercury ($\text{HgBa}_2\text{CuO}_{4+x}$, $\text{HgBa}_2\text{CaCu}_2\text{O}_6$) and yttrium ($\text{YBa}_2\text{Cu}_3\text{O}_{7-x}$). The electron-doped cuprates follow the same rule with: neodymium ($\text{Nd}_{2-x}\text{Ce}_x\text{CuO}_4$), praseodymium ($\text{Pr}_{2-x}\text{Ce}_x\text{CuO}_4$), samarium ($\text{Sm}_{2-x}\text{Ce}_x\text{CuO}_4$) and lanthanum ($\text{LaPr}_{1-x}\text{Ce}_x\text{CuO}_4$). Doping these material is done either by cation substitution and (or) variation of the oxygen content. In the former case the doping level is chosen by carefully selecting the initial stoichiometry and growth conditions. In the latter case, and especially for $\text{HgBa}_2\text{CuO}_{4+x}$, the doping is done by annealing the samples in air at low pressure. This is an important step and requires a lot of time in order to obtain a homogenous oxygen depletion of the sample.

At zero doping, these materials are antiferromagnetic Mott insulators (e.g.. La_2CuO_4). Upon hole doping, the antiferromagnetic insulator order persists up to around 5%. At higher doping, the superconducting dome appears at low temperature with a maximum of T_c at 16%. Below and above this doping the material is respectively described as *underdoped* or *overdoped*. Most of underdoped region is characterized by the *pseudogap* phase, which is characterized by a partially opened gap in the density of states at the Fermi surface. Above this phase and above the superconducting dome in the overdoped region the strange metal takes place, which is commonly characterized by unconventional electronic properties. The precise description of the T^* line and especially its description near the superconducting dome remains an open question of the cuprates. At higher doping the overdoped region is characterized by a simple metallic phase, which shows conventional Fermi-liquid properties.

3.1.2 Electronic structure

The tetragonal/orthorhombic structure of the cuprates is made of alternating layers of copper oxide (CuO_2) and insulator metal oxides. The superconductivity arises in the copper oxide conducting planes while the metal oxides, in between, form an insulating block layer serving as a charge reservoir. The copper cation and the oxygen anion form an octahedron (one copper, six oxygen) than can be viewed within the plane as a checkerboard (see Figure 3.2 (a)). The electronic structure can be understood as follows: The crystal field splits the copper $3d$ orbitals into two e_g states ($d_{x^2-y^2}$, d_{z^2}) and three t_{2g} states (d_{xz} , d_{xy} , d_{yz}). Owing to the highest energy, the $d_{x^2-y^2}$ is occupied by one electron ($1-x$) in average when the sample is doped). The oxygen $2p$ are also splitted and before hybridization the levels are shown in Figure 3.2 (b). Finally, the hybridization occurring between the oxygen p_x/p_y orbitals and the copper $d_{x^2-y^2}$ allows to use a three-band model represented by these orbitals as depicted in Figure 3.2 (d). At that point, band structure calculations predict that at exactly zero doping the material is metallic [88, 89]. However, experimentally the cuprates remain insulating up to about 5%, which is explained by the strong correlations present at low doping. This problem can be simplified by noting that in Figure 3.2 (d), only the $d_{x^2-y^2}$ band is crossing the Fermi energy. It is then natural to

3. FERMI-LIQUID LIKE PROPERTIES IN THE PSEUDOGAP OF THE CUPRATES

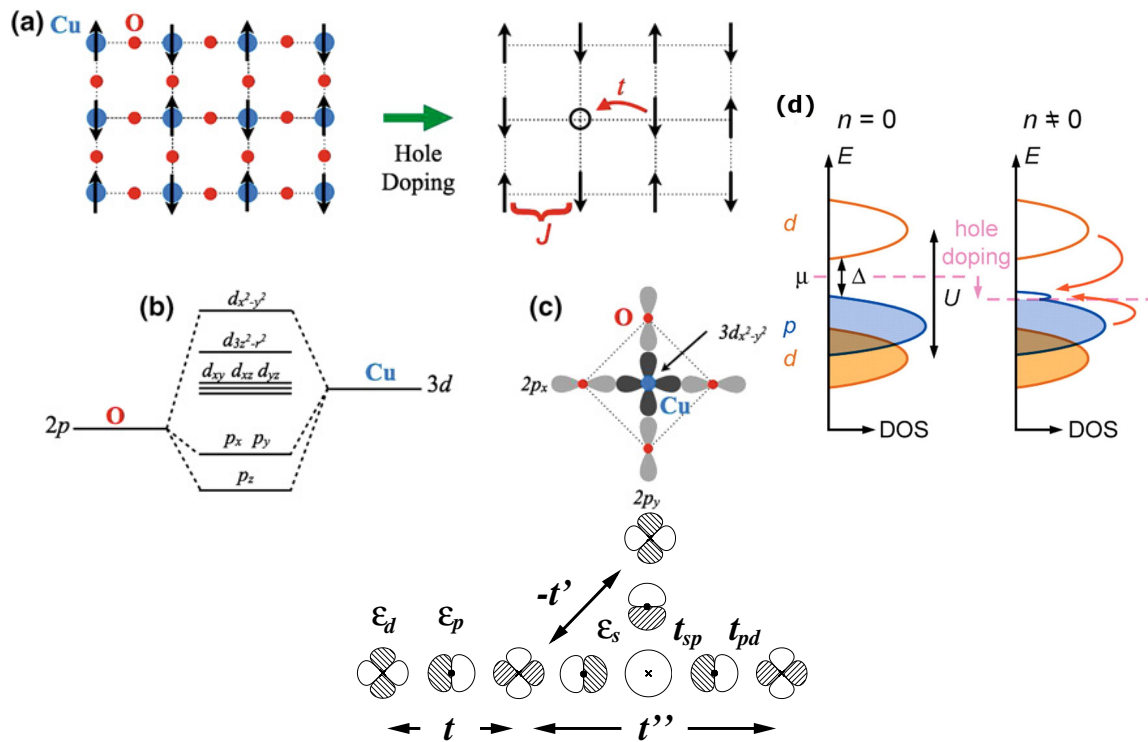


Figure 3.2: Schematic material and electronic structure of the cuprates. The copper oxide plane forms a checkerboard pattern of copper cations surrounded by oxygen anions. (a) At zero doping there is exactly one electron per site so that the electrons are localized. (b) Splitting of the Cu 3d and O 2p orbitals. (c) Hybridization of the Cu 3d and O 2p orbitals. (d) Density of states (DOS) of the Mott state ($n = 0$) and in the pseudogap state. μ is the chemical potential, U is Coulomb energy and Δ is the charge transfer gap. Adapted from [86]. (e) Representation of the hopping integral t , t' , t'' for the CuO_2 lattice. Reproduced from [87]

use the tight-binding approach, mapping the problem onto a single band Hubbard model on a two-dimensional square lattice [90].

$$H = -t \sum_{\langle i,j \rangle, \sigma} (c_{i,\sigma}^\dagger c_{j,\sigma} + h.c.) + U \sum_i n_{i,\uparrow} n_{i,\downarrow}. \quad (3.1)$$

i and j are the indices of the sites, $\langle \dots \rangle$ stands for the nearest neighbors and $\sigma = \uparrow, \downarrow$ is the spin. In addition t is the hopping parameter (kinetic energy term), U is the onsite repulsion, c^\dagger and c are respectively the creation and annihilation operators. The Mott state is then described with exactly one electron per site. For the cuprates the Coulomb interaction U is large, approximately 8 eV so that that the limit $U \gg t$ can be taken. In that limit the model reduces to the $t - J$ model

$$H = -t \sum_{\langle i,j \rangle, \sigma} (c_{i,\sigma}^\dagger c_{j,\sigma} + h.c.) + J \sum_{\langle i,j \rangle} (\mathbf{S}_i \cdot \mathbf{S}_j - \frac{1}{4} n_i n_j). \quad (3.2)$$

Where $J = 4t^2/U$ is the exchange energy. Even if electrons are totally locked due to the large onsite repulsion, the system is lowering its energy by orienting their spin anti-parallel, which drives the low doping cuprates to an antiferromagnetic insulating phase (AFM). The gap is usually referred as charge transfer gap, since excitations are done between the oxygen ($2p$) and copper ($3d$) orbitals [88], a rough estimation of its energy spread gives 2 eV. A schematic view of the resulting density of state is shown in Figure 3.2 (d). It can be seen that at higher doping a quasiparticle band develops at the Fermi level while the Hubbard gap remains large, which implies a well-defined Fermi surface and Fermi-liquid behavior.

3.1.3 Superconductivity in the cuprates

Cuprates are fascinating because of their puzzling superconducting mechanism. It took almost twenty years of effort to develop and refine phase and symmetry sensitive experiments [91, 92]. From the experimental point of view, the problem is almost settled and the symmetry of cuprates order parameters is $d_{x^2-y^2}$ [93, 94]. However, there is still no clear theoretical consensus and the constraints it makes to most of the actual theories is important. The original BCS theory –which was developed for standard type-I and type-II superconductors– is using s -wave superconducting state. With that approach, the cuprates were certainly not ideal so that the theory was extended in order to describe, at least, part of the picture. As an example, the $d_{x^2-y^2}$ orbital of the copper cations suggest that electron-electron interactions are more prominent than BCS-type electron-phonon; this is also demonstrated by the small isotope effect seen in these materials.

If there are now good candidates to replace the standard BCS phonon pairing mechanism, the debate is ongoing. First cuprates are not s -wave isotropic superconductors, that means that the gap has a momentum dependence around the Fermi surface. Below T_c the gap gradually opens at the antinodes. Additionally, nesting of the Fermi surface is seen at the four antiferromagnetic

3. FERMI-LIQUID LIKE PROPERTIES IN THE PSEUDOGAP OF THE CUPRATES

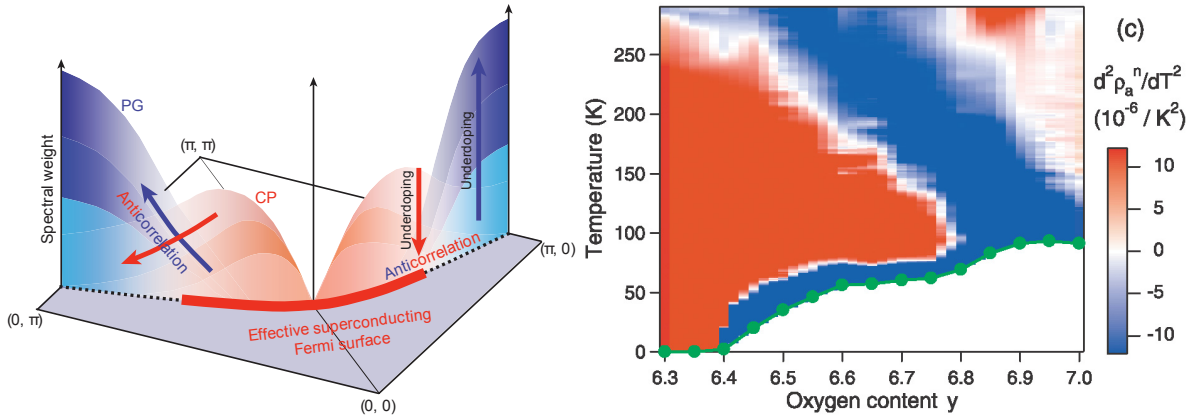


Figure 3.3: (left) Schematic view of the pseudogap (PG) doping dependence. The lower the doping is the stronger the gap at the antinodes $(\pi, 0)$ and $(0, \pi)$. The momentum dependence of the coherence peak (CP) is also shown. Reproduced from Ref. [99]. (right) Resistivity curvature mapping of the dc transport measurement of $\text{YBa}_2\text{Cu}_3\text{O}_{7-x}$. The broad white area decreasing with the doping correspond to the T^{**} in Ref. [104]; this crossover correspond to the dc resistivity gets a pure quadratic temperature dependence. The green circles indicates the T_c . Reproduced from Ref. [105]

points of the Brillouin zone. Many more phenomena are reviewed by Leggett in [95]. For optics, it may be interesting to point that at T_c only the weight of the coherent Drude peak was transferred to the condensate [96]. This phenomenon will be discussed and shown in section 3.4.6 and section 3.5.4. Additional information related to electrodynamics of high- T_c superconductors can be found in reviews [67, 68].

3.1.4 Pseudogap

After three decades of investigations, the origin of the anomalous normal state –or pseudogap– remains a subject of debate. At first glance increasing the doping goes in the direction of a lower pseudogap temperature (T^*) while at the same time the critical temperature (T_c) increases toward the optimal doping. But the mechanism is indeed much more complex to understand and the interplay with superconductivity is usually divided into two antagonistic pictures which are both supported by numerous experiments: it is either seen as a precursor [97, 98] or as competing state [99–103]. The pseudogap is characterized by a loss in the low energy spectral weight arising from an opening of a partial gap at the anti-nodes as seen by ARPES and other spectroscopic techniques [99, 106]. Shown in Figure 3.3 (left), the strength of the pseudogap is anticorrelated to the doping. Early deduced by nuclear magnetic resonance from an emergence antiferromagnetic correlation [107], the pseudogap was then observed with other experimental probes. Notably by dc transport measurements that pointed out two different conduction regimes: at high temperature a strange metal phase was identified as a linear temperature dependence of the dc resistivity that was gradually lost upon reducing the

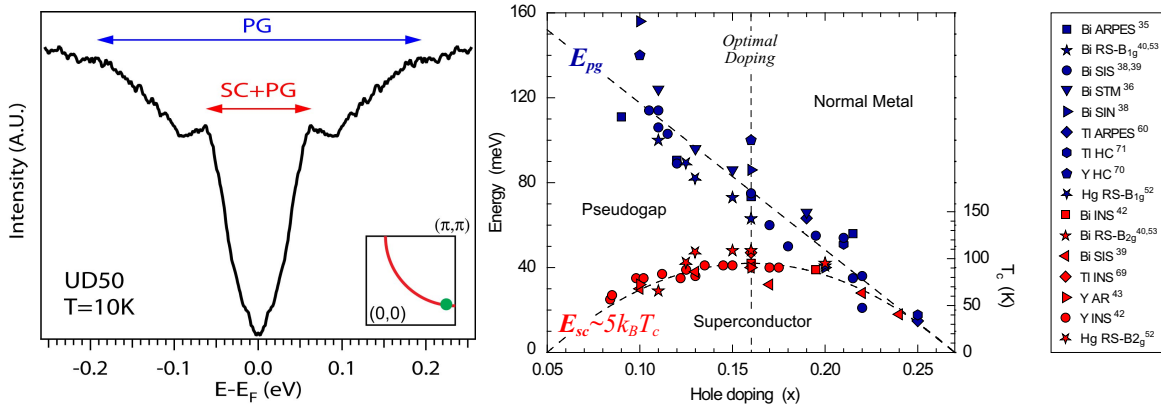


Figure 3.4: (left) ARPES symmetrized energy distribution curve near the antinode for the underdoped $\text{Bi}_2\text{Sr}_2\text{CaCu}_2\text{O}_{8+x}$ ($T_c = 50$ K). The pseudogap (PG) peak has a large energy broadening at this doping. Adapted from Ref. [115]. (right) Doping dependence of the pseudogap and superconducting gap energy scales. Adapted from Ref. [116]

temperature. Figure 3.3 (b) is showing the resistivity curvature mapping of a $\text{YBa}_2\text{Cu}_3\text{O}_{7-x}$ sample that. The modification of the electronic properties is shown by the significant variation of the color at high and low temperature. Today, with the increase of crystal quality, there are strong evidence that below the temperature T^{**} defined in [105], the resistivity ends in a pure quadratic regime [104, 105, 108]. This is exactly what is expected for a Fermi liquid. Although the underdoped cuprates have a Fermi surface that is still debated [109–111], quantum oscillation experiments and a negative Hall resistance at high magnetic field revealed its well-defined electron-like nature [112, 113]. In optics, the first doping dependent study was done on $\text{YBa}_2\text{Cu}_3\text{O}_{7-x}$ and showed that for the underdoped samples, at a temperature much higher than T_c , the low energy conductivity was suppressed [92, 114]. This effect is also seen in the other cuprates, notably for the $\text{HgBa}_2\text{CuO}_{4+x}$ samples in section 3.4.6. In addition to the scenario of two different energy scales and thus two separate gaps (partial gaps), ARPES measurements pointed out competition between these two phenomena, notably with the influence of pseudogap on the superconductivity features seen in the spectra in Ref. [115, 116] and shown in Figure 3.4. The impact of the pseudogap on the superconducting gap is increasing upon lowering the doping such that the standard $d_{x^2-y^2}$ gap form is affected at the antinodes, where the competition of the two gap is the strongest. From the theory point of view, the difficulty lies mainly in the lack of a microscopic theory capable of describing the entire phase diagram. The starting point is thus usually either the Mott state or the strongly doped simple metal and describes the doping dependence toward optimal doping. At low doping, the review of Lee *et al.* [88] is a good starting point on the doped Mott insulators. The current approaches are based on the renormalized mean-field theory, variational Monte Carlo calculations from the Gutzwiller-resonant valence bond theory [117, 118] or from the $t - J$ model [119].

Other approaches, describing, in particular, the origin of the pseudogap have emerged: 1)

3. FERMI-LIQUID LIKE PROPERTIES IN THE PSEUDOGAP OF THE CUPRATES

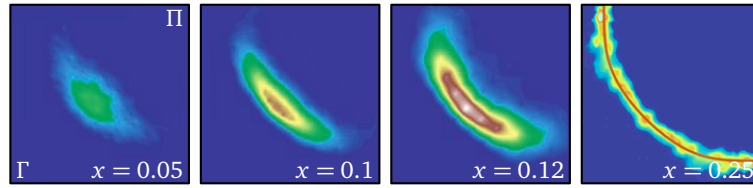


Figure 3.5: Fermi surface of $\text{Ca}_{2-x}\text{Na}_x\text{CuO}_2\text{Cl}_2$ seen by ARPES. At high doping, the Fermi surface is a well-defined circle. But the question remains open whether below 19% the Fermi surface reconstruction occurs toward small electronic pockets or remains disconnected arcs with suppressed intensity at the antinodes. Adapted from [111]

The description of Varma *et al.* [120, 121] of an order involving circulating orbital currents which would give rise to a collective magnetic mode and break time-reversal symmetry, as seen experimentally in polar Kerr experiments in $\text{YBa}_2\text{Cu}_3\text{O}_{7-x}$ [122] and $\text{La}_{2-x}\text{Sr}_x\text{CuO}_4$ [123] but also with inelastic neutron scattering [124]. However, the experimental evidence for other cuprates families is still lacking. 2) The Yang-Rice-Zhang (YRZ) theory [125] describes the Fermi surface reconstruction happening at the critical doping x_c as shown by ARPES data in Figure 3.5. This theory uses a phenomenological Ansatz of the self-energy, based on the Mott localization at weak coupling in low dimension.

Research has also been focused on charge and spin density waves. If the latter as an onset temperature much lower than the pseudogap, recent experiment tends to show that the charge density wave order may be not so far from T^* so that its relation with the pseudogap has been much debated [126–129]. With an increasing number of observations in the different cuprates families, the doubt on the intrinsic and universal character of these modes is reduced, but the natural question whether the pseudogap may be produced by an ordered state, or being both parts of the same physics remain at that time an open question.

3.2 Samples

Several single crystals of $\text{HgBa}_2\text{CuO}_{4+x}$ (Hg1201) were grown using the two-flux method as presented in [130]. From this technique, the resulting samples were all underdoped with a critical temperature of about 78 K. In order to obtain the desired doping level a long annealing procedure was done in air, at different pressure (10^{-6} mbar to 10^{-1} mbar) and temperatures (460 K to 550 K). The resulting mm-sized crystals shown in Figure 3.6 (b-d) are labeled Hg1201-UD45, UD55, UD67, OpD97, which indicate their superconducting transition temperature measured by magnetometry (see Figure 3.7). The optimally doped sample OpD97 data is reproduced from the previous study of van Heumen *et al.* [22, 35] and is used as a comparison with the underdoped samples. In addition the measurement of the underdoped UD67 was recently published in [2, 131]. Table 3.1 summarizes the different characteristics of the crystals. In this study, in order to keep a logical order, the values will always be listed from the most

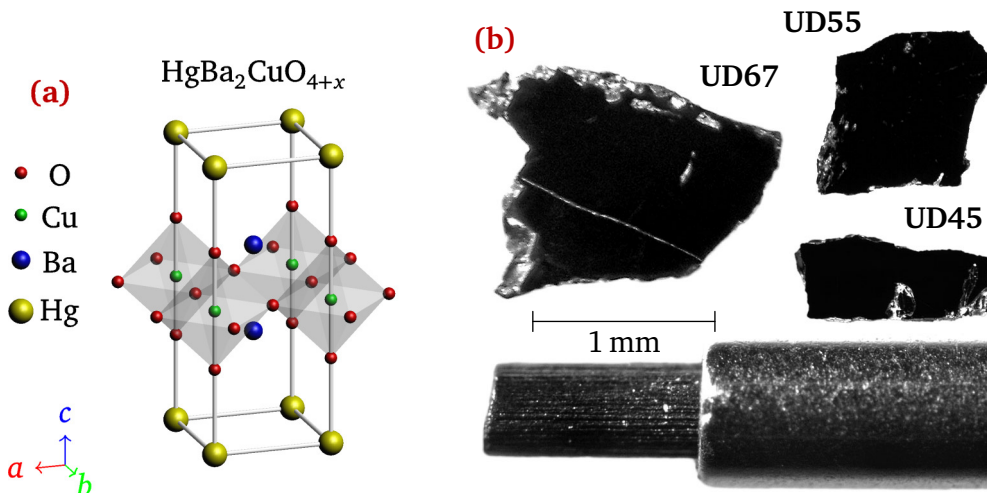


Figure 3.6: (a) Crystal structure of the single-layer mercury-based cuprate superconductor: $\text{HgBa}_2\text{CuO}_{4+x}$. (b) $\text{HgBa}_2\text{CuO}_{4+x}$ samples grown by the group of Greven and used in this study; respectively UD67, UD55 and UD45. The 0.5 mm carbon tip of a mechanical pencil is shown as a comparison.

underdoped sample (UD45) to the optimally doped one (OpD97).

3.3 Transport measurements

Transport measurements were performed by Barisic *et al.* using the 4-terminal method and shown in Figure 3.7. The data was published in [81, 104, 132]. In addition to the pseudogap temperature where the resistivity deviate from the linear regime, they introduce a region $T' \geq T \geq T^{**}$ where the resistivity is purely quadratic. T' is defined as the onset of the superconducting fluctuations. Due to the small size and irregular shape of the samples, the absolute resistivity results are flawed by a large uncertainty which can be corrected by comparing the data to the resistivity obtained from the low-energy Hagen-Rubens fit to the reflectivity (see section 3.4.2). The rescaling constants used for the transport measurement are respectively 0.21, 0.58, 0.50 and 0.53 from OpD97 to UD45. Above T_c , the excellent match of the temperature dependence of the two different probes shown in Figure 3.7 is a guarantee of data quality. The temperature and scaling parameters of the resistivity data are summarized in Table 3.1. It could be noted that the critical temperature measured by the dc-transport is not corresponding to the one found in magnetometry. The discrepancy is explained in [81, 104]; the difficulty comes from the contact of the samples with gold wires which required a cure for several minutes under the same annealing conditions done for the doping procedure. Even if the duration of this procedure was very short compared to the total annealing process, a small portion of the sample resulted with an enhanced hole doping and thus a higher critical temperature. The overall bulk properties of the sample were unchanged with a 10% to 90% characteristic drop of the

3. FERMI-LIQUID LIKE PROPERTIES IN THE PSEUDOGAP OF THE CUPRATES

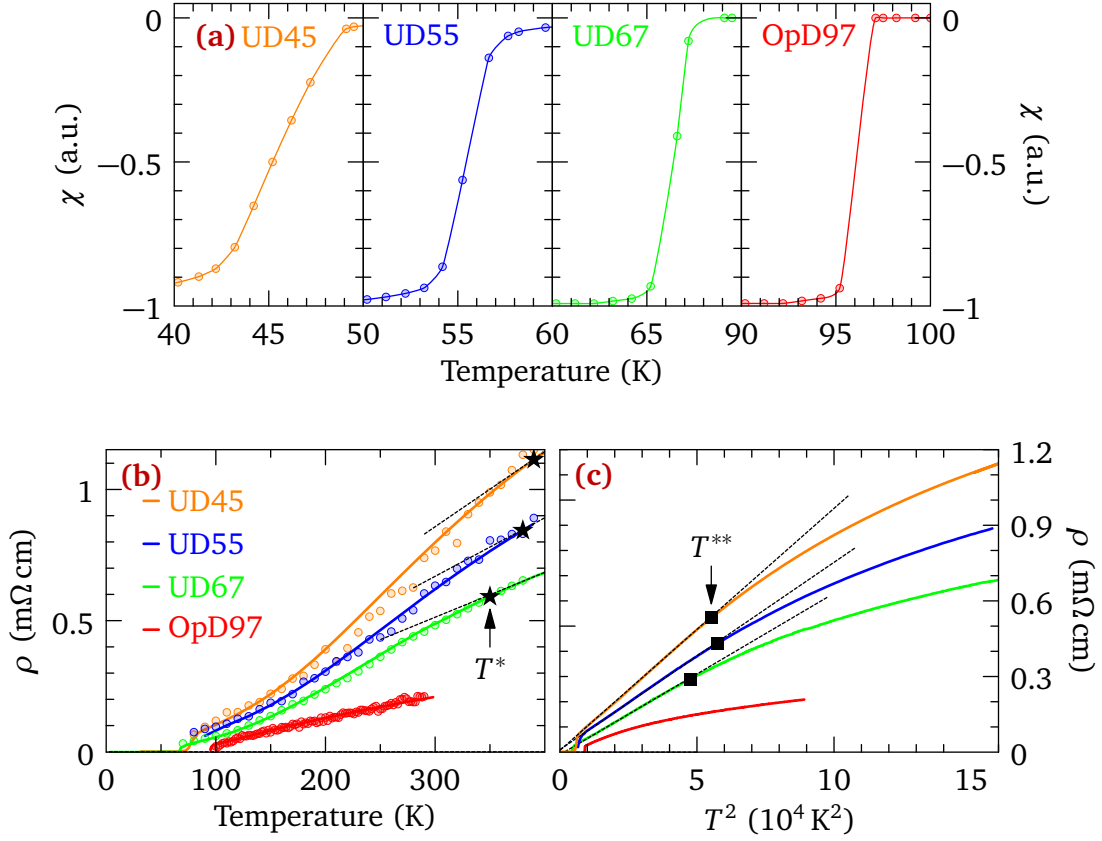


Figure 3.7: (a) Zero field cooling susceptibility of the $\text{HgBa}_2\text{CuO}_{4+x}$ samples. The susceptibility was rescaled to the lowest temperature value. The transition width is much larger for the strongly underdoped samples. (b) dc resistivity measurement from transport experiment (plain lines) and optical resistivity extrapolated using either the Hagen-Rubens equation or Drude-Lorentz fit to the low energy reflectivity. T^* are shown by the black stars. (c) Resistivity plotted against squared temperature. T^{**} are shown by the black squares. The dc transport and magnetometry data is kindly provided by Barisic and Greven.

susceptibility at T_c within 1 K for OpD97. On the other hand, the resistivity measurement of the lowest doping samples is affected and Figure 3.7 (b,c) shows a filamentary superconductivity at temperature much higher than the bulk susceptibility measurement of Figure 3.7 (a). Another side effect is a small narrowing of the T^2 regime, which nevertheless doesn't affect the linear and quadratic transport coefficients [104].

Table 3.1: Parameters and characteristics temperatures of the different $\text{HgBa}_2\text{CuO}_{4+x}$ samples shown in Figure 3.6.

x (%)	T_c	T'	T^{**} (K)	T^*	dimensions (mm)	usable area (mm ²)
5.5	45	100	235	390	0.77 × 0.81	0.577
6.3	55	90	240	380	0.40 × 1.02	0.350
10	67	84	218	350	1.51 × 1.22	1.205
16	97	-	-	-	1.1 × 1.4	1.007

3.4 Optical measurements

As described in section 2.2 the entire data spectrum consists of several measurements involving different detectors and sources but also different spectrometers and cryostat. In this study, the normal incidence reflectivity and ellipsometric measurements were carried out with two FTIR spectrometers and an ellipsometer. The measurements of the three samples span an energy range starting from the xFIR to the UV.

3.4.1 Sample preparation

Samples were cleaved along the ab -plane resulting in clean and almost flat surfaces while in some parts of the surface remaining small terraces were visible. The samples were glued onto specially sized OFHC copper sample holder using silver paste. $\text{HgBa}_2\text{CuO}_{4+x}$ being a very hygroscopic and self-doping material, no curing of the silver paste was done; the paste was dried in dry air resulting in weakened contact strength, but ensuring that the sample surface would not be doped through the procedure. As an extra care, the surface was micro-polished under a continuous nitrogen flow prior to any measurement; the gentle polishing of the surface was done with a 0.1 μm abrasive tape. The disadvantage of that technique is the risk of introducing a small tilt to the exact ab -plane surface and thus a potential inclusion of spurious c -axis features such as phonons or a decrease of the overall reflectivity. Such features can be partly suppressed with s -polarized light using the adequate polarizer. After the polishing process, the sample surface was checked and immediately transferred in an ultra high vacuum home made cryostat.

3.4.2 Normal incidence reflectivity

3.4.2.1 In-plane measurement

The FIR to NIR in-plane reflectivity at near-normal incidence of these extremely small samples was measured using the Bruker IFS 113v spectrometer coupled to the ultra-high vacuum and high stability home-made cryostat presented in section 2.2.3. The regular working vacuum of the order 10^{-8} mbar was necessary to avoid as much as possible condensation of water and other residual vapors on the sample surface. For the UD55 sample, a high-energy upgraded Bruker IFS 66v/S extended this reflectivity range to 3 eV; for which another cryostat was used to fit the apparatus. In both setups, the gold and silver evaporators allowed an in situ deposition of a thin reference layers on the sample surface. This technique produced reproducible absolute reflectivity for these mm-sized samples. Several detectors and beam-splitters were used; Table 3.2 summarizes the couples of detectors for sample UD67. The spectral resolution is 0.1 meV in the FIR. Due to the small sizes of UD55 and UD45, the measurement used slightly different energy ranges.

Due to the high stability of the cryostat, the measurements were conducted from 9 K to 390 K at a cooling speed of about 1 K min^{-1} . This also corresponds to one spectrum per kelvin. In order to increase the signal to noise ratio, the data were averaged over 10 K intervals. The long-term drift of the light sources and detectors was calibrated using the high-stability flipping-mirror placed in front of the cryostat window. The mirror was flipped up and down every 20 minutes, providing a continuous monitoring of the light intensity drift. The remaining uncorrected drift was analyzed during the warm-up process, which leads to a thermal hysteresis effect below the noise level in the FIR and below 0.5 % at higher energies. The final absolute and calibrated reflectivity data are shown in Figure 3.8 for the three samples at selected temperatures, together with the data of van Heumen *et al.*.

Between each measurement, the evaporated metallic layer was removed using scotch tape. It was common that some part of gold was remaining on the sample surface, which in these cases required re-polishing the surface. The good overlap of the data along the different spectral ranges confirms that the bulk properties are not affected by the procedure. Prior transferring the sample to the cryostat, the sample surface quality was verified using an optical microscope.

The reflectivity data of the three dopings is shown in Figure 3.8 at selected temperatures. The data of Ref. [22] ranging from 20 K to 290 K is shown as a comparison. Most of the temperature dependence is happening at low energy, this part is magnified in the right graphs. The metal-like reflectivity shown in Figure 3.8 is dominated by the excitations in the CuO_2 plane which are strongly influenced by the sample doping [66]. The relative accuracy of the low-energy reflectivity as a function of temperature can be assessed by fitting the low-energy reflectivity to the Hagen-Rubens equation presented in section 1.2.1.3, which is accurate in the $\omega \ll 1/\tau$ regime. This assumption is at least fulfilled above T_c for UD45 but the range

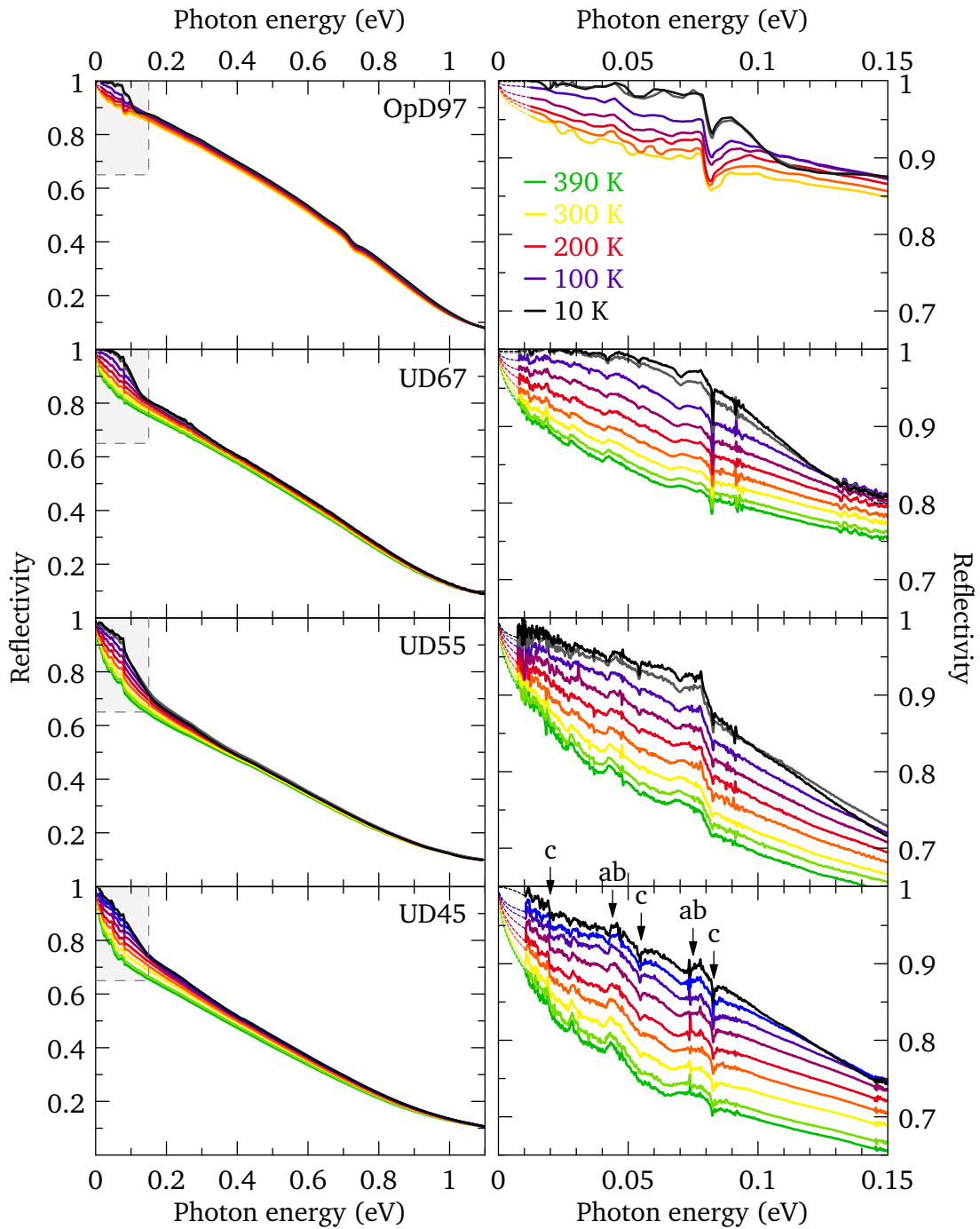


Figure 3.8: In-plane reflectivity of the $\text{HgBa}_2\text{CuO}_{4+x}$ samples at selected temperatures. From top to bottom: OpD97 [22], UD67, UD55, UD45. **(left)** Full energy span. The dashed gray rectangles indicate the magnified FIR range **(right)**. In-plane and residual c -axis phonons are shown by the black arrows in the last graph.

3. FERMI-LIQUID LIKE PROPERTIES IN THE PSEUDOGAP OF THE CUPRATES

Table 3.2: Combination of sources, beam splitters and detectors used for the measurement of the underdoped $\text{HgBa}_2\text{CuO}_{4+x}$ samples. The low cutoff energy was respectively 11, 7 and 8 meV respectively starting from UD45.

High energy cutoff (meV)						
UD45	-	72	145, 372	471	1240	-
UD55	9	74	149	471	1054	3100
UD67	11	80	130	366	1240	-
Source	Hg	Hg	Globar	Globar	Tungsten	Tungsten
Beam splitter	Si 10 μm	Ge/Mylar 6 μm	Ge/KBr	Ge/KBr	Si/CaF	Si/CaF
Detector	Bolo 1.6K	Bolo 4K	Bolo MIR	MCT	MCT	Diode
Polarizer	PE	Gold	KrS-5	KrS-5/MIR	MIR/NIR	Visible

of the fit is reduced to lower energies for UD67 since the scattering rate is about 15 meV at 70 K. The comparison of the infrared data to the dc transport shown in Figure 3.7 confirms that $\text{HgBa}_2\text{CuO}_{4+x}$ exhibits the lowest residual resistance among the cuprates. The transition from a quadratic to a linear temperature dependence of the resistivity at about T^{**} is also confirmed such as the linear temperature dependence at T^* .

The FIR reflectivity increases by lowering the temperature. This is directly due to the lowering of the carrier scattering rate. At about 0.5 eV, the broad bump-like structure is gradually phased out by going underdoped; for UD45, the reflectivity is almost linearly decreasing in that range. This effect can be ascribed to the decrease of metallicity and has a direct impact on the optical phonons that are less screened and thus more apparent at low doping. For instance, the in-plane oxygen vibration mode at about 42 meV is much stronger in the reflectivity of UD45. In contrast, The weak doping dependence is seen as a slight decrease of the reflectivity from 11 % for UD45 to about 9 % for OpD97. At the same time, the reflectivity minimum is almost at the same energy [66]. In Figure 3.9 the reflectivity is shown for the entire energy range, including the ellipsometric measurements (see section 3.4.3). Up to around 2 eV, the reflectivity shows a featureless region, which is an illustration of the charge transfer gap between the O_{2p} orbital and the Cu $3d$ upper Hubbard band (see section 3.1.2). Comparing with Figure 3.10 of the next section, the arrows shown on the last graph of Figure 3.8 point three residual c -axis phonons (19.2, 52.7 and 80.6 meV). This observation emphasizes that the use of s -polarized light didn't suppress all the phonons so that a small inhomogeneity in the samples is probable. The highest mode shouldn't be confused with a strong in-plane phonon mode close to 80 meV [133]. It is also important to remember that the phonon dip is the tail of the phonon mode so that in the real part of the conductivity, the energy of the phonon mode is a bit lower as can be seen in Figure 3.10.

The reflectivity is a useful way of analyzing strong and sharp modes such as phonons. Nevertheless, the subtle change of the low-energy reflectivity slope due to the low energy

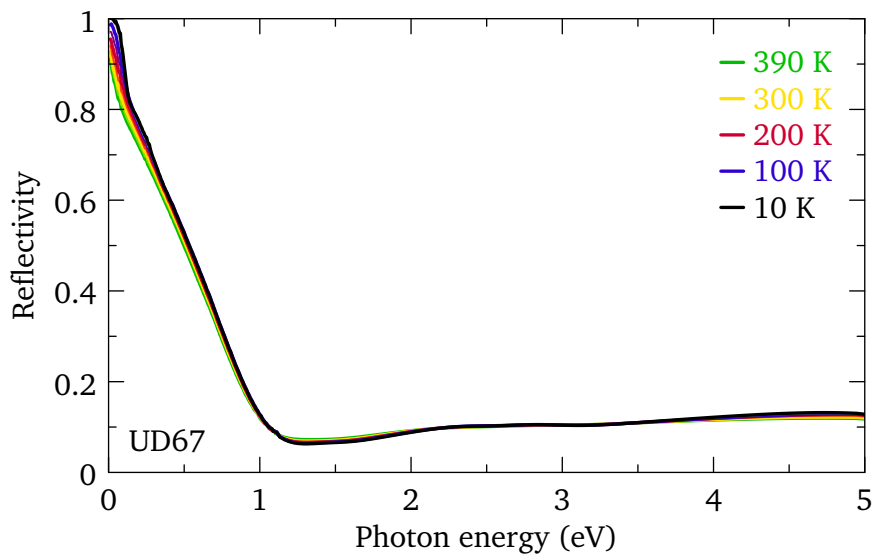


Figure 3.9: Reflectivity of $\text{HgBa}_2\text{CuO}_{4+x}$ UD67 at selected temperatures. The high energy data were converted from the dielectric function of the ellipsometric measurements.

correlation is difficult to interpret. Such analyze is better done by using the optical conductivity, which is shown in section 3.4.6.

3.4.2.2 *c*-axis measurement

Using a Bruker 70v coupled to a IR-microscope the *c*-axis reflectivity of the $\text{HgBa}_2\text{CuO}_{4+x}$ UD67 and UD45 reflectivity $R(\omega)$ was also measured at room temperature using the polished edge of the samples. The data from OpD97 was measured on the *ac*-plane of a different sample from 3.7 meV to 2.5 eV by C.C. Homes. A thin gold layer was sputtered on one side of the sample while the other part was kept protected with a thin aluminum foil. The *c*-axis reflectivity was measured by taking spectra on either side of the interface with the portion covered with gold. The measurement was repeated several times and the reproducibility was within 1 % at 0.1 eV. Compared to the optimally doped sample which was measured using a large surface and a conventional technique, the diffraction limits of the IR-microscope limited the low-energy data to about 50 meV; the highest energy was 1.5 eV. By virtue of an almost flat reflectivity at high energy, the reflectivity was fitted using the Drude-Lorentz model and extrapolated as a constant to high energy. The reflectivity curves are shown at room temperature in Figure 3.10; the four expected phonons are the mercury and barium vibration modes at about 11 meV and 19 meV [22] and also the vibration of the in-plane oxygen at 44 meV and 74 meV. The highest mode is the apical oxygen vibration mode, which is probably split due to disorder. in chapter 4 other possible scenarios for the phonon splitting are introduced for Sr_2RuO_4 . The *c*-axis optical conductivity of the cuprates is known to be dramatically different from the in-plane which emphasize the strong anisotropy of quasiparticles around the Fermi surface [134, 135].

3. FERMI-LIQUID LIKE PROPERTIES IN THE PSEUDOGAP OF THE CUPRATES

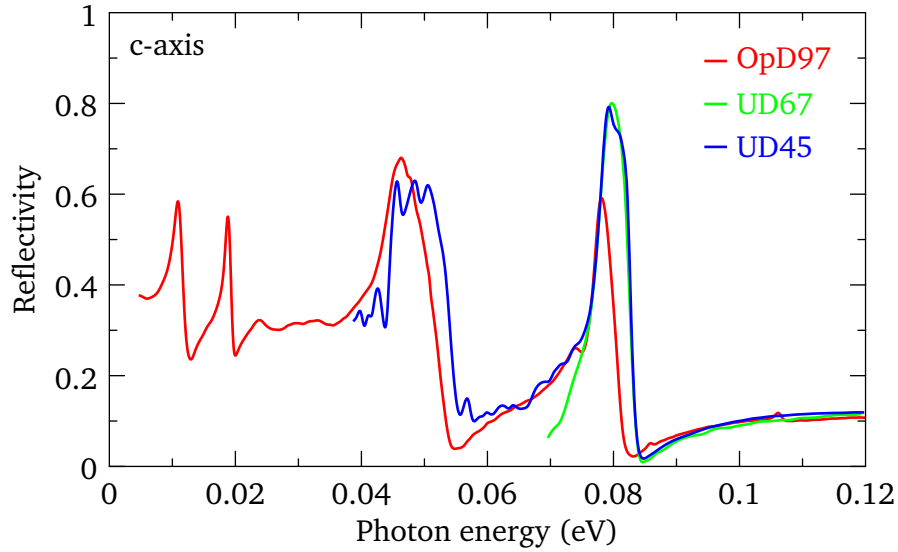


Figure 3.10: *c*-axis reflectivity of $\text{HgBa}_2\text{CuO}_{4+x}$ at room temperature. The data of UD67 and UD45 was measured on a Bruker 70v attached to a IR-microscope thus limiting the beam size to about $50\ \mu\text{m}$. The small sample size and the diffraction limit restricted the measurement to about 40 meV. The OpD97 data are reproduced from Ref. [22].

3.4.3 Ellipsometry

The ellipsometric measurements complete and extend the data up to 5 eV for the UD67 and 3.1 eV for the UD45. Due to a technical issue, no ellipsometric data were taken for the UD55 but the spectral range was obtained the mean of reflectivity measurement. The temperature resolution is 2 K. The angle of incidence of light was respectively 61° and 62° . As explained in section 2.2.6.5, the dielectric function is a mix of the *ab*-plane and *c*-axis response. In the limit described in section 2.2.6.5, the true *ab*-plane dielectric function $\epsilon(\omega) = \epsilon_1(\omega) + i\epsilon_2(\omega)$ was extracted from $\tilde{\epsilon}(\omega)$ by inverting the Fresnel equations. In order to do so, the complex *c*-axis dielectric function $\epsilon_c(\omega)$ was obtained from the *c*-axis reflectivity measurement. This procedure was performed using the RefFIT software [16, 22]. Measurements were also performed for different angles of incidence, 65° , 70° and 80° with no notable difference on the final dielectric function. The resulting dielectric function is shown in Figure 3.11 for the UD67 sample and for few selected temperatures. Converting the ellipsometric data using Equation 1.27 in the 0.8 eV to 1.2 eV range shows a good agreement with FTIR measurements.

3.4.4 High-energy spectral weight transfer

Ellipsometric data was used to extrapolate and safely anchor the reflectivity measurements at high energy in order to provide a correct Kramers-Kronig transformation of the reflectivity data, which is necessary in order to obtain reliable optical functions in the same energy region. But this technique is also very powerful technique to unveil subtle changes of the electronic

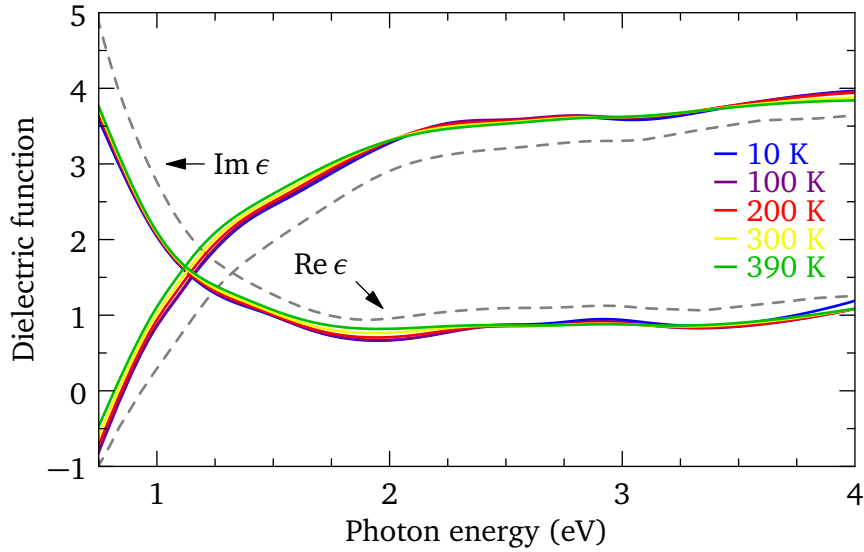


Figure 3.11: Real and imaginary parts of the dielectric function ϵ of $\text{HgBa}_2\text{CuO}_{4+x}$ UD67 extracted from Equation 2.10. The dashed lines indicate the complex pseudo dielectric function ϵ_{pd} at 290 K.

properties at critical temperatures. This technique will show that compared to the transfer of weight from the coherent quasiparticle peak to the superconducting condensate [96], the incoherent MIR conductivity is also transferred to the interband.

In order to unveil the changes at T_c , the pseudo-dielectric function was used and the optical conductivity was directly derived using Equation 1.17. The real part of the pseudo optical conductivity is shown at selected temperatures in Figure 3.12 (a) and may differ from the actual in-plane conductivity, which has been corrected for the c -axis admixture. Above 1.3 eV the onset of the charge transfer (interband) excitations appears as numerous bumps in the conductivity at 1.4, 2.6, 2.9, 3.8 and 5 eV. These excitations are almost identical for all cuprates [22, 66]. The 2.6 eV and 3.8 eV are close to the resonance observed in the RIXS experiment [136]. Panel (b) shows the ratio of conductivity with respect to the 400 K curve. Temperature traces shown for selected energies in panel (c) indicates a strong change at T_c which suggest that part of the MIR spectral weight is transferred from below 2.3 eV to above. This phenomenon is even more clearly observed by plotting the difference of conductivity below and above T_c , here between 60 K and 80 K or 60 K and 110 K. As a result, the negative (red) area is transferred to the green one. Meanwhile a careful analysis of difference of the conductivity at 1.4 eV displays a weakening of the spectral weight transfer exactly where the first interband is located. As a consequence this strongly suggest the scenario of a transfer of spectral weight from the free charges to the bound charges which is consistent with numerous studies [137–142] and recent pump-probe techniques [143], which the authors attribute to probable kinetic-energy scenario for the cuprates superconductors [144–148].

Lastly, it is interesting to see that the premise of the superconducting transition already starts around 100 K. The most intriguing scenario would rely on the pre-pairing and superconducting

3. FERMI-LIQUID LIKE PROPERTIES IN THE PSEUDOGAP OF THE CUPRATES

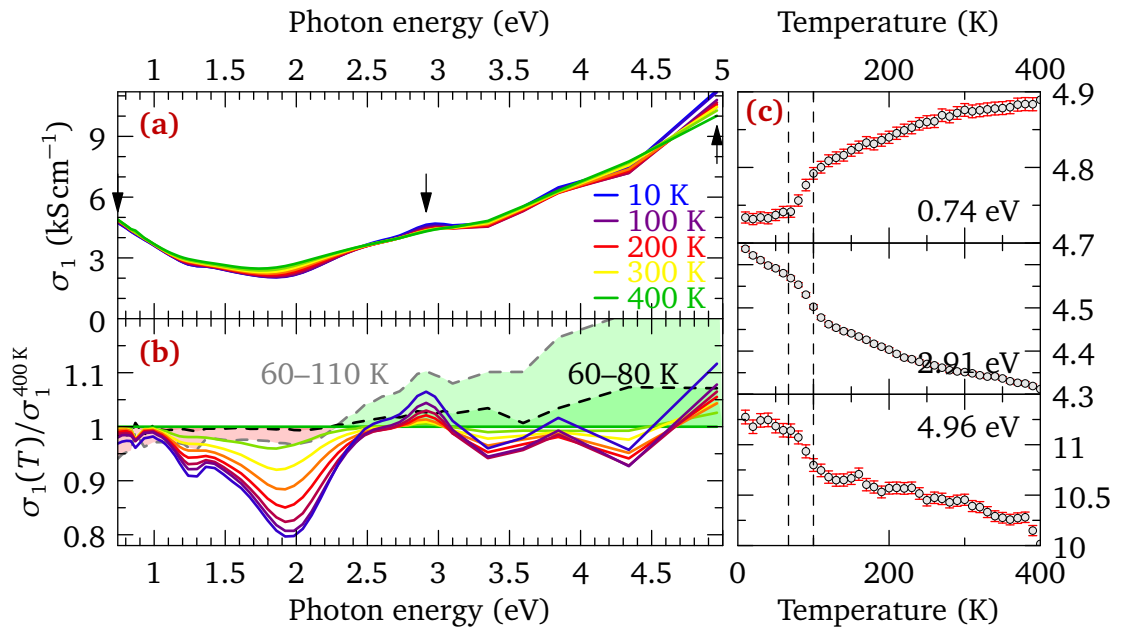


Figure 3.12: Ellipsometric optical conductivity of HgBa₂CuO_{4+x} UD67 shown at selected temperatures and photon energies. **(a)** Real part of the optical conductivity. The arrows point out the selected photon energies of the three subplots **(c)**. **(b)** Ratio of conductivity to the 400 K data. The gray and black dashed curves are the difference of conductivity below and above T_c . The former is taken between 110 K and 60 K, the later between 80 K and 60 K. These curves are difference of conductivity (not ratio) and are shown to highlight of the subtle change at T_c so that they have been shifted to unity for readability.

fluctuations. However ellipsometric measurements in the UV are especially sensitive to the surface condition, so that even if the samples might have been in contact with air for a very short period of time, a very thin layer of higher inhomogeneous T_c would show up in the spectra and broaden the transition.

3.4.5 Drude-Lorentz analysis

Using the RefFIT software [16, 28], the reflectivity and ellipsometer data were fitted simultaneously using the Drude-Lorentz model for all temperatures. The UD55 sample has only reflectivity data up to 3.1 eV. The room temperature Drude-Lorentz parameters are summarized in Table 3.3 for sample UD67. The other doping analysis obtained comparable results with the exception that UD45 required an extra secondary Drude peak; this can be understood from the fact that this sample almost loses entirely its coherent spectral weight at room temperature, while the MIR component is much less dependent on temperature [65, 96, 149]. As shown in Figure 3.12 (a), the model and Kramers-Kronig transformation of the data are almost indistinguishable which indicate the quality of the fitting procedures. The lowest interband transition starts at about 1.4 eV that allows to adequately set the limit between the free and bound charges response at 1 eV. All the modes below this energy can be either the coherent carrier response (Drude peak), the incoherent free carrier response (σ_{MIR}) or any mode such as phonons and magnons. The free carrier plasma frequency is formed by the geometric sum of the spectral weight of intraband contributions except the phonons and is not very sensitive to doping nor temperature: 2.000(24), 2.008(21), 2.053(20) and 2.046 eV starting from UD45. And for ϵ_b , respectively 4.59(5), 5.13(5), 4.10(2) and 3.66, the singular ϵ_b measurement observed in UD55 might come from the different experimental technique used at high energy (reflectivity instead of ellipsometry). Comparing to the expected value of 3.57 calculated with the Clausius-Mossotti relation in section 1.2.3.1 the experimental values are higher and anti-correlate with doping. This is an indication that the oxygen cation is responsible for an important part of the high energy response although other contributions are also required to describe the entire picture, notably the fact that ϵ_b increases at low doping which is seen by a higher reflectivity in both our data and in $\text{La}_{2-x}\text{Sr}_x\text{CuO}_4$ [66].

In the $\hbar\omega < 1$ eV energy range which is the region of interest for this study, the interband transitions are represented through the bound-charge dielectric function defined using Equation 1.60. As shown in Figure 3.14, this function is practically constant in that range and does only contribute as a constant parameter, which is combined with ϵ_∞ as the total high energy response. The confirmation of the energy independence of this parameter on the low energy part of the spectra is shown in Figure 4.19 Using the fit parameters, the data was extrapolated to zero energy and to much higher energies following the procedure explained in section 1.2.4. The complex part of the reflectivity (or its phase) was completed through Kramers-Kronig

3. FERMI-LIQUID LIKE PROPERTIES IN THE PSEUDOGAP OF THE CUPRATES

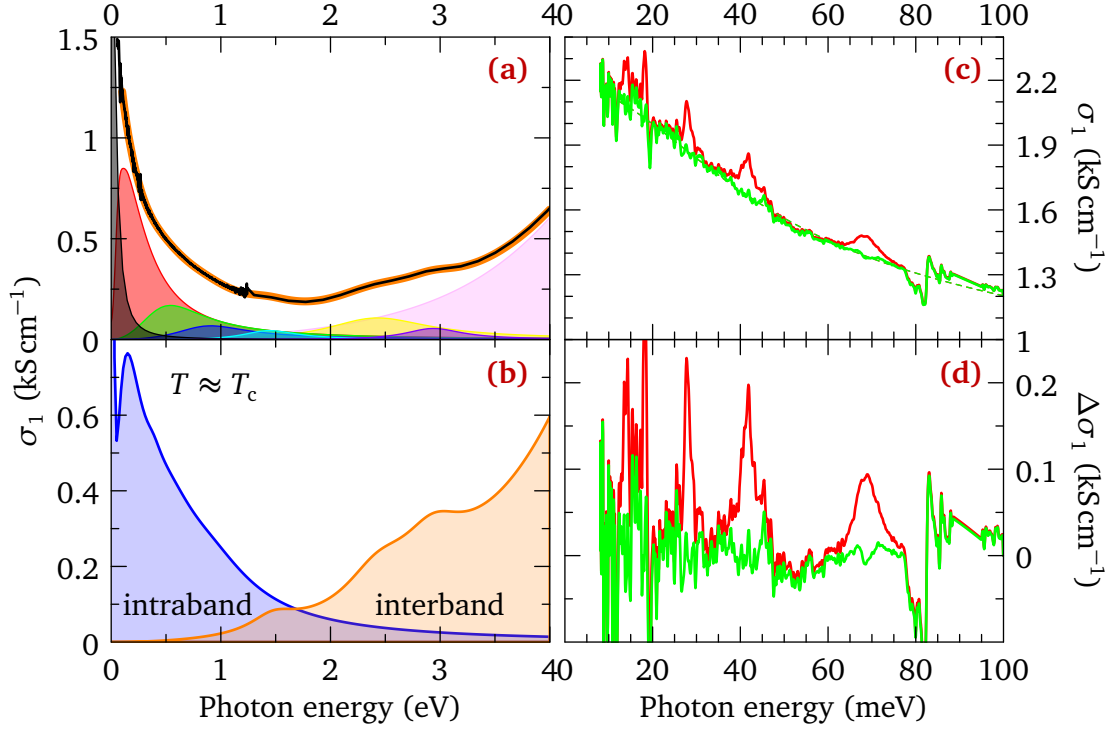


Figure 3.13: (a) Real part of the optical conductivity at room temperature for the Drude-Lorentz fit to the data by Equation 1.56 and Table 3.3. The thick orange line represents the total conductivity of the fitted model; the first oscillator in black is the Drude peak. The solid line is the conductivity obtained from the reflectivity and ellipsometry data using Kramers-Kronig relations. (b) intraband and interband conductivities from the model. (c) Comparison of the fit (dashed line) and Kramers-Kronig transformed data at 390 K, with and without phonon subtraction. (d) Difference between the Kramers-Kronig conductivity and the Drude-Lorentz fit with and without the phonon subtraction. The phonons at 15, 28, 30, 42, 69 and 78 meV were fitted using standard Drude-Lorentz line shape. The feature at 82 meV is due to the small reflectivity mismatch of two measurement ranges and was not fitted. Some parts of the phonons are still noticeable which indicates that the phonons are not completely fitted and might be better described by adding electron-phonon coupling.

Table 3.3: Room temperature Drude-Lorentz model parameters of the in-plane optical response of HgBa₂CuO_{4+x} UD67. All numbers are given in eV. The high-energy dielectric constant is $\epsilon_\infty = 2.2$. The intraband plasma frequency obtained from the intraband response is $\hbar\omega_p = 2.053(20)$ eV.

	intraband				interband			
	$j = 0$	$j = 1$	$j = 2$	$j = 3$	$j = 4$	$j = 5$	$j = 6$	$j = 7$
$\hbar\omega_{0,j}$	0	0.116	0.542	0.908	1.443	2.430	2.939	5.204
$\hbar\omega_{p,j}$	0.857	1.461	0.969	0.638	0.444	0.947	0.510	4.390
$\hbar\gamma_j$	0.046	0.337	0.747	0.805	0.598	1.126	0.636	2.723

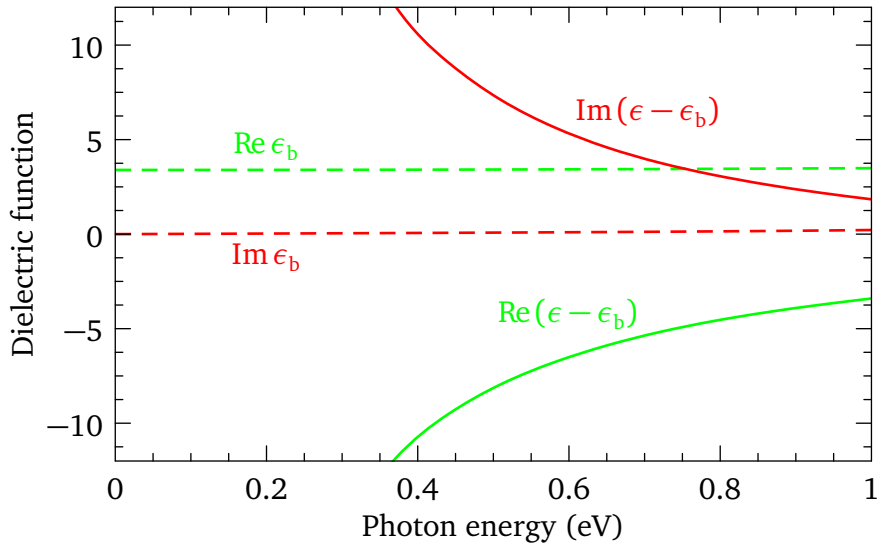


Figure 3.14: Free-charge and bound-charge contributions to the dielectric function of $\text{HgBa}_2\text{CuO}_{4+x}$ at 290 K. The negligible energy dependence of the bound-charge response indicates a clear separation between the intraband and interband responses below 1 eV.

relations and the resulting data were then transformed to the complex dielectric function using Equation 1.27. The consistency of the procedure was checked by comparing the output real and imaginary parts of the dielectric function to the ellipsometric data but also by comparing optical conductivity obtained by the Kramers-Kronig transformation of the reflectivity to the model (see Figure 3.13). The resulting $\epsilon(\omega)$ is shown in Figure 3.11 along with the pseudo-dielectric function at room temperature.

3.4.6 Optical conductivity

The optical conductivity is obtained from the dielectric function using Equation 1.15 and shown in Figure 3.15 at selected temperatures (30 K steps). For clarity the curves under T_c are plotted in gray. The small but sharp low energy features at 15, 28, 30, 42, 69 and 78 meV are the optical phonons also seen in Figure 3.13 (b,c). Below 140 meV and below T_c a strong gap-like suppression of conductivity is observed for both OpD97 and UD67; this effect is caused by the transfer of spectral weight into the zero-energy condensate peak [149, 150]. However, only the coherent spectral weight is removed by the superconducting transition, keeping the MIR conductivity (σ_{MIR}) unaffected. Additionally the suppression remains visible up to about 250 K which is much higher than the temperature of the superconducting fluctuation scenario ($T' \approx 84$ K) for UD67 [104]) and thus is a clear optical signature of the pseudogap.

A direct comparison of the different samples at room temperature is shown in Figure 3.16. The Drude peak due to the free coherent carrier response progressively narrows upon lowering the temperature. If the coherent weight is strong and indicates a Drude response for the optimally doped sample, it clearly weakens by decreasing the doping and the response becomes

3. FERMI-LIQUID LIKE PROPERTIES IN THE PSEUDOGAP OF THE CUPRATES

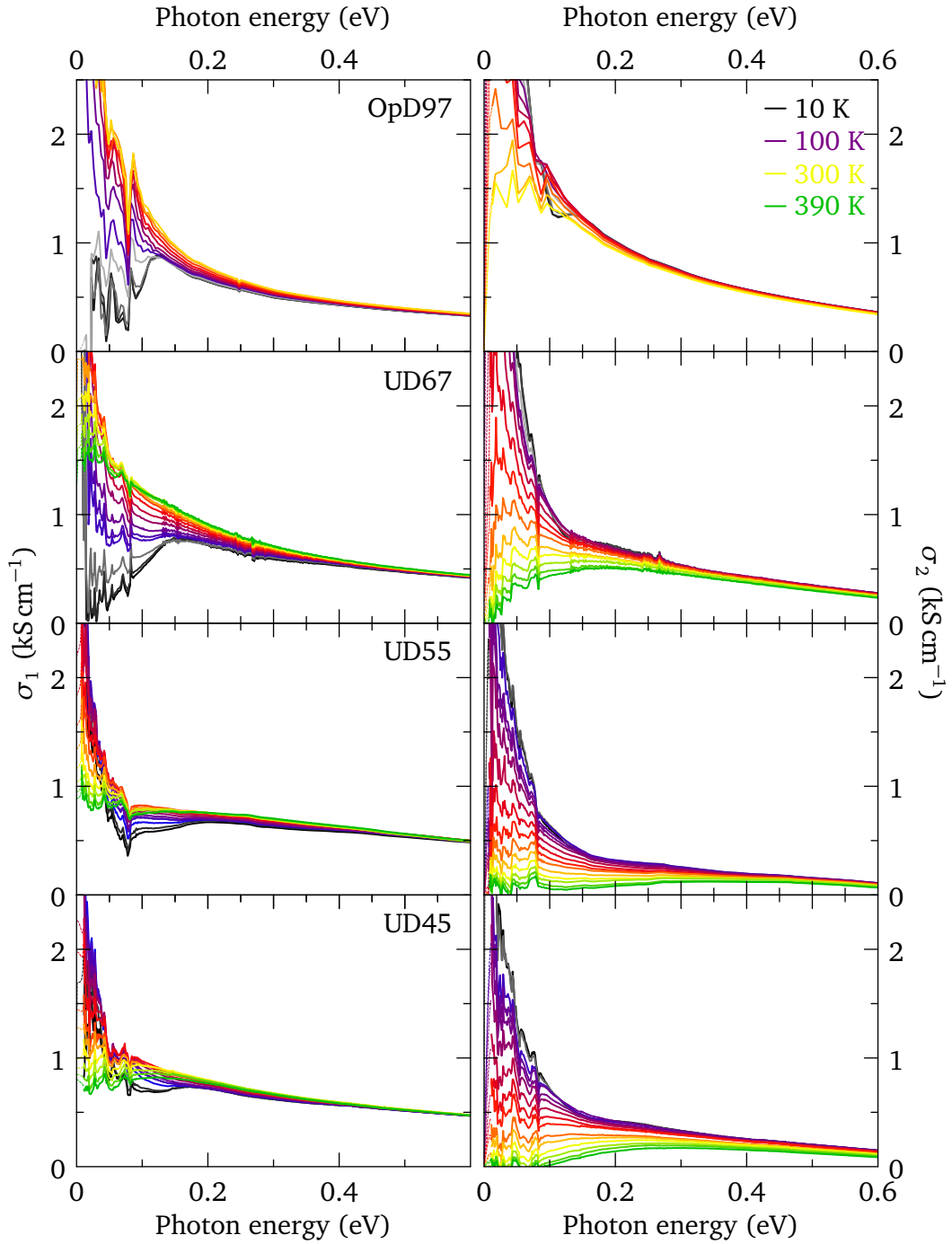


Figure 3.15: Real and imaginary parts of the in-plane optical conductivity of four different dopings of $\text{HgBa}_2\text{CuO}_{4+x}$ at selected temperatures. From top to bottom: OpD97 from [22], UD67, UD55, UD45. The gray curves represent the data for $T \leq T_c$ and the dashed lines are the low energy extrapolation.

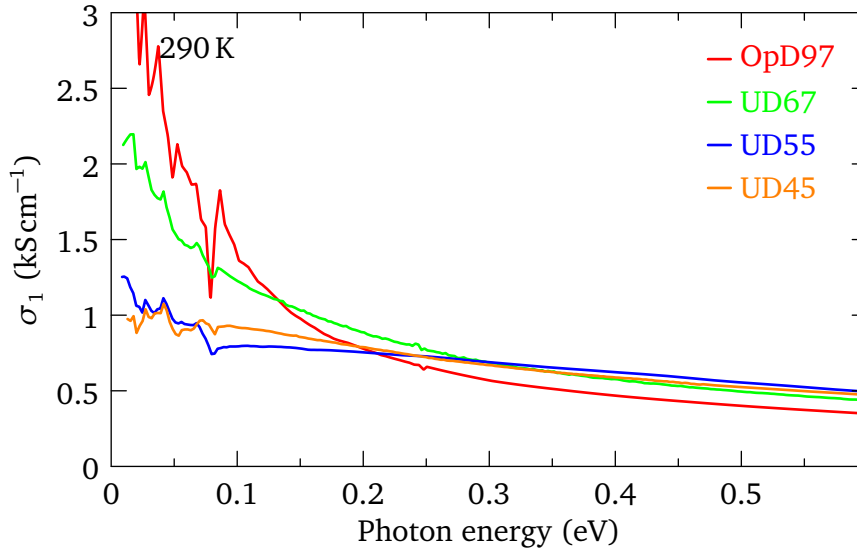


Figure 3.16: Comparison of the real part of the optical conductivity of the underdoped $\text{HgBa}_2\text{CuO}_{4+x}$ samples at room temperature. The data of OpD97 is reproduced from Ref. [22]

increasingly incoherent which is typically the case at high temperature for the UD45. Seen as a negative σ_2 , the absence of coherent peak makes the extended Drude analysis meaningless for this sample at high temperature.

For UD55 and UD45 the hallmark of the superconducting transition in the optical conductivity data is less clear; this can be understood by calculating the superfluid density for $T \ll T_c$ which is directly proportional to the strength $\omega_{p,s}$ of the superconducting condensate peak [59]. This can either be done by fitting the low energy reflectivity to a two fluid model consisting of a standard Drude plus a zero scattering or δ peak, or by assuming that the condensate peak gives rise to a $\epsilon_1(\omega) \approx -\omega_{p,s}/\omega^2$ contribution, so that it can be estimated by extrapolating the data to zero energy. Using the later estimation, the superfluid density ρ_s is much smaller for the underdoped samples which is directly seen in the superfluid strength $\hbar\omega_{p,s} = 0.61(6)$, $0.69(7)$, $1.03(11)$ and $1.19(5)$ eV starting from UD45. This strong suppression is also seen in other studies [59, 139, 151] and the linear scaling with T_c was first observed by Uemura *et al.* in Ref. [152]. Later Homes *et al.* expanded the relation by taking $\sigma_{dc}(T = T_c)$ as an additional parameter into account [153]. The reported experimental scaling form follows the scaling relation $\rho_s \equiv \omega_{p,s}^2 = (120 \pm 25)\sigma_{dc}T_c$. Using the calibrated dc conductivity or an quadratic extrapolation these measurement for the samples that have filamentary superconductivity (UD45 and UD55), the product with $\sigma_{dc}T_c$ is respectively $31.8(9)$, $29.6(7)$, $44.2(10)$ and $39.2(8)$ $\text{kS cm}^{-1} \text{K}$. The new data is introduced in the Homes scaling shown in Figure 3.17. Even using the uncalibrated conductivity given in Ref. [81] the data for the $\text{HgBa}_2\text{CuO}_{4+x}$ samples seems to have a much higher conductivity at T_c which moves all the points toward the right part of the graph. The scaling is also observed but the slope is smaller. There is presently no explanation to this mismatch.

3. FERMI-LIQUID LIKE PROPERTIES IN THE PSEUDOGAP OF THE CUPRATES

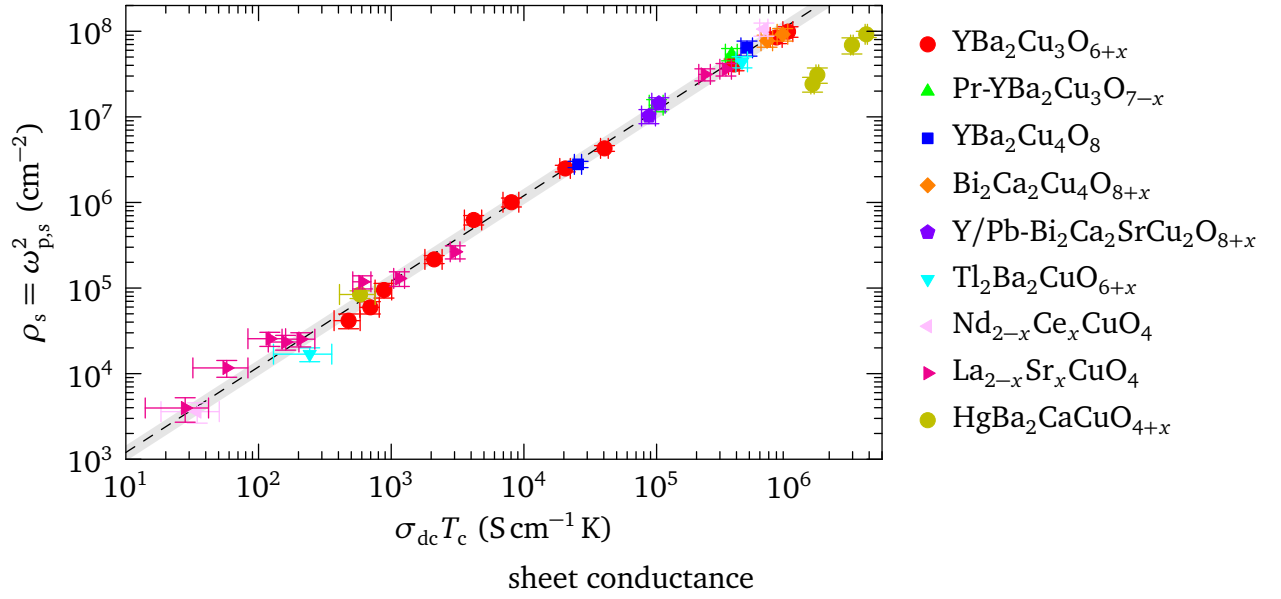


Figure 3.17: Homes scaling plot with the additional values of this study (dark yellow circle). The reference to the literature can be found in Ref. [153]

3.4.7 Sheet conductance and spectral weight

From the free carrier plasma frequency found in the previous section, the spectral weight of the sheet conductance Equation 1.45 corresponds to K and was defined as minus the kinetic energy of the charge carrier in section 1.2.1.1. Using the plasma frequency and the c -axis lattice parameter for $\text{HgBa}_2\text{CuO}_{4+x}$, $d_c = 0.952$ nm, the spectral weight is respectively $K = 210, 212$ and 222 meV for the underdoped samples. The coherent spectral weight is renormalized by the effective mass $K^* = \frac{m}{m^*}K$. The results are summarized in Figure 3.18 for the three samples but also for a number of hole-doped cuprates of previous studies [22, 139, 154, 155]. For some of the strongly underdoped samples K^* cannot be calculated due to the near-absence of coherent quasiparticles (coherent Drude peak). It will be shown in section 3.4.8 that this regime corresponds to having a negative real part of the memory function for $\omega \rightarrow 0$ which indicate that a two-component model is necessary as discussed in [156].

K decreases when the hole doping decreases, but does not extrapolate to zero for zero doping in accordance with the analysis of Comanac *et al.* [157]. In contrast, the coherent spectral weight is proportional to the hole doping x : $K^*(x) = K_0x$, where $K_0 = 511(11)$ meV, in agreement with the trend observed for $\text{La}_{2-x}\text{Sr}_x\text{CuO}_4$ [66] and $\text{YBa}_2\text{Cu}_3\text{O}_{7-x}$ [158]. This provides strong evidence that the Mott insulator is approached when the doping is reduced. Nevertheless, it cannot be determined whether this occurs because (i) the quasiparticle residue is gradually suppressed [117, 159] or (ii) the Fermi surface arcs shrink to zero without vanishing of the nodal spectral weight [112, 160].

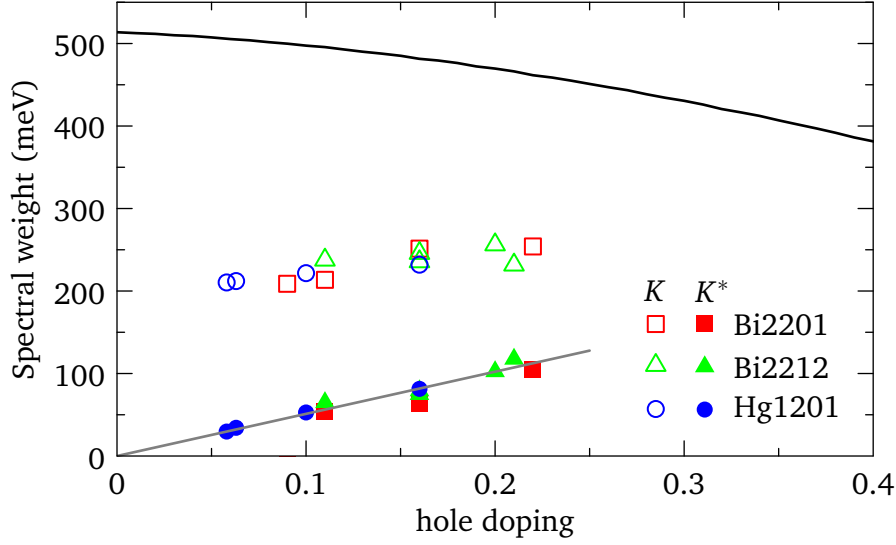


Figure 3.18: Intraband spectral weight per CuO_2 layer for a large number of cuprate superconductors. The data of $\text{Bi}_2\text{Sr}_2\text{CuO}_{6+x}$ and $\text{Bi}_2\text{Sr}_2\text{CaCu}_2\text{O}_{8+x}$ are taken from previous study Ref. [139, 154, 155]. The total spectral weight K is shown as open symbols and the coherent spectral weight K^* with plain ones. The grey line is a linear least squares fit to $K^*(x) = xK_0$ with $K_0 = 511(11)\text{meV}$ and x is the nominal hole-doping; the Pearson correlation factor is 0.998 which indicates excellent agreement and improve the result described in [2]. The solid black curve displays K calculated from ab initio band parameters for $\text{HgBa}_2\text{CuO}_{4+x}$ (Equation 3.3).

The spectral weight can also be estimated theoretically [161, 162]

$$K = \frac{d_c}{V} \sum_{k,\sigma} n_{k,\sigma} \frac{\partial^2 \epsilon_{k,\sigma}}{\partial k_j^2}. \quad (3.3)$$

With $n_{k,\sigma}$ the average occupation of the state with momentum k and spin σ ; V the sample volume. For a parabolic dispersion relation $\epsilon_k = \hbar^2 k^2 / 2m$, the Fermi energy is πK . Using a tight-binding approach, this energy can also simply be computed through ab initio LDA band-calculations using specific parameters for the cuprates. The dispersion thus reads

$$\epsilon_k = -2t [\cos k_x a + \cos k_y a] + 4t' \cos k_x a \cos k_y a - 2t'' [\cos 2k_x a + \cos 2k_y a], \quad (3.4)$$

with a , the in-plane lattice parameter and t, t', t'' the hopping integral defined in Figure 3.2. The spectral weight K was calculated numerically as a function of hole density, inserting Equation 3.4 in Equation 3.3, and adopting the parameters for the cuprates [87]: $t = 0.45\text{eV}$, $t'/t = 0.35$ and $t''/t' = 0.5$. The parametric plot of K versus hole density is presented in Figure 3.18. The expected value are a factor 2 larger than the measured values which is principally due to the strong correlation predicted by the Hubbard model for $U/t \geq 4$ [163].

These results also corroborate the observation of Santander-Syro *et al.* [164]; the integrated optical conductivity does not decrease when the temperature decreases, so that no opening of

3. FERMI-LIQUID LIKE PROPERTIES IN THE PSEUDOGAP OF THE CUPRATES

an optical pseudogap is seen when, at T^* , part of the Fermi surface is removed by a pseudogap, despite the emergence at this temperature of a novel ordered state with two Ising-like magnetic collective modes at 39 meV and 54 meV as observed with inelastic neutron scattering [165].

3.4.8 Extended Drude analysis

The extended Drude model is used to describe the single component low energy excitations through an energy dependent optical scattering rate $1/\tau_{\text{opt}}$ and a dynamical mass renormalization factor m^*/m . This single component model does not intend to describe the interband transitions so that they need to be removed prior to the conversion. It was shown that the high-energy oscillators fitted using the Drude-Lorentz model had a constant dielectric function (ϵ_b) below about 1 eV so that the natural way was to subtract them from the total dielectric constant following Equation 1.67b. The phonons are also sharp features that could in principle be removed from the electronic background. They were kept in order to avoid the residual features shown in Figure 3.13 (b) and (c) an increased number of parameters, which would lead to higher uncertainty of the procedure. Additionally, even if very small, there is an indication of certain asymmetry of the phonon modes that may introduce important bias in the data analysis if not removed properly.

Using the plasma frequency, the memory function was calculated from the interband free dielectric constant Equation 1.64; the real and imaginary part of the memory function are displayed at selected temperatures in Figure 3.19. The curves below T_c are plotted in grayscale and are not of physical relevance since the Drude model is not able to describe superconductivity. At high temperature, the real part of the memory function of UD45 and UD55 is negative which indicates that for these temperatures, the samples have an incoherent transport and that the single component approach can not be used anymore. This trend is increasingly observed by lowering the doping which indicates that the cuprates also become increasingly incoherent by losing their coherent spectral weight (see next section 3.4.7). Putting the phonon peaks aside, the common trend observed for all dopings and for temperatures $T_c < T \lesssim T^*$, is the linear slope of M_1 extrapolating to $\omega = 0$. This behavior is exactly the expected from the Fermi liquid theory (see Equation 1.124); the slope of this function corresponds to $m^*/m - 1$ and it is not constant over the whole temperature range. The sharp structure at about 0.1 eV in M_1 appears only below T_c for the optimally doped sample while it is much broader and appears at higher temperatures for the underdoped samples. For UD67, this feature disappears at around 300 K which is somewhat lower than $T^* \approx 350$ K. In the case of UD55 and UD45 the maximum becomes less noticeable, probably due to the considerable broadening. The dynamical relaxation rate $M_2(\hbar\omega, T) = \hbar/\tau(\hbar\omega, T)$ has an energy dependence exhibiting an upward curvature for all temperatures and for all dopings. Plotting the optical scattering rate as the squared photon energies in Figure 3.20 points out that the ω^2 dependence is clearly

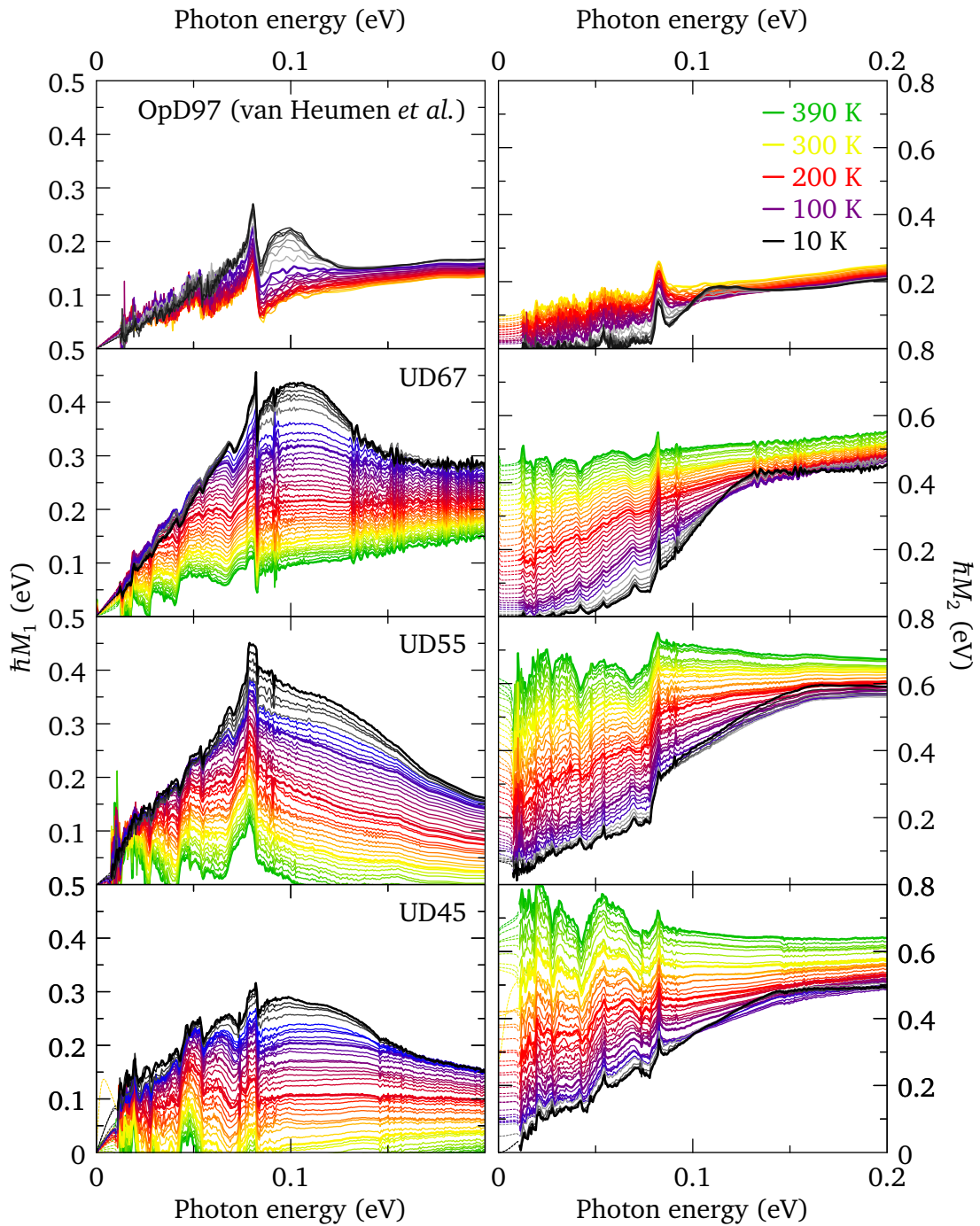


Figure 3.19: Real and imaginary part of the $\text{HgBa}_2\text{CuO}_{4+x}$ memory function at selected temperatures. The temperatures of the legend are shown as thick lines in the graphs.

3. FERMI-LIQUID LIKE PROPERTIES IN THE PSEUDOGAP OF THE CUPRATES

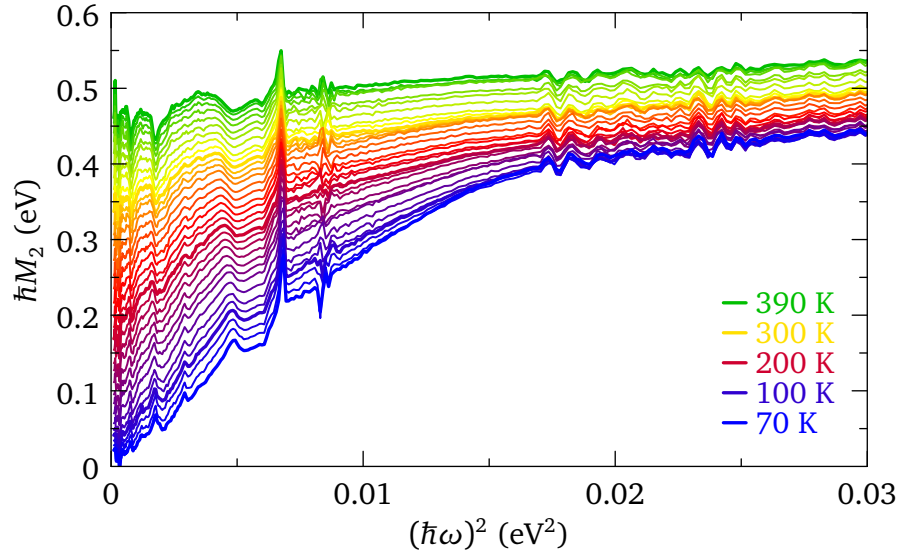


Figure 3.20: Optical scattering rate of $\text{HgBa}_2\text{CuO}_{4+x}$ UD67 plotted as a function of ω^2 for temperatures above T_c . The thick lines represent the temperature shown in the legend.

observed for UD67. On the other hand, it is totally linear for OpD97 and remains questionable mostly due to suppression of the coherent spectral weight and the strong phonon background for the two strongly underdoped samples. The maximum seen in M_1 is associated with an inflection point in M_2 and shifts from roughly 200 K to 100 K when the energy is raised from 10 meV to 50 meV. The interesting feature appears at T_c with a suppression of scattering below about 0.1 eV which seems to be transferred above that energy, producing a plateau-like structure with an onset evolving from 115 meV for the optimally doped sample to 135, 160 and 145 meV for the underdoped. Very recently the expected superconducting d -wave gap of $\text{HgBa}_2\text{CuO}_{4+x}$ was reliably measured [166]. Its maximum amplitude was found at 39 meV and a quasiparticle peak was found in the nodal dispersion at approximately 51 meV below the Fermi level which is different from the other cuprates with similar T_c . It would, therefore, be tempting to look at the same energies in optics and following Ref. [22] with the new values of the gap [166] the onset of the gap in optics would happen at $\approx 130(35)$ meV. In optics if the onset is defined where \hbar/τ is the steepest, it correspond where the M_1 reaches its maximum near 100 meV which agrees very well for all doping.

Figure 3.21 shows the temperature dependence of the dynamical effective mass and the optical scattering rate and for the three samples. The T^2 dependence of the optical scattering rate is seen at low energy and temperature for all three underdoped samples. For these samples, it is also possible to guess the onset of the linear regime at about T^* . On the other hand, the optimally doped sample clearly shows a linear temperature trend right above T_c .

The temperature dependence for selected energies of m^*/m is shown in Figure 3.21. The black round dot is the zero energy and zero temperature effective mass $m^*/m(\omega = 0, T = 0)$. The 10 meV and 20 meV curves of all dopings point out two characteristic behaviors: at low

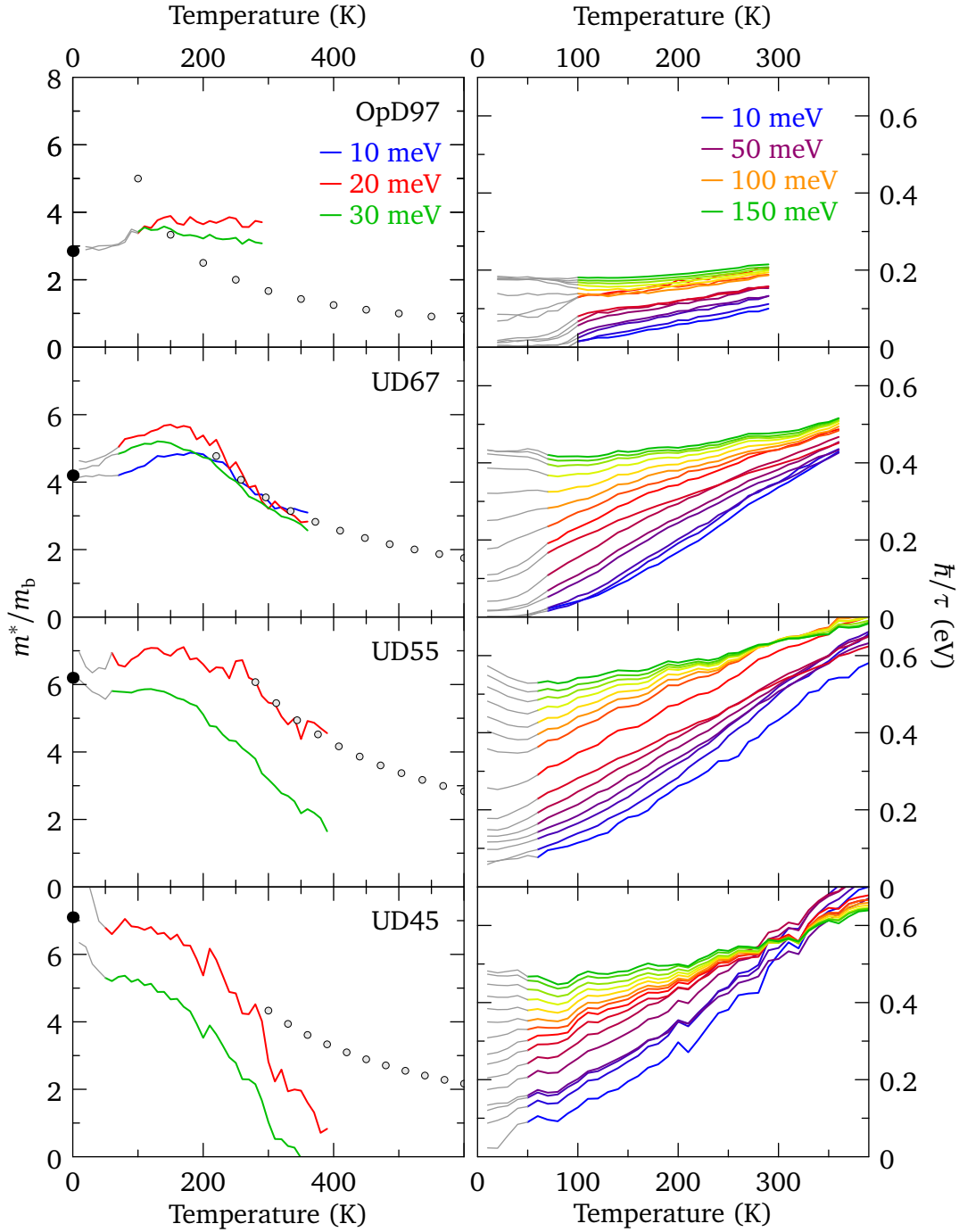


Figure 3.21: Temperature dependence of **(left)** the dynamical mass renormalization factor and **(right)** the optical scattering rate for the four different dopings and selected photon energies. The thick black dots represent the mass renormalization factor extrapolated from the data. The 10 meV data for sample UD45 and UD55 lies outside the experimental range or is too noisy. The gray area represents the data under T_c which are kept but are out of validity of the extended Drude model. The gray dashed points represent the expected scenario of an effective mass varying as T^{-1} for $T \geq T^{**}$.

3. FERMI-LIQUID LIKE PROPERTIES IN THE PSEUDOGAP OF THE CUPRATES

temperature but above T_c , the effective mass is almost flat with a small hump like structure for UD67 and UD55. Whereas at a higher temperature it decreases monotonously for the underdoped sample but not for the optimally doped sample. By plotting the maximum of effective mass at point T_{\max} as a function of the selected energy, it is interesting to see that for UD67 it decreases and extrapolates to $212\text{K} \approx T^{**}$ for $\omega \rightarrow 0$, which is another way of identifying T^{**} . Furthermore in the Fermi-liquid model the energy scale is given by $\xi^2 = (\hbar\omega)^2 + (p\pi k_B T)^2$ so that if the Fermi-liquid disappears at about 212K in the dc limit it should disappear at lower temperatures once the energy is finite and increases. This observation is an indirect confirmation that UD67 possesses Fermi-liquid like properties. Above 60 meV the plateau goes below T_c so that the maximum is very roughly extrapolated to about 80 K a value not so far from $p\pi k_B T = 88\text{K}$ if the value of the scaling parameter $p = 1.5$ is taken (see section 3.5). A similar trend is observed in UD55 and the plateau gets to higher temperatures accordingly to the higher T^{**} . However, it is much more difficult to confirm this trend with UD45 since this sample has indeed a very weak coherent carrier peak so that it would necessitate to go much lower in energy to precisely see the extension of the plateau. For UD67 the effective mass indeed increases from about 3 at 390 K to 5 at T^{**} , taken together with the strong temperature dependence of M_1 near its maximum at 0.1 eV, indicates that the charge carriers become increasingly renormalized when the temperature decreases. The effective mass at zero temperature is respectively 7.1, 6.2, 4.2 and 2.85 starting from UD45. In Figure 3.21, the gray circles represent a fit to $m^*/m_b = a/T$ for the lowest energy data and $T \geq T^{**}$. A recent study by Barišić *et al.* is pointing to a new interpretation of the phase diagram which reveals, in fact, the hidden Fermi-liquid behavior throughout the entire doping range [132]. This scenario is based on the assumption that the resistivity that is seen proportional to the temperature appears as a result of a temperature-dependent carrier density n . They propose that the real archetypal Fermi-liquid behavior has to be seen in a quadratic scattering rate and that below T^* , the resistivity $\rho = m^*/(ne^2\tau)$ ($T \leq T^*$) is obtained from a constant carrier density and effective mass. But the difference comes above T^* where the ratio m^*/n vary with temperature as $1/T$. This scenario implies that the lowest energies presented of m^*/m_b follow the gray circles, which is the case for UD67 and UD55 but not for the optimally doped sample which show a rather linear optical scattering rate above T_c and a constant effective mass.

3.5 Fermi liquid-like behavior in the underdoped cuprates

Illustrated by the saturation of $m^*(\omega, T)$ and the merging of the optical scattering rate with a T^2 and ω^2 dependence, Figure 3.20 and Figure 3.21 showed that the UD67 sample enters a Fermi-liquid like state at approximately 210 K. In optics $\hbar/\tau_{\text{opt}} \propto \hbar/\tau \propto [(\hbar\omega)^2 + (p\pi k_B T)^2]$ so that this function has to show both T^2 and ω^2 linked through the scaling parameter $p = 2$ [38].

3.5 Fermi liquid-like behavior in the underdoped cuprates

The first part of this section focuses on the optical scattering rate scaling of the three underdoped samples. The scaling parameter is found to be equal to $p = 1.5$ for the three samples. The scaling analysis is then extended to the other cuprates, which indicate that $p = 1.5$ is universal for this family of superconductors. The third section uses the Fermi-liquid model to fit the three underdoped samples. The resulting parameters are compared within the samples. The last section uses the strong coupling formalism to describe the different coupling modes in the cuprates. Finally, a discussion is presented to conclude the chapter.

3.5.1 Scaling in the underdoped $\text{HgBa}_2\text{CuO}_{4+x}$

In the thermal regime ($\hbar\omega \approx k_B T$), the memory function of a local Fermi liquid can be written as

$$M(\omega) \approx \left(\frac{1}{\tilde{Z}} - 1 \right) \omega + \frac{2i}{\hbar\tilde{Z}} \left[\frac{(\hbar\omega)^2 + (p\pi k_B T)^2}{3\pi k_B T_0} + Z\Gamma_{\text{imp}} \right]$$

where \tilde{Z} is the quasi-particle residue, T_0 is the Fermi-liquid temperature scale and $p = 2$. The scaling behavior is unveiled in the normal state by plotting the optical scattering rate as a function of $\xi^2 = (\hbar\omega)^2 + (p\pi k_B T)^2$. The effect of this procedure is to shift the curves to higher energy in proportion to the square of their temperature. If the relation between the temperature and the energy is good, the scaling will result in a collapse of all experimental curves into a general scaling function. An example is shown for UD67 in Figure 3.22 (a). In order to find the optimal value of p , this parameter was varied from 1 to 2 by steps of 0.1, searching for best overlap of the low- ξ data. Taking $p = 1$ underestimate the scaling while the expected parameter $p = 2$ overestimate the low energy scaling but matches the curves at high energy for $T > T^*$. As shown in Figure 3.22 (a), the optimal scaling parameter is $p = 1.5(1)$. The data above 320 K is beyond the Fermi-liquid T^2 regime so that it is beyond the range of validity of single-parameter scaling. Panel (b) is a comparison of the optimal scaling for the three underdoped samples, the temperature range is restricted to $T' < T \leq T^{**}$.

Comparing the functional form of $M_2(\xi)$ for these three materials, we make the following observations: (i) The collapse of UD67 is excellent. But the scaling is also observed given the relative uncertainty of the energy dependence of M_2 for UD55 and UD45. (ii) The residual ($\xi = 0$) value of $M_2(\xi)$ for the three samples is respectively 106, 72 and ≈ 0 meV from UD45. It is thus possible to presume that the Fermi-liquid-characteristics are affected to some extent and appear to be relatively fragile with respect to disorder, which could explain the difficulties to see the proper energy dependence of M_2 . (iii) The pronounced feature in the reflectivity at 80 meV is responsible for the sharp upshift of M_2 above 0.015 eV^2 . The implications of the loss of overlap are not entirely clear although in principle there is no reason to expect overlap since this is clearly beyond the range of "universal" Fermi-liquid behavior. However, the single parameter scaling seems still to persist into this regime for UD67, leading to the speculation

3. FERMI-LIQUID LIKE PROPERTIES IN THE PSEUDOGAP OF THE CUPRATES

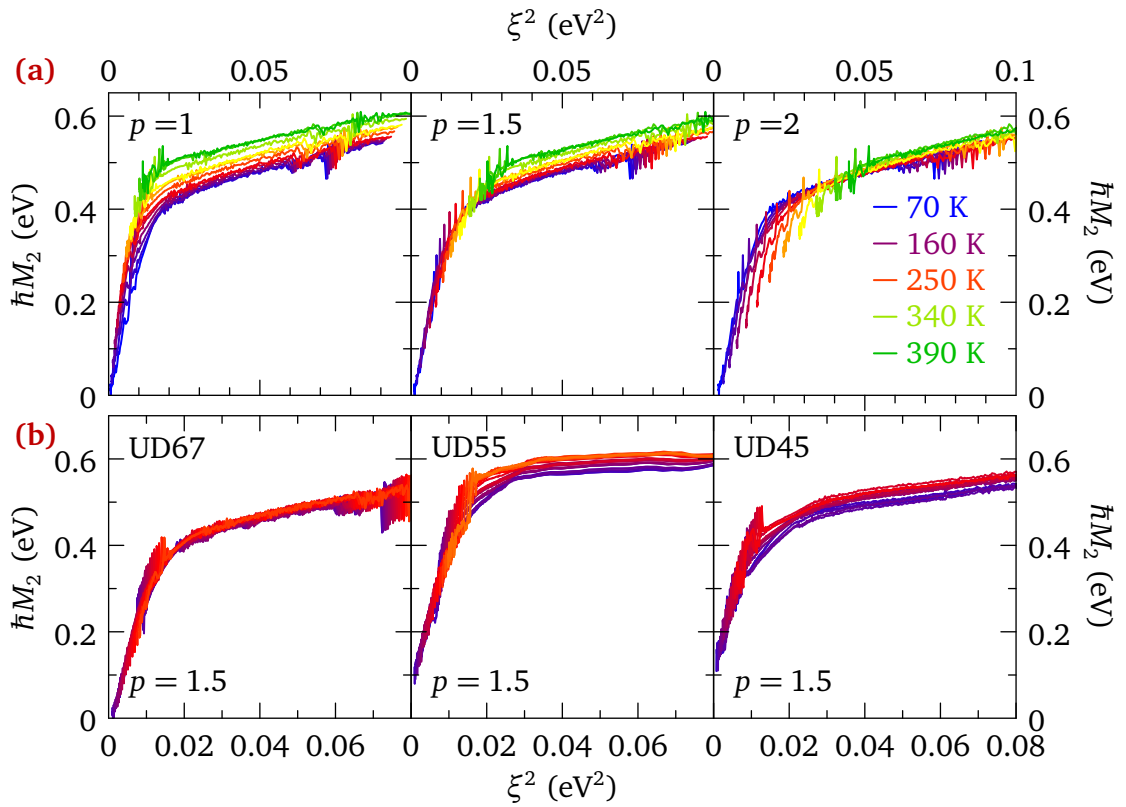


Figure 3.22: (a) Example of the scaling of the optical scattering rate of the UD67 using different value for p . Temperature are selected above T_c (b) Comparison of the scaling for the three underdoped samples. The temperatures are selected above T' and below T^{**} .

that impurity scattering contributes to the disappearance of overlap above 0.015 eV^2 for UD55 and UD45.

3.5.2 Scaling in the cuprates family

Figure 3.23 presents a summary of some published optical data of other cuprates such as $\text{Bi}_2\text{Sr}_2\text{CaCu}_2\text{O}_{8+x}$ [151]; $\text{Bi}_2\text{Sr}_2\text{CuO}_{6+x}$ [155]; the optimally doped $\text{HgBa}_2\text{CuO}_{4+x}$ [22] and finally ortho-II $\text{YBa}_2\text{Cu}_3\text{O}_{7-x}$ data [167]. These cuprates have hole concentration similar to UD67 ($x \approx 0.1$) but also overdoped and optimally doped samples. The ξ is not squared so that the curvature of the scaling form can be observed. The scaling parameter p was adjusted by steps of 0.1 and the optimal value is shown for each sample. The temperatures were selected to above T_c and below T^{**} for the underdoped and from T_c to room temperature for the optimally doped and overdoped. In order to understand the difference of scattering between the low and high ξ regimes, the point where the two regimes crosses is defined as ξ^* .

The first observation is pointing at the residual optical scattering rate. As expected, $\text{HgBa}_2\text{CuO}_{4+x}$ UD67 and OpD97 show the lowest residual scattering among the other families. This has to be put in contrast with the $\text{Bi}_2\text{Sr}_2\text{CuO}_{6+x}$ family for which it is believed that the relatively low values of T_c have to do with strong scattering by disorder [168]. It is also interesting to compare the high- ξ^* energy dependence, which points that the $\text{Bi}_2\text{Sr}_2\text{CuO}_{6+x}$ family also have a broader transition compared to $\text{YBa}_2\text{Cu}_3\text{O}_{7-x}$ and $\text{HgBa}_2\text{CuO}_{4+x}$. The underdoped $\text{HgBa}_2\text{CuO}_{4+x}$ have an almost exact linear ξ dependence above 0.2 eV.

Next, it can be noted that the increase of scattering rate below ξ^* is large for the underdoped sample and almost inexistent for the overdoped sample. In order to understand quantitatively this effect as a function of doping, the high and low- ξ regime were fitted to linear and quadratic models respectively. The results are shown in Figure 3.24. The high ξ regime was defined by the lowest temperature above T_c and data were fitted using a standard linear regression between 160 meV to 300 meV; the lower bound was slightly increased for the $\text{Bi}_2\text{Sr}_2\text{CuO}_{6+x}$ UD10 sample. The low energy part was fitted using a quadratic equation $\hbar M_2(\xi) = a\xi^2 + b\xi + c$ with an upper energy kept at 80 meV for all samples; the parameters a, b, c were kept positive. The value ξ^* is doping independent with a value of 110(11) meV; it is nearly insensitive to the effect of shifting up and down the fitting boundaries by 10 meV. The difference of scattering was either defined from the value at $\xi = \xi^*$ or by extrapolating the linear regime $\hbar \tilde{M}$ down to $\xi = 0$ which should represent an approximate value of what would be the scattering if no low- ξ scattering had occurred. In the two cases the doping dependence is equivalent and can be observed in Figure 3.23. The amplitude of scattering is increasing by lowering the doping, which indicate that the effective mass is reduced upon going to the overdoped regime. Taking the estimation at $\xi = \xi^*$, the amplitude decreases by 23(2) meV per percent, which is equivalent to the value found with the other description, $\xi = 0$, 22(3) meV per percent

3. FERMI-LIQUID LIKE PROPERTIES IN THE PSEUDOGAP OF THE CUPRATES

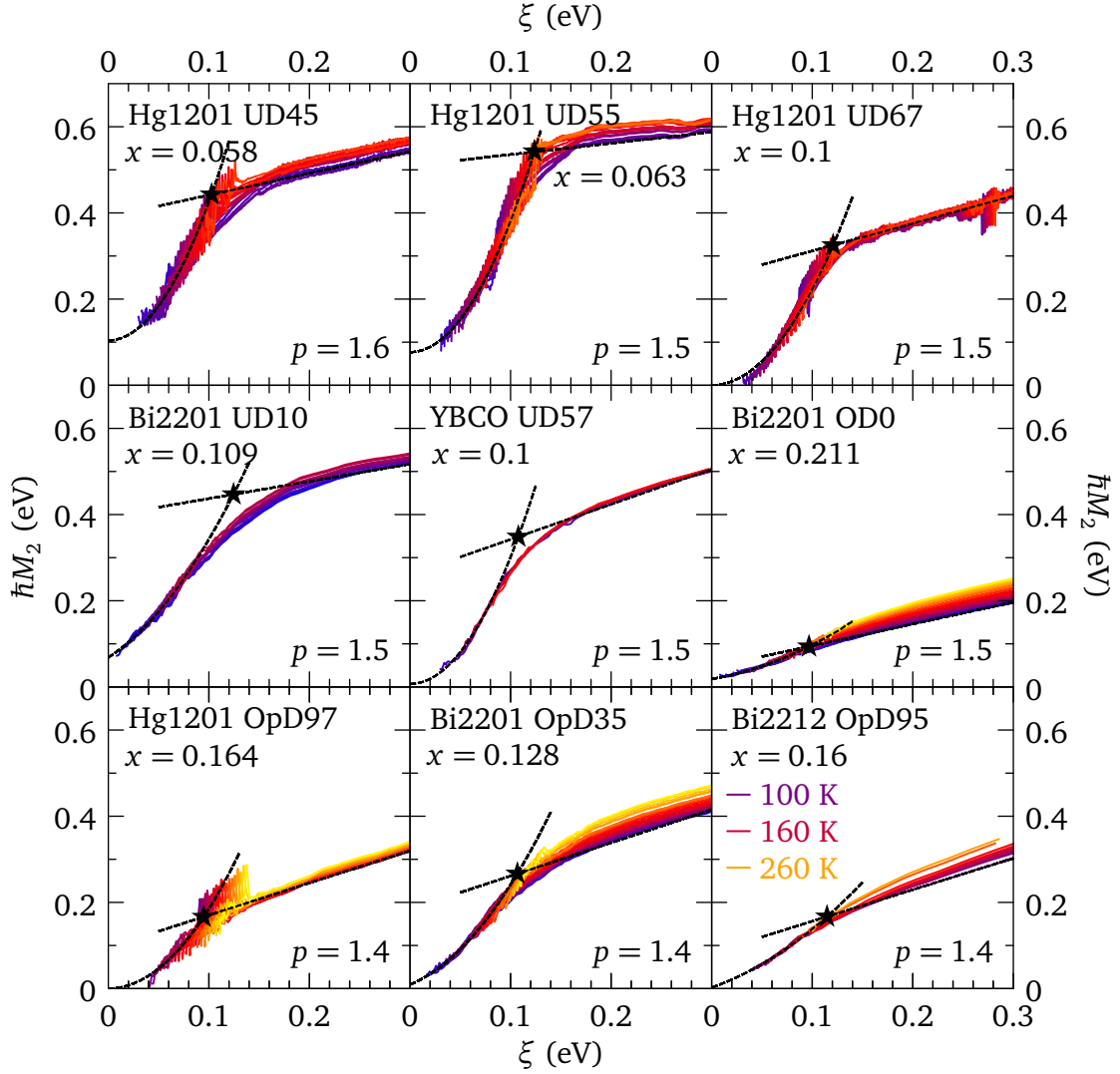


Figure 3.23: Scaling of the optical scattering rate of different cuprates from this study and the literature; The $\text{Bi}_2\text{Sr}_2\text{CaCu}_2\text{O}_{8+x}$ data are from Ref. [151], $\text{Bi}_2\text{Sr}_2\text{CuO}_{6+x}$ from Ref. [155], optimally doped $\text{HgBa}_2\text{CuO}_{4+x}$ from Ref. [22] and finally ortho-II $\text{YBa}_2\text{Cu}_3\text{O}_{7-x}$ data from Ref. [167]. The best scaling parameter is shown for each doping with an uncertainty of 0.1. The dashed lines represent a quadratic fit to the low energy with positive parameters; the high energy is a linear fit to the lowest used temperature. The temperature used for the fit are selected in the range $T_c < T \leq T^{**}$ for the underdoped and $T_c < T \leq 290\text{K}$ for the optimally doped and overdoped samples. The black star identifies the crossing at the position $(\xi^*, \tilde{M}(\xi^*))$.

3.5 Fermi liquid-like behavior in the underdoped cuprates

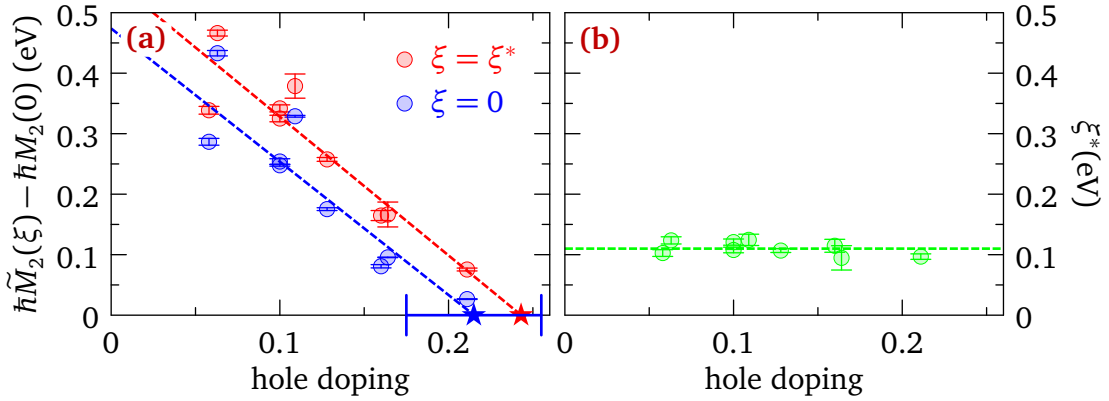


Figure 3.24: Doping analysis of the scattering rate suppression for different cuprates. **(a)** Doping dependence of the amplitude suppression. **(b)** Doping dependence of ξ^* .

doping. Continuing the linear regime up to a complete disappearance of the amplitude lead to respectively $(24.3 \pm 3.0)\%$ and $\xi = \xi^*$ and $(21.5 \pm 3.9)\%$ using the other extrapolation method. It is, therefore, possible to conclude that the amplitude of the scattering is related to the pseudogap which also decreases while increasing the doping. Unfortunately, the large error bars do not allow to decide between the two scenario: if the closing occurs at either 19% [169] or at the value where the T_c dome goes to zero.

3.5.3 Discussion

The ξ^2 dependence of the relaxation rate can be understood as follows [63]: An electron at a distance ξ above the Fermi energy can, as a result of electron-electron interactions, decay to a final state $\xi - \Omega$ by creating an electron-hole pair of energy. The density of states of electron-hole pairs is the spin (charge) susceptibility $\chi_2(\omega)$ where spin (charge) refers to electron-hole pairs carrying (no) net spin. $\chi_2(\omega)$ can be strongly renormalized, but the property that $\chi_2(\omega) \propto \Omega$ in the limit $\Omega \rightarrow 0$ is generic for Fermi liquids [170]. Integration of the susceptibility multiplied with the interaction vertex, $\alpha^2 \chi_2(\omega)$, over all possible decay channels from zero to ξ allows to conclude that indeed $M_2 \propto \xi^2$ reported experimentally. In this description the cross-over ξ^* corresponds to the energy where $\alpha^2 \chi_2(\omega)$ is truncated, leading to a leveling off of M_2 for $\xi > \xi_0$. The strong temperature dependence of $M_1(\hbar\omega, T)$ is also a natural consequence of this description; it was shown in Ref. [171] that, in leading orders of temperature, $\chi_2(\omega)$ of a correlated Fermi-liquid decreases as a function of temperature.

3.5.4 Fermi-liquid optical conductivity

In this section the underdoped $\text{HgBa}_2\text{CuO}_{4+x}$ are assumed to be Fermi-liquid-like materials which are governed by the experimentally-defined scaling parameter $p = 1.5$. The Fermi-liquid Equation 1.119 developed in Ref. [38] and shown in section 1.4.1 is used to characterize the

3. FERMI-LIQUID LIKE PROPERTIES IN THE PSEUDOGAP OF THE CUPRATES

three temperature-independent parameters: T_0 the Fermi-liquid scale, $Z\Phi(0)$ the coherent weight and $Z\Gamma$ the impurity scattering rate. Note that the impurity scattering rate of the model is linked to the experimental value through $1/\tau(\omega = 0, T = 0) = 2Z\Gamma_{\text{imp}}/(\hbar\tilde{Z})$. In order to unveil the incoherent MIR intraband conductivity, assumption have to be made on the temperature dependence of this conductivity [65, 172]. Without having enough arguments in hand for deciding between the scenarios, it was chosen to keep the two scenarios and use two fitting procedures, keeping the Fermi-liquid parameters either free or fixed upon increasing the temperature. The intraband response was extracted and becomes prominent when the coherent transport disappear at very low doping.

In a log-log plot, the Fermi-liquid optical conductivity exhibits a characteristic non-Drude feature at the thermal energy $\hbar\omega \approx k_B T$, in fact exactly where it gets its scaling form. Shown in Figure 1.11, this hump-like structure can easily be misleading and either is interpreted as a finite energy mode. Compared to a single Drude peak, the fit of the low-energy data using the complete Equation 1.119 (not an approximation) is the correct way of describing the low-energy optical properties of the $\text{HgBa}_2\text{CuO}_{4+x}$ samples, but extra care has to be taken since the incoherent MIR response is close in energy and may strongly influence the results [173, 174].

Due to the complexity of Equation 1.119, the fitting procedure is performed using a Fortran routine [43] that uses the standard Nelder-Mead (Simplex) algorithm for unconstrained minimization [175, 176]. The input data was either the reflectivity or directly the complex optical conductivity. It was found that using the latter was more convenient but the fit of the reflectivity could also be advantageous as a better extrapolation to the low energy Hagen-Rubens regime (see Figure A.1 in the appendix for an example). For all samples the real and imaginary parts of the optical conductivity data were simultaneously fitted at temperatures above T' ; the routine was kept fitting up to the higher temperature since the deviations above T^* are meaningful for the discussion. Except for UD45, the data were fitted from the lowest photon energies. For all samples and at low temperature, the data strongly deviate from the model at approximately 33(3) meV. In order to test for a possible sensitivity to the fit boundaries, several limits were tested. It was found that changing the energy from 30 meV to 80 meV by steps of 10 meV was not affecting the onset of the deviation whereas the low energy conductivity was overshoot by pushing the limit above 40 meV. Consequently, this indicated that 33 meV is about the energy where the MIR incoherent response becomes dominant over the coherent free carriers. Subsequently the maximum energy used for the fit was fixed at 33 meV for all the samples

The first procedure (procedure A) consisted in fitting all temperatures with free parameters. It was found that the impurity scattering $Z\Gamma$ was usually zero or fluctuating at very small values so that it was simply set to zero. The results are presented for UD67 in Figure 3.25. In the pure Fermi-liquid model, the temperature dependence is directly imposed in the model of the self-energy Equation 1.117 and in the Bose and Fermi functions so that in principle in this regime the fitting should in principle give constant parameters. Keeping the parameters free

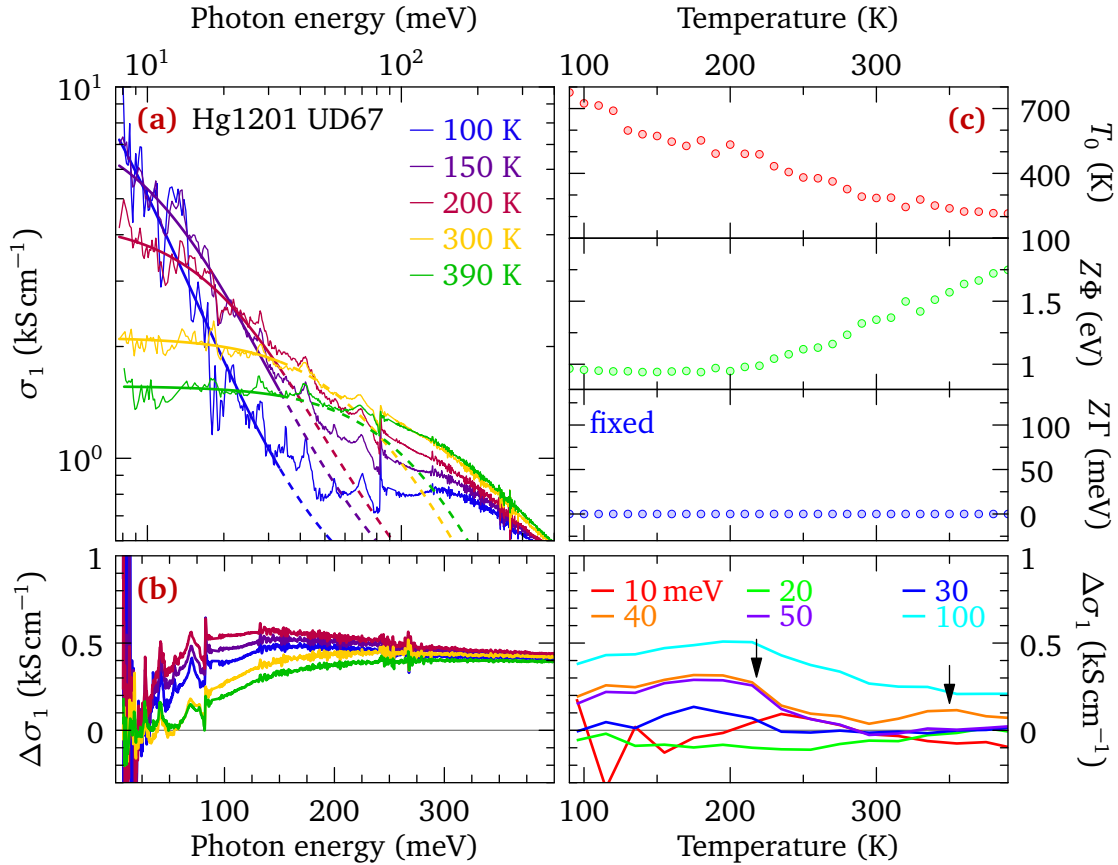


Figure 3.25: Fermi-liquid fit to the low energy optical conductivity of $\text{HgBa}_2\text{CuO}_{4+x}$ UD67. The Fermi-liquid parameters T_0 and $Z\Phi(0)$ are allowed to vary for as a function of temperature while $Z\Gamma$ is fixed at zero. **(a)** Experimental conductivity (thin lines). The Fermi-liquid model (dashed lines + thick lines). The thick line represent the fitting region $\hbar\omega \leq 33$ meV. **(b)** Subtraction of the model to experimental data as a function of energy (left) or as a function of temperature (right). The black arrows indicates T^{**} and T^* . **(c)** Temperature variation of the Fermi-liquid parameters; fixed parameters are labeled as is.

3. FERMI-LIQUID LIKE PROPERTIES IN THE PSEUDOGAP OF THE CUPRATES

allowed to see the deviations from constant values: while the coherent quasiparticle weight is about remaining constant, the Fermi-liquid scale is strongly reduced already above T^* . It is interesting to note that $Z\Phi(0)$ is nearly constant below T^{**} and starts to increase linearly at a higher temperature. This phenomenon is seen for all underdoped samples. The figures for the other samples are presented in the appendix, see Figures A.2, A.4 and A.6. The optimally doped sample was also fitted as a comparison; no kink is observed in the 150 K to 250 K regions so that the kink present for the underdoped sample is intrinsic. At 100 K, the energy onset of the thermal regime is predicted to be 40 meV, a slight change of slope is already seen at 25 K. At 150 K, it is already corresponding to 61 meV which is in the incoherent region. Compared to the strongly underdoped samples, UD67 is the only one clearly showing the Fermi-liquid thermal regime. In section 1.4.1, the Fermi-liquid thermal regime was predicted to occur for temperature much lower than T_0 . If it is indeed the case for UD67 with $T_0 \approx 700$ K, it becomes questionable for UD55 and UD45 where T_0 is respectively ≈ 300 K and 240 K for the low temperature fit. In contrast, it will be shown that for Sr_2RuO_4 the Fermi-liquid regime is seen at temperatures one ordre of magnitude below the Fermi scale T_0 . At very low doping, it is possible that the Fermi-liquid regime survives but is strongly weakened by the increasing lack of coherent spectral weight.

Figure 3.25 (b) shows the data subtracted from the fitted conductivity. The residual conductivity is attributed to the intraband MIR peak which is described in the two component model of Ref. [96, 149, 172]. The difference here is that the Fermi-liquid model is used in place of a simple Drude component

$$\sigma(\omega, T) = \sigma_{\text{FL}}(\omega, T) + \sigma_{\text{MIR}}(\omega, T) \quad (3.5)$$

Illustrated in Figure 3.15 at 10 K, where the superconducting gap suppresses most of the coherent peak the Fermi-liquid, keeping only σ_{MIR} fit of the data allows in the same fashion to unveil the temperature dependence of the MIR which turns out to indicate a suppression of the low energy part upon increasing the temperature. This scenario is found in good accordance with the prediction of Miley *et al.* in [65]. Their study states that the increase of temperature is setting more free carriers in the MIR peak which in turn induces a spectral weight transfer to the Fermi-liquid Drude. Whereas this scenario could, at first sight, weaken the Fermi-liquid picture by contributing extrinsically to the spectral weight. It could explain the deviations with the expected scaling parameter $p = 2$.

The second procedure (procedure B) shown in Figure 3.26 was used to find the best Fermi-liquid parameters for the data between 90 K and 100 K. At higher temperature, $Z\Phi(0)$ was kept free. While in a pure Fermi-liquid regime the parameters would remain constant as it is the case for Sr_2RuO_4 (see next chapter), the coherent spectral weight is decreasing linearly as a function of temperature. Moreover, the temperature trace indicates that at T^{**} , the deviations

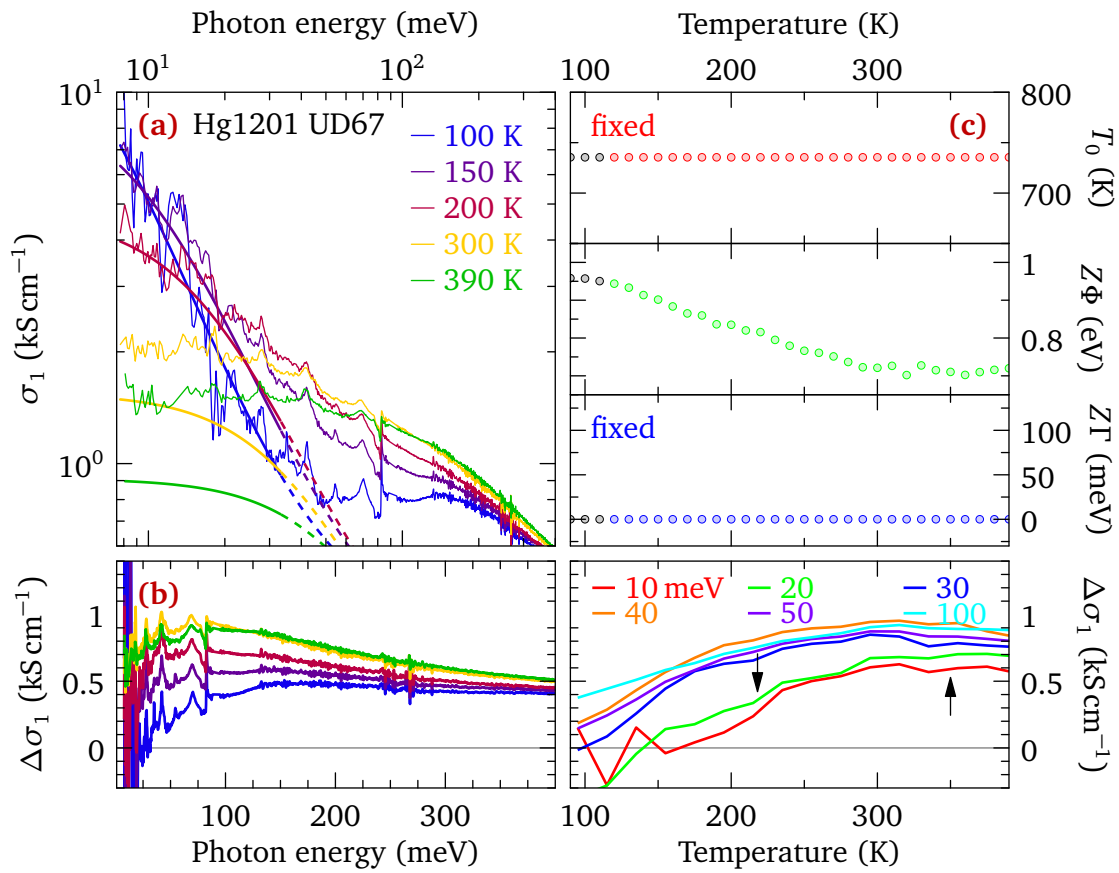


Figure 3.26: Fermi-liquid fit to the low energy optical conductivity of $\text{HgBa}_2\text{CuO}_{4+x}$ UD67. The Fermi-liquid parameter T_0 and $Z\Gamma$ are fitted below 110 K and fixed at higher temperature, $Z\Phi(0)$ is kept free for all temperatures.

3. FERMI-LIQUID LIKE PROPERTIES IN THE PSEUDOGAP OF THE CUPRATES

occur already at zero energy, which is expected in the scenario when $\xi_{\max}^2 = 88.5 \text{ meV} = (\hbar\omega)^2 + (p\pi k_B T)^2$ has to be conserved.

3.5.5 Strong Coupling Formalism

In this section, the Migdal-Eliashberg formalism presented in section 1.3.2 (or strong coupling formalism) is used to fit the optical spectra of $\text{HgBa}_2\text{CuO}_{4+x}$ UD67. The main goal of this analysis is to clarify the different correlation mechanisms present in the cuprates by extracting the bosonic spectral (glue) function $\Pi(\omega)$ from the optical spectra. The first part presents the fit of the data using the histogram representation presented in section 3.5.5.1. Next, the Fermi-liquid model is fitted to the dc-transport conductivity. Finally the improved model that combines both approaches is introduced and shows that the Fermi-liquid electron-electron coupling and the other bosonic coupling are distinguishable but also partly overlapping in energy which causes a complex interplay in this energy scale.

In previous works, the bosonic spectral function fit procedure was developed by van Heumen *et al.* and was based on the fit of the $\text{Bi}_2\text{Sr}_2\text{CuO}_{6+x}$ and optimally doped $\text{HgBa}_2\text{CuO}_{4+x}$. The results published in Ref. [35, 154] had led to the conclusion that among different models the simple histogram representation was an efficient way of extracting the bosonic spectral function compared to the model constrained marginal Fermi-liquid (MFL) [60] and the MMP [61]. The histogram model was representing $\Pi(\omega)$ by six amplitude and energy dependent *blocks* (or histograms). In this study, the procedure of van Heumen *et al.* was extended with more blocks of fixed width, which indeed increases the number of free parameters. The extended model was initially developed using the RefFIT program, but then it was realized that a more efficient algorithm was crucial for an increased number of fitting parameters. The fitting procedure was then adapted to a multicore and GPU-enabled MATLAB[®] fitting algorithm, which resulted in a nearly instantaneous fitting of the data. In addition the combined Fermi-liquid and histogram model was further refined in the Ph.D. thesis of Mirzaei [131] to which the reader may refer for further details of the computation. The different models may have a slightly different output, so that the mean squared error $\langle\chi^2\rangle$ is a good indication of fitting quality.

3.5.5.1 Histogram model

The results of the histogram model are summarized in Figure 3.27. The fitting procedure was done simultaneously on the real and imaginary parts of the memory function but also on a weighted point at zero energy of the dc transport. The model is built on 40 blocks ranging from 0^+ to 150 meV which corresponds to an energy resolution of 3.75 meV. The model has the advantage of showing the best fit but it also has the higher number of free parameters. One can expect that with such a high resolution, the phonon peaks may be also fitted which could either

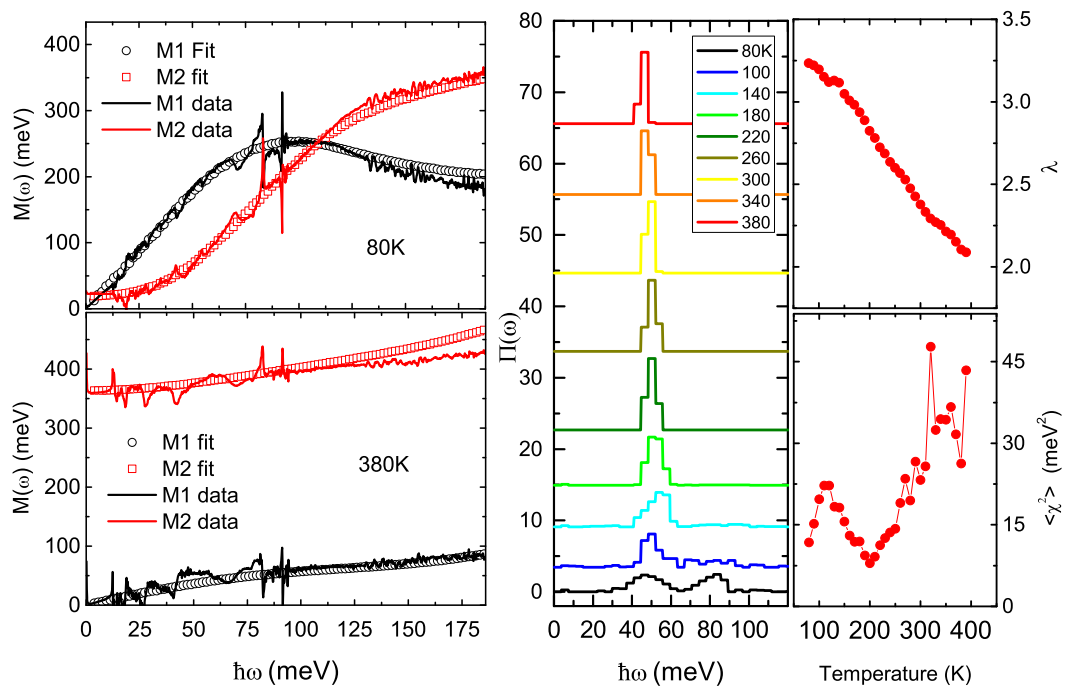


Figure 3.27: Results of the histogram model fit to the memory function of UD67. **(left)** Comparison between the model (circles) and the data (plain lines) for the real and imaginary part at 80 K and 380 K. **(middle)** Resulting bosonic spectral function at selected temperatures; the data is stacked up for clarity. **(right)** Temperature dependent coupling constant λ and mean squared error $\langle \chi^2 \rangle$.

3. FERMI-LIQUID LIKE PROPERTIES IN THE PSEUDOGAP OF THE CUPRATES

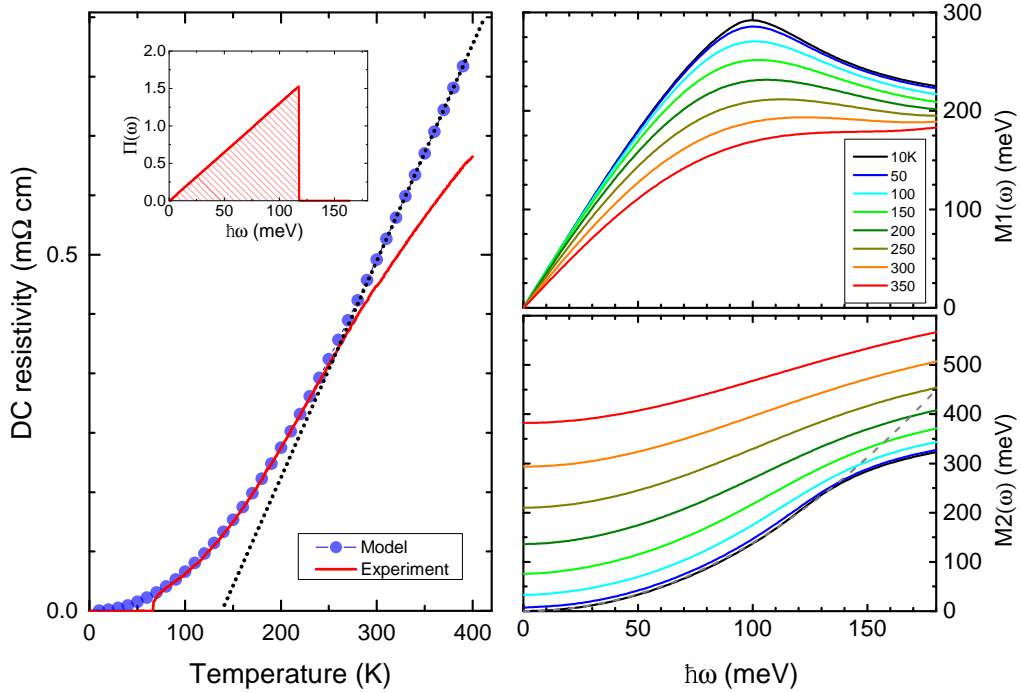


Figure 3.28: (left) Results of the Fermi-liquid model fit (blue dots) and the dc resistivity of UD67 (plain line). The dashed line represents the extrapolation of the high temperature linear regime. The inset shows the resulting bosonic spectral function with a cutoff at about 118 meV. (right) Real and imaginary part of the memory function obtained from the fit.

suppress or increase any block intensity depending on the width of the phonon. This model allows anyways disentangling the different features appearing in the optical data: Below 200 K and roughly 15 meV the bosonic spectral function has a very small but non-zero amplitude which corresponds to the Fermi-liquid interactions. Above this energy, no correlations are seen up to about a peak at about 50 meV. This peak is a common feature of the cuprates [59, 154, 177] and can directly be linked to the saturation of the real part of the memory function. The sharpening of this feature upon increasing the temperature is comparable to the underdoped $\text{Bi}_2\text{Sr}_2\text{CuO}_{6+x}$, but the strong increase of its amplitude seems to be sample dependent. The broad feature at 80 meV is quickly suppressed above 100 K, which suggests that it could be related to the superconducting fluctuations. Note that in the analysis of van Heumen *et al.* this feature is persistent up to room temperature.

3.5.5.2 Fermi-liquid model

In the Fermi-liquid theory, the number of particle-hole excitations is proportional to the energy. The bosonic glue function is then modeled by a linear function of energy and has a cutoff at ω_c representing either theoretically the bandwidth or simply the boundary of the model. The slope and the cutoff energy were adjusted in order to match the dc transport

3.5 Fermi liquid-like behavior in the underdoped cuprates

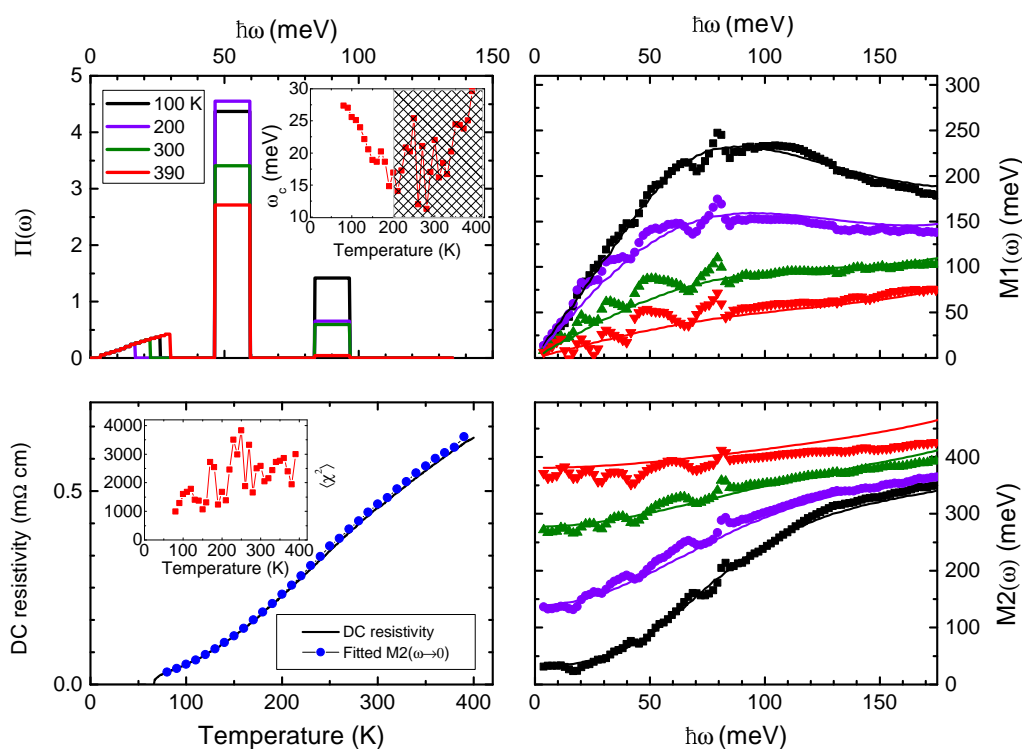


Figure 3.29: Results of the combined model fit to the memory function of UD67. The inset of the top left figure shows the value of the cutoff energy used for the low energy Fermi-liquid model, the shaded area represents the region where the temperature is above T^{**} that is seen by a strong fluctuation of the parameters.

data. Shown in Figure 3.28, the match is excellent up to 220 K, after which a deviation toward a lower linear but lower resistivity is seen. The subtle deviation from the Fermi-liquid above T^{**} is very important: First, it was shown that a cutoff at 118 meV corresponds to a change from a quadratic to a linear behavior at $p\pi k_B T \approx 218$ K which is exactly T^{**} with $p = 2$. With $p = 1.5$ it should correspond to 88.5 meV. Then, if the resistivity changes in both case to a linear behavior above T^{**} , the slope at high temperature but also the way it change between T^{**} and T^* is completely different, which indicates that this model is oversimplified to accurately describe the Fermi-liquid to non-Fermi-liquid transition in the cuprates. In addition, this model moves the maximum of M_1 to 118 meV which is not representing the energy dependent data anymore. It is then clear that the 50 meV to 80 meV features obtained in the histogram model are necessary to describe the entire spectra and that the 118 meV cutoff needs to be lowered in accordance with these changes.

Finally, the two models with the common features seen in the two previous models were combined together [131]. It was shown that either using a free cutoff energy or a free slope parameter for the Fermi-liquid model gave almost the same mean squared error. The first procedure was preferred because it was closer to the bare histogram representation and also because a change of slope for the Fermi-liquid model would have corresponded to a change of

3. FERMI-LIQUID LIKE PROPERTIES IN THE PSEUDOGAP OF THE CUPRATES

density of states The results shown in Figure 3.29 indicate an excellent description of both the dc transport measurement and the optical spectra. Compared to the previous model the cutoff energy of the Fermi-liquid model is reduced from 118 meV to about 27 meV which is very close to the 33 meV found as boundary to the Fermi-liquid in section 3.5.4. From 70 K to 210 K the cutoff energy is decreasing with increasing the temperature while the 50 meV peak is slightly increasing.

3.5.5.3 Discussion

This analysis points out three different components: at low energy the Fermi liquid is responsible for a coupling proportional to the energy up to about 30 meV, followed at higher energy by a sharp temperature dependent mode at 50 meV and a broad feature around 80 meV. The precise interplay of the different components is still confusing since they are close in energy and may probably overlap. In addition, the phonon energy range is right in the 10 meV to 100 meV which may also have a large coupling with the electrons resulting in an asymmetric shape that would certainly play a role in an artificial increase (or decrease) of the bosonic glue function [178]. As an example, the effect of a peak in the bosonic spectral function is a bending down of the real part memory function; indeed in [154] the bosonic spectral function was never zero so that it is possible that the strong phonon dip seen in real part of the memory function would have: 1) forced a higher amplitude of the bosonic spectral function 2) decreased the memory function over an energy span and 3) suppressed $\Pi(\omega)$ in the same energy range. Such effect could typically cause local minima which in principle should be less prevailing in the van Heumen 6-block model.

This analysis was done using the UD67 memory function. If the phonons are problematic for this sample, they should be even more for the lower dopings. However, it would indeed be tempting to remove the phonon features prior to the fit, which may be done in a later study.

3.5.6 Conclusions

The most important observation borne out by these data is that the energy dependence of $M_1(\hbar\omega, T)$ and $M_2(\hbar\omega, T)$ follows by and large the behavior expected for a Fermi liquid: At low energies and temperatures $M_1(\hbar\omega, T)$ is indeed a linear function of ω , and $M_2(\hbar\omega, T)$ scales with $(\hbar\omega)^2 + (p\pi k_B T)^2$. The energy dependence of UD55 and UD45 was inconclusive mainly due to a drastic reduction of the coherent spectral weight at those low dopings. On the other hand, the observations made on the temperature dependence of the memory function leave no doubt on the membership of these two materials to the same class as UD67. Recent theories [179–181] have emphasized the possible relevance of Fermi-liquid concepts –or a hidden form of these in the superconducting regime [182]– to the metallic state of hole-doped

3.5 Fermi liquid-like behavior in the underdoped cuprates

cuprates. The experimental results of this study provide a strong incentive for further theoretical work in this direction. Notably two striking aspects of the data: (i) The slope $\partial M_1(\hbar\omega, T)/\partial\omega$ for $\omega \rightarrow 0$ decreases significantly as a function of increasing temperature, (ii) $p < 2$. One can speculate that these issues are related to the progressive filling-in of the pseudogap as a function of increasing temperature. Already in a two-fluid picture of a nodal Fermi liquid in parallel to an anti-nodal liquid, non-universal features are introduced in the optical conductivity, since the properties at the Fermi surface change gradually from Fermi-liquid at the nodes [183] to strongly incoherent and pseudo-gapped at the hot spots near the anti-nodes [184]. Recently Maslov and Chubukov also interpreted this as a combination of Fermi-liquid scattering and an additional source of elastic scattering from magnetic moments or resonant levels [171]. In comparison to the other material pointing Fermi-liquid behavior it is important to remember that the cuprates are all scaling with the same parameters $p = 1.5 \pm 0.1$ so that this parameter is indeed –among other– a universal feature of this family of superconductors. The next chapter discusses the special case of Sr_2RuO_4 . This material is currently the only one pointing toward the exact scaling with $p = 2$, allowing an interesting comparisons.

Theoretically it is expected that the T^2 and ω^2 dependence of $M_2(\hbar\omega, T)$ is limited to $\hbar\omega$ and $p\pi k_B T$ lower than some energy scale ξ_{max} , which in the context of single parameter scaling behavior of a Fermi-liquid is proportional to the effective Fermi energy. Strong electronic correlations strongly reduce this energy scale, as compared to the bare Fermi energy. For most materials the issue of the Fermi-liquid like energy dependence of $M_2(\hbar\omega, T)$ has remained largely unexplored. This is related to the difficulty that, in cases such as the heavy fermion materials where this type of coupling dominates, the range of Fermi-liquid behavior is smaller than 10 meV, making particularly difficult to obtain the required measurement accuracy in an infrared experiment. Clean underdoped cuprates present in this respect a favorable exception since as can be seen from Figure 3.20 and Figure 3.23 that the relevant energy scale ξ_{max} is about 100 meV for a doping level around 10%. Above this energy $M_2(\hbar\omega, T)$ crosses over to a more linear trend both as a function of ω and T . This suggests that in the cuprates the range of applicability of Fermi-liquid behavior is limited by a different scattering mechanism that develops at high- T and high- ω , as the pseudogap gets filled.

3. FERMI-LIQUID LIKE PROPERTIES IN THE PSEUDOGAP OF THE CUPRATES

Low energy optical response of Sr_2RuO_4

The Fermi-liquid theory is one of the major key to understand pairing mechanism in both high- T_c and unconventional superconductors. Despite more than sixty years of research, the complete physical picture of these correlated materials is still not experimentally demonstrated from optics. Underdoped and overdoped cuprates are now proven to be Fermi-liquids [104, 185], but as shown in the previous chapter, the scaling parameters p differs from the expected value [2, 18, 19, 38, 68].

This parameter, which links the temperature and the energy in the scattering processes, is expected to be equal to 2 in the Fermi-liquid regime, which however has never been reported even for materials known to be excellent Fermi liquids. In this respect, the single layer ruthenate Sr_2RuO_4 was chosen to be investigated for several reasons. First, there are absolutely no doubts that the transport measurement and the specific heat exhibit perfect Fermi-liquid behavior: the temperature dependence of the resistivity and specific heat are quadratic [186] and linear [186] respectively. Secondly, this transition metal oxide is also heralded as the solid-state analog of ^3He [187] which is the archetypal Fermi-liquid, but Sr_2RuO_4 has the advantage of being much easier to study. An example is the striking evidence of p -wave symmetry of their superconducting phase [188].

In this chapter, the in-plane low-energy scaling of the optical scattering rate is shown for the first time to be exactly the theoretical Fermi-liquid expected value of $p = 2$. Moreover, thanks to recent progress in many-body electronic structure calculations using dynamical mean-field theory (DMFT), the comparison with the experimental data point to an excellent agreement. The low-energy Fermi-liquid regime of this material is confirmed and allows attributing the high-energy deviations to the recent concept of resilient quasiparticles [189]. Based on the in-plane transport measurements, a double Fermi-liquid model is presented and compared to the transport experiments. Furthermore, the low energy c -axis optical conductivity is studied. The different samples indicate that the c -axis phonons are split; a feature existing in all the published data but never explained. A statement is made on the presence of impurities in small

amount, which affect the out of plane properties.

The first section introduces a brief review of the literature and the experimental details for growing, characterizing and measuring the samples; the different impurities of the samples are presented through different techniques. The second section is the main subject and shows the Fermi-liquid scaling behavior of the ab -plane both experimentally and numerically. The concept of resilient quasiparticles appearing at above the Fermi-liquid temperature and energy scale is discussed. This section has been published in [1]. The third part discusses the probable theoretical scenario for the transports measurement both in ab -plane and c -axis. The fourth and last part discusses the c -axis optical conductivity of the samples.

4.1 Introduction

4.1.1 The Ruddlesden-Popper family

Sr_2RuO_4 is the first member of the ruthenate Ruddlesden-Popper series perovskites [191]. The chemical structure shown in Figure 4.1 is given by the general formula $\text{Sr}_{n+1}\text{Ru}_n\text{O}_{3n+1}$ and consists of two-dimensional perovskite slabs interleaved with alkaline earth cations, here strontium. The perovskite slabs are formed by a transition metal, here ruthenium, enclosed in an anionic octahedron made of six oxygen; n is the number of octahedron in the center of the unit cell. A summary of the structure parameters is shown in Table 4.1. The unit cell height is elongated while the ab -plane lattice constant remain almost constant. Both, experiments and theoretical calculations, tend to agree that the underlying lattice structure has major impacts on the electronic and magnetic properties [195, 196]. Shown in Figure 4.3, a complex phase diagram emerges depending on the number of intralayers, giving rise to extremely rich magnetic properties. The single layer ruthenate, Sr_2RuO_4 has a simple body-centered tetragonal structure and is diamagnetic, while the other member of the family have structure distortions caused by the tilting of the RuO_6 octahedron and a stronger tendency of ferromagnetism. As an example, $\text{Sr}_3\text{Ru}_2\text{O}_7$ ($n = 2$) is believed to be a paramagnetic conductor with antiferromagnetic correlations. The structure of this material is still under debate [197], but it has been recently shown that despite having a tilt of RuO_6 octahedron, the unit cell remains tetragonal [193]. This ambiguous scenario is reflected in its magnetic properties since this material has a metamagnetic transition at about 6 T [198, 199]. The trilayer ruthenate $\text{Sr}_4\text{Ru}_3\text{O}_{10}$ ($n = 3$) and the last member of the family SrRuO_3 ($n \rightarrow \infty$) are ferro-metamagnetic and ferromagnetic metals respectively.

4.1.2 Band structure

The tetragonal K_2NiF_4 type structure of Sr_2RuO_4 is identical to the lanthanum doped cuprate superconductor $\text{La}_{2-x}\text{Ba}_x\text{CuO}_4$ [202]. The ruthenium is typically playing the role of copper

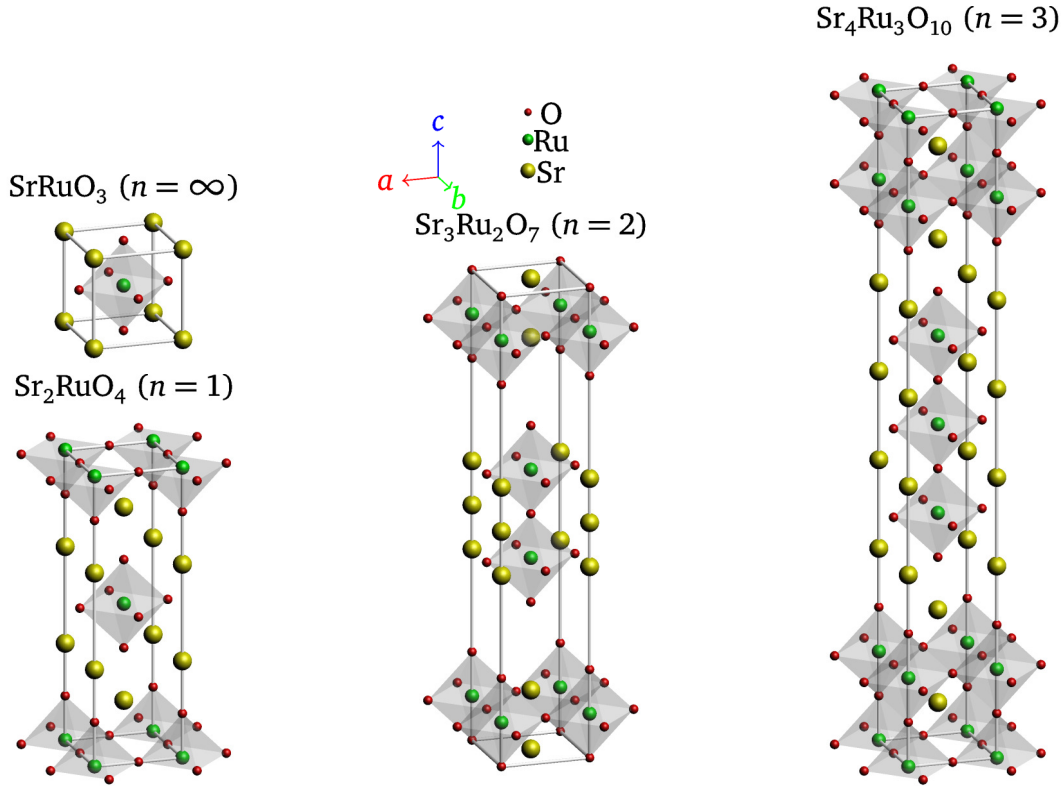


Figure 4.1: Crystal structure of the ruthenate Ruddlesden-Popper series $A_{n+1}B_nO_{3n+1}$ [191]. Crystal parameters for $n = 1$ [192], $n = 2$ [193], $n = 3$ [192] and $n = \infty$ [194]. Aspect ratio is conserved and the pseudo-tetragonal structure is used for the triple-layer compound.

and the response of the crystal lattice to pressure suggested that, like in the cuprates, most of the physics is linked to the d shell of these cations [203]. Counting the valences states of the strontium and oxygen, the ruthenium cation Ru^{4+} is in a $4d^4$ configuration, which is different to cuprates $3d_{x^2-y^2}$. The crystal field of the O^{2-} lift the degeneracy of the band, giving rise to a low-lying t_{2g} state with the d_{xy} , d_{xz} , d_{yz} orbital and unoccupied higher e_g , the $d_{x^2-y^2}$ and $d_{r^2-3z^2}$ as shown in Figure 4.2 (a). The two dimensional nature of the crystal can be understood, from the crystalline structure and the fact that the large c -axis separation of the octahedron and the small orbital radius of the d -electrons induce only a small overlap of the orbitals along the c -axis direction and thus strong confinement of the itinerant electron to the ab -plane. A simple toy-scenario can be used to explain the band formation; it is depicted in Figure 4.2. The spatial extent of d_{xz} and d_{yz} in orbitals Figure 4.4 have mainly their overlap respectively along the x and y -axis, which allows a band dispersion along these directions. The resulting Fermi surface is a sheet perpendicular to these directions as shown in Figure 4.2 (b). In the plane, the oxygen ions are π -bonded with the ruthenium ions which increase the hybridization and allows a transport both in the x and y direction thus forming an open cylindrical Fermi surface perpendicular to these direction (the opening in direction of the z component). Finally the d_{xz} and d_{yz} sheet hybridize and form a gap at the corner of the Brillouin zone forming

4. LOW ENERGY OPTICAL RESPONSE OF Sr_2RuO_4

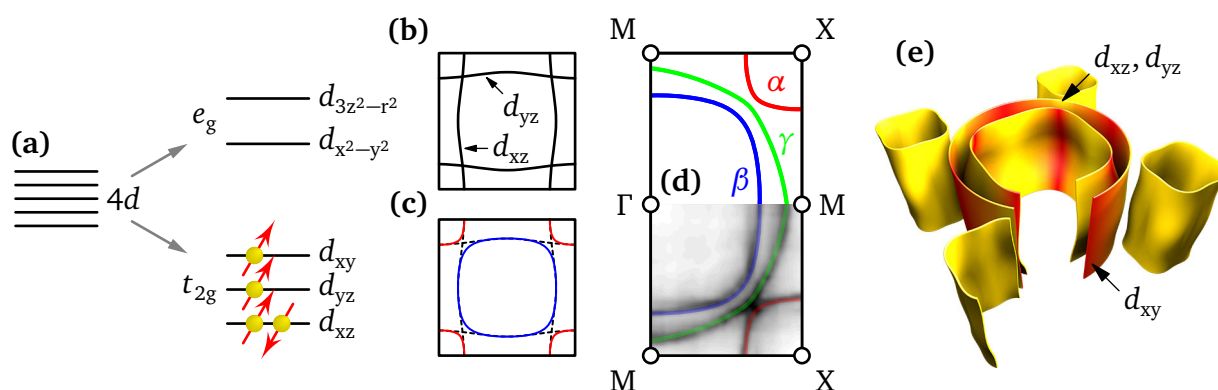


Figure 4.2: (a) Ruthenium $4d^4$ electrons splitted in (b) e_g and t_{2g} states by crystal field splitting. (c) Individual d_{yz} and d_{xz} prior to hybridization. (d) Half of the Brillouin zone showing part of the ARPES map with the three bands crossing the Fermi energy shown as thick color lines. ARPES data from [200]. (e) Schematic view of the 3D Fermi surface. The orbital composition of the bands is shown in color scale, red for d_{xy} and yellow for both d_{xz} and d_{yz} .

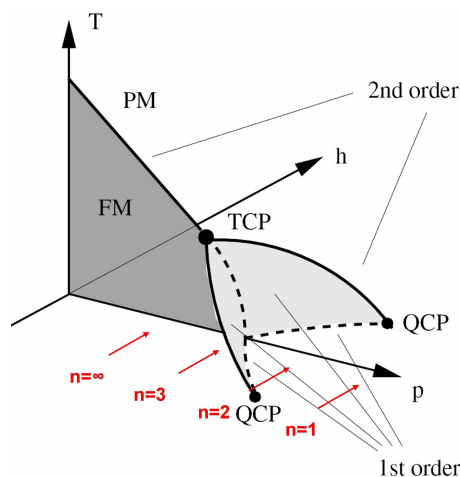


Figure 4.3: Temperature, pressure and magnetic-field phase diagram of the Ruddlesden-Popper series ruthenate. A tricritical point and two quantum critical points are expected. Reproduced from [201]

Table 4.1: Structure and lattice parameters of the ruthenate Ruddlesden-Popper series. (*) For $n = 3, \infty$ the parameter of the simplified structure is shown; for $\text{Sr}_3\text{Ru}_2\text{O}_7$ the tetragonal $I4/mmm$ is taken in place of the orthorhombic $Pbam$.

$\text{Sr}_{n+1}\text{Ru}_n\text{O}_{3n+1}$	n	structure	a (\AA)	b (\AA)	c (\AA)	Reference
Sr_2RuO_4	1	tetragonal	3.8730(3)	3.8730(3)	12.7323(9)	[192]
$\text{Sr}_3\text{Ru}_2\text{O}_7$	2	tetragonal	3.890(1)	3.890(1)	20.732(6)	[193]
$\text{Sr}_4\text{Ru}_3\text{O}_{10}$	3	tetragonal*	3.9001(3)	3.9001(3)	28.573(3)	[192]
		orthorhombic	5.5280(11)	5.5260(11)	28.651(6)	
SrRuO_3	∞	cubic*	3.930	3.930	3.930	[194]
		orthorhombic	5.5670	5.5304	7.8446	

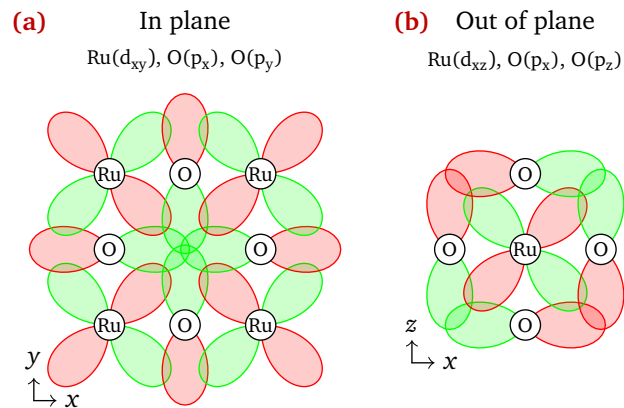


Figure 4.4: Schematic view of the oxygen and ruthenium orbital of Sr_2RuO_4 . The area in red and green represent respectively the positive and negative amplitude of the wave function. (a) Orbitals overlap from the inplane part of the octahedron. (b) Out of plane cut.

the so-called electron β and hole α bands, shown in Figure 4.2 (d). The d_{xy} cylinder doesn't hybridize and remains nearly unaffected by the hybridization of the d_{xz} , d_{yz} orbitals, forming the γ band. Thanks to the dimensional extent of the d orbital, the α and β band are quasi one-dimensional, while the γ is quasi two-dimensional [187]. This simple scenario has been confirmed by ARPES (see Figure 4.2 (d)) and de Haas-van Alphen effect oscillations [200, 204]. The real composition of the α , β and γ bands is shown in Figure 4.2 (e). The γ -band is mainly of d_{xy} nature, while having a mix of the other bands near the X point (π, π) [205].

4.1.3 Unconventional superconductivity

The discovery of the superconducting transition of Sr_2RuO_4 by Maeno and coworkers in 1994 [206] opened a new era of the unconventional superconducting mechanisms. Some times earlier, the highest high- T_c cuprate $\text{HgBa}_2\text{Ca}_2\text{Cu}_3\text{O}_{8+x}$ with a record temperature of 150 K was found [207]. However, the novelty was not its critical temperature, which was not more than 0.93 K at that time, but the fact that it was the first superconducting layer perovskite without copper. Despite sharing different structural properties with the cuprates seen the previous section, Sr_2RuO_4 presents remarkable differences [202]. The family of cuprate include hundred of different compounds with various critical temperature and a strong robustness against disorder. In comparison, Sr_2RuO_4 is also pretty much alone in its family. Nevertheless, substitution of the strontium by other atoms, such as titanium, maintains the superconducting properties but reduce it to very low temperatures [25]. Compared to the standard s -wave superconductors, the Sr_2RuO_4 critical temperature depends much on the impurity level. This phenomenon can be directly seen in Figure 4.5, which shows that the superconducting phase transition is totally suppressed when the residual resistivity of the sample reaches about $1 \mu\Omega \text{ cm}$ [208]. It was suggested early on that the underlying superconductivity mechanism was probably totally

4. LOW ENERGY OPTICAL RESPONSE OF Sr_2RuO_4

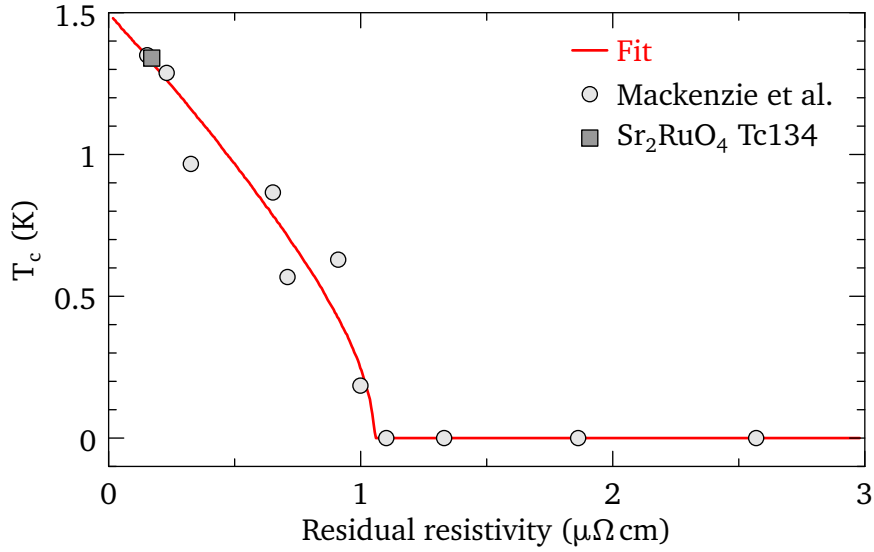


Figure 4.5: T_c dependence under non-magnetic doping. Data reproduced from [208]

different from the cuprates [203].

Table 4.2: Symmetry classification of pairing correlations [209, 210]. As an example, the p -wave pairing is odd in parity, even in respect to the time reversal symmetry and the cooper pair forms a triplet. The standard BCS s -wave pairing is also shown. Hybrid pairing is usually obtained in heterostructures as shown in [211].

	Spin S	Time reversal symmetry T	Parity P	Cooper pair STP = -1
singlet (odd)	$\uparrow\downarrow - \downarrow\uparrow$	even odd	even odd	s ($S=0, l=0$) and d ($S=0, l=2$) hybrid structures
triplet (even)	$\uparrow\downarrow, \downarrow\uparrow$ $\uparrow\downarrow + \downarrow\uparrow$	even odd	odd even	p ($S=1, l=1$) and f hybrid structures

Currently, the most convincing scenario of pairing symmetry in Sr_2RuO_4 , which is demonstrated by the largest number of experience, is the chiral p -wave which is a form of odd parity spin-triplet pairing. But the question of the internal symmetries of the cooper pairs is still debated and requires a careful experimental analysis of the spin, time reversal, and parity symmetries, which are summarized in Table 4.2. Under particle interchange, the electron's wave function forming the Cooper pair needs to be antisymmetric. So that the spin and angular momentum taken together need to be antisymmetric. The conventional BCS s -wave scenario was among the first to be rejected. The strong dependence of T_c under non-magnetic doping as shown in Figure 4.5 [208] is in opposition with s -wave superconductors; the Anderson theorem and the conservation of time reversal symmetry implies that T_c is unaffected by nonmagnetic impurities [212] which is clearly not the case. From heat capacity experiments, the observed linear dependence of C_e/T [213] indicates a line node in the gap dependence. SQUID in-

terferometer experiments revealed that the superconducting order parameter has a π -phase under inversion which is in agreement with the odd-parity pairing [214]. Additionally, NMR knight shift measurements are consistent with an equal-spin spin-triplet pairing state [215]. Concerning the time reversal symmetry, both muon spin relaxation spectroscopy, and optical Kerr effect show that the pairing order of Sr_2RuO_4 breaks time reversal symmetry [216,217]. A recent Josephson interferometry study has shown the presence of domain walls in Sr_2RuO_4 which were explained theoretically from modeled microscopic structure within the chiral p -wave state [218,219]. Finally, spin-polarized neutron scattering measurements confirmed spin-triplet pairing with spins lying in the basal plane [220]. Other experimental and theoretical evidence can be found in the following reviews [188,221]

While the scenario of the spin-triplet pairing is almost settled, the debate is concentrated on whether this state is chiral or not [188], the $p_x + ip_y$ states or the impact of the band responsible for the pair formation. A recent STM spectroscopy study put forward that, the magnetically mediated odd-parity superconductivity was generated by dominant, near-nodal, Cooper pairing on the α and β bands [222]. This scenario is also in favor of theoretical studies; recently Raghu *et al.* suggested that the pairing is driven by large momentum spin fluctuations associated with the quasi-1D α and β bands [223,224]. This study was recently extended by Scaffidi and coworkers which used spin-orbit and multi-band effects in order to see the impact on the pairing symmetry when either the γ or the α/β bands are dominant [225]. Other studies suggested topologically protected edge states and half-flux quantum vortices with Majorana zero modes [226,227]. Finally it has been shown that using tensile and compressive strain increased T_c up to 3 K [228,229]. The T_c change along the different direction of strain lead the authors to suggest that Sr_2RuO_4 may have degenerate order parameters, which would certainly explain a large part of the experimental discrepancies. Solving this issue will help to make a step forward in regard to the pairing mechanism.

4.2 Samples and crystal growth

The Sr_2RuO_4 single crystal can be synthesized in very pure form. However it will be shown that depending on the type of impurity, the electronic properties can be arbitrarily affected. First, the synthesis technique (e.g. crucible, transport agent) or the precursor material introduces a type of impurities that strongly suppress T_c [208]. In contrast, the presence of ruthenium inclusions (3K-phase) is increasing the sample T_c , see section 4.7.3. A relatively high amount of intertwined layers of the Ruddlesden-Popper series compound can be found in the material without affecting T_c nor the in-plane transports.

Improvement in crystal growth allowed the use of the floating zone technique (FZT) [230], which in turn allowed cm-sized crystals to be grown in a very pure form (no contamination

4. LOW ENERGY OPTICAL RESPONSE OF Sr_2RuO_4

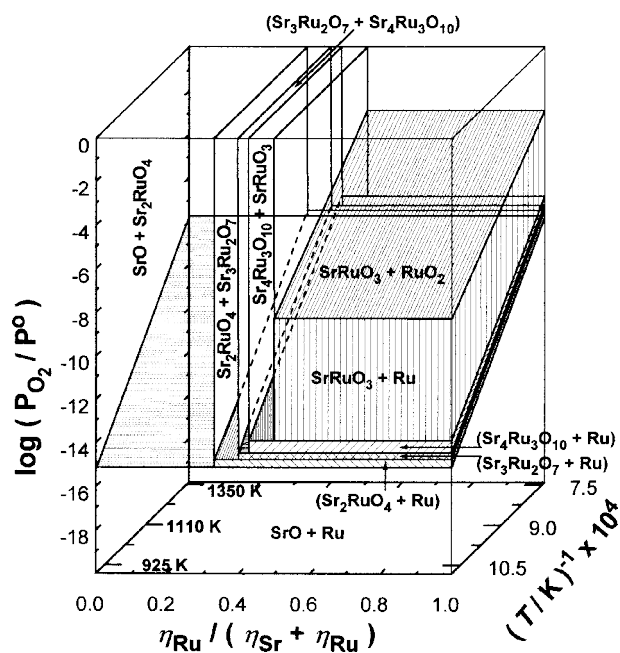


Figure 4.6: Oxygen potential diagram for the growing condition such as the temperature and initial stoichiometric composition. The vertical axis show the partial oxygen pressure (P^0 is the ambient pressure), The composition variable, cationic fraction $\eta_{\text{Ru}} / (\eta_{\text{Sr}} + \eta_{\text{Ru}})$, where η is the mole of either ruthenium or strontium. The image is reproduced from [231].

from the crucible). Different methods exist for the FZT. The raw materials are usually ground together; the powder is pressed in a pellet and kept above 1000 °C for about one day. The polycrystalline material is then re-ground and pressed into a rod which is usually 10 cm in length and 5 mm in diameter. In order to harden the material, the rod is sintered at high temperature for several hours. This initial procedure allows to get a polycrystalline material free from unwanted precursor material –e.g. carbon– used to embed the alkaline earth metals (calcium, strontium, barium). Later the polycrystalline rod is encased inside a quartz tube with gas and pressure. The sealed tube is placed at the focal point of an image furnace, which radiates the light emitted by a halogen tube. Slowly pulled from the melting zone, the rod crystallizes into a single crystal, while the rest of the rod is continuously leveled to that zone.

In the case of the ruthenate, the precision of the growth parameters is essential. Shown in Figure 4.6 from [231], the oxygen potential diagram suggests that small amount of impurity phase may be present in any samples. Moreover, the high volatility of ruthenium at the temperature of coexisting melt and the target crystal is usually causing the crystallization of undesired phases. To counteract this problem the feed rod precursor has a larger amount of the volatile element; this method is called the FFFZ technique. The excess constituents, here the ruthenium, act as a flux for the floating zone and compensate the evaporation loss. However the counterpart of the technique is that the initial excess of ruthenium has to be carefully chosen; too much of it results in the random formation of μm -sized pure ruthenium inclusions (See Figure 4.42) causing the so-called 3K-phase and the onset of the inhomogeneous

superconductivity critical temperature. [232].

The high quality Sr_2RuO_4 crystals employed in this work were grown by the FFFZ technique following the procedure of [230, 233, 234]. The Tc134 and Tc128 samples were grown by Tatiana Fittipaldi and Antonio Vecchione in University of Salerno, Italy; the C362 sample was grown in the group of Yoshiteru Maeno in Kyoto, Japan. A picture of the crystals is shown in Figure 4.14 In both cases, the initial precursor powders were SrCO_3 (99.9 % and RuO_2 (99.9 %, a very small amount of Ba (< 7 ppm) can be found. The superconducting critical temperature was determined using ac-susceptibility measurement; for the Tc134, Tc128 and C362 it was respectively 1.34 K, 1.28 K and 1.3 K.

4.3 Fermi-liquid in transport experiments

Sr_2RuO_4 is probably the layered perovskite with the most thoroughly studied Fermi-liquid properties. Notably by transport [186], quantum oscillation experiments [235] and ARPES [236]. Unlike the single band ^3He [237], Sr_2RuO_4 is a multi-band system. However as shown in different papers, the low temperature characteristics of the material are mostly dominated by the γ band [238] granting the use of the single band picture.

As it was shown in the previous chapter, the hallmark of a Fermi-liquid is the T^2 temperature dependence of the resistivity which is observed in Sr_2RuO_4 for both, the in-plane and out-of-plane components [186, 206, 239, 240]. Interestingly, there is no consensus for the interpretation of the transport above 25 K. Measuring the transport of the sample has two main objectives, first checking the sample was essential, but also understand the deviation from the Fermi-liquid picture at high temperature. For that reason, a new model was developed and presented in section 1.4.4.2. In this section, the different models and experiments found in the literature are introduced. The quantitative transport measurements are then introduced and compared to a phenomenological model for the low energy electron-electron scattering as described in the Fermi-liquid model. The Fermi-liquid temperature is shown to be directly dependent on the model parameters –such as the cutoff energy– of Equation 1.133.

4.3.1 Experimental

In this study, the transport measurement of Tc134 has been performed in a Janis VTI cryostat allowing a very stable measurement of the resistivity from 1.4 K to 300 K. The transport measurement has been performed using the four-point technique; in order to get an accurate absolute value of resistivity, the Tc134 sample was cut in slabs after the optical measurements. The two measured pieces are shown in Figure 4.7. Conventional silver paste is applied in a small droplet to connect 20 μm gold wires. An insulating varnish was used to glue the sample to a SiO_2 wafer and then dried in dry air at 50 K for 2 h. The absolute c -axis resistivity was obtained

4. LOW ENERGY OPTICAL RESPONSE OF Sr_2RuO_4

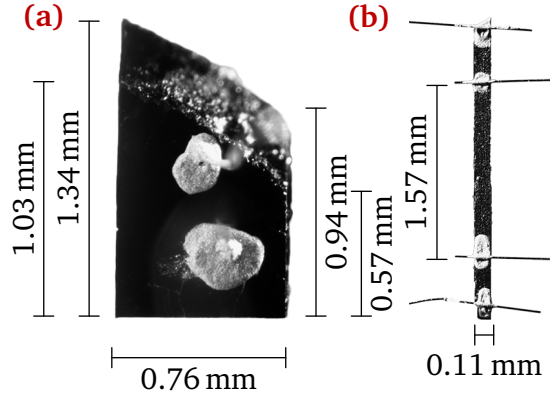


Figure 4.7: (a) Piece of the sample for the c -axis transport measurement. The thickness of the c -cut is 0.29 mm. (b) Sample for the ab -plane transport measurement. The thickness of the a -cut is 0.45 mm

in two steps: first a very tiny slab along the c -axis was carefully cut with a ratio of length by width of about 3:1; long integration time of the measurement was used at high temperature in order to obtain low noise data. Nevertheless measuring temperature dependence with such a sample was unsuccessful, the thermal contractions cleaved the sample at about 200 K. The sample shown in Figure 4.7 (a) was used instead by assuming that the very high anisotropy of this material allowed to glue the contact apart on the ab -plane surface. This is justified by the fact that, taking into account the asymmetry, the ratio of length by width is 60:1 at room temperature and increases to about 300:1 at 4 K.

An high temperature resolution was achieved for both in-plane and c -axis resistivity, 50 mK at high temperature and 5 mK below 2 K, the low temperature results are shown in Figure 4.10 (a-b). While no signature of T_c is expected down to 1.4 K for both ab -plane and c -axis transport of Tc134, the c -axis resistivity has a higher T_c of about 1.5 K which suggest low but finite inhomogeneity.

Table 4.3: Fit parameters of the quadratic equations of Figure 4.10 for sample Tc134

Geometry	Range (K)	\mathbf{a} ($\mu\Omega \text{ cm K}^{-2}$)	\mathbf{b} ($\mu\Omega \text{ cm K}^{-1}$)	\mathbf{c} ($\mu\Omega \text{ cm}$)
ab -plane	1.8–8	4.8(2) $\times 10^{-3}$	0(1)	0.171(4) $\times 10^{-3}$
ab -plane	60–220	0.63(3) $\times 10^{-3}$	2.15(4) $\times 10^{-1}$	$-0.337(1) \times 10^1$
c -axis	3–7	0.618(2) $\times 10^1$	0.84(2) $\times 10^1$	1.97(1) $\times 10^2$
c -axis	60–100	$-0.215(1) \times 10^1$	5.327(4) $\times 10^2$	$-9.778(2) \times 10^2$
c -axis	220–290	5.130(5) $\times 10^{-2}$	$-4.038(3) \times 10^1$	2.9525(3) $\times 10^4$

Two methods were used to deduce the power-law exponent (μ) of the temperature dependence: a fitting routine to $\rho(T) = aT^\mu + \rho_0$, and derivative of the logarithm $d \ln(\rho - \rho_0)/dT$. For the former, the low temperature ab -plane resistivity was fitted between $1.8 \text{ K} \leq T' \leq T$ and $3 \text{ K} \leq T' \leq T$ for the c -axis. By decreasing the maximum temperature used for the fit from 60 K

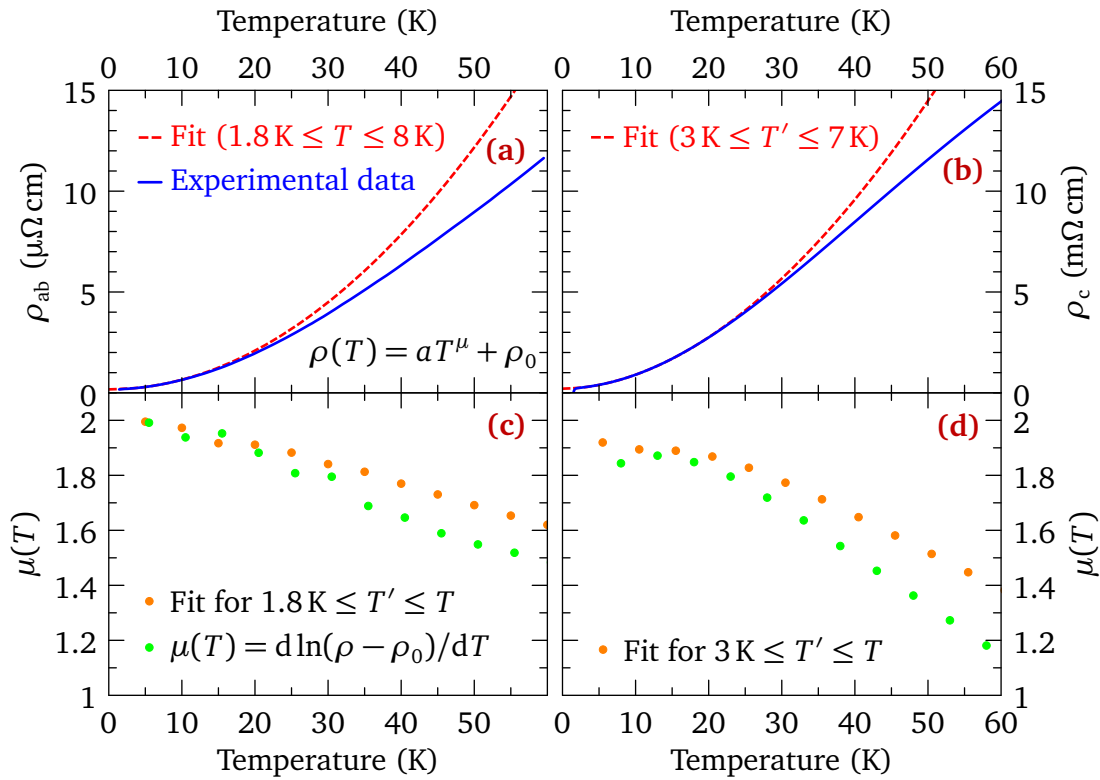


Figure 4.8: Power law fit to the Sr_2RuO_4 Tc134 sample using $\rho(T) = aT^\mu + \rho_0$. In-plane (a) and c-axis (b) low-temperature resistivity. (c-d) μ exponent from the power law fit and the logarithmic derivative of the resistivity. The minimal fitting temperature T_{\min} is 1.8 K for the in-plane and 3 K for the c-axis. In the case of the ab -plane measurement the flow goes exactly to the expected $\mu = 2$ and about $\mu = 1.92$ for the c-axis.

4. LOW ENERGY OPTICAL RESPONSE OF Sr_2RuO_4

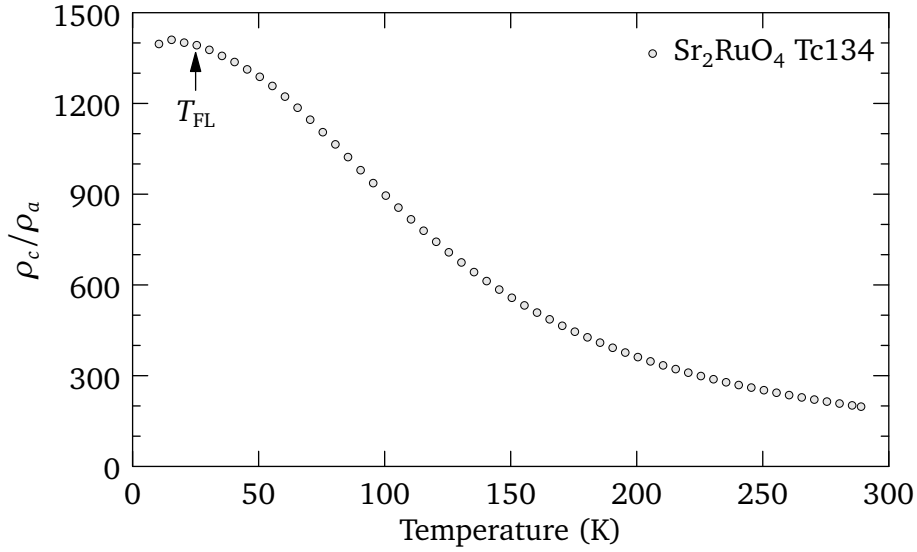


Figure 4.9: Sr_2RuO_4 temperature dependent resistivity anisotropy between the ab -plane and c -axis components. The Fermi-liquid temperature is shown by a black arrow, where the anisotropy saturates.

to 5 K, a flow toward exactly $\mu = 2$. The exponent then becomes constant below about 8 K for the ab -plane. Whereas the exponent is 1.92 at 5 K for the c -axis. Below $T_{\text{FL}} \approx 25$ K a clear deviation from the Fermi-liquid is seen, which is undoubtedly easier to see for the c -axis.

While T_c is increased under uniaxial pressure [229], hydrostatic pressure decreases it, allowing to probe the normal state below 0.9 K for pressure as high as 3.3 GPa [241]. At this pressure, the T^2 resistivity was seen to remain while the μ was decreased by a factor two. Such effect contrasts with the underdoped cuprates which shows Fermi-liquid properties but in competition with other states of matter that suppress the T^2 behavior at temperature of the order of T_c [132]. Shown in Figure 4.9, the ratio of the in-plane and out-of-plane resistivity is saturating at about 1400 at low temperature, which indicate the very high anisotropic nature of the electronic transport of Sr_2RuO_4 . The saturation of the ratio below about T_{FL} is very important because it indicates that this highly anisotropic material has the same transport mechanism prevailing in the two directions at low temperature.

4.3.2 Results

To show the Fermi-liquid properties of a metal, the resistivity is usually fitted or shown against T^2 [186]. Another way of observing this regime is to use the resistivity derivative in Figure 4.10. The Sr_2RuO_4 resistivity was never reported in such a form, which unveils a very interesting trend. The low temperature derivative is linear with zero intercept which means that indeed below T_{FL} $\rho_1(T) = a_1 T^2 + c_1$. At the same time, the resistivity at high temperature has a quadratic form, but with an additional linear component $\rho_2(T) = a_2 T^2 + b_2 T + c_2$; the fitted

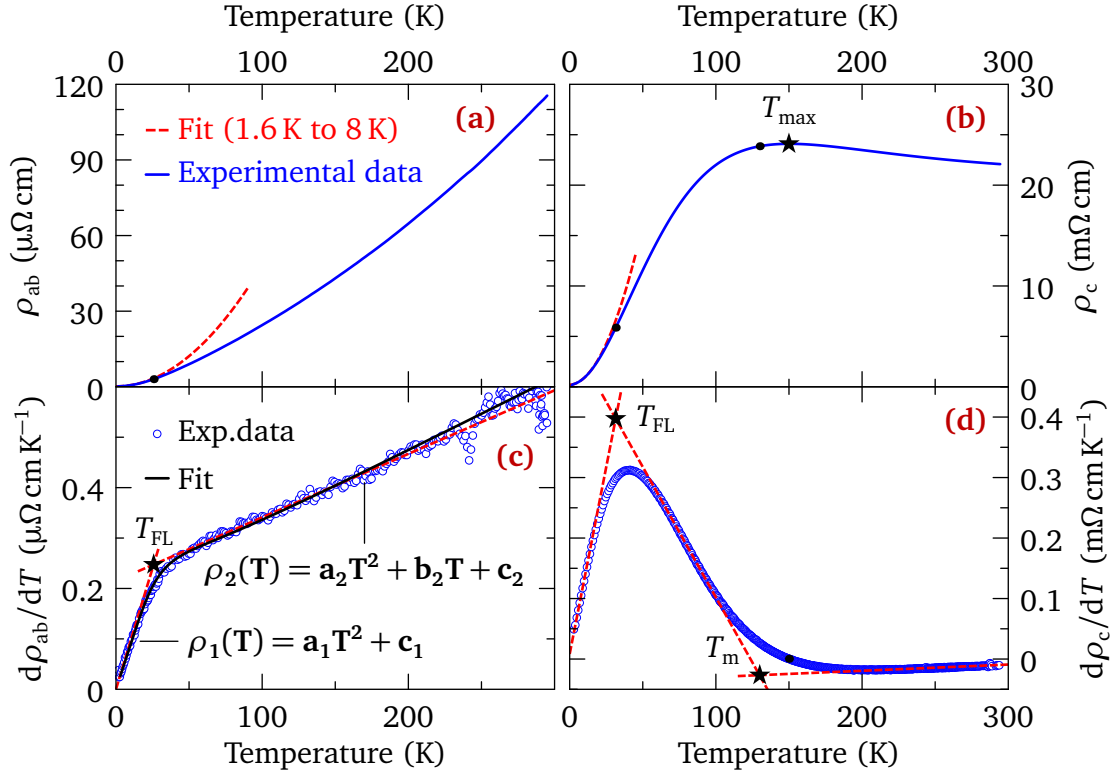


Figure 4.10: *ab*-plane and *c*-axis resistivity of Sr_2RuO_4 , sample Tc134. **(a)** The resistivity is fitted using a polynomial equation $\rho(T) = aT^2 + bT + c$ both at low (1.6 K to 8 K) and high temperature (60 K to 220 K). **(b)** *c*-axis transport and derivative. **(c)** In-plane resistivity derivative is showing the two fitted models. $T_{\text{FL}} = 25.8\text{ K}$ is defined as the crossing temperature of the two models and shown with a star, reported as a thick point in the upper graph. The double triangle model is shown as a black thick line **(d)** with corresponding Fermi-liquid temperature.

parameters are shown in Table 4.3 and the models as red dashed lines in Figure 4.10 (a-d). The crossover is defined by the temperature at which the two models cross and correspond to T_{FL} at 25.8 K. The transition is rather broad and occurs in a range of about 15 K around T_{FL} , which explain why the μ exponent of Figure 4.8 (a) gets constant at about 10 K.

In section 1.4.4.2 it was shown that Equation 1.138 produces a T^2 resistivity up to $\omega_c/2\pi k_B$; above, when the susceptibility (bosonic spectral function) remains zero, the regime is linear. Here, in order to reproduce the exact behavior of the *ab*-plane resistivity, two superimposed linear susceptibilities were used. The model has five parameters: the slope of the two triangles, their respective cutoff, and the constant impurity scattering rate. The data of Tyler *et al.* were used from 300 K to 1300 K without any scale adjustment [242]. The resulting fit is shown as a black line in Figure 4.10 (c) and Figure 4.12 reproduces exactly the correct temperature behavior from 1.8 K to 1300 K. The resulting fitted susceptibility is shown in Figure 4.11. The first triangle is extremely narrow, its cutoff energy is 13.8 meV which corresponds to T_{FL} $\omega_c/2\pi k_B = 25\text{ K}$. The second cutoff has is at 500(50) meV, or about 900(100) K. The fit of the high-temperature data is shown in Figure 4.12. The slope of these susceptibilities is proportional

4. LOW ENERGY OPTICAL RESPONSE OF Sr_2RuO_4

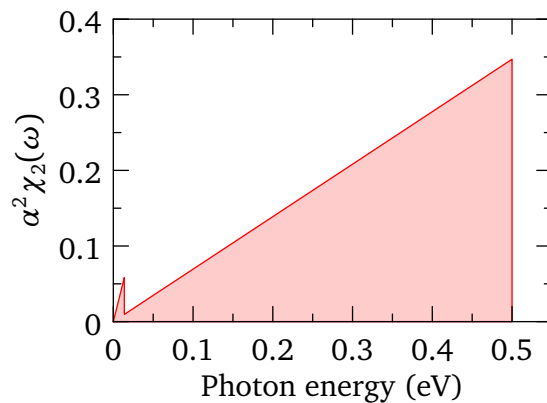


Figure 4.11: Inplane susceptibility of Sr_2RuO_4

to the density of states at the Fermi energy, which indicates that the second triangle has a smaller impact on the total density of states and the low-energy electronic properties.

One possible scenario of the very low energy cutoff and steep slope of the first triangle is the presence of a Van Hove singularity close to the Fermi energy. Predicted both in cuprates and in the early ruthenates papers [243, 244] this scenario was claimed to change the scattering rate properties from T^2 to a T transport at about one-quarter of the energy of the singularity. At that time, the Van Hove singularity of the d_{xy} orbital was predicted to be at about 20(2) meV above the Fermi energy which was somewhat corresponding to the apparition of linear regime at 58 K in the early samples [206]. Nowadays, recent calculations Figure 4.2 showed that the Van Hove singularity has a strong impact of the resistivity regime, allowing to move from a T^2 behavior at low temperature to a linear dependence at a temperature above the singularity energy [245]. Additionally, further refinement of the Van Hove singularity energy [246, 247] leads to reduction of this value down to about 10 meV due multi-bands effects (narrowing of the d_{xz} and d_{yz} orbitals and transfer of spectral weight to the d_{xy} orbital). This energy is very close to the cutoff of the first triangle, which is a good indication that below about 25 K, the quasi-2D γ band dominates the electronic properties and displays Fermi-liquid behavior. This picture is fully consistent with [238]. From another point of view, the susceptibility is a convolution of the occupied and unoccupied states in the density of states. In Figure 4.13, the DOS is almost constant below the Fermi energy which in principle should create a much broader transition and thus, if taken without additional assumptions, contradicts the former scenario. Another scenario would directly explain the data by coupling to 2D bosonic modes such as spin fluctuations. They have an energy scales either smaller or larger with $T_{\text{SF}} = 5$ meV, or the Debye energy $T_{\text{D}} = 35$ meV [236]. However, based on their dispersion relation in 2D, a linear susceptibility can be reproduced. Assuming that the 2D-modes happen at long wavelength

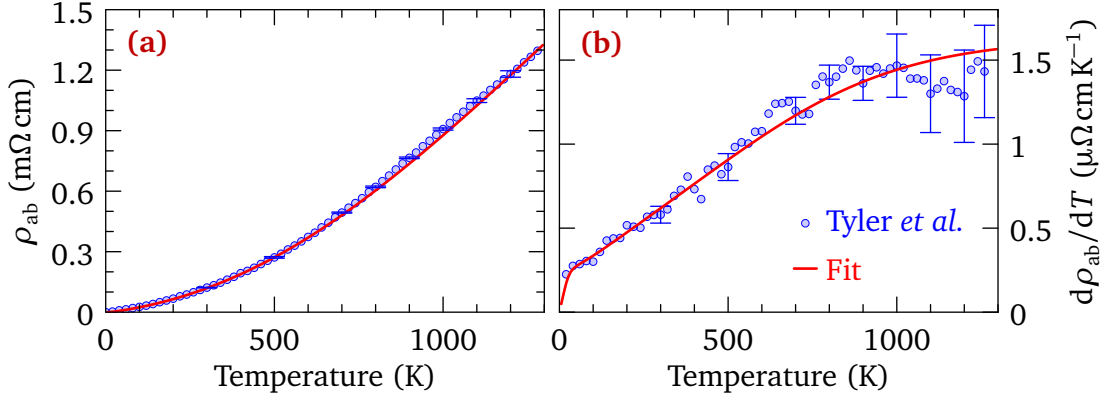


Figure 4.12: High-temperature fit of the Sr_2RuO_4 in-plane resistivity using the double triangle model. (a) Resistivity and its derivative (b). The data are reproduced from [242]

(acoustic dispersion) $v\hbar k = \omega_k$, the density of states can be obtained by summing all the i states

$$N(\omega) = \frac{1}{V} \sum_i \delta(\omega - \omega_k) \quad (4.1)$$

with V , the volume. Taking the continuous limit in k -space

$$\begin{aligned} N(\omega) &= \frac{1}{(2\pi)^2} \int_0^\infty d\omega \delta(\omega - \hbar v |\mathbf{k}|) \\ &= \frac{1}{(2\pi)^2} \int_0^\infty dk \int_0^{2\pi} d\theta \delta(\omega - \hbar v k) \\ &= \frac{1}{2\pi} \int_0^\infty dk \frac{k}{\hbar v} \delta(k - \omega/\hbar v) \\ &= \frac{1}{2\pi} \frac{\omega}{(\hbar v)^2}. \end{aligned} \quad (4.2)$$

If the electron-mode coupling is independent of k [248], the susceptibility is

$$\alpha^2 \chi_2(\omega) = \alpha^2 C \omega, \quad (4.3)$$

where $C = \frac{1}{2\pi} \frac{1}{(\hbar v)^2}$. In such a case, the 2D antiferromagnetic fluctuations (paramagnons) are the reminiscent of the physics of ^3He , which would be an interesting scenario [249].

It is striking to see that the transport could so easily be described at 1000 K. However, this model is a simplification of the physics of Sr_2RuO_4 which is a multi-band system. It is totally believable that like for the cuprates (section 3.5.5.3), the susceptibility may be temperature dependent which would imply smaller cutoff energies. Nevertheless, it was shown that the main structures of the susceptibility persist, so that this analysis would still indicate that the first Fermi-liquid regime is hiding a second regime above.

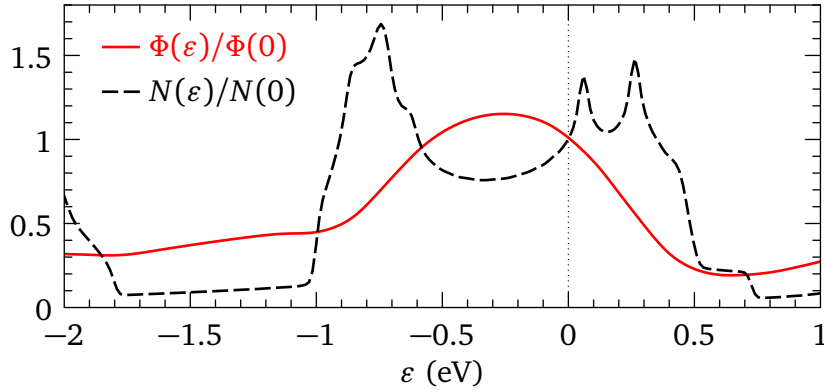


Figure 4.13: *ab*-plane transport function $\Phi(\varepsilon)$ and DOS $N(\varepsilon)$ of Sr_2RuO_4 . These functions are normalized to their Fermi level values. $\Phi(0) = \epsilon_0 \omega_p^2 = 0.38 \times 10^{21} \Omega^{-1} \text{ms}^{-1}$ ($\hbar\omega_p = 4.3 \text{ eV}$), in reasonable agreement with previous results [250, 251].

4.3.3 The anomalous transports of the *c*-axis

The *bad metals* terminology specifies materials with unconventional conduction mechanism such that the absence of resistivity saturation above the Mott-Ioffe-Regel limit temperature [252]. In this respect the bad metal can be seen as a quasiparticle insulator whose conduction is given by collective modes [253].

The *c*-axis transport of Sr_2RuO_4 is shown in Figure 4.10 (b) and (d). Fitting the data with quadratic models above and below T_{FL} gives a somewhat higher Fermi-liquid temperature $T_{\text{FL}} = 31 \text{ K}$. However, the temperature derivative of the resistivity indicates a remaining linear component (zero temperature intercept) which is equivalent to the fact that the exponent fit of section 4.3.1 was not exactly 2. The anomalous high-temperature transport is showing an insulating to metal regime at about 150 K. The definition of this temperature is difficult, it can either be taken from the maximum of resistivity (T_{max}) or the crossing of the fit of two quadratic model leading to T_{m} in Figure 4.10 (d). From early quantum oscillation measurements, the Fermi surface parameters such as the band mass or the Fermi wave vectors k_{F} were measured [235]. Using $l_{\text{c}} = lc\Delta k_{\text{F}}/\sqrt{2}$ with the mean free path $l = \hbar\sqrt{\pi c/n}/e^2\rho_{\text{ab}}$. With n the carrier density, c the *c*-axis lattice parameter and Δk_{F} the band splitted Fermi wave vector, the electron mean free path for the three band were calculated at low temperature to be 3, 36 and 30 Å for the α , β and γ band. Already from the lowest reachable temperature the α band $l_{\text{c}} < c$ such that only the β and γ bands are able to sustain coherent transport. Interestingly it was also reported that T_{max} , either in the *ab*-plane [242] or in the *c*-axis transport, was not corresponding to the MIR temperature limit for the β and γ bands since the MIR criterion is already reached above 30 K for the *c*-axis [240]. Several approaches are used in the literature to describe the *c*-axis transport crossover. The first approach is based on a dimensional crossover from 3D characteristics Fermi-liquid to 2D dynamics [254, 255]. Another point of view comes from [189] and a review of the Mott-Ioffe-Regel limit is given in [256]

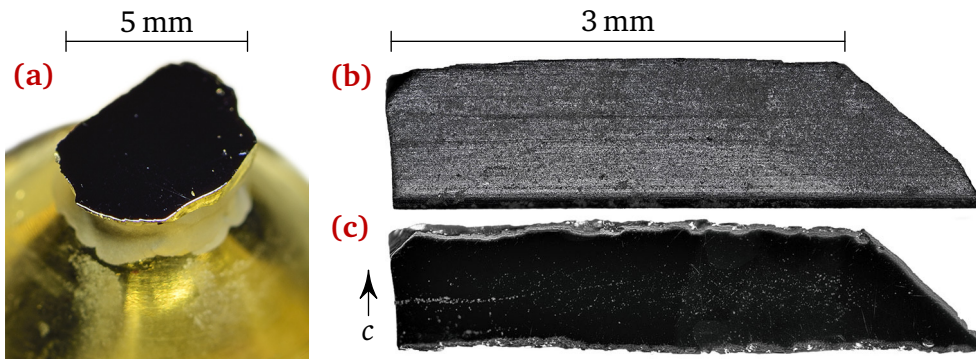


Figure 4.14: Sr_2RuO_4 sample with $T_c = 1.34\text{ K}$ (Tc134). (a) ab -plane face polished and mounted on a copper sample holder, here covered by the remaining gold evaporations. (b) ac -plane surface of the Tc134 sample after the cut, but before polishing. Some part of the sample cleaved and were removed due to the polishing of the surface. (c) ac -plane of the sample after the micro-polishing process. The c -axis is shown by the black arrow.

4.4 Universal Fermi-liquid scaling in optics

This section shows that the low-energy scattering rate of the conduction electrons in Sr_2RuO_4 obeys scaling relations for its energy (ω) and temperature dependence in accordance with the Fermi-liquid theory. Unlike the cuprates, the thermal relaxation regime of Sr_2RuO_4 , $1/\tau \propto (\hbar\omega)^2 + (p\pi k_B T)^2$, is obeyed with the exact scaling parameter $p = 2$. The second part focuses on many-body electronic structure calculations using dynamical mean-field theory and confirm the low-energy Fermi-liquid scaling. Both, experiments and numerical calculations, point to the ω/T scaling in the optical conductivity data.

4.4.1 Sample preparation

4.4.1.1 In-plane measurement

For the in-plane measurement, the Tc134 sample was used. The procedure is almost the same as the one described in chapter chapter 3. The ab -plane crystal surface of $5.1\text{ mm} \times 3.6\text{ mm}$ was cleaved along the ab -plane, micro-polished with a $1\text{ }\mu\text{m}$ diamond suspension and also a dry polishing disc, of $0.1\text{ }\mu\text{m}$ roughness, to achieve a perfectly reflective surface. The sample was glued onto a copper sample holder using silver paste; a picture is shown in Figure 4.14. The sample surface was carefully cleaned and checked prior of transferring the sample-holder to the UHV cryostat.

4.4.1.2 c -axis measurements

In the second part of the experiment, section 4.7, the Tc134 and Tc128 samples were cut parallel to the c -axis. The resulting $\tilde{a}c$ surface is mix of the a and b axis which are identical; it will

4. LOW ENERGY OPTICAL RESPONSE OF Sr_2RuO_4

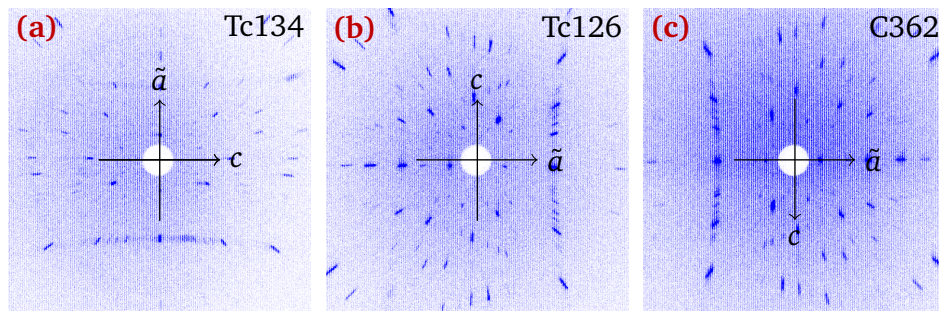


Figure 4.15: Back reflection Laue images of the Tc134 and Tc128 Sr_2RuO_4 samples. The notation \tilde{a} indicates an admixture both a and b axis which are equivalent. (a) the sample $\tilde{a}c$ -plane vector is pointing along the X-ray beam although in (b) the c -axis is aligned vertically. (c) Similar patterns for C362 which indicates that the c -axis is pointing antiparallel to (b).

be named ac for simplicity. The surface of the samples was micro-polished using the same procedure than for the ab -plane and its alignment was done using a Laue diffractometer. The ac -plane is an extremely polarization-sensitive surface (see Figure 2.4 (b) of section 2.2.2). In order to avoid any contamination from the opposite axis, the sample surface was aligned with the axis of interest vertically; in such a way, the incident light had a pure s -polarization. The result of the alignment for the crystals is shown in Figure 4.15, the diffraction pattern from the crystal is seen as darker spots. The alignment of the surface was verified within 1° . The procedure was the same for the second sample Tc128 and C362.

4.4.2 Optical measurement

The normal incidence reflectivity and ellipsometric measurements were almost following exactly the measurement procedure presented in the previous chapter. The measurement of both in-plane and c -axis reflectivity were carried out with two FTIR spectrometers and a Woolam VASE ellipsometer. From the FIR to NIR, the reflectivity at near-normal incidence was measured from 1.9 meV to 1.1 eV using a Bruker IFS 113v spectrometer; an high-energy upgraded Bruker IFS 66v/S extended this range to 3 eV. The spectral resolution is 0.1 meV in the FIR which was also a motivation to for this study, since this value is much better than previous ARPES studies in the field [238] and [257], with 25 meV and 14 meV respectively. The ellipsometry measurements extended the data up to the UV (0.47 eV to 6.2 eV). The two spectroscopic techniques overlap from 0.47 eV to 3 eV.

4.4.2.1 Normal incidence reflectivity

Temperature sweeps were conducted between 9 K and 290 K at a speed of 1 K min^{-1} . One reflectivity spectrum was collected every Kelvin. Using polarizers the light was s -polarized in order to suppress remaining c -axis features coming either from near-normal geometry or crystal

miscut as described in Ref. [22]. In order to conduct the wide frequency range of measurement, several detectors and beam-splitters were used as in Table 3.2, with cutoff energies at 1.9, 7.7, 64.5, 124, 471, 1042 and 3000 meV. The overlap of the data was carefully checked and the matching was within the experimental noise. The gold or silver reference layers were removed between each measurement using scotch tape. Every 2 to 3 measurements a soft polishing using 0.1 μm paper was done on the surface of the sample and the surface was checked using an optical microscope prior to the transfer in the cryostat.

The long-term drift of the light sources and detectors was calibrated using the high-stability flipping-mirror and following the same procedure of section 3.4.2.1. The remaining uncorrected drift was analyzed during the warm-up process, which leads to a thermal hysteresis effect below the noise level in the FIR, below 0.2% in the MIR, and below 0.4% in the NIR and above.

The Tc134 sample absolute reflectivity $R(\omega)$ is shown at selected temperatures in Figure 4.16. The c -axis measurement, also shown, was measured after the publication of Ref. [1] so that the room temperature c -axis reflectivity of Ref. [77] was used instead to extract the ab -plane dielectric function of the ellipsometric measurement. The analysis of the c -axis reflectivity will be discussed in more detail in section 4.7.2. In Figure 4.16 (b), the features in parenthesis correspond to optical phonons. For the ab -plane at room temperature, the feature (3) correspond to the 83 meV longitudinal in-plane bond-stretching mode of the RuO_2 layer (zone center double degenerated E_u). The slight softening and broadening upon heating indicate a decrease of screening. The structures (1) at 41 meV and (2) at 55 meV most likely also correspond to phonons. At room temperature, the small features of the reflectivity were fitted and compared to the c -axis. The c -axis phonons are barely observable, or within the noise level; they are not corresponding to feature (1). The second structure (2) is close in energy to first part of third c -axis 56 meV phonon, but with an 30 % larger width and a missing second splitted part prominent in the c -axis reflectivity.

4.4.2.2 Ellipsometry

The ab -plane ellipsometry data were used to extend the energy range up to 6.2 eV and are shown in Figure 4.17. The angle of incidence of light from the surface normal was $\theta = 70^\circ$. Like for the $\text{HgBa}_2\text{CuO}_{4+x}$ compound, the high anisotropy of Sr_2RuO_4 doesn't allow to directly measure the dielectric function of the material but the so-called pseudo-dielectric function $\tilde{\epsilon}(\omega)$ which is a mix of the ab -plane and c -axis responses. The ab -plane dielectric function $\epsilon(\omega) = \epsilon_1(\omega) + i\epsilon_2(\omega)$ was extracted from $\tilde{\epsilon}(\omega)$ by inverting the Fresnel equations, using the complex c -axis dielectric function $\epsilon_c(\omega)$ deduced from the c -axis reflectivity of Ref. [77]. The consistency of the procedure for extracting $\epsilon(\omega)$ has been checked by repeating the ellipsometry measurements at different angles of incidence. The resulting dielectric function is shown in Figure 4.17.

4. LOW ENERGY OPTICAL RESPONSE OF Sr_2RuO_4

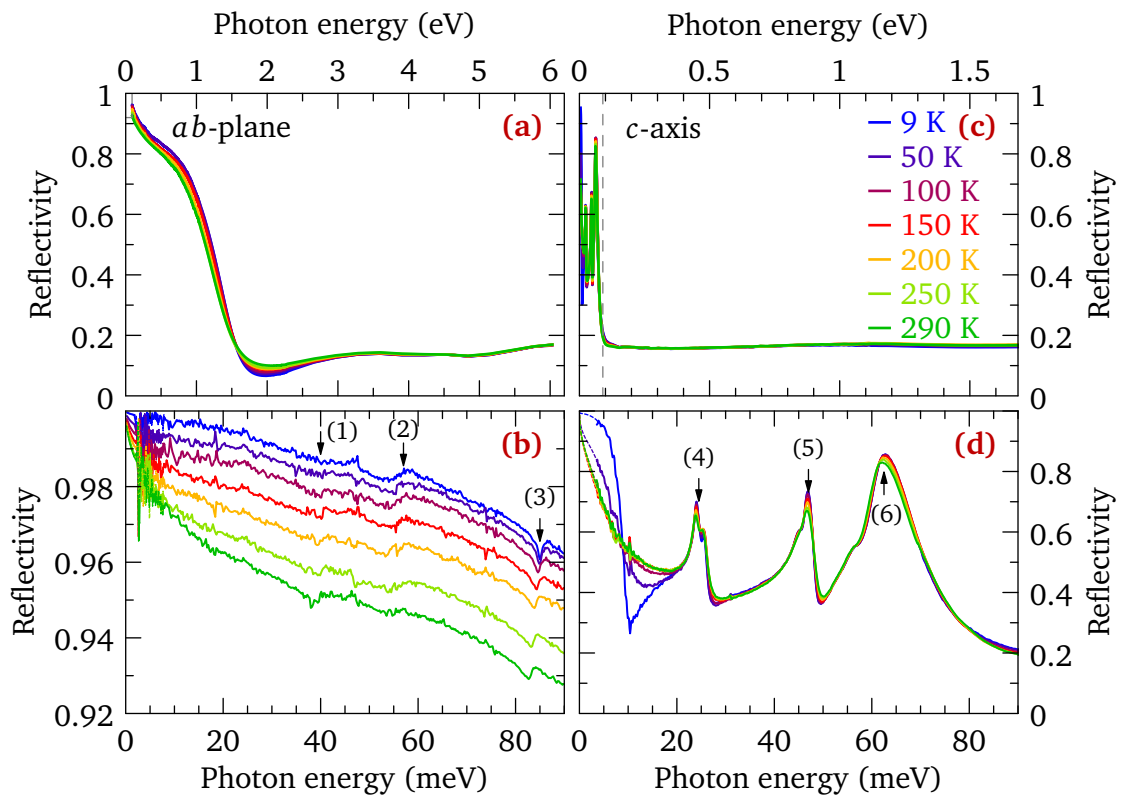


Figure 4.16: Reflectivity of Sr_2RuO_4 sample Tc134 at selected temperatures. **(a)** Measurement along the ab -plane taken from FTIR spectrometry and ellipsometry dielectric constant. **(b)** Expanded view of the low energy area of the ab -plane reflectivity. The Hagen-Rubens extrapolation to zero energy, Equation 1.49, is shown as dashed lines. The 85 meV feature (3) is a longitudinal in-plane bond-stretching phonon mode of the RuO_2 layer (zone center double degenerated E_u). The structures (1) at 40 meV and (2) at 57 meV also correspond most likely to phonons. **(c)** Measurement along the c -axis. The three splitted structures (4 to 6) are A_u c -axis phonons. They are further referenced as A_i , B_i and C_i with the index $i = 1, 2$ for the low or energy part.

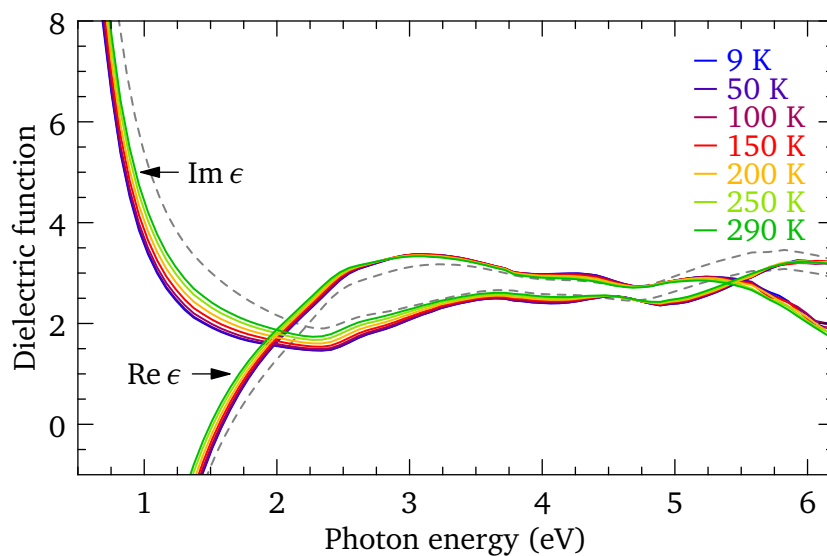


Figure 4.17: Real and imaginary parts of the dielectric function ϵ of Sr_2RuO_4 Tc134 extracted from Equation 2.10. The dashed lines indicates the complex pseudo dielectric function ϵ_{pd} at 290 K.

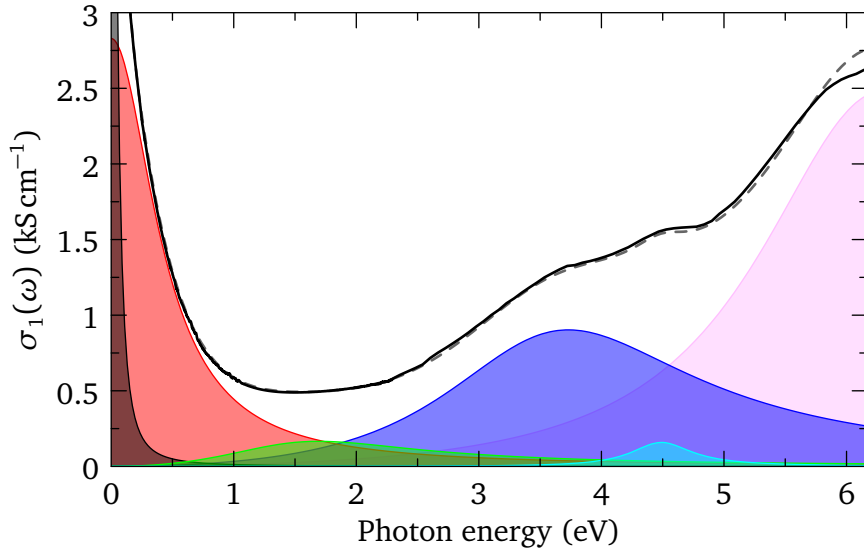


Figure 4.18: Real part of the optical conductivity at 290 K, calculated from the Drude-Lorentz model given by Equation 1.57 and Table 4.4 (dashed line). The shaded curves show the contributions of the six oscillators, with the two Drude oscillators in black and red. The solid line is the conductivity obtained directly from the reflectivity and ellipsometry data using Kramers-Kronig relations.

4.4.2.3 Drude-Lorentz analysis

Using the RefFIT software [16, 28], the Drude-Lorentz fit was performed simultaneously on the reflectivity and the ellipsometry data. This allowed to have a correct determination of the reflectivity and its phase up to 6.2 eV, but also to extrapolate the data both to zero energy and up to 150 eV, which is required for an accurate Kramers-Kronig transformation of the data.

The low-energy response (below ≈ 1 eV) is well described at all temperatures by the superposition of two Drude peaks and four additional Lorentz oscillators; the oscillators at energies above the limits of the experiment are taken as a constant, $\epsilon_\infty = 2.3$. The parameters of the model fitted to the room-temperature data are given in Table 4.4. The real part of the conductivity obtained from this model is displayed in Figure 4.18, and compared with the conductivity determined by Kramers Kronig analysis of the reflectivity. The match is excellent up to 5.8 eV. At a first glance, the two Drude modes mimic the *foot* structure of the low-energy Fermi-liquid response described in Figure 1.11 (c). The lowest-lying interband transitions, located above 1 eV, have been previously identified as *d-d* transitions [20] so that the two Drude oscillators are ascribed to the intraband response of mobile carriers, and all finite-energy modes to the bound charges. In the optical conductivity of Sr_2RuO_4 , the first interband transition is shown by a Lorentzian peak at 1.693 eV (Figure 4.18). These transitions do not contribute to the energy dependence of the total dielectric function below about 1 eV. This can be verified in Figure 4.19, that shows that the bound charge dielectric function is constant and equal to $\epsilon_b(0) = 5.6$ at 290 K.

The spectral weight of the charge carriers was calculated as the geometric sum of the

4. LOW ENERGY OPTICAL RESPONSE OF Sr_2RuO_4

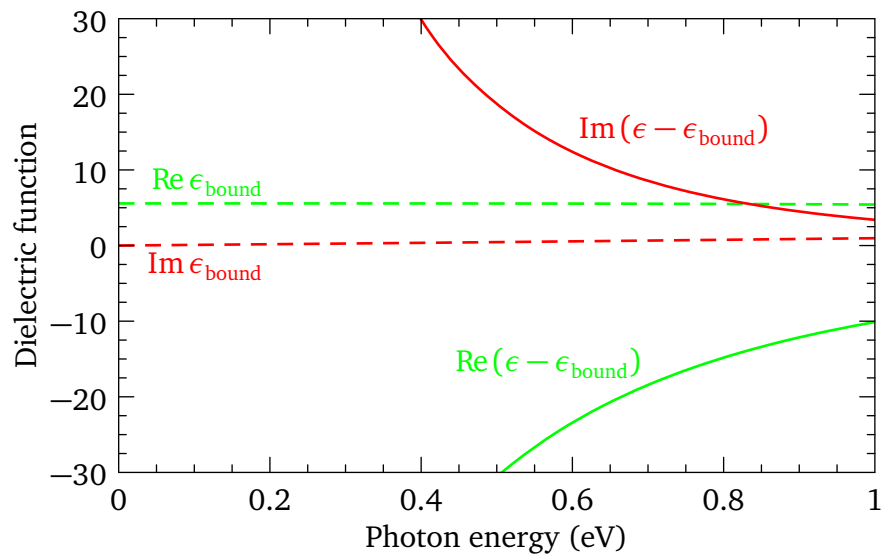


Figure 4.19: Mobile- and bound-charge contributions to the dielectric function at 290 K. The negligible energy dependence of the bound-charge response indicates a clear separation between the intraband and interband responses below 1 eV.

intraband response following Equation 1.59 and is almost temperature independent with a value of 3.3 eV at low temperature and 3.4 eV at room temperature. On the other hand, the spectral weight of the sharpest Drude peak is smaller, and decreases from $\hbar\omega_{p1} = 1.8$ eV at low temperature to 1.6 eV at room temperature.

Table 4.4: Parameters of the Drude-Lorentz oscillators for the in-plane optical response of Sr_2RuO_4 at 290 K. All numbers are in eV. The high-energy dielectric constant is $\epsilon_\infty = 2.3$. The intraband plasma energy obtained from the two Drude oscillators is $\hbar\omega_p = 3.4$ eV.

	intraband		interband			
	$j = 0$	$j = 1$	$j = 2$	$j = 3$	$j = 4$	$j = 5$
$\hbar\omega_{0,j}$	0.000	0.000	1.693	3.730	4.489	6.298
$\hbar\omega_{p,j}$	0.038	0.432	1.952	2.533	0.602	2.527
$\hbar\gamma_j$	1.568	3.014	1.552	4.123	0.843	6.826

4.4.3 Optical conductivity

The discussion continues using the complex in-plane and c -axis conductivity obtained from Kramers-Kronig relations. The data are shown at selected temperatures in Figure 4.20. The relative accuracy of the low-energy conductivity as a function of temperature was assessed by fitting the low-energy reflectivity to the Hagen-Rubens equation and comparing the results to the dc-transport shown in Figure 4.16 (a-b). In (b) the dc-resistivity was also obtained by the Drude-Lorentz model which gives almost the same results. Both techniques are generally

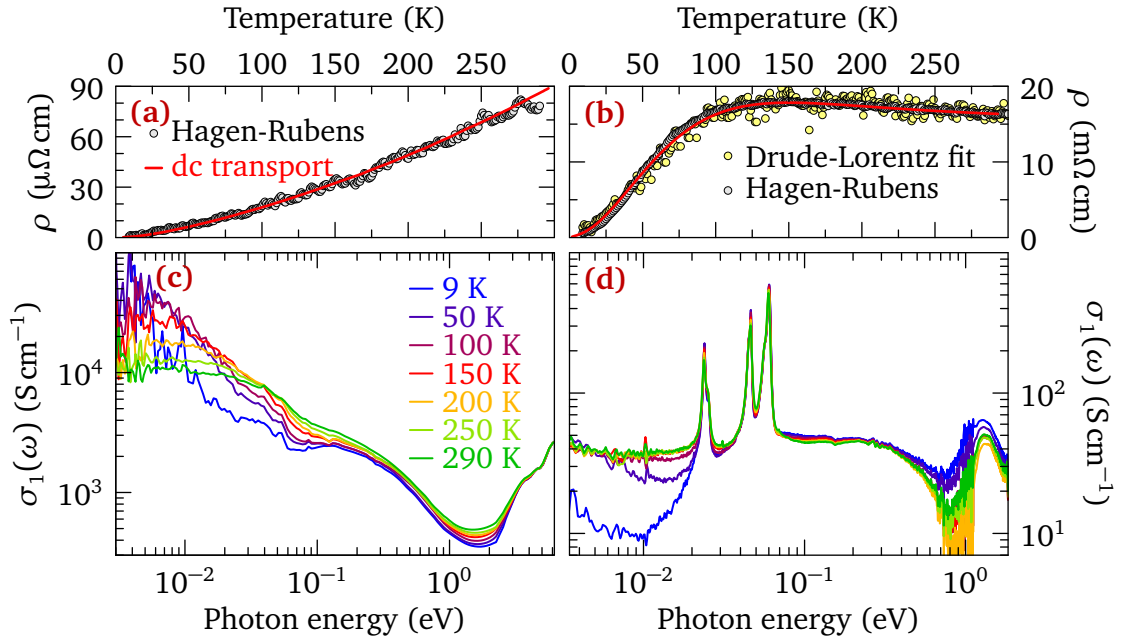


Figure 4.20: (a-b) *ab*-plane and *c*-axis resistivity of Sr_2RuO_4 from dc-transport measurement (solid red curve), from Hagen-Rubens equation fit to the low energy data (gray open circles) and from Drude-Lorentz model (yellow). The transport measurement done on the *ab*-plane has been multiplied with a factor 0.84 and 1.2 for the *c*-axis, which is within the range of error by geometrical factors due to sample shape. (c-d) The real part of the *ab*-plane and *c*-axis optical conductivity of Sr_2RuO_4 for both *ab*-plane and *c*-axis selected temperatures between 9 K and 290 K.

equivalent, but the advantage, in terms of noise, often goes to the Hagen-Rubens extrapolation, which is not disturbed by the higher energy data.

The two Drude peaks used in the Drude-Lorentz model represent the two main structures seen below 1 eV in Figure 4.20 (c). Upon lowering the temperature from 290 K to 9 K, the first Drude peak becomes extremely narrow, and its maximum at $\omega = 0$ increases by two orders of magnitude. The second peak is much broader and extends up to 1 eV. The weak features at 40, 57, and 85 meV correspond to optical phonons seen in the reflectivity.

The *c*-axis conductivity shows a gap-like structure at low energy, a broad and temperature independent MIR peak and the onset of interband transitions. The three sharp features are the split optical phonons. Further details will be discussed in section 4.7.2.

4.4.4 Thermal regime in the optical scattering rate

In this section, the universal value $p = 2$ is established experimentally. The remarkable agreement is also shown between the experimental data and the theoretically derived scaling functions in the thermal regime of the Fermi liquid. The identification of the precise Fermi-liquid response also enables to characterize its deviations at high energy and temperature, shown in section 4.6. Realistic DMFT calculations for Sr_2RuO_4 are shown and yield excellent agreement

4. LOW ENERGY OPTICAL RESPONSE OF Sr_2RuO_4

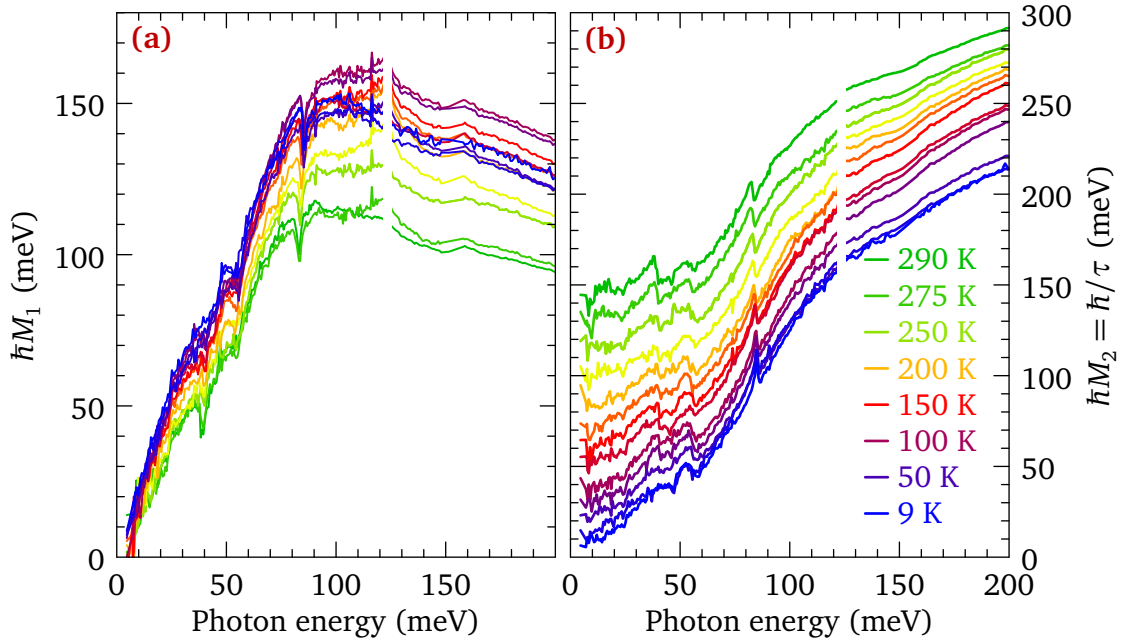


Figure 4.21: Real part (left) and imaginary part (right) of the Sr_2RuO_4 memory function at selected temperatures between 9 K and 290 K. A white space is introduced near 130 meV where data sets from different detectors were linked.

with the measured optical spectra.

Knowing the intraband spectral weight $\epsilon_0\omega_p^2$, Equation 1.64 was inverted to the energy-dependent memory function $M(\omega)$ as described in section 1.2.3 [17]. The results are displayed at selected temperatures in Figure 4.21 and the mass enhancement factor in Figure 4.22. It presents an overall behavior determined by the charge-carrier dynamics, as well as sharp superimposed Fano-like structures corresponding to dipole active optical phonons. Phonon were not subtracted, which would have required a specific modeling and introduce unwanted ambiguities.

The universal characteristics of the optical response in a Fermi-liquid have been described in the previous chapter, in section 1.4.1 and in Refs. [19, 38, 56]. The intraband optical absorption process excites electron-hole pairs, with the consequence that the optical relaxation rate $M_2(\omega)$ is proportional to $(\hbar\omega)^2 + (p\pi k_B T)^2$ with the value $p = 2$.

The energy dependence of $M_2(\omega)$, shown in Figure 4.23, is therefore manifestly non-Drude like and indicates the presence of a dynamical component in the quasiparticle self-energy. Moreover, below 0.1 eV, $M_2(\omega)$ has a positive curvature for all temperatures corresponding to ω^η with $\eta = 1.7$ to 2.3, with one outlier ($T = 15$ K), where the least-squares fit gives $\eta = 1.15$. $M_1(\omega)$ has a linear energy dependence expected in the Fermi-liquid model. The low-energy mass enhancement factor $m^*(\omega)/m = 1 + M_1(\omega)/\omega$ varies from 3.3 at 9 K to 2.3 at 290 K. This variation is much smaller than in the underdoped cuprates. The $m^*(\omega)/m$ curves (Figure 4.22) fall slightly below the one of a previous room temperature study [258].

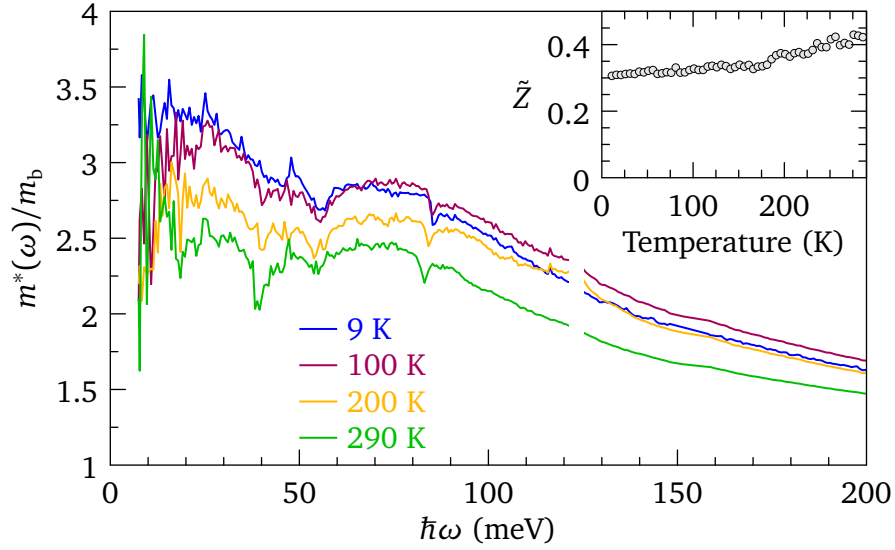


Figure 4.22: Energy-dependent mass enhancement $m^*(\omega)/m = 1 + M_1(\omega)/\omega$ at selected temperatures, and temperature dependence of $\tilde{Z} = m/m^*(\omega)$ extrapolated to zero energy. The white space close to 130 meV indicates the region where two data sets have been linked.

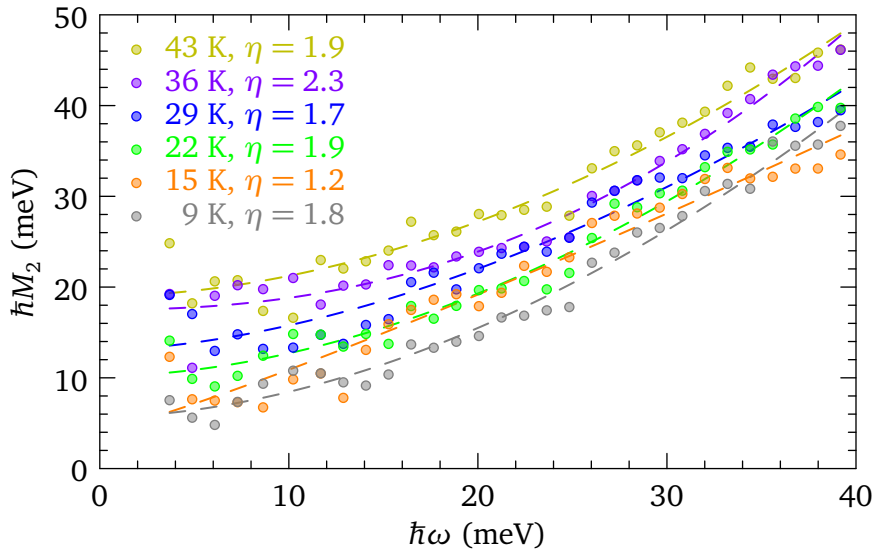


Figure 4.23: Imaginary part of the memory function binned in 2 meV intervals (points) at selected temperatures. The data are fitted below 40 meV using the power law $M_2(\omega) = M_2(0) + A\omega^\eta$ (dashed lines). The η exponent is indicated for each temperature.

4. LOW ENERGY OPTICAL RESPONSE OF SR_2RUO_4

Several recent optical studies have reported ω^2 and T^2 for $M_2(\omega)$ in a number of different materials. The corresponding scaling parameter is shown in Table 4.5 and vary from less than 1 to 2.38 with the corresponding temperature and energy range (when available) in which the scaling is valid. In the case of the cuprates, the scaling parameter was found to be $p = 1.5(1)$. One possible scenario that has been proposed to explain this discrepancy is the presence of magnetic impurities [19].

Table 4.5: Review of the different scaling parameters p found in the literature and their corresponding energy and temperature range.

Compounds	Material	T_{\max} (meV)	ω_{\max} (meV)	p	Ref
Heavy fermions	UPt ₃	1	1	< 1	[259]
	CePd ₃	–	–	1.14	
	URu ₂ Si ₂	2	10	1.0	[18]
Titanates	Ce _{0.95} Ca _{0.05} TiO _{3.04}	25	100	1.31	[260]
	Nd _{0.95} TiO ₃	24	50	1.05	[261]
Transition metals	Cr	28	370	1.6	[262]
Organics	κ -(BEDT-TTF) ₂	4	70	2.38	[4]
Cuprate	HgBa ₂ CuO _{4.1}	19	100	1.5	[2]
Ruthenate	Sr ₂ RuO ₄	3.4	36	2	[1]
Magnetic moments	<i>Resonant levels</i>	–	–	1–∞	[19, 171]

Due to the small temperature range and the very high low-energy reflectivity, the precise determination of the p scaling parameters required a quantitative analysis. The procedure thus extends the previous one used for the underdoped HgBa₂CuO_{4+x}. $M_2(\omega, T)$ was plotted parametrically as a function of ξ_p^2 for different choices of p and the root-mean square deviation of this plot was calculated from a straight line. The slope of the line is corresponding to $2/(3\pi k_B T_0 \tilde{Z})$, and the intercept is $2Z\Gamma/\tilde{Z}$. The energy range used in this analysis was limited to $\hbar\omega \leq 36$ meV, and the largest temperature considered, T_{\max} , was allowed to vary down to $T_{\max} = 35$ K, below which the fitted temperature range becomes too small to produce reliable output. The result of the scaling collapse for $p = 2$ and $T \leq T_{\max} = 40$ K is displayed in Figure 4.24 (b). The root-mean square minimum for each T_{\max} defines p^* , shown as a function of T_{\max} in the inset.

When the range T_{\max} was decreased from 100 K to 35 K, p increased from 1.5 towards the plateau value $p = 2$, which is already approached for $T_{\max} \leq 50$ K. This confirms the expectation of a flow towards universal Fermi-liquid behavior for $T \rightarrow 0$, for which a collapse of all data on a universal function of ξ_p with $p = 2$ is expected. A similar analysis was conducted on the raw reflectivity data; for all temperatures $T \leq T_{\max}$ and all energies $\hbar\omega \leq 36$ meV, the reflectivity is plotted as $1 - R(\omega)$ as a function of $\xi_p^2 = (\hbar\omega)^2 + (p\pi k_B T)^2$, and the value of p which minimizes

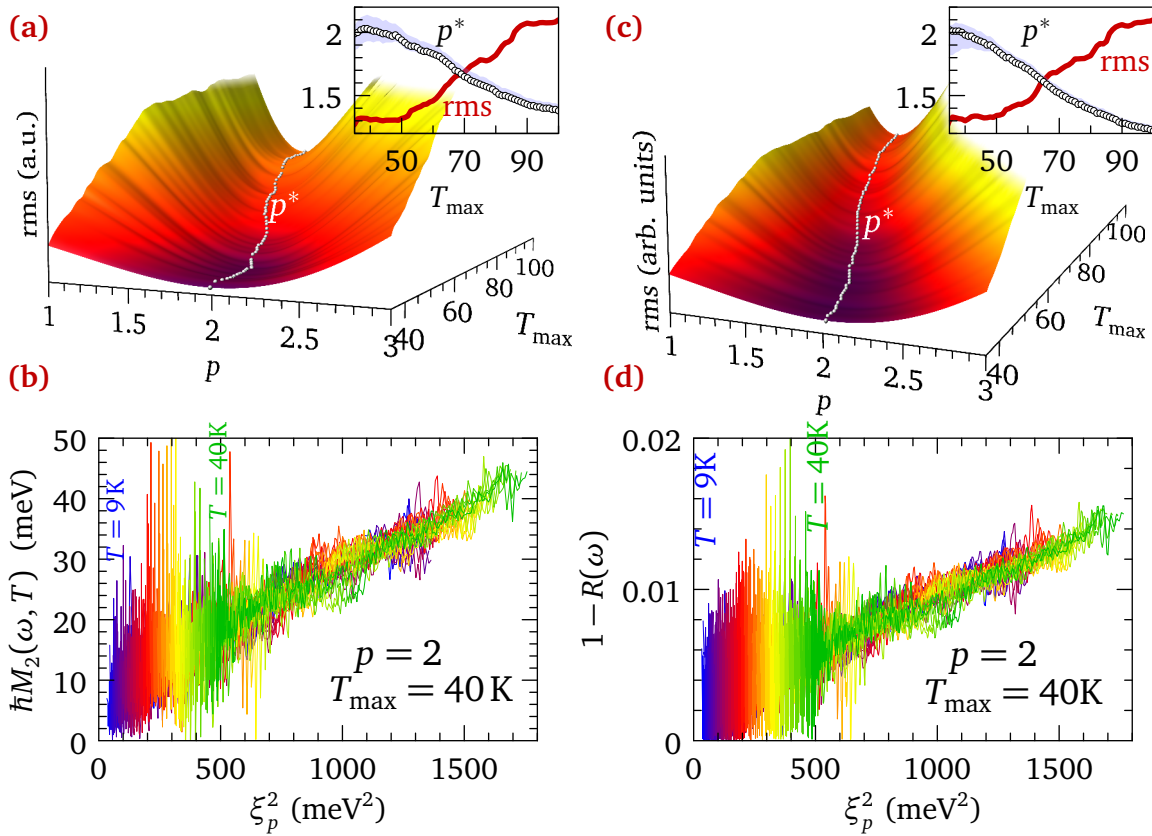


Figure 4.24: (a) Root-mean square deviation of the relaxation rate $M_2(\omega, T)$ from a linear dependence in ξ_p^2 , for $\hbar\omega \leq 36$ meV and $T \leq T_{\max}$, as a function of p and T_{\max} . The inset shows the value p^* and the root-mean square at the minimum versus T_{\max} . A value $p^* = 2$ is found below $T_{\max} \sim 40$ K. The shaded region shows how p^* changes if the energy range is varied by ± 5 meV. (b) Collapse of the relaxation rate data for $T \leq 40$ K. (c) and (d) Same analysis for the reflectivity data plotted as $1 - R(\omega)$. The linear correlation coefficient for the reflectivity scaling is 0.9.

4. LOW ENERGY OPTICAL RESPONSE OF Sr_2RuO_4

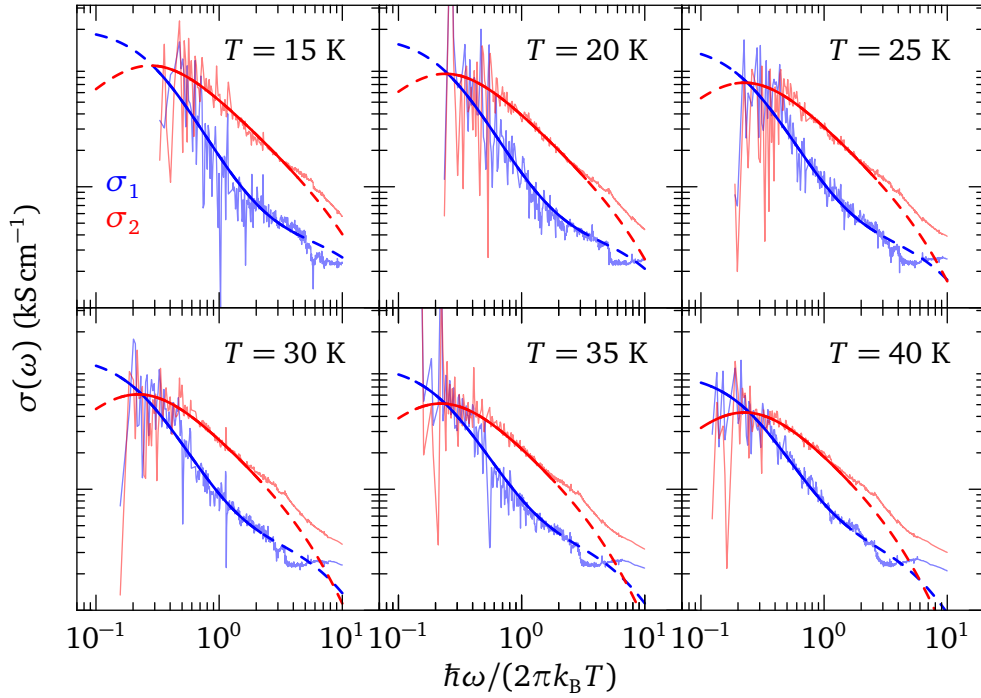


Figure 4.25: In-plane optical conductivity of Sr_2RuO_4 in the Fermi-liquid regime. The thin lines show the real (blue) and imaginary parts (red) of the measured conductivity. The thick lines indicate the fit to the Fermi-liquid model. The lines are solid in the energy range below $\hbar\omega \leq 36$ meV considered for the fit, and dashed outside this range.

the root-mean square deviation of the data from a straight line is determined. The result of this analysis is shown in Figure 4.24 (c-d) and leads to the same conclusion that $p = 2$. Note that the optimal value of p depends to some extent on the window of energies considered. Extending the window up and down by 5 meV leads to changes in the curve $p^*(T_{\max})$ as indicated in the inset of Figure 4.24 (a). With the reflectivity data, which is not affected by uncertainties of the Kramers-Kronig transformation, the curve is less sensitive to the energy window than with the memory function.

4.4.5 Thermal regime in the optical conductivity

In the energy and temperature domain where the above analysis points to Fermi-liquid behavior with $p = 2$, the real and imaginary parts of the Sr_2RuO_4 optical conductivity display a characteristic change of curvature around $\hbar\omega = 2\pi k_B T$. This is appearing most clearly as a shoulder in a log-log as shown in Figure 4.20: the low-energy Drude behavior of σ_1 changes to a weaker energy dependence for $\hbar\omega > 2\pi k_B T$. A similar change of slope was identified in Ref. [38] in the previous chapter to be a signature of the universal Fermi-liquid response. Adjusting the local-Fermi liquid model to the data in the domain $\hbar\omega \leq 36$ meV and $T \leq 40$ K, it provides a very good fit of the measured conductivity (see Figure 4.25). This should be regarded as an effective one-band description of the three-band response of Sr_2RuO_4 . The effective model

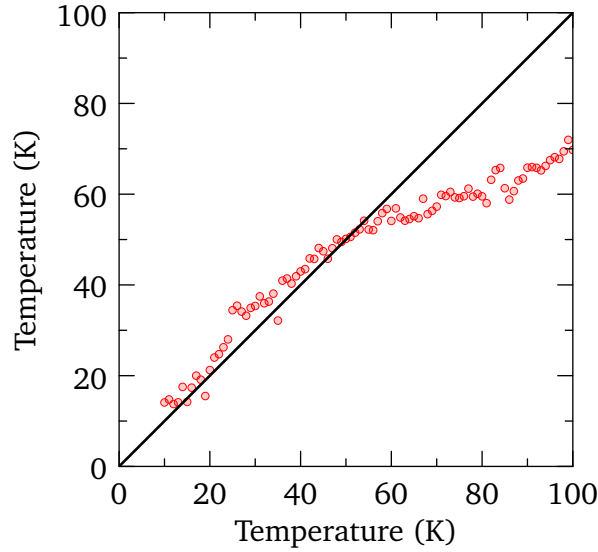


Figure 4.26: Fermi-liquid thermometry consisting of adjusting the temperature in the Fermi-liquid model of the real and imaginary $\sigma(\omega)$ to fit the experimental data.

parameters resulting from the fit are $T_0 = 316\text{ K}$, $\hbar^2 Z\Phi(0) = 3.5\epsilon_0\text{ eV}^2$, and $Z\Gamma = 0.9\text{ meV}$. The Drude weight $Z\Phi(0)$ corresponds to a plasma energy $\approx 1.87\text{ eV}$, in good agreement with the value of $\hbar\omega_{p1}$ obtained from the Drude-Lorentz analysis at $T = 9\text{ K}$. As expected, T_0 is about ten times larger than T_{FL} . Compared to the cuprates, the thermal "foot" of the optical conductivity is much more clear, which is mainly due to the onset of deviations appearing at about 55 meV compared to 33 meV found for the underdoped cuprates, but also by the fact that $T_{\text{FL}} \ll T_0$ which is not the case for the strongly underdoped samples.

Another way of seeing the deviation of the Fermi-liquid regime is to observe the departure in the temperature fit of the conductivity; This procedure is a sort of Fermi-liquid *thermometry*. First, the low-temperature best parameters (T_0 , $Z\Phi(0)$ and $Z\Gamma$) found below 23 K are used. Then, these parameters were fixed and the model of the optical conductivity was fitted to the experimental data by adjusting only the expected temperature. Figure 4.26 is a plot of the fitted temperature as a function of the real temperature of the sample. Here the departure appears at about 50 K , this is nearly equal to the temperature where $p^* = 2$ in the scaling analysis of the scattering rate. This technique is thus an adequate way of testing the temperature regime of Fermi-liquids but it could also be seen as a novel way of measuring the temperature of such materials by measuring their optical characteristics.

4.5 Numerical calculations

In this section, the optical conductivity is calculated within an *ab-initio* framework that combines density-functional theory (DFT) in the local-density approximation (LDA) as implemented in

Wien2k [263], with the many-body dynamical mean-field theory (DMFT) [264]. The calculation presented here were carried out by Georges, Mravlje and Deng as part of a collaboration on the optical properties of correlated electrons systems described in this thesis and in Ref. [265, 266].

4.5.1 DMFT + LDA

The Kubo optical conductivity in DFT+DMFT is expressed as

$$\sigma(\omega) = \frac{2\pi e^2}{\mathcal{V}} \sum_{\mathbf{k}} \int_{-\infty}^{\infty} d\varepsilon \frac{f(\varepsilon) - f(\varepsilon + \hbar\omega)}{\hbar\omega} \text{Tr} v_{\mathbf{k}}^x A_{\mathbf{k}}(\varepsilon) v_{\mathbf{k}}^x A_{\mathbf{k}}(\varepsilon + \hbar\omega). \quad (4.4)$$

This form of the Kubo formula is equivalent to Equation 1.98. \mathcal{V} is the normalization volume, $f(\varepsilon)$ is the Fermi function, $v_{\mathbf{k}}$ and $A_{\mathbf{k}}(\varepsilon)$ are the band velocities and the spectral functions, respectively, both evaluated at wave-vector \mathbf{k} . $v_{\mathbf{k}}^x$ and $A_{\mathbf{k}}$ are matrices in the band indices. The velocities are obtained from DFT as described in Refs. [263, 267], and the spectral functions are calculated as described in previous works [265, 268], using the same interaction parameters. The theoretical results are presented in Figure 4.27 as circles.

The overall shapes of experimental data and theoretical DMFT results match closely; satisfactory agreement is also found for absolute values. Note that the comparison in Figure 4.27 involves no scale adjustment. At low energy and low temperature, the *ab initio* calculations show a Drude peak and a thermal shoulder, in excellent agreement with the experimental data and with the Fermi-liquid model. The differences at the lowest energies can be attributed to impurity scattering, included in the Fermi-liquid model but not in the DMFT calculations, in order to keep the latter parameter-free. More interestingly, above 0.1 eV, the theory deviates from the Fermi-liquid model in precisely the same manner as the experiment does. At higher temperatures, while the predictions extrapolated from the low-temperature Fermi-liquid severely underestimate the conductivity, the agreement between DFT+DMFT and experiments remains excellent in the 0.1 eV to 0.5 eV range. However, the calculated imaginary part of the optical conductivity is systematically lower than the experimental data. The difference increases with the temperature and becomes clearer at 290 K. Electron-phonon interactions in fact cause additional mass-enhancement, which leads to a suppression of both σ_1 and σ_2 for $\omega \rightarrow 0$ and an increase of optical conductivity in the phonon energy range. This effect is not included in the DMFT calculations and may explain the remaining differences with experimental data.

4.6 Resilient quasiparticles

While optical conductivity is matching the expected Fermi-liquid regime below 0.1 eV, strong deviations are clearly identifiable in both the real and imaginary part of the optical conductivity

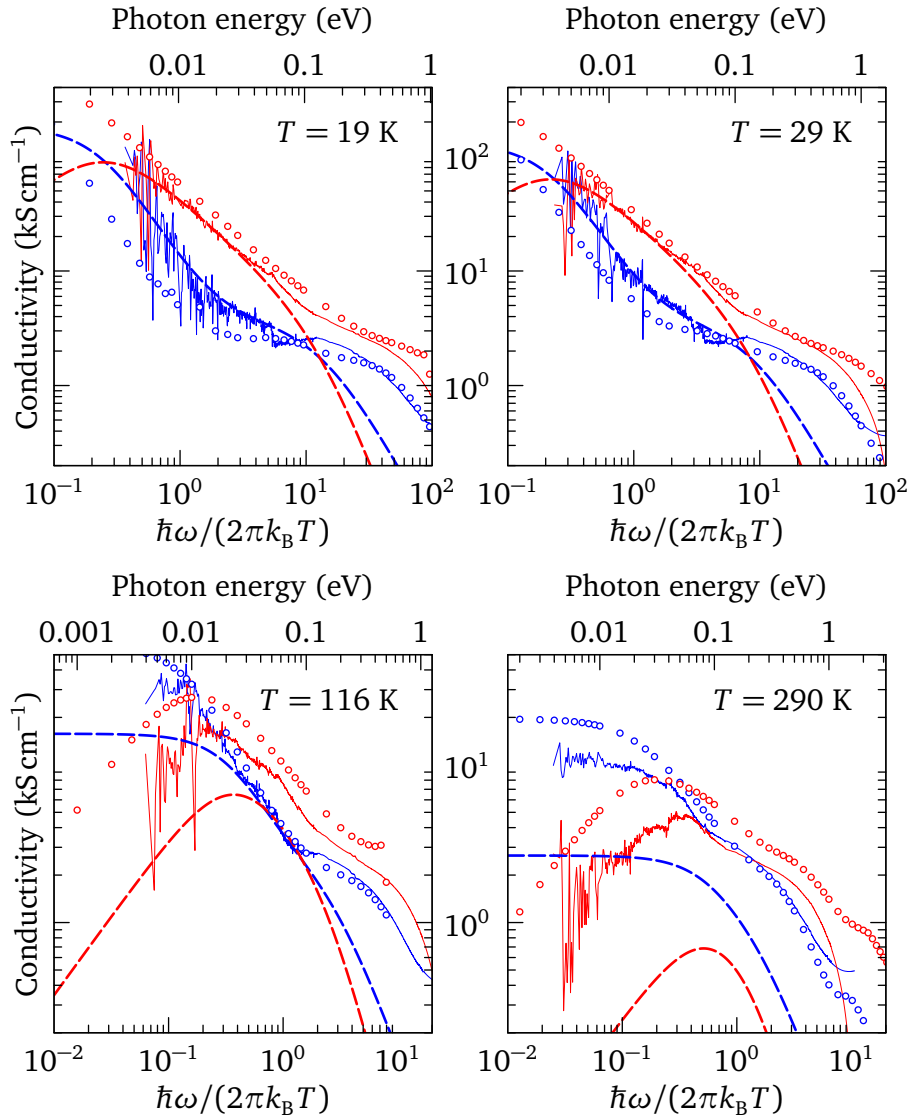


Figure 4.27: Comparison of the experimental optical conductivity (solid lines), Fermi-liquid model (dashed lines), and DFT+DMFT calculation (open circles) at selected temperatures. The real and imaginary parts of the optical conductivity are shown in blue and red, respectively. The three parameters of the Fermi-liquid model, including impurity scattering, are fit to the experimental data in the range $\hbar\omega \leq 36$ meV and $T \leq 40$ K.

4. LOW ENERGY OPTICAL RESPONSE OF Sr_2RuO_4

starting at about 50 meV. Affecting both experimental and numerical results in the same way at much lower energies than the first expected interband transition [20]. This excess spectral weight, in particular in 0.1 eV to 0.5 eV spectral range and/or temperatures above 40 K, is the fingerprint of the resilient quasiparticle excitations associated with unoccupied states. This confirms the recent prediction on the basis of dynamical mean-field theory (DMFT), that well-identified peaks in the spectral function persist far above the asymptotic low-energy and low-temperature Landau Fermi-liquid regime where the relaxation rate has a strict ω^2 dependence [189].

In order to provide a quantitative understanding of the deviations from Fermi-liquid behavior at higher energy and temperature and understand the nature of the strongly dispersing resilient quasiparticle excitations a series of numerical experiments were performed on the self-energy of the different bands.

4.6.1 Band velocities for the intraband conductivity

One can address the question whether the increase of optical conductivity for energies above 0.1 eV, with respect to the universal Fermi-liquid behavior, could be a consequence of the bare electronic dispersions. The possible effects of the band structure must be considered, because the density of states (DOS) of Sr_2RuO_4 has a rich structure at low energy, in particular, a Van Hove singularity about 70 meV above the Fermi level (see Figure 4.13). The quantity that is relevant for the optical properties is not the DOS, but the band structure enters the optical conductivity from the transport function $\Phi(\varepsilon)$ Equation 1.100, proportional to the average of the squared velocities at a given energy. As can be seen in Figure 4.13, the transport function is much more smooth than the DOS, and presents no significant feature at the energy of the Van Hove singularity. This can be understood, since the band velocity vanishes at the Van Hove points.

The absence of structure in $\Phi(\varepsilon)$ suggests that the excess conductivity above 0.1 eV is not due to the band structure. To be more quantitative, a simplified spectral function is constructed, taking for all orbitals the Fermi-liquid self-energy Ansatz (Equation 1.117) instead of $\Sigma_{\mathbf{k}}(\varepsilon)$ [38]. Parameters that fit the self-energy of the d_{xy} band at low energy for $T = 29$ K were used, namely, $1/Z = 5.12$ and $T_0 = 400$ K. This model reproduces the universal Fermi-liquid result if $\Phi(\varepsilon)$ is approximated by $\Phi(0)$. In Figure 4.28, a comparison is done on the real part of the conductivity obtained using the full energy dependence of $\Phi(\varepsilon)$ and the Fermi-liquid result. The energy dependence of the transport function does produce a deviation from the Fermi-liquid curve, but in the direction of a *smaller* conductivity, which is opposite to the experimentally observed deviation.

This analysis indicates that the excess spectral weight is, therefore, due to electronic correlations and must be linked to a structure in the single-particle self-energies and that the

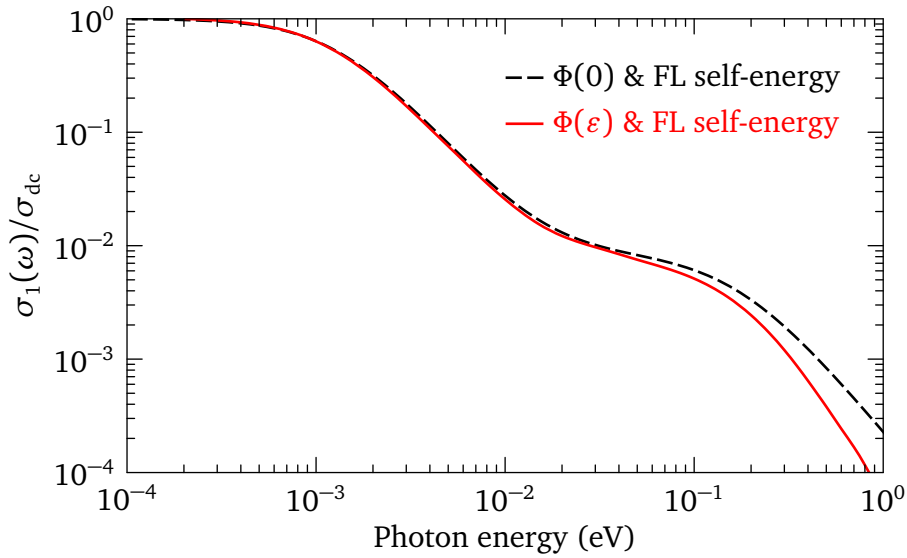


Figure 4.28: Role of the energy dependence of the transport function $\Phi(\epsilon)$. The solid line is the real part of the conductivity obtained by using the same Fermi-liquid self-energy, Equation 1.117, for the three t_{2g} bands. The dashed line is the universal Fermi-liquid result, where the energy dependence of $\Phi(\epsilon)$ is neglected.

replacement of $\Phi(\epsilon)$ by its Fermi-surface value $\Phi(0)$ causes no significant change in the theoretical curves of Figure 4.27.

4.6.2 DFT+DMFT self-energies

The local DMFT self-energies for the d_{xy} and d_{xz}/d_{yz} orbitals are shown in Figure 4.30. At low energy, both follow the Fermi-liquid behavior, with a parabolic dependence of the imaginary part and a linear dependence of the real part. As discussed earlier [268], the d_{xy} orbital is more correlated, with steeper real part and stronger curvature of the imaginary part.

The self-energies start to deviate from strict Fermi-liquid behavior in the direction of a weaker scattering already at low energy and in particular, between 0.2 eV to 0.4 eV above the Fermi energy, which is still in the domain of intraband transitions. The electron-hole asymmetry becomes markedly at high energy where the hole-scattering rate goes through a maximum at around 0.3 eV and decreases slightly at higher energy. A similar phenomenon with a saturation of the scattering rate was observed in the single-band Hubbard model and was shown to give rise to resilient quasiparticles [189]. The deviation is also seen in the real part, whose differences with Fermi-liquid become substantial above 0.05 eV, especially on the electron side, where a drastic change of slope is observed.

Above 0.35 eV the signature of resilient quasiparticles is even more striking: It is signaled by a drop of the scattering rate for empty states. Consistently with Kramers-Kronig relations, this drop implies a sharp minimum in the real part of the self-energy which is found in the energy range 0.1 eV to 0.15 eV. As a consequence, quasiparticles above this energy scale have

4. LOW ENERGY OPTICAL RESPONSE OF Sr_2RuO_4

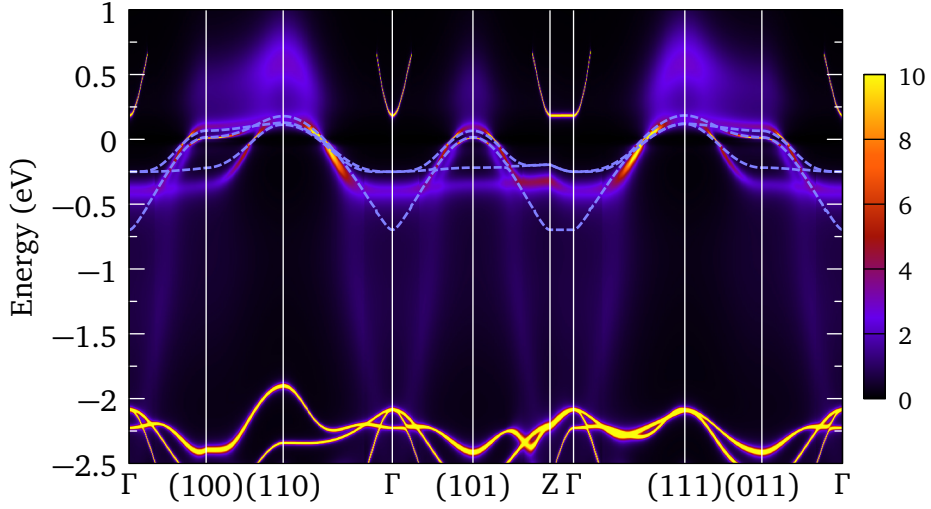


Figure 4.29: Color map of the k -resolved spectral function. The LDA t_{2g} bands are renormalized by a factor of 4, they are shown as dashed lines.

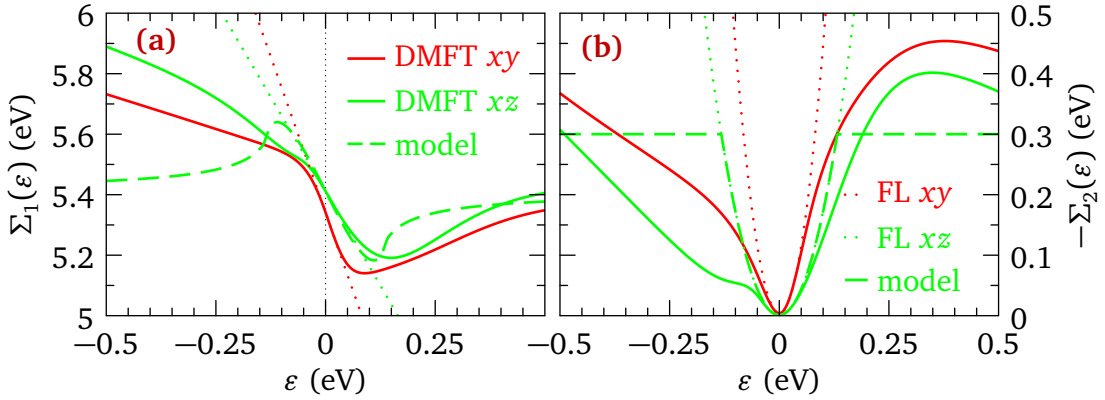


Figure 4.30: Local self-energies for the d_{xy} and d_{xz} bands at $T = 29\text{K}$. **(a)** The real part is linear at low energy. **(b)** and the imaginary part (bottom) is quadratic, as shown by the dotted lines. The dashed lines show a model with bounded quadratic imaginary part, and the corresponding real part.

velocities larger than the bare velocities. In the theoretical spectral function, these appear as peaks which are broader than the low-energy Landau quasiparticle peaks and have a very steep dispersion in the range 0.2 eV to 0.4 eV, leading to an inverted waterfall-like structure that can be seen in Figure 4.29.

Figure 4.30 displays a simple model for the self-energy with an imaginary part, which is purely quadratic up to a cutoff energy $\varepsilon_c = 0.125\text{ eV}$, and constant with a value $\gamma_c = -0.3\text{ eV}$ above this cutoff. The corresponding real-part, displayed in Figure 4.30, is obtained by Kramers-Kronig relations as:

$$\text{Re } \Sigma(\varepsilon) = \frac{\gamma_c}{\pi} \left(\frac{\varepsilon^2}{\varepsilon_c^2} - 1 \right) \ln \left| \frac{\varepsilon - \varepsilon_c}{\varepsilon + \varepsilon_c} \right| + \frac{2\gamma_c}{\pi} \frac{\varepsilon}{\varepsilon_c}. \quad (4.5)$$

This model reproduces the main qualitative aspects of the data, especially the strong feature in the real part.

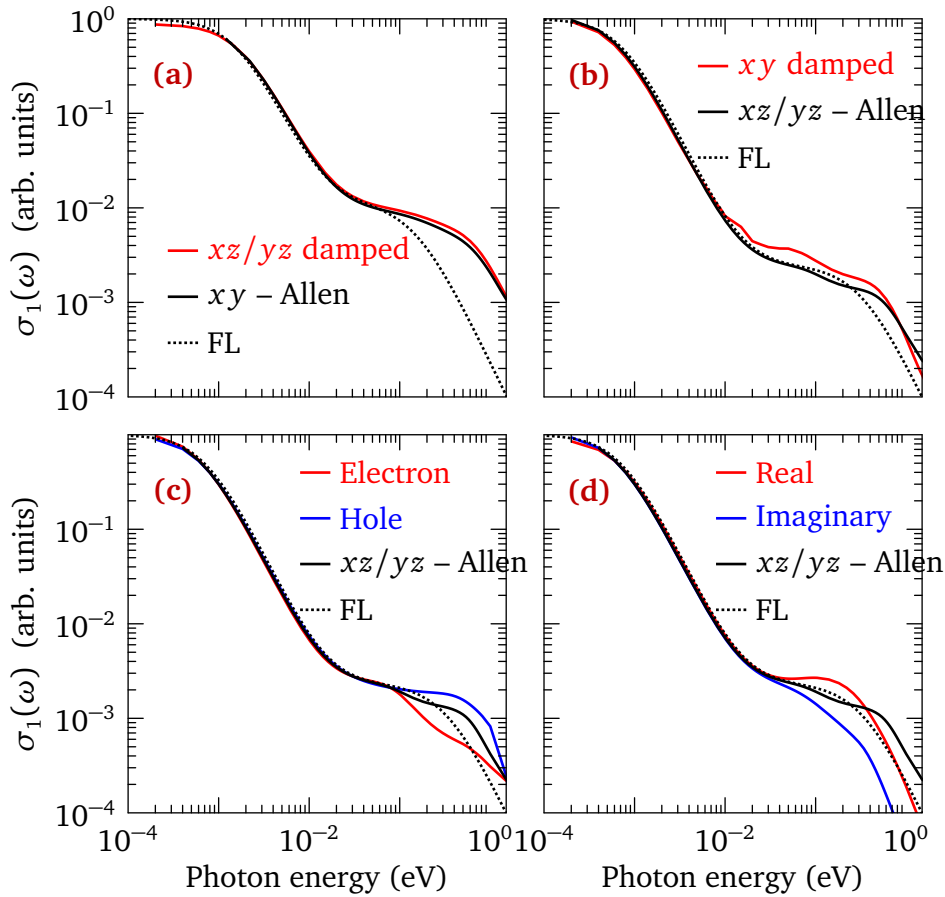


Figure 4.31: (a) optical conductivity obtained from Equation 4.4, after suppressing the contributions of the d_{xz}/d_{yz} orbitals (red), compared with the result of Allen formula Equation 1.101 evaluated with the self-energy of the d_{xy} orbital (black), and with the universal Fermi-liquid curve (dotted). (b) Same as (a), with the roles of d_{xy} and d_{xz}/d_{yz} exchanged. (c) Contribution of the d_{xz}/d_{yz} orbitals (d_{xy} damped), with modified self-energies having either electron, or hole character. (d) Contribution of the d_{xz}/d_{yz} orbitals (d_{xy} damped), with modified self-energies having DMFT real part and Fermi-liquid imaginary part (Real) or Fermi-liquid real part, and DMFT imaginary part (Imaginary).

4.6.3 Orbital dependence

It is convenient to look separately at the contribution of each orbital to the conductivity. It was done in two ways: first Equation 4.4 was evaluated using spectral functions in which one of the orbitals was heavily damped, by adding a very large imaginary part to its self-energy; then the optical conductivity is calculated using the Allen formula Equation 1.101 and the local self-energy of each band independently. The results are displayed in Figure 4.31 (a-b). For both orbitals, a deviation from Fermi-liquid is seen above 0.05 eV to 0.1 eV, in the direction of an increased conductivity. One also sees that the Allen formula describes the data reasonably well. The next step is to investigate which of the electron or hole part of the self-energy plays the key role in the extra conductivity. For this purpose, the particle-like orbital self-energy $\Sigma_p(\varepsilon)$ was defined, whose dependence at negative energy is obtained by the reflection of the

4. LOW ENERGY OPTICAL RESPONSE OF Sr_2RuO_4

positive-energy dependence. For the imaginary part, $\Sigma_{p2}(\varepsilon) = \Sigma_2(|\varepsilon|)$, and for the real part, $\Sigma_{p1}(\varepsilon < 0) = 2\Sigma_1(0) - \Sigma_1(-\varepsilon)$, $\Sigma_{p1}(\varepsilon > 0) = \Sigma_1(\varepsilon)$. Similarly, hole-like self-energies are constructed by a reflection of the negative-energy data to positive energy. The resulting optical conductivities (contribution of the d_{xz}/d_{yz} orbitals) are presented in Figure 4.31 (c), from which it is evident that the electrons (particle-like states of positive energy), rather than the holes, give rise to the extra spectral weight.

Lastly, an investigation was done whether the extra conductivity must be ascribed to the real, or to the imaginary part of the self-energy. For this purpose, a trial self-energy is constructed by replacing the real or imaginary part of the DMFT self-energies with their low-energy Fermi-liquid extrapolations (in strong violation of Kramers-Kronig relations). The result is shown in Figure 4.31 (d). One sees that keeping just the DMFT imaginary parts leads to a pronounced downward deviation from the Fermi-liquid result. Only when the nonlinear real parts are included does a deviation in the upward direction appear. This deviation, however, quickly dies off with such trial self-energies that violate the Kramers-Kronig relations. The reason is the rapid increase of scattering, as the Fermi-liquid result has already entered the dissipative regime, where increasing $|\Sigma_2|$ diminishes the conductivity.

The deviation from Fermi-liquid dependence can be reproduced qualitatively by means of the model self-energy shown in Figure 4.30. This self-energy has a quadratic imaginary part at low energy, $-\Sigma_2(\varepsilon) \propto \varepsilon^2 + (\pi k_B T)^2$ for $|\varepsilon| < \varepsilon_c$, followed by a saturation for $|\varepsilon| > \varepsilon_c$. The real part obtained by Kramers-Kronig displays sharp kinks at ε_c . As shown in Figure 4.32, this very rough model reproduces the data quite well. The description can be improved if the parabolic dependence of the imaginary part is kept at negative energies and saturation is only imposed on the positive side.

4.6.4 Discussion

The essence of the departure from the Fermi-liquid form is thus related to the sharp saturation of the scattering rate on the positive energy side, and the related sharp feature in the real part at a scale of 0.1 eV. The pronounced action takes place on the electron (positive energy) side. The saturation of the scattering rate and the associated robust dispersing resilient quasiparticle excitations were found in the context of the Hubbard model [189]. Strikingly, in Sr_2RuO_4 this saturation occurs in a more pronounced way and leads to a strong change of slope of the real part of the self-energy. The consequences of this change of slope can be most directly seen in the colormap of the \mathbf{k} -resolved spectral function, that is presented in Figure 4.29. Superimposed are also the LDA t_{2g} bands that are renormalized by a factor of 4. Whereas at low energies these renormalized bands describe the data reasonably well, above ≈ 0.1 eV (below -0.5 eV) the dispersion abruptly increases, giving rise to the pronounced inverted waterfall structure.

Above those energies, broad and strongly dispersing resilient quasiparticle excitations appear

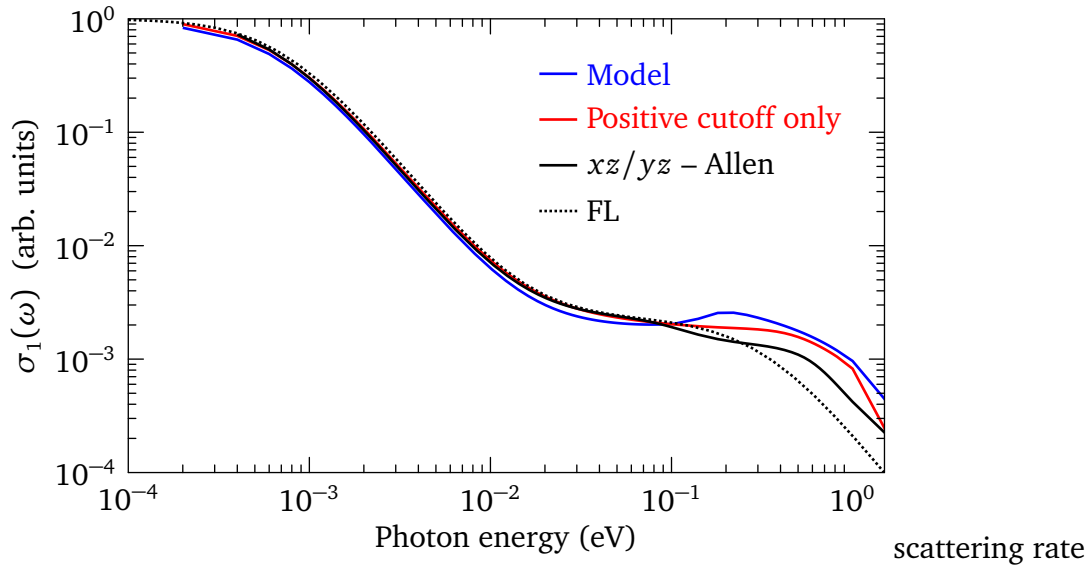


Figure 4.32: Optical conductivities calculated using the Allen formula Equation 1.101 with the model self-energy of Figure 4.30 (blue), and the self-energy of the d_{xz}/d_{yz} orbitals (black), compared with the Fermi-liquid result (dotted). The red curve is obtained by sending the negative-energy cutoff of the model self-energy to $-\infty$.

very clearly in the k -resolved spectral function. The excess conductivity found in the experiment and in DFT+DMFT calculations is thus a consequence of highly dispersive states that exist above the Fermi energy. This is also reflected in the memory function, that is shown in Figure 4.33. The change of slope that appears due to the resilient quasiparticle states is seen clearly in the real part of the theoretical and experimental memory function.

We also note that more subtle changes in quasiparticles dispersions (kinks) at ≈ 30 meV, previously found in both ARPES [257, 269] and DMFT [268], are also visible in M_1 and M_2 at lower energy but do not change the energy dependence of the optical conductivity so strikingly.

The resilient quasiparticle excitations above the Fermi level predicted by the calculations

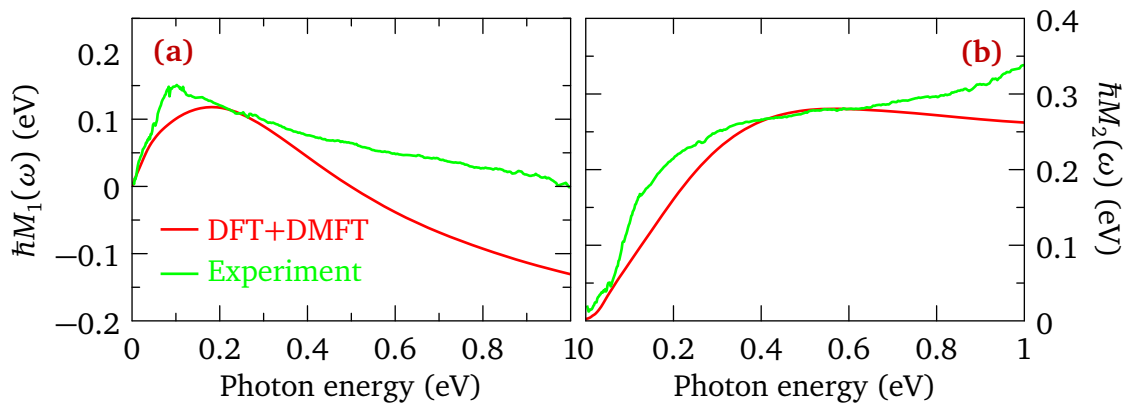


Figure 4.33: Comparison of the memory function from theory and experiment at low temperature. The memory function was constructed using the experimentally determined $\hbar\omega_p = 3.3$ eV.

and leading to the sharp feature in M_1 are not directly accessible to conventional ARPES, which probes only occupied states. Recently, two-photon ARPES has been shown to provide energy and momentum-resolved information on unoccupied states [270], and it could be interesting to put the theoretical results (Figure 4.29) to the test in the future by using this technique for Sr_2RuO_4 .

4.7 Phonon splitting in the c -axis spectra of Sr_2RuO_4

Shown in Figure 4.16, the c -axis reflectivity of the Sr_2RuO_4 Tc134 illustrates the three c -axis phonons whose structure is split in two distinct modes. In this section, the c -axis phonons of the three samples are analyzed in detail. Comparing the results with data found in the literature, it will be shown that the splitting is present, to some extent, in all samples. Different scenarios will be presented, notably strain effects, oxygen vacancies, or intercalation of the other members of the Ruddlesden-Popper series ruthenate family.

The first section discusses the c -axis phonon spectra measured in reflectivity experiments. The Fano model is introduced in order to fit the different phonon in the spectra. The second section discusses Raman spectroscopy experiments. The third section presents a bulk characterization of the Tc134 ac -plane using scanning electron microscope (scanning electron microscope), X-ray structure analysis and magnetometry. Finally, conclusions are made on the nature of the splitting of the c -axis phonons.

4.7.1 Optical phonon of the single layer ruthenate

The phonon analysis is a complete study in its own as shown by numerous studies in the domain [271–274]. This section introduces the necessary elements for understanding the optical phonons in the Sr_2RuO_4 . For a more detailed study, the reader can find additional information in Ref. [271].

As a reference material for the large class of transition metal oxides, Sr_2RuO_4 has a perovskite structure with an interesting anomalous phonon dispersion, which could be put in parallel with its unconventional superconductivity. This material seems to show a normal in-plane bond-stretching dispersion, while its c -axis features indicate electron-phonon coupling which produces a softening of the phonon mode and requires an extended description of their energy dispersion through the Fano model [271].

In the tetragonal K_2NiF_4 structure, 21 phonon modes are expected and 7 shown in Figure 4.34. These modes are sorted in accordance to the irreducible representations, with different main-symmetry directions. In this study the modes of interest are grouped into the A_u , A_g , E_g and E_u representations and are polarized along the Λ (c -axis) direction. It is also interesting to introduce the O_{zz} mode which is not optical active but is the c -axis polarized analogue of the

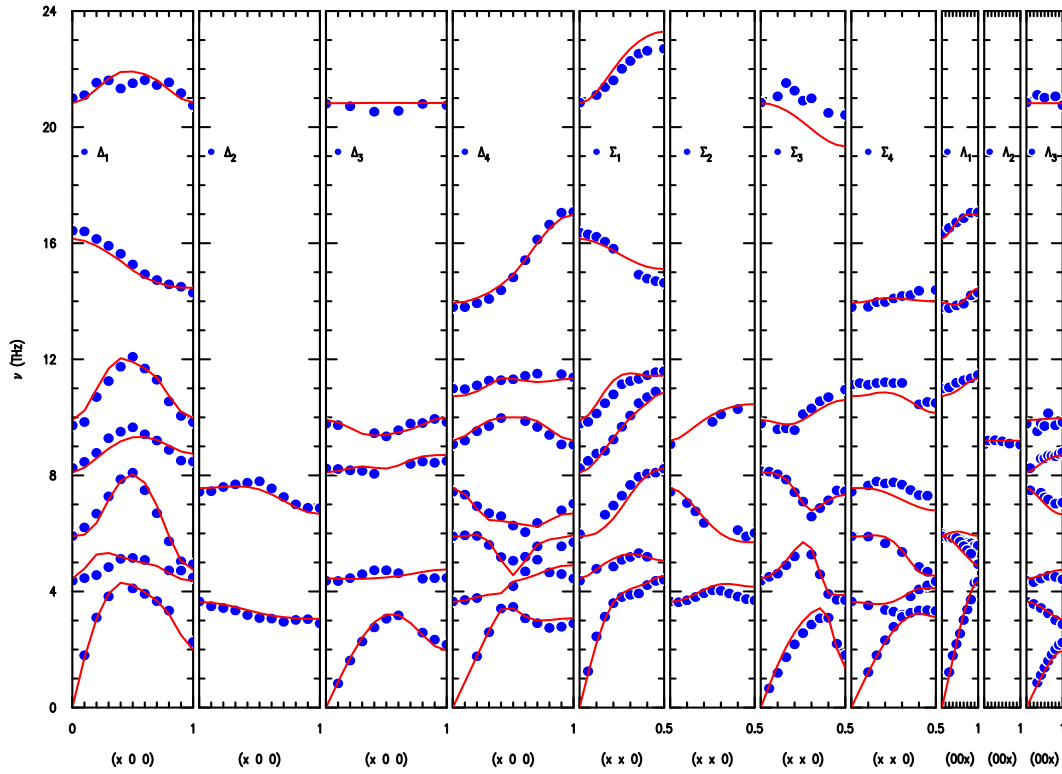


Figure 4.34: Phonon dispersion in Sr_2RuO_4 from Braden *et al.* [271]. The blue points represent the neutron scattering data while the line are the lattice dynamical model presented in their study. The A_g , A_u and E_g mode are included in the $[00x]$ Λ representation.

linear breathing mode; this mode has a very large electron-phonon coupling. The modes are at the Brillouin-zone center while the O_{zz} mode is at the Z point. Four phonon modes are Raman-active, two A_g and two E_g mode [271, 274]. The A_g phonon modes are the vibrations of the strontium and the apical oxygen along the c -axis; these modes are presented in Figure 4.35 (b). Using infrared spectroscopy, the expected phonons are either the in-plane double degenerated bond stretching E_u seen at 83 meV in Figure 4.16 or the c -axis polarized A_u . The A_u modes are shown in Figure 4.35 (a). An additional silent mode B_u is also expected [275].

4.7.2 Optical spectroscopy

4.7.2.1 Fano lineshape

When the electronic background is sufficiently high ($\epsilon_2 > 0$), the asymmetry of the phonons can be phenomenologically described by a modification of the standard Lorentz oscillators [276]. The Kramers-Kronig relations has to remain consistent has well as the $\omega \rightarrow -\omega$ symmetry relation and the sum-rule of section 1.2.1.1. Such requirement where developed in [277, 278]

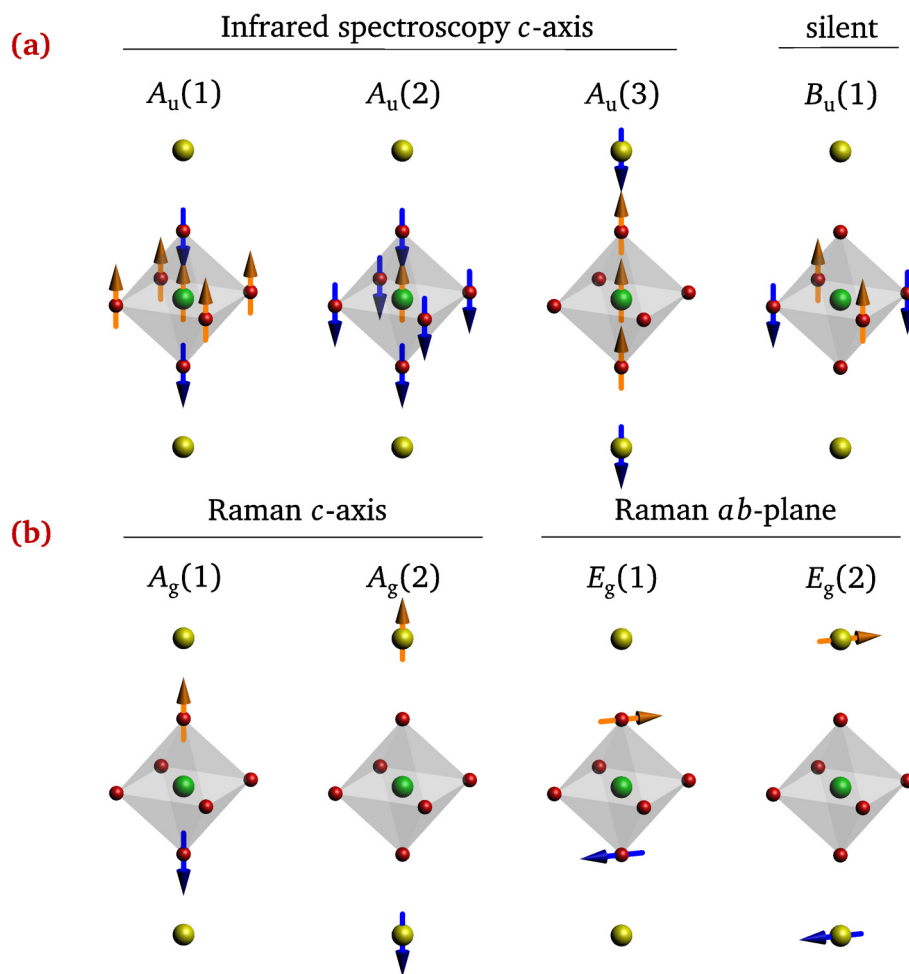


Figure 4.35: Representation of polarized zone-center (Γ) bond stretching modes. (a) The A_u optical modes and B_u silent mode. (b) Raman c -axis A_g and ab -plane E_g modes.

through the following Fano-shaped Lorentz oscillator

$$\epsilon = \frac{\omega_p^2}{\omega_0^2 - \omega^2 - i\gamma\omega} \left(1 + i \frac{\omega_q}{\omega} \right)^2 + \left(\frac{\omega_p \omega_q}{\omega_0 \omega} \right)^2 \quad (4.6)$$

The asymmetric parameter is defined as $q = \omega_0/\omega_q$. The standard symmetrical Lorentzian is recovered by taking the limit $\omega_q \rightarrow 0$ or $q \rightarrow \infty$.

4.7.2.2 Comparison with the literature

The comparison with the data found in the literature is presented in Figure 4.36. The top graph (a) presents the real part of c-axis optical conductivity for the three samples of this study (Tc134, Tc128 and C362). The bottom graph is the c-axis reflectivity with additional data of the literature. The three-phonon structures are labeled A_i , B_i and C_i , with $i = 1, 2$ numbering the splitted phonons. At a first sight, C362 shows strong and sharp peaks, while Tc134 and Tc128 have much broader phonons. In fact, the structure of the phonon peak is doubled and asymmetric in all cases. If the C_i splitting is easy to observe in the case of sample Tc134 and Tc128, the C362 crystal has also a second peak C_2 , which has a much smaller strength. Whereas this structure tends to be more prominent for the last phonon, the lowest lying phonons also have the effect proportional to their strength.

Turning now to the literature, the reflectivity data of different studies is summarized in Figure 4.36 (b) [71, 77, 273] and is compared at low temperature (except the data of Katsufuji *et al.* that is only at room temperature). Here again, the structures are all different. The data of Hildebrand *et al.* was taken on the 3K-phase of Sr₂RuO₄. The low reflectivity is flat compared to the pure samples. Although this data is limited to 25 meV, it demonstrates that the 3K-phase is not present in sufficient quantity to have an impact on the reflectivity of the pure crystals. In addition, Pucher *et al.* [279] noticed the splitting of the high-energy phonon and shown that the 4P-oscillator presented in [280] was not adequate to fit the structure. From the strength of the two modes, they also excluded splitting by misalignment of the crystal. It is interesting to see that their plasma edge, at about 10 meV, is much less steep compared to the other pure samples which would indicate that the effect seen in the phonon might also affect the c-axis electronic properties. The C_i phonons are almost identical to the ones of the C362 sample except the tail at about 75 meV. Finally the data of Katsufuji *et al.* were only shown at room temperature and up to the energy of the B_i phonon. It is indeed indicating a broadened phonon structure. Unfortunately without knowing precisely the samples composition, it is impossible to assess a quantitative comparison between the samples. However with an almost similar critical temperature, the difference seen in the splitting of phonons point to the fact that this effect is not affecting the superconducting phase.

4. LOW ENERGY OPTICAL RESPONSE OF Sr_2RuO_4

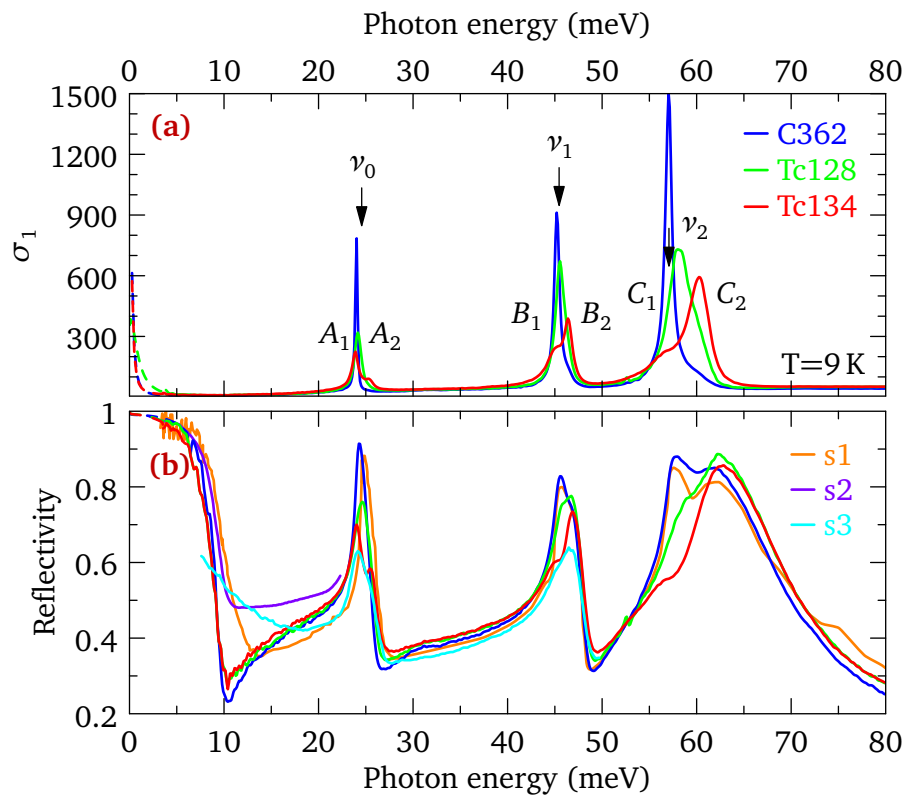


Figure 4.36: Comparison of the three splitted A_u optical phonons for different samples measured in this study (Tc134, Tc128 and C362) and in the literature. **(a)** Real part of the optical conductivity. The A_1 to C_2 labels refers to the splitted phonons. ν_0 , ν_1 and ν_2 are the phonon energies seen in neutron experiments [271]. **(b)** s1, s2 and s3 are reproduced from the literature. s1 is reproduced from a 5 K reflectivity curve of [273,279]. s2 is reproduced from [71] and represent the reflectivity of the 3K-phase of Sr_2RuO_4 measured at just above T_c . s3 is reproduced from [77] and is a measurement at room temperature.

4.7.2.3 Phonon fitting

The Drude-Lorentz fitting procedure was done in RefFIT for the three samples. For Tc134 the model was made out of one Drude component D_0 , two intraband components D_1 and D_2 , six Lorentz oscillators for the phonons and one interband I_1 at about 1.3 eV. For the B_2 and C_2 phonons, a Fano line shape was required. It is not certain if the Fano line shape is only helping to fit the unconventional shape of phonon splitting or is a real feature. However as a result of the fit, the asymmetry parameter q of B_1 and C_1 was always tending to infinity, which indicates that a Fano line-shape was not required for these phonons. The comparison of the phonon parameters is shown in Figure 4.37. The first phonon splitting is only clearly observed for Tc134, while no noticeable effects were obtained. In most of the cases, the phonons of Tc134 have the smallest mode energy, followed by C362 and then Tc128. The separation of these mode goes from 0.5 meV for A_1 , to 1.5 meV for C_1 . For B_2 and C_2 C362 has by far the most symmetric shape. Turning to the strength of the phonons indicate that phonon B_i and C_i shows about the same ratio of strength $B_1/B_2 \approx C_1/C_2$ for the Tc134 and C362 samples, whereas the first phonon has an opposite trend.

Next, the temperature dependence of all parameters is shown in Figure 4.38. In order to reduce the noise, the parameters shown are binned in 10 K intervals. As a confirmation of the fit quality, the total model, and the data is shown in Figure 4.39, the squared error χ is shown in the top Figure 4.39 (a) and point that the fit quality is very good down to about 25 K. The difference of reflectivity shown in graph (b) illustrates the remaining feature that the model missed. Better shown as a difference of conductivity (see Figure B.1 in the appendix), the difference of conductivity is symmetric around each phonon; this is an indication that the model reproduce the key features of the data.

Comparing the temperature dependence of the phonons, B_1 and B_2 but also C_1 and C_2 does not have the same temperature dependence. However, B_1 and C_1 have surprisingly the same trend, which is connected to the Drude peak. This is mostly seen in the width of the phonons, but the temperature behavior of their strength and energy also indicate a rather broad change at 150 K. On the other hand, B_2 and C_2 are also linked, but the link with the Drude peak is less clear.

Given the number of parameters, it is not possible to draw firm conclusions. But the fit certainly indicates that each phonon can be identified individually suggesting that they are not emerging from a random inhomogeneous structure distortions which would broaden the phonon peak. It was recently shown in EuTiO₃, that if the TiO₂ allowed tilting, the oxygen vacancies were able to displace the titanium cations not only around the vacancy but also in other neighboring titanium which has the effect of breaking the local inversion symmetry [281]. In this respect, the presence of titling was observed in (Sr_{2-x}Ca_x)RuO₄, which indicates that Sr₂RuO₄ may have a natural tendency to allow the tilting of the octahedron [282], which may

4. LOW ENERGY OPTICAL RESPONSE OF Sr_2RuO_4

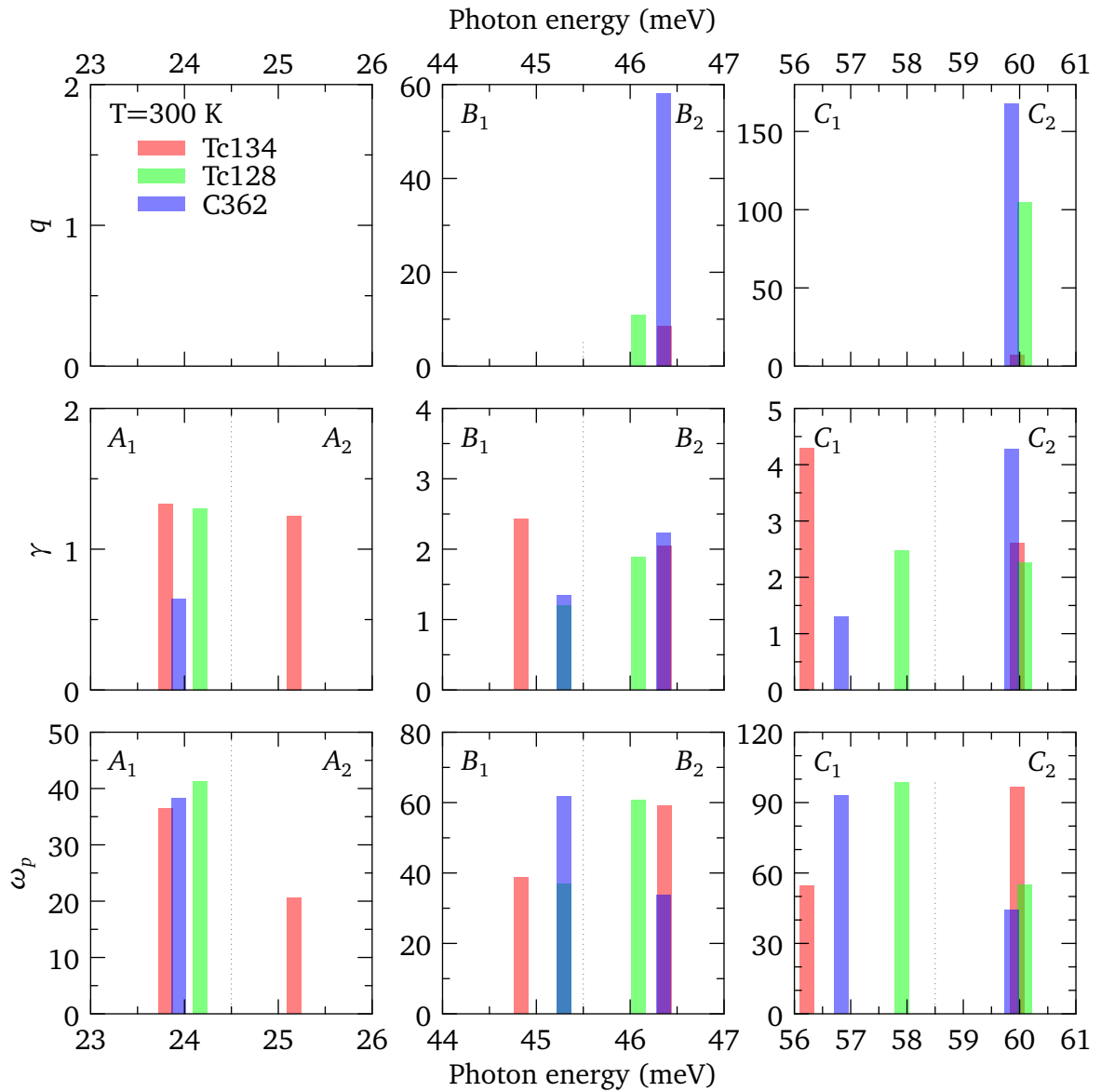


Figure 4.37: Comparison of the phonon parameters at room temperature and for the three samples measured in this study. In each graph, the two phonon modes are shown and separated by a dashed line; the phonon energy is encoded in the histogram. The top row presents the asymmetry parameter q , the second row γ and the third row the phonon strength ω_p .

4.7 Phonon splitting in the c-axis spectra of Sr₂RuO₄

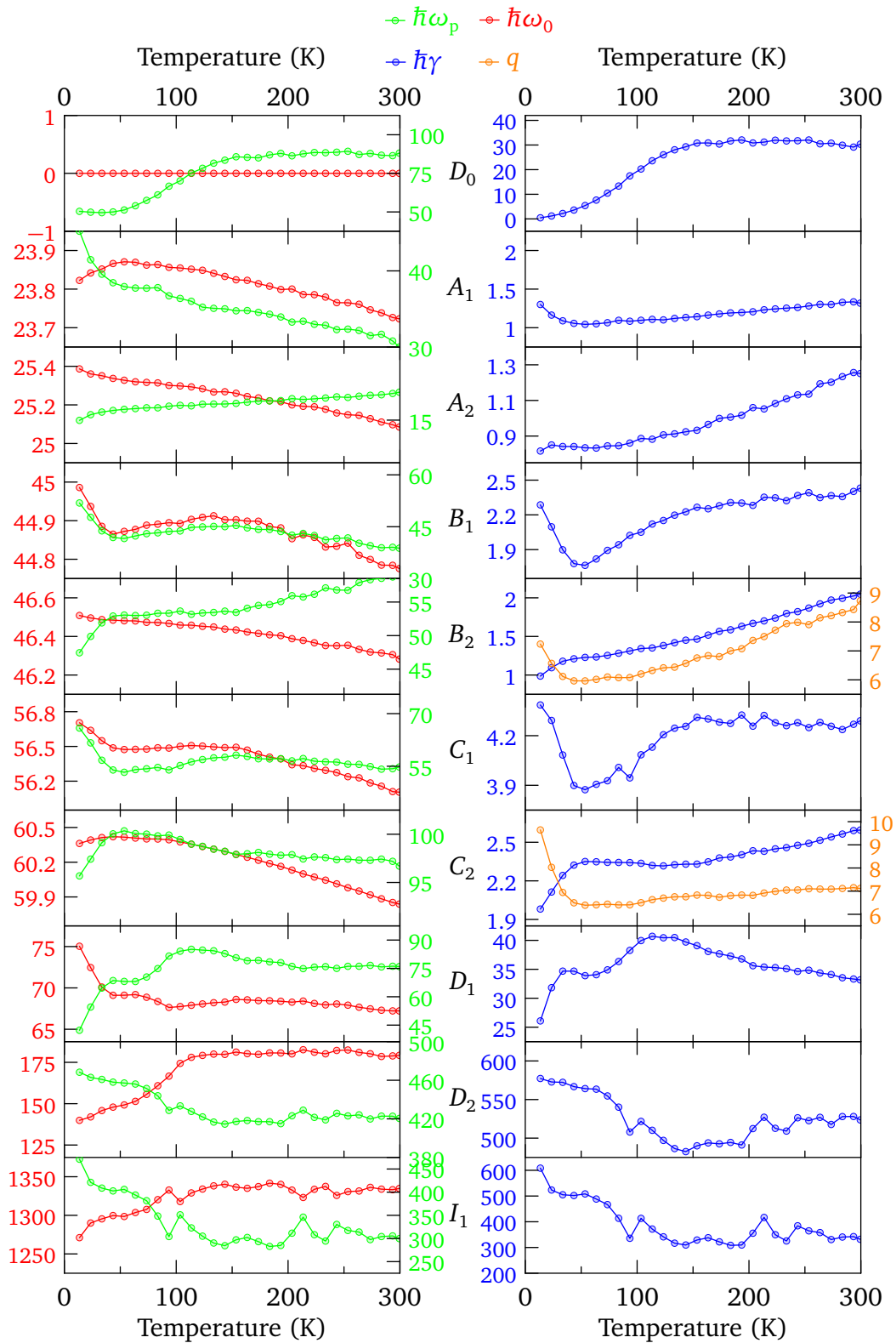


Figure 4.38: Temperature dependence of the Drude-Lorentz fit to the c-axis reflectivity of Sr₂RuO₄ Tc134 sample. In order to reduce the noise the parameters were binned in 10 K intervals. The asymmetry parameter q is shown when a Fano oscillator was used in place of the standard symmetric phonon. All parameters except q , which is dimensionless, are given in units of meV.

4. LOW ENERGY OPTICAL RESPONSE OF Sr_2RuO_4

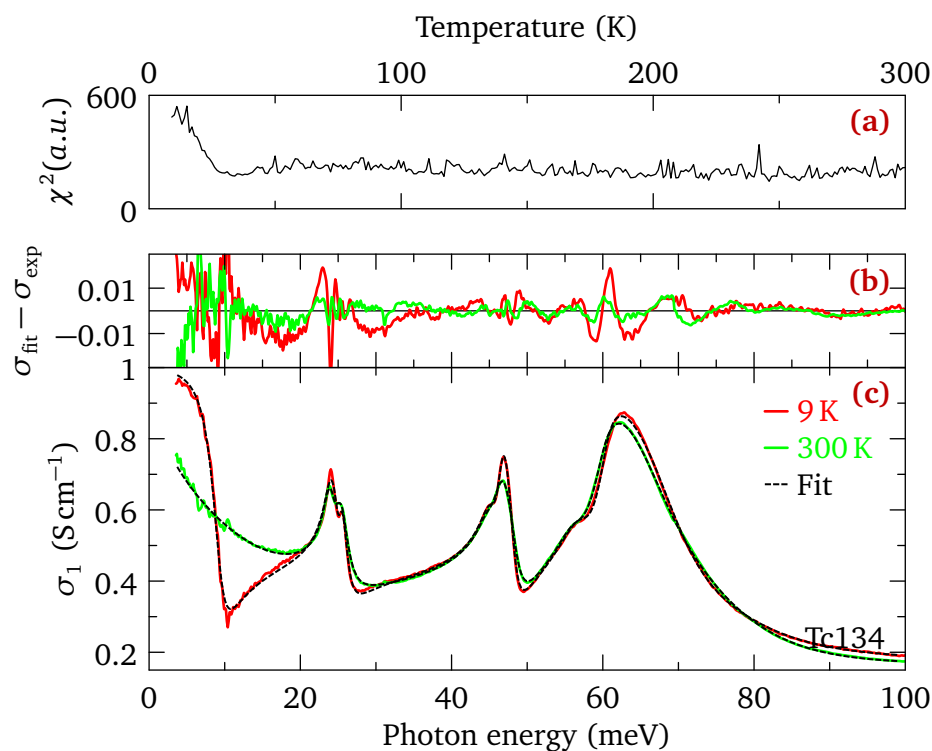


Figure 4.39: Comparison between the reflectivity fit and the experimental data of sample Tc134.

in turn allows for the displacement of the ruthenium cation. However Sr_2RuO_4 in itself seems to accept oxygen vacancies only if the strontium gets substituted by dopants [25] which forbids the scenario of having sizeable amount of oxygen vacancies. On the other side, $\text{Sr}_3\text{RuO}_{5+x}$ is another impurity phase, which could be intercalated with Sr_2RuO_4 and present oxygen vacancies. Introduced by Mao et al. [234] this material is an insulating Sr_3WO_6 non-standard double perovskite structure.

4.7.2.4 Raman spectroscopy

The ac surface of samples Tc134 and C362 was measured at room temperature with a home-made micro-Raman spectrometer. The surface characterization was performed with a 50x magnification while the overall defect size were measured using the 5x and 20x lenses. The photon energy of the incoming monochromatic light was 2.41 eV (514.5 nm). The Raman Stokes lines were recorded using liquid N_2 cooled CCD detector coupled to a Czerny-Turner monochromator between 10 meV to 105 meV. Using the two linear polarizers, one for the incoming light and one on the detector, the measurement was performed on the ac surface of the samples in four different geometries: $k_i(p_i, p_s)k_s$. the Porto's notations stands with k and p , the direction of propagation and polarization of the incoming (i) and scattered (s) light. The four room temperature Raman spectra, $b(c, c)\bar{b}$, $b(c, a)\bar{b}$, $b(a, c)\bar{b}$ and $b(a, a)\bar{b}$ are shown in Figure 4.40, for sample Tc134 and C362. The c -axis is totally included in the surface, the

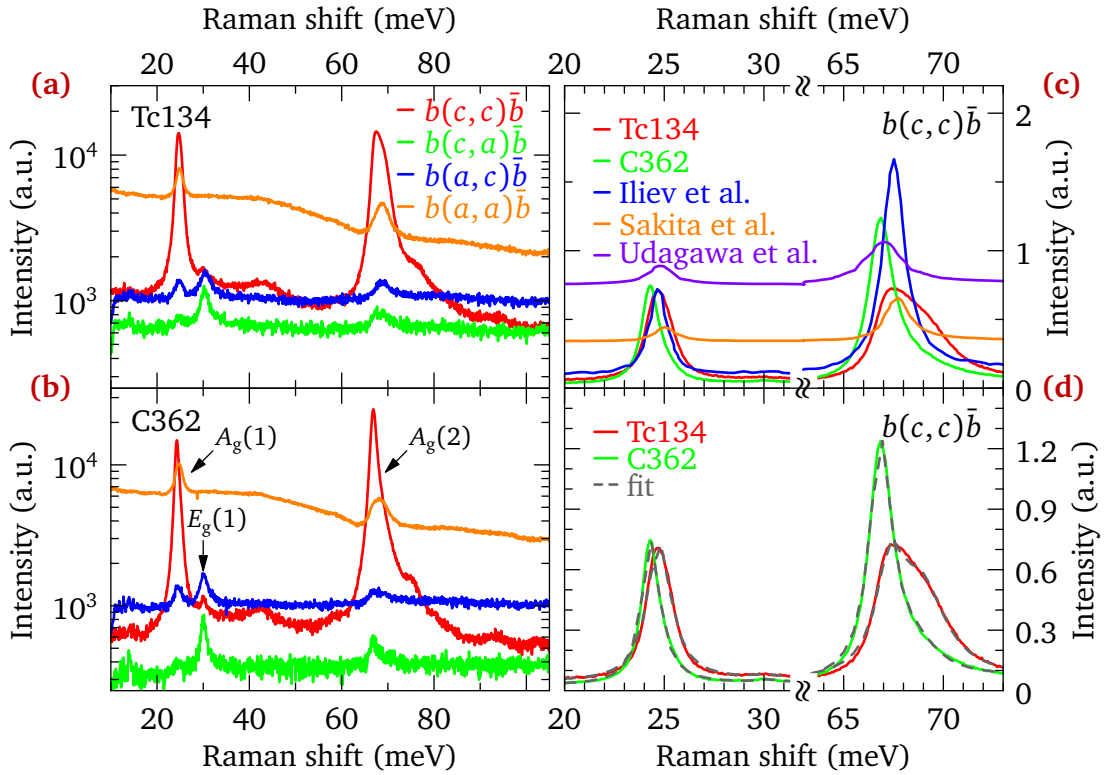


Figure 4.40: Raman spectra of Sr₂RuO₄. *ac*-plane surface of Tc134 (a) and C362 (b) at room temperature for four different geometries of measurement. (c) Comparison with the literature for the $b(c,c)\bar{b}$ geometry. The spectra have been rescaled for comparison. (d) Fit of the $b(c,c)\bar{b}$ geometry.

perpendicular axis is a mix of the a and b axis which makes no differences with the unmixed axis. Given a small possible misalignment of the optical path by changing the polarizer angle, the Raman spectra had an energy uncertainty of 0.1 meV.

As explained in the previous section, three phonon modes are Raman-active, $A_g(1)$, $A_g(2)$ $E_g(1)$ [271, 274]. The A_g are the vibrations of the strontium and the apical oxygen along the c -axis are observable in the $b(c,c)\bar{b}$ and $b(a,a)\bar{b}$ geometry of Figure 4.40 (a), while the $b(c,c)\bar{b}$ is shown in Figure 4.40 (c). In addition, the spectra are fitted using standard Lorentzian line shapes and the resulting mode energies (ω_0), weight (W) and width (Γ) are presented in Table 4.6. The quality of the fit is shown in Figure 4.40 (d) for the $b(c,c)\bar{b}$ geometry. Furthermore the data of Iliev *et al.* [283] is also fitted for comparison.

The energy of $A_g(1)$ is 24.7 meV for the Tc134 sample while it is about 24.3 meV for the C362 sample. In the literature both study by Iliev *et al.* [283] and Sakita *et al.* [284] have almost exactly the same energy, as observed for the Tc134 sample. In the early study of Udagawa *et al.* [274], the phonon mode was observed at 24.4 meV which is close to value found for the C362 sample. Interestingly, in the case of Tc134, the mode is somewhat 40 % broader than for the other crystals. However, It is not possible to resolve any double structure or splitting within the resolution of the spectrometer. If the difference of width, about 0.5 meV, is taken to be the

4. LOW ENERGY OPTICAL RESPONSE OF Sr_2RuO_4

Table 4.6: Room temperature parameters of the Lorentzian fit to the data of this study and from Iliev *et al.* [283]. The E_g mode was measured in the $b(a, c)\bar{b}$ geometry for this study and in the $b(c, a)\bar{b}$ for the data of Iliev *et al.*. For A_g the $b(c, c)\bar{b}$ geometry was used.

Sample	Mode	Geometry	ω_0 (meV)	W (meV)	Γ (meV)
Tc134	$E_g(1)$	$b(c, a)\bar{b}, b(a, c)\bar{b}$	30.8	117.3	3.5
	$A_g(1)$	$b(a, a)\bar{b}, b(c, c)\bar{b}$	24.7	386.0	1.5
	$A_g(2a)$	$b(a, a)\bar{b}, b(c, c)\bar{b}$	67.3	342.9	1.6
	$A_g(2b)$	$b(a, a)\bar{b}, b(c, c)\bar{b}$	68.9	443.0	2.9
C362	$E_g(1)$	$b(c, a)\bar{b}, b(a, c)\bar{b}$	30.4	100.0	2.0
	$A_g(1)$	$b(a, a)\bar{b}, b(c, c)\bar{b}$	24.3	345.7	1.1
	$A_g(2a)$	$b(a, a)\bar{b}, b(c, c)\bar{b}$	66.9	486.5	1.4
	$A_g(2b)$	$b(a, a)\bar{b}, b(c, c)\bar{b}$	68.5	261.1	3.0
Iliev <i>et al.</i>	$E_g(1)$	$b(c, a)\bar{b}, b(a, c)\bar{b}$	30.5	0.8	1.0
	$A_g(1)$	$b(a, a)\bar{b}, b(c, c)\bar{b}$	24.7	3.1	1.0
	$A_g(2)$	$b(a, a)\bar{b}, b(c, c)\bar{b}$	67.5	5.5	1.3

splitting between the two phonons, it corresponds to about 2 % difference between the peaks.

The higher energy A_g mode has a clear double structure ($A_g(2a)$ and $A_g(2b)$). For the Tc134 samples, the peak energy is 67.3 meV to 68.9 meV, respectively, which corresponds to a difference of 2.3 %. For the C362 the weight of the second peak is much smaller but the energy difference is comparable, about 2.4 %. This difference is close to the difference estimated for the $A_g(1)$ modes. The shift of the peaks between the two samples is the same for the two A_g mode and is 0.4 meV. Now comparing with optical spectroscopy of section 4.7.2, the splitting of A_u apical oxygen mode is about 6.6 % which is nearly three times the splitting of the A_g mode. The ratio of weight between the splitted peaks is roughly the same for the Raman and optical spectroscopy for the Tc134 and C362 sample it is 0.77 and 1.86 which is not far from 0.57 and 2.1. The fit shown in Figure 4.40 is also indicating that the second peak is twice as large as the first one, which is comparable to the A_u apical oxygen mode of C362 but not for the Tc134 or Tc128. If the admixture of different constrained phase of Sr_2RuO_4 would produce only a shift of the phonon energy without modifying the phonon line-shape, the actual fit would make the Maxwell-Garnett approximation scenario unfavorable.

The difference of background level between the in-plane $b(a, a)\bar{b}$ and out of plane $b(c, c)\bar{b}$ geometry is a good indicator of the presence of a high electronic background and the high anisotropy with the c -axis. In this respect, the C362 sample has a larger anisotropy ratio than the Tc134. From the $b(c, c)\bar{b}$ geometry to the $b(a, a)\bar{b}$, the phonon weight is suppressed against a strong increase of the electronic background implying a strong interplay between the two phenomena. Moreover Sakita *et al.* [284] claimed that the asymmetrical lineshape of the A_g apical oxygen mode in the $b(a, a)\bar{b}$ geometry was a proof of good crystals quality since the

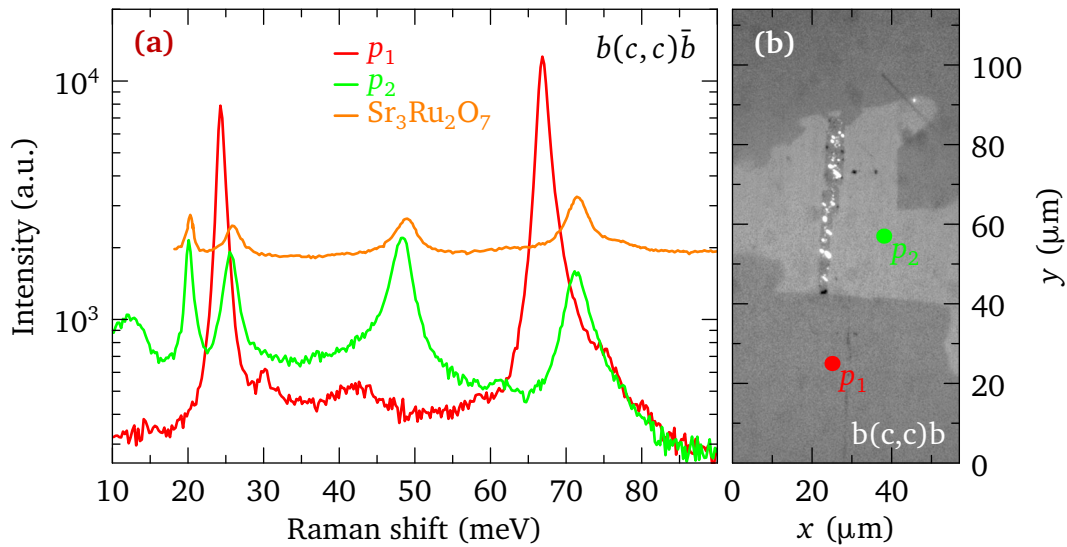


Figure 4.41: Raman analysis of Sr_2RuO_4 ac -plane of sample C362. **(a)** Raman spectra for two different positions of the surface and a comparison with the $\text{Sr}_3\text{Ru}_2\text{O}_7$ data of Iliev et al. [283]. **(b)** The polarized light picture of the area of interest and the position taken for the measurement. The dark grey area is Sr_2RuO_4 , while the light grey is $\text{Sr}_3\text{Ru}_2\text{O}_7$ and the white inclusion is pure ruthenium

asymmetry is not present for crystal with critical temperature below 1 K. They also compared this mode in the $c(a,a)\bar{c}$ channel and noted that the observed phonon was depending on the propagation direction of light although this shouldn't be the case if the mode was at the Brillouin-zone center. This led to the idea that the anisotropic interactions could be linked with electronic or magnetic excitations coupled with the phonons, which could strongly depend on the propagation and polarization of light.

The E_g modes represent the vibration of strontium atoms in the a -axis and are observed in $b(c,a)\bar{b}$, $b(a,c)\bar{b}$ geometries at about 30 meV, in good agreement with the neutron diffraction data of Braden *et al.* [271]. The appearance of the A_g mode in the $b(a,c)\bar{b}$ may be due to a slight misalignments of the crystal. The fit of both C362 and Tc134 gives a width at least two time larger than in other study.

In addition to the phonon analysis, polarized light micrography was performed on the full surface of the samples. This technique allows to see a contrast with impurity phases, given it has a large difference of reflectivity with the main material. Among the Ruddlesden-Popper series of ruthenate, Sr_2RuO_4 is having the larger anisotropy and subsequently the lowest c -axis reflectivity at low energy. Therefore, the presence of e.g. $\text{Sr}_3\text{Ru}_2\text{O}_7$ would be seen as a brighter area. Although no difference of brightness is seen for the Tc134 sample, the surface of the C362 sample has many small bright stripes mainly aligned along the c -axis. The area covered by impurity is estimated to be 3%. A micrography of a small patch of the C362 surface of is shown in Figure 4.41 (b), the contrast is increased for readability. Measuring a Raman spectrum inside the bright spot and outside allows to clearly identify the presence of $\text{Sr}_3\text{Ru}_2\text{O}_7$ comparing the

4. LOW ENERGY OPTICAL RESPONSE OF Sr_2RuO_4

spectra of the same geometry reproduced from [283]. In addition, the small bright inclusions observable on the image are pure ruthenium of about $1\ \mu\text{m}$ size. It is important to note that since the $\text{Sr}_3\text{Ru}_2\text{O}_7$ phase can be clearly separated from the pure Sr_2RuO_4 , the splitting of the $A_g(2)$ mode can't be directly attributed to the admixture of Ruddlesden-Popper series impurities in the crystal.

To conclude, the Raman shifts have shown that the presence of the $\text{Sr}_3\text{Ru}_2\text{O}_7$ is probably not directly linked to the splitting of the apical oxygen vibration which appear not equally for the samples of this study. The likelihood of having a stacking of homogeneous layers of Sr_2RuO_4 and $\text{Sr}_3\text{Ru}_2\text{O}_7$ is not excluded but strongly reduced by the fact that $\text{Sr}_3\text{Ru}_2\text{O}_7$ seems to appear around ruthenium inclusions which gather in small pockets along the c -axis. The phonon energy seems otherwise to be very close to the literature, while their width is somewhat larger for the Tc134 sample.

4.7.3 Characterization

In this section, an extensive analysis of the samples characteristics is shown. Scanning electron microscope but also X-ray and magnetometry results will be discussed.

4.7.3.1 Scanning electron microscope

The system used a X-ray detector to detect the elements present in the crystal by recording the characteristic X-ray photons emitted by the atoms after relaxation of the ionized electrons. The second electron (SE) detector and back-scattered electron detector (BSED) were used to image the samples. Micrographies taken at 20 kV are shown in Figure 4.42 (f) and (h). The surface analysis can be performed point by point, along a line scan or over a full area. An extensive analysis of the surface has been performed for the three samples. Selected surface scans of about $40\ \mu\text{m}$ to $60\ \mu\text{m}$ are shown in Figure 4.42 (c) and (e). No sizeable trace of ruthenium inclusion were found for the Tc134 and Tc128 samples, but a very small amount were found for C362. This observation is comparable to the Raman analysis section 4.7.2.4. The ruthenium area is shown as darker zones in the ruthenium map or white spots in the strontium or oxygen maps. Furthermore, an extended area of $\text{Sr}_3\text{Ru}_2\text{O}_7$ around the inclusion was also found. It is expected to form a dark band in the ruthenium map which should be seen lighter for the strontium and have no effects in the oxygen map. In Figure 4.42 (a-b), the expected ratio for $\text{Sr}_3\text{Ru}_2\text{O}_7$ are shown as the dotted lines, this confirms the assumption that this phase is also present around some of the ruthenium inclusions. In (c), the small peak at about $15\ \mu\text{m}$ is an inclusion smaller than the beam size. Very roughly, the contamination by pure ruthenium is below 500 ppm, which confirms the good crystal quality and discard ruthenium inclusions as a direct cause for the c -axis phonon splitting in optical spectroscopy. No μm -sized phase of

Sr₃RuO_{5+x} was found in the samples.

4.7.3.2 Xray diffraction

A qualitative X-ray analysis has been performed on the Tc134 crystal. Rocking curve and $\omega - 2\theta$ diffraction pattern are shown in Figure 4.43. At a first glance it is possible to see that these crystals are difficult to grow without having a partial inter-growth of the other Ruddlesden-Popper series [285]. The peak positions were reported and fitted (wavelength of the Cu K _{α}); the estimated c-axis lattice parameter is 12.7502(5) Å, which is almost identical to 12.759 Å found by the crystal synthesis in Salerno [230]. This value is about 0.14 % higher compared to the value found in the latest literature report and shown in Table 4.1. On the other hand, earlier studies have reported different values: $c = 12.74$ Å [206], 12.68 Å [286], 12.746 Å [287] and 12.7397(1) Å [288].

The diffraction pattern also shows other peaks of much smaller intensity, which are mainly attributed to Sr₃Ru₂O₇. From the four first Bragg reflections (006–0012), the c lattice parameter of the Sr₃Ru₂O₇ impurity phase is estimated to be 20.79(11) Å. For a single crystal, seeing this phase in a diffractogram indicates that it is, at least partly, closely intertwined with the Sr₂RuO₄ planes, which also confirms the presence of a crystallized embedded phase of Sr₃Ru₂O₇ in the Tc134 and Tc128 samples. Using the Scherrer formula [289] applied on (006) Miller index, the estimation of the typical thickness of the Sr₃Ru₂O₇ embedded phase is 70 Å (3-4 unit cells). The same analysis was performed on sample Tc128 gives an impurity phase of less than 5 %.

The two remaining unidentified peaks may be partly attributed to Sr₄Ru₃O₁₀. The 37.77° peak which is close to the (0012) Bragg peak of this material, but much stronger peaks at 6.16° (002) or 12.35° (004) should have been detected in order to confirm this assumption. Nevertheless, it is unfavorable that these peaks correspond to pure ruthenium such that the closest ruthenium reflection is at 38.6°, which is much larger than the overall difference in peak position with data of Mao *et al.* [234]. This phase is much less abundant or unaligned with the main Sr₂RuO₄ lattice, which could explain the observations.

4.7.3.3 Magnetometry

The susceptibility measurement has been achieved in two different setups. First the low temperature superconducting transition of sample Tc134 and Tc128 were measured in Salerno by Fittipaldi and co-workers. With a temperature range of 343 mK to 2 K, the susceptibility is shown in the inset of Figure 4.44. The normal state is shown in the two main graphs of Figure 4.44, was measured in Geneva both in field cooling (FC) and zero field cooling (ZFC), from room temperature to 1.8 K. In order to allow a better comparison of the phenomenon, the data were scaled in order to obtain the same magnetization at high temperature. For comparison, the data of Maeno *et al.* [290] is added in Figure 4.44 whose temperature dependence (without

4. LOW ENERGY OPTICAL RESPONSE OF Sr_2RuO_4

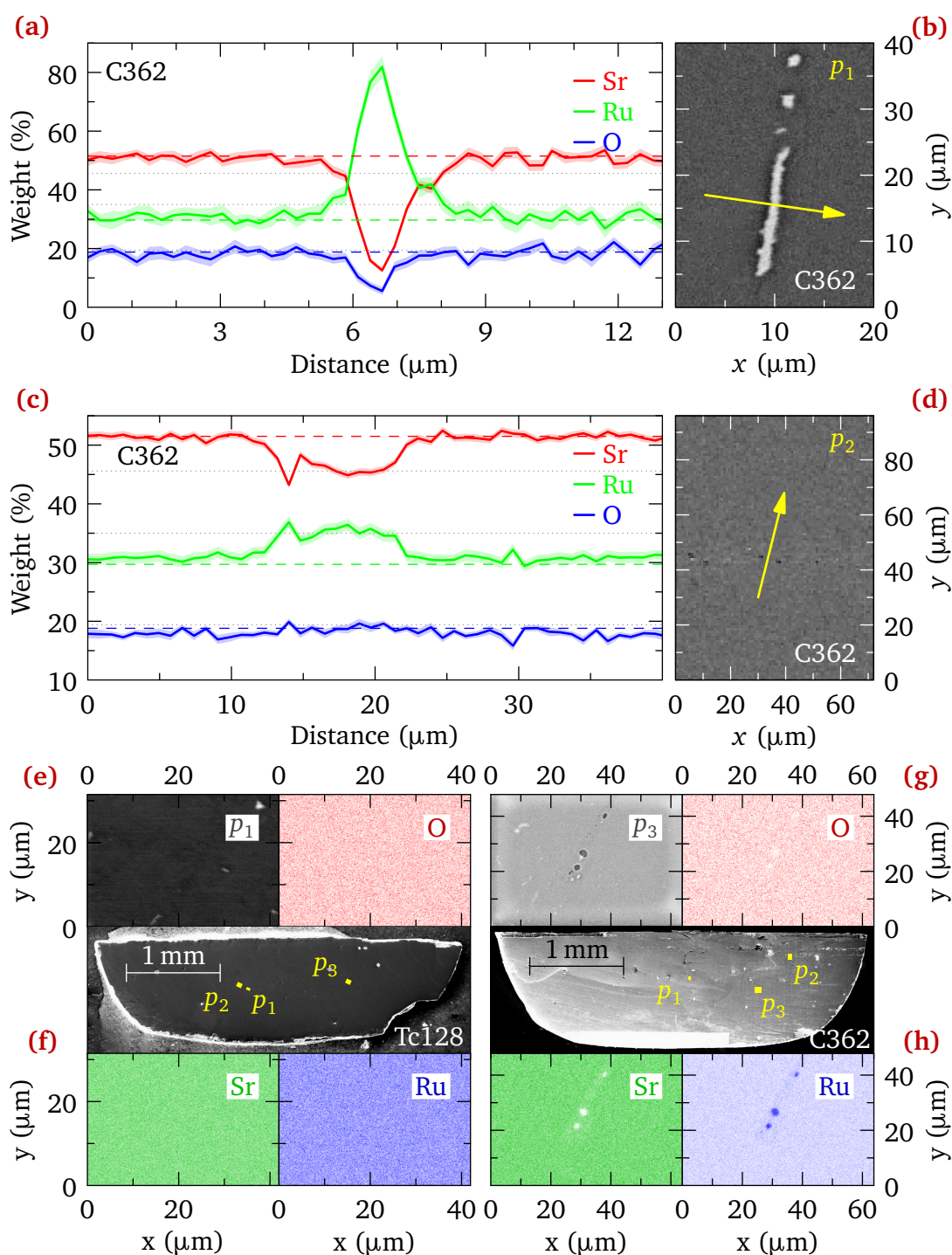


Figure 4.42: Scanning electron microscope surface topography of the Tc128 and C362 Sr_2RuO_4 samples. (a) Line scan taken at position p_1 of sample C362. The data are shown in weight percentage along the line crossing a pure ruthenium inclusion in yellow in (b). Error bars are shown as light color areas. The color dashed lines show the expected weight for Sr_2RuO_4 . The grey dotted line are for the expectation values of $\text{Sr}_3\text{Ru}_2\text{O}_7$. (c) and (d) Similar scan at position p_2 , crossing small ruthenium μm -sized dots. (e) Surface scan. The composition homogeneity of the Tc128 sample at position p_1 . The darker the pixel is the higher the proportion of the element. (f) Overall secondary electrons scan of sample Tc128. An extensive analysis was achieved for three position (yellow). The remaining surface was qualitatively checked for other different inclusions. No trace of pure ruthenium is observed. (g) and (h) Same analysis for position p_1 of sample C362. Trace of pure ruthenium are observed as small round shaped area.

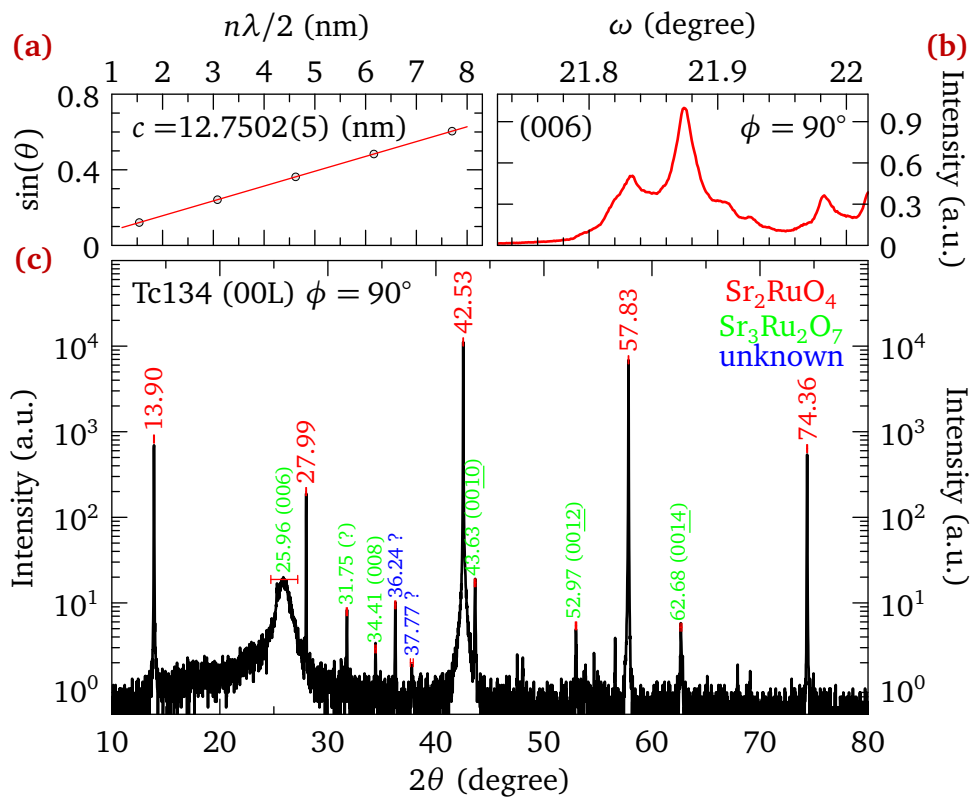


Figure 4.43: X-ray diffraction pattern of the Tc134 sample. The indexed peaks in red correspond to Sr_2RuO_4 ; in green to $\text{Sr}_3\text{Ru}_2\text{O}_7$ and the remaining peak are unknown (a) Linear fit of the (00L) peaks of the diffractogram. (b) ω scan of the (006) peak.

4. LOW ENERGY OPTICAL RESPONSE OF Sr_2RuO_4

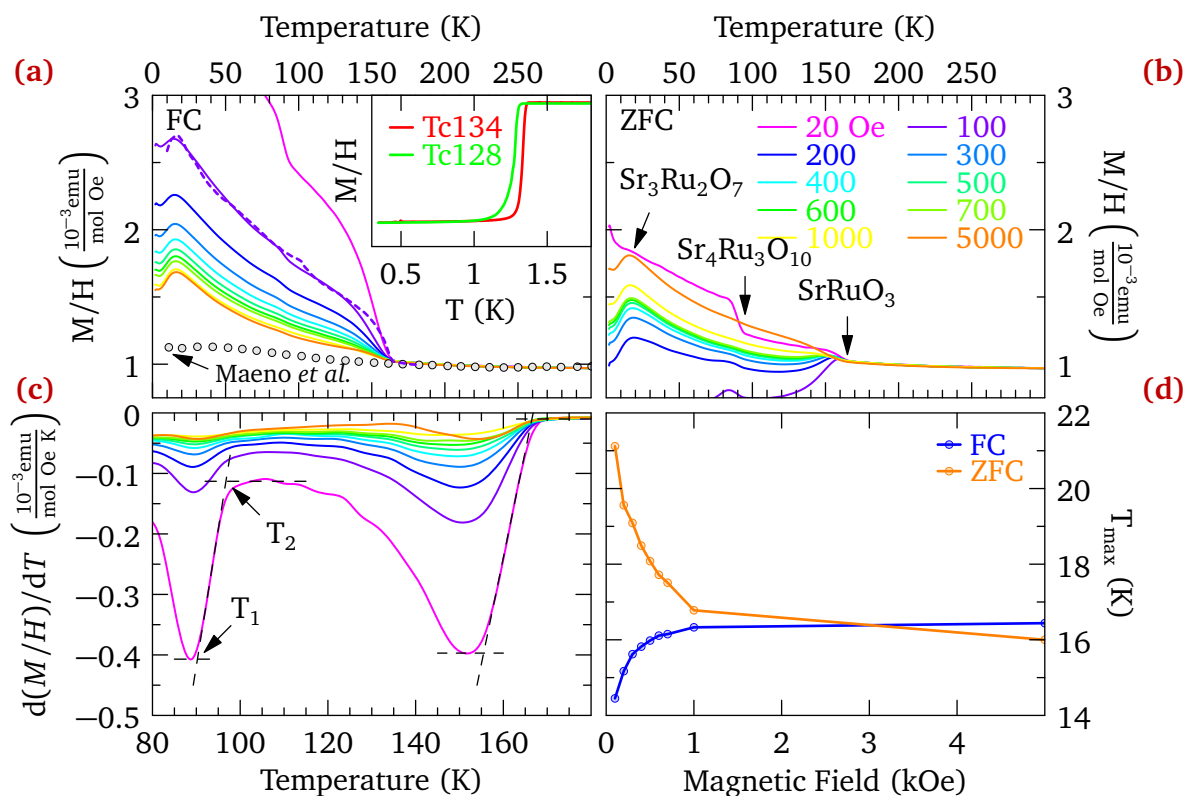


Figure 4.44: Susceptibility measurement of the Tc134 Sr_2RuO_4 sample for different applied fields along the c -axis. (a) Field cooling and (b) zero field cooling. The data of Maeno *et al.* is reproduced from [290]. The data are scaled in order to obtain the same magnetization at high temperature. (c) Temperature derivative of the field cooled magnetization curves. The onset of the transition at about 93 K and 161 K is defined by the average of T_1 and T_2 . (d) Magnetic field dependence of the ≈ 18 K maximum temperature peak for both field cooling and zero field cooling measurement.

magnetic impurities) is very small such that the spin susceptibility χ_{spin} can easily be extracted and estimated to be 0.9×10^{-3} emu/mol. The Ruddlesden-Popper series have different magnetic structures happening at different temperatures so that it is easy to determine the impurities present in the material, the double and triple layer, but also the last element of the series (SrRuO_3) is present. Moreover, it is possible to determine the percentage of present impurities in the crystals. The data of different Ruddlesden-Popper series is taken from the literature: The double layer data are from [291], the third layer from [292] and SrRuO_3 from [293]. All the contribution are summed up with a weighting factor in order to reproduce the field cooling magnetization data at 100 Oe. The artificially reproduced curve is shown as the purple dashed line in Figure 4.44 (a). Taking into account the magnetic response of the impurity phase allows to match exactly the single layer magnetization at high temperature. From room temperature to low temperature, the first feature is the ferromagnetic transition of SrRuO_3 which is only accounting for 12.5 ppm of entire crystal in weight. The second transition is attributed to $\text{Sr}_4\text{Ru}_3\text{O}_{10}$ present at 448 ppm. The last feature is clearly attributed to $\text{Sr}_3\text{Ru}_2\text{O}_7$ and with 4% in weight is the most abundant impurity.

4.7 Phonon splitting in the c-axis spectra of Sr₂RuO₄

The different transition temperatures were determined by taking the temperature derivative of the magnetization $d(M/H)/dT$ shown in Figure 4.44 (c). A constant fit was applied in the almost flat region before and after the transition. In between these regions a linear fit was applied and the minimum and maximum temperatures were determined at the intersection point of the adjacent lines. The critical temperature is defined as the average of T_1 and T_2 [294]. The ferromagnetic transition of SrRuO₃ is found at 161.0(5) K. However, it was shown that this material undergoes a structural phase transition driven by biaxial strain imposed by substrate mismatch on which the material is grown [295]. With that strain, the SrRuO₃ structure is changing from orthorhombic to tetragonal, which affects its electronic properties, notably its ferromagnetic transition that tends to increase upon reducing the c-axis lattice parameter [294]. In such a case, the lattice parameter is found to be 3.917(5) Å, which shows that the material is probably present at the interface with Sr₄Ru₃O₁₀. This also suggests that the impurity layers are stacked together as suggested in the previous sections. The magnetic transition of Sr₄Ru₃O₁₀ is found at 93.5(5) K which is different from the value 105 K found in the literature [192], this suggests as well that this material is strained in the main Sr₂RuO₄ lattice.

Another interesting aspect is the emergence of short-range antiferromagnetic correlations below approximately 20 K [291]. The maximum of susceptibility at low temperature is attributed to Sr₃Ru₂O₇ and its temperature dependence is shown in Figure 4.44 (d). Also shown in [291], this peak shifts with temperature, but seems to stabilize at high field while it is suppressed down to temperatures below 5 K above 6 T for very pure Sr₃Ru₂O₇ samples [198].

Finally based on the onset of a very small decrease of the susceptibility above 1.5 K the pure ruthenium volume fraction in the Tc134 is very roughly estimated to be 5 ppm to 50 ppm.

4.7.3.4 Discussion

In this section the splitting of the optical phonon were reviewed through different scenarios. The impact was shown to be different for all the samples, even between two samples coming from the same batch (Tc134 and Tc128). Surprisingly, this effect is not affecting T_c , which indicated that the interpretation from impurities coming from the precursor material was not valid. The strength of the splitted phonon peaks is almost evenly distributed so that a scenario with a mix of two different phases could in principle be also rejected. The remaining scenario is relying on strain effects which would slightly lower the symmetry of the crystal. In this case the idea of having a tilt of the ruthenium octahedron is the most probable scenario which could be involved by a lattice strain from the Sr₃Ru₂O₇ impurity layers.

4.8 Conclusions

In this chapter, the Fermi-liquid Sr_2RuO_4 was heralded as the first material showing the expected relation between energy and temperature in the optical scattering rate with $p = 2$. Despite being a multi-band system the electrical resistivity was described using a simple Fermi-liquid pointing to two different energy scales, a low temperature Fermi-liquid and a second component in parallel which could be described by standard electron-electron interaction in a 3D Fermi-liquid or any 2D modes with a linear dispersion. Numerical calculation through DFT+DMFT were carried out, which in combination with the optical data allowed to demonstrate the existence of high-energy and temperature resilient particle-hole excitation. Finally reflectivity measurements on the ac -plane of the material showed a sample dependent splitting of the c -axis phonon. Extensive research is still needed but the scenario of a internal stress due to the presence of layers of $\text{Sr}_3\text{Ru}_2\text{O}_7$ in the crystal was put forward. That scenario is compatible with the various bulk characterization measures that have been undertaken.

Appendices

Fermi-liquid like properties in the pseudogap phase of the cuprates

A.1 Fermi-liquid fit of the reflectivity

The reflectivity of any Fermi-liquid can be fitted using the Fermi-liquid model instead of the standard Drude formula. As shown in Figure A.1, the low energy reflectivity is correctly reproduced by the model and its extrapolation down to zero can be used during the Kramers-Kronig analysis.

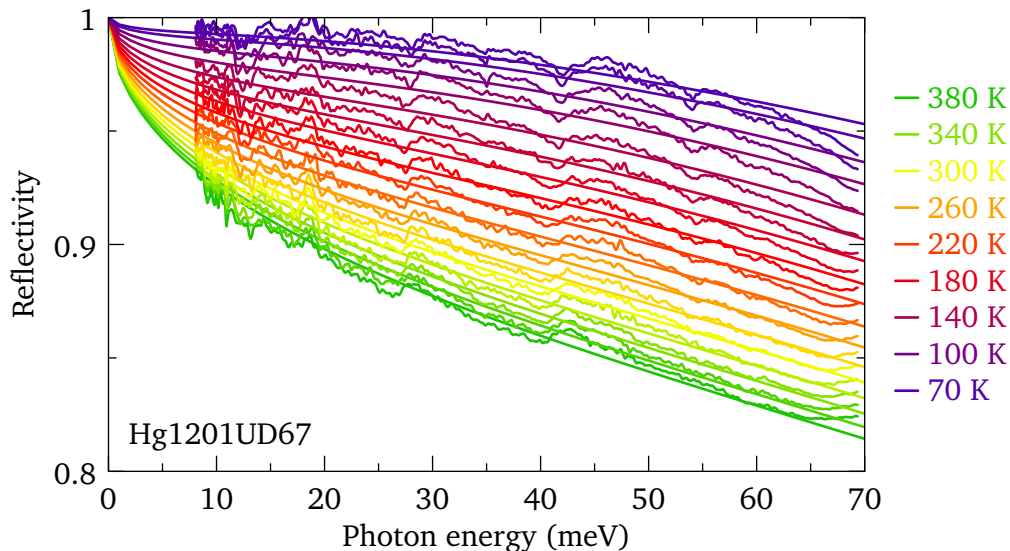


Figure A.1: Fermi-liquid model fitted to the FIR reflectivity of $\text{HgBa}_2\text{CuO}_{4+x}$ UD67. The fit was done at selected temperature above T_c . The fitting extend up to 70 meV and except the sharp phonons, the fit quality is excellent up to 60 meV. The fitting procedure uses the temperature as a fixed parameter while finding the best Fermi-liquid parameters : T_0 , $Z\Phi(0)$ and $Z\Gamma$.

A.2 Fermi-liquid fit of the optical conductivity

In this section the supplemental graphs for the UD55, UD45 and OpD97 are shown. The data were fitted to the Fermi-liquid model, fixing either the Fermi-liquid parameters $Z\Gamma$ or T_0 and $Z\Phi(0)$.

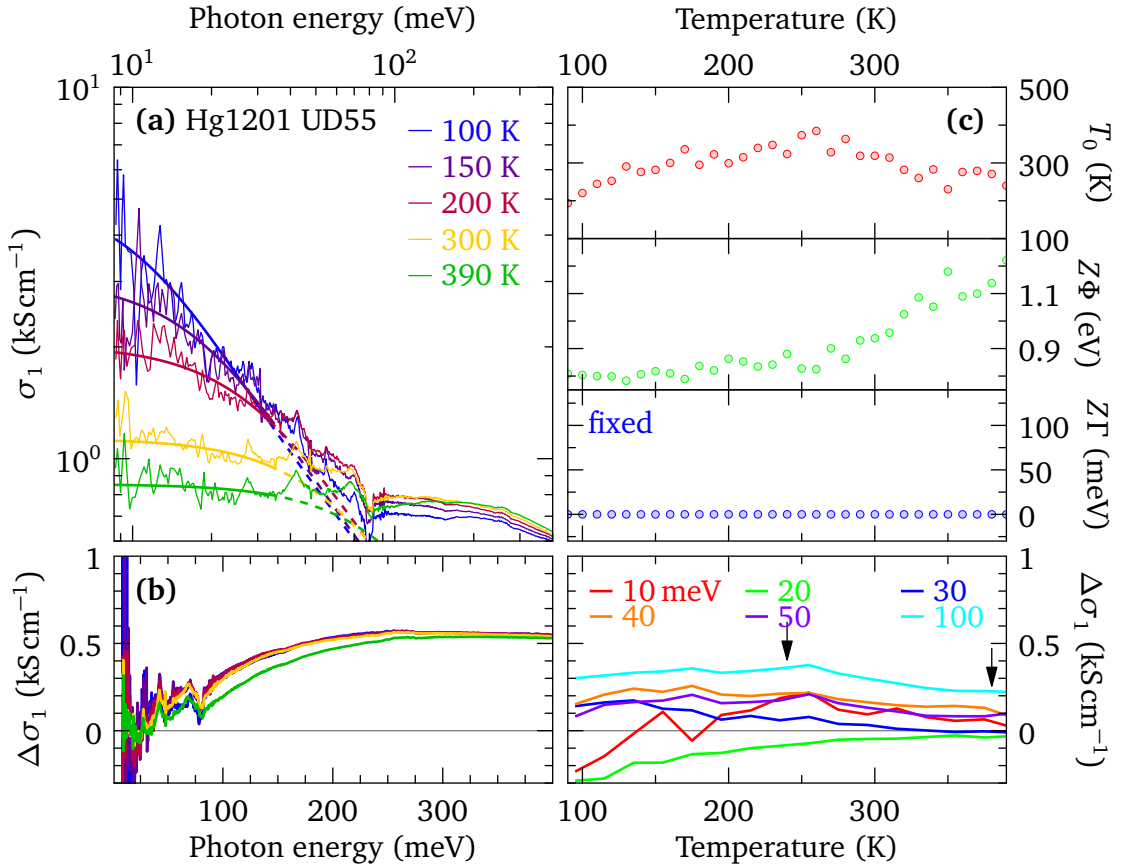


Figure A.2: Fermi-liquid fit to the low energy optical conductivity of $\text{HgBa}_2\text{CuO}_{4+x}$ UD55 (Procedure A). The Fermi-liquid parameters T_0 and $Z\Phi(0)$ are allowed to vary for all temperature while $Z\Gamma$ is fixed at zero. (a) Experimental conductivity (thin lines). The Fermi-liquid model (dashed lines + thick lines). The thick line represent the fitting region $\hbar\omega \leq 33$ meV. (b) Subtraction of the model to experimental data as a function of energy (left) or as a function of temperature (right). The black arrows indicates T^{**} and T^* . (c) Temperature variation of the Fermi-liquid parameters; fixed parameters are labeled as is.

A.2 Fermi-liquid fit of the optical conductivity

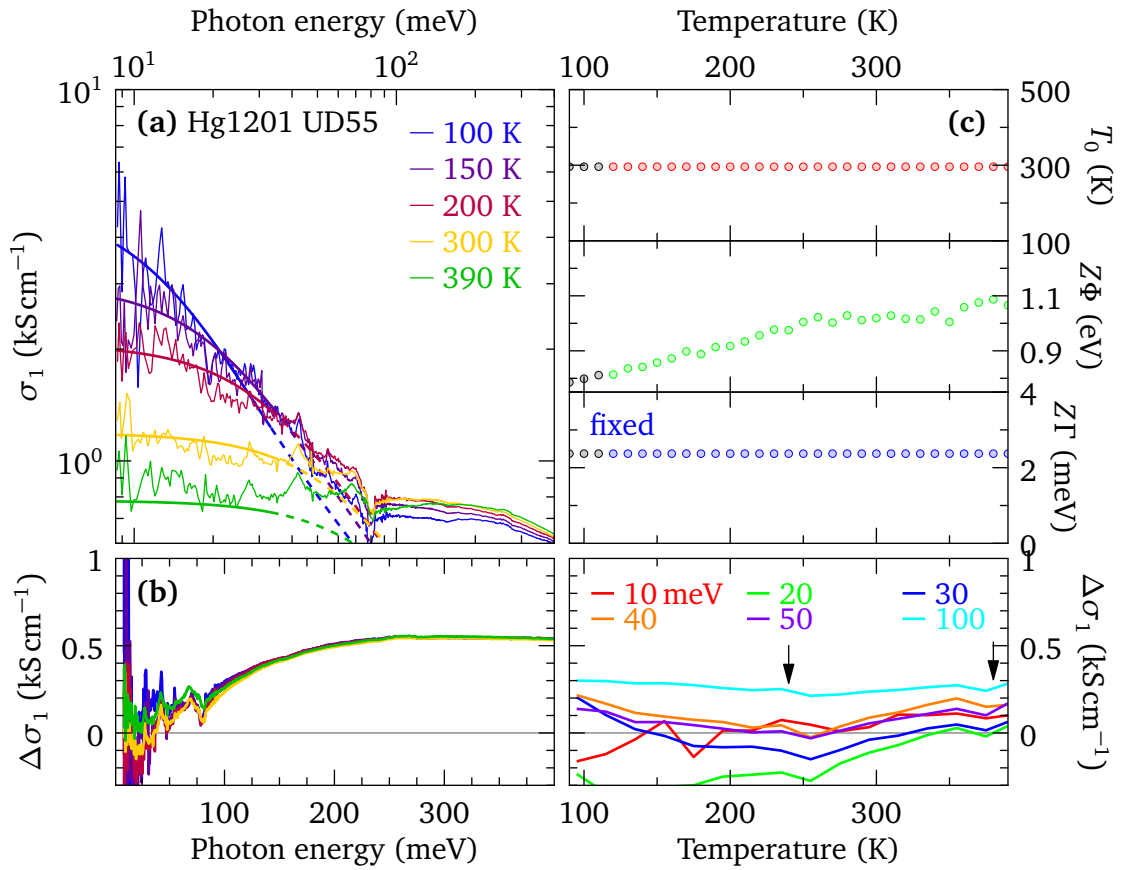


Figure A.3: Fermi-liquid fit to the low energy optical conductivity of $\text{HgBa}_2\text{CuO}_{4+x}$ UD55 (Procedure B). The Fermi-liquid parameter T_0 and $Z\Gamma$ are fitted below 110 K and fixed at higher temperature, $Z\Phi(0)$ is kept free for all temperatures. For more details see Figure A.2

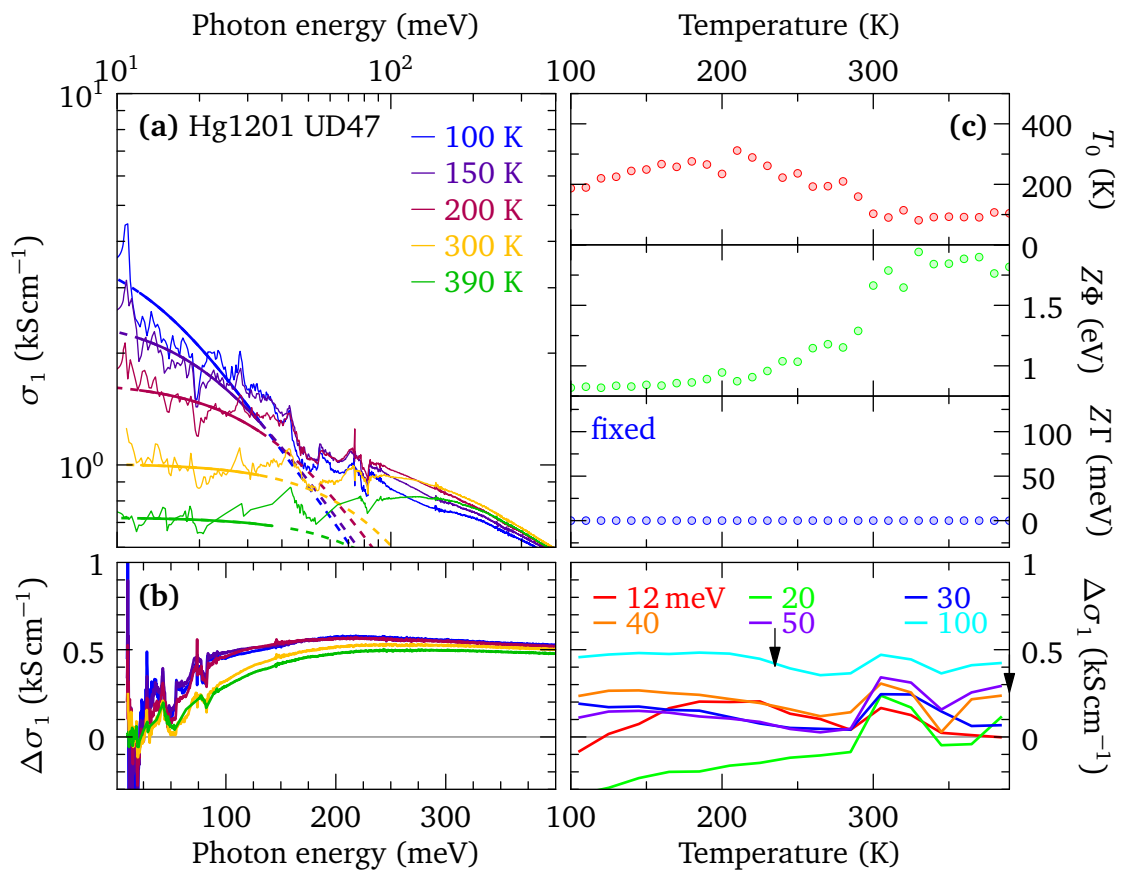


Figure A.4: Fermi-liquid fit to the low energy optical conductivity of HgBa₂CuO_{4+x} UD45 (Procedure A). The Fermi-liquid parameters T_0 and $Z\Phi(0)$ are allowed to vary for all temperature while $Z\Gamma$ is fixed at zero. (a) Experimental conductivity (thin lines). The Fermi-liquid model (dashed lines + thick lines). The thick line represent the fitting region $\hbar\omega \leq 33$ meV. (b) Subtraction of the model to experimental data as a function of energy (left) or as a function of temperature (right). The black arrows indicates T^{**} and T^* . (c) Temperature variation of the Fermi-liquid parameters; fixed parameters are labeled as is.

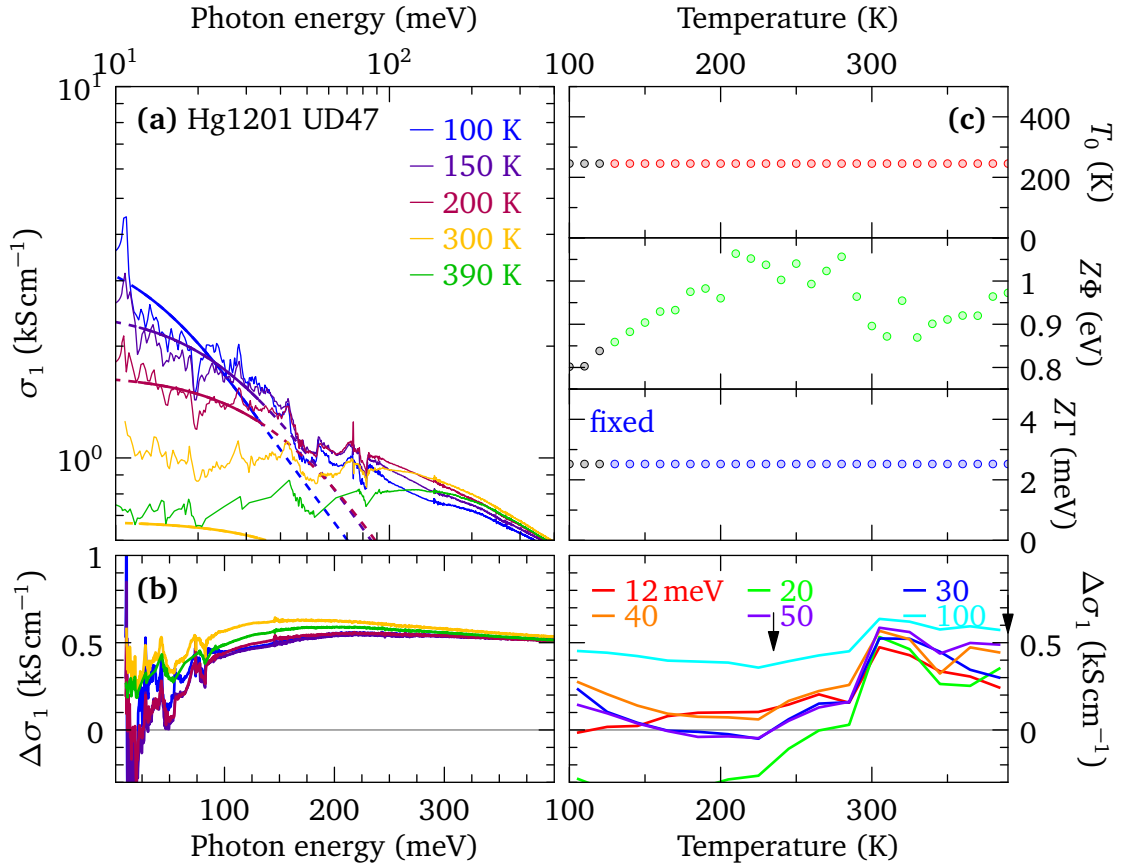


Figure A.5: Fermi-liquid fit to the low energy optical conductivity of HgBa₂CuO_{4+x} UD45 (Procedure B). The Fermi-liquid parameter T_0 and $Z\Gamma$ are fitted below 110 K and fixed at higher temperature, $Z\Phi(0)$ is kept free for all temperatures. The strong increase of $\Delta\sigma$ seen at 300 K in panel (b) is due to the fact that at these temperatures the coherent peak disappears, so that the fit is then totally unreliable. For more details see Figure A.4

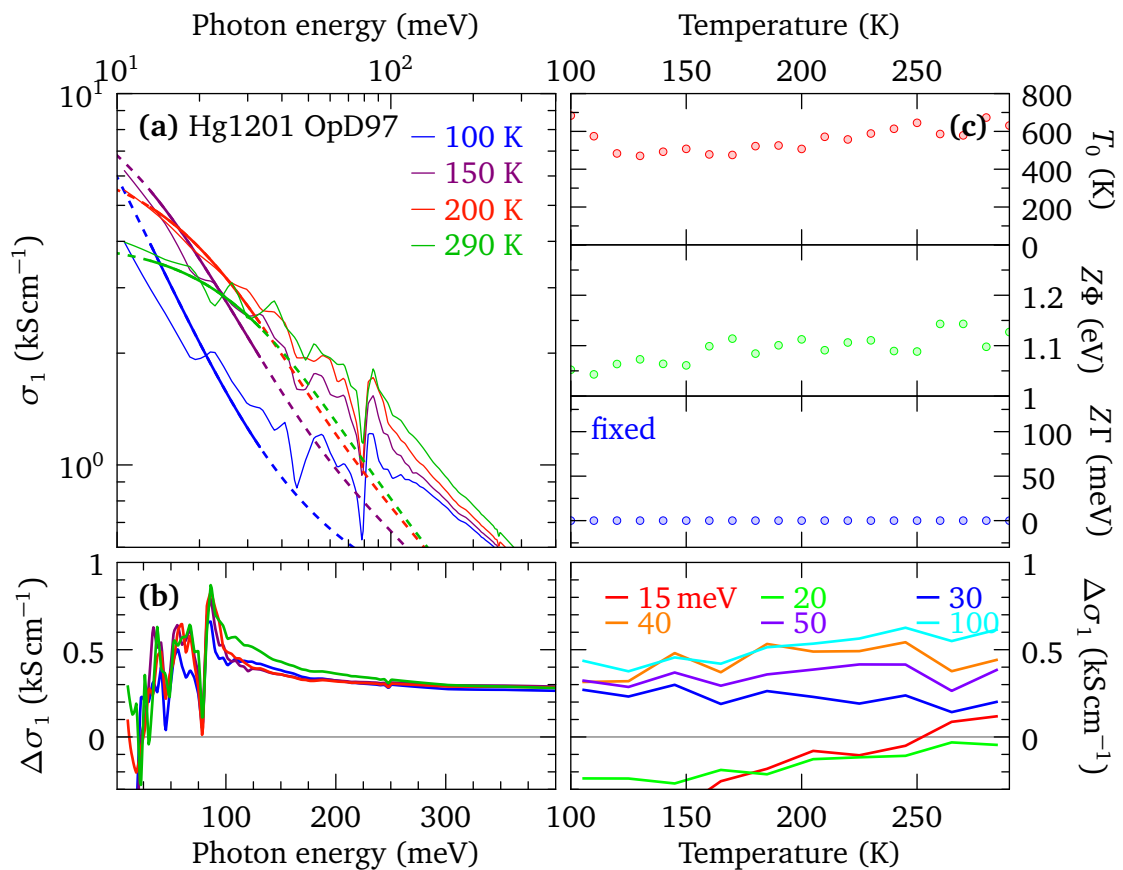


Figure A.6: Fermi-liquid fit to the low energy optical conductivity of HgBa₂CuO_{4+x} OpD97 (Procedure A). The Fermi-liquid parameters T_0 and $Z\Phi(0)$ are allowed to vary for all temperature while $Z\Gamma$ is fixed at zero. (a) Experimental conductivity (thin lines). The Fermi-liquid model (dashed lines + thick lines). The thick line represent the fitting region $\hbar\omega \leq 33$ meV. (b) Subtraction of the model to experimental data as a function of energy (left) or as a function of temperature (right). The black arrows indicates T^{**} and T^* . (c) Temperature variation of the Fermi-liquid parameters; fixed parameters are labeled as is.

Optical phonon of the single layer ruthenate

The fit of the real part of the *c*-axis optical conductivity is shown in Figure B.1 at 9 K and 300 K. The conductivity difference with the model is shown in graph (b) and the temperature dependence of the mean squared error related to the fit is shown in (a).

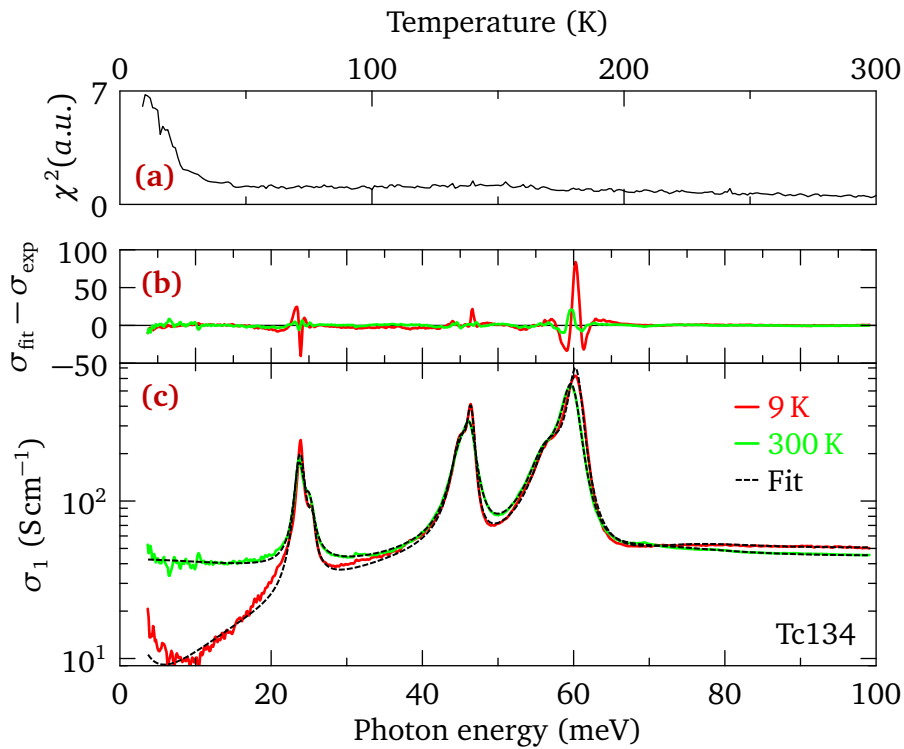


Figure B.1: Comparison of the Drude-Lorentz fit with the direct Kramers-Kronig transformation of the data for the real part of the optical conductivity. (a) Total squared difference for each temperature spectra. $\chi^2 = \sum_{\hbar\omega} (\sigma_{\text{fit}}(\hbar\omega) - \sigma_{\text{exp}}(\hbar\omega))^2$ (b) Difference as function of photon energy for the room temperature and the lowest temperature. (c) Comparison of the optical conductivity.

Bibliography

- [1] D. J. Griffiths, *Introduction to Electrodynamics*. Addison-Wesley, 4th ed., 2012.
- [2] M. Dressel and G. Grüner, *Electrodynamics of solids optical properties of electrons in matter*. Cambridge University Press, 2002.
- [3] P. Drude, “Zur Elektronentheorie der Metalle,” *Annalen der Physik*, vol. 306, no. 3, p. 566, 1900.
- [4] M. Dressel, “Quantum criticality in organic conductors? Fermi liquid versus non-Fermi-liquid behaviour,” *Journal of Physics: Condensed Matter*, vol. 23, no. 29, p. 293201, 2011.
- [5] M. Tinkham and R. A. Ferrell, “Determination of the superconducting skin depth from the energy gap and sum rule,” *Phys. Rev. Lett.*, vol. 2, pp. 331–333, Apr 1959.
- [6] M. A. Ordal, L. L. Long, R. J. Bell, S. E. Bell, R. R. Bell, R. W. Alexander, and C. A. Ward, “Optical properties of the metals Al, Co, Cu, Au, Fe, Pb, Ni, Pd, Pt, Ag, Ti, and W in the infrared and far infrared,” *Appl. Opt.*, vol. 22, pp. 1099–1119, Apr 1983.
- [7] P. H. Citrin, G. K. Wertheim, and Y. Baer, “Core-level binding energy and density of states from the surface atoms of gold,” *Phys. Rev. Lett.*, vol. 41, pp. 1425–1428, Nov 1978.
- [8] A. Barrie and N. E. Christensen, “High-resolution X-ray photoemission spectra of silver,” *Phys. Rev. B*, vol. 14, pp. 2442–2447, Sep 1976.
- [9] J. Teyssier, “private communication.”
- [10] H.-J. Hagemann, W. Gudat, and C. Kunz, “Optical constants from the far infrared to the X-ray region: Mg, Al, Cu, Ag, Au, Bi, C, and Al_2O_3 ,” *J. Opt. Soc. Am.*, vol. 65, pp. 742–744, Jun 1975.
- [11] A. D. Rakić, A. B. Djurišić, J. M. Elazar, and M. L. Majewski, “Optical properties of metallic films for vertical-cavity optoelectronic devices,” *Appl. Opt.*, vol. 37, pp. 5271–5283, Aug 1998.
- [12] J. I. Larruquert, J. A. Méndez, and J. A. Aznárez, “Optical constants of aluminum films in the extreme ultraviolet interval of 82–77 nm,” *Appl. Opt.*, vol. 35, pp. 5692–5697, Oct 1996.
- [13] M. Ordal, R. Bell, R. A. Jr, L. Long, and M. Query, “Optical properties of fourteen metals in the infrared and far infrared: Al, Co, Cu, Au, Fe, Pb, Mo, Ni, Pd, Pt, Ag, Ti, V, and W,” *Applied Optics*, vol. 24, no. 24, pp. 4493–4499, 1985.
- [14] H. Bennett and J. Bennett, *Validity of the Drude theory for silver, gold and aluminum in the infrared, in: optical properties and electronic structure of metals and alloys*. Amsterdam: North-Holland, 1966.
- [15] D. W. Lynch and W. Hunter, “Comments on the optical constants of metals and an introduction to the data for several metals,” in *Handbook of Optical Constants of Solids* (E. D. Palik, ed.), pp. 275 – 367, Burlington: Academic Press, 1997.
- [16] A. B. Kuzmenko, “ReFFIT (software to fit optical spectra).” online, 2004–2015.
- [17] W. Götze and P. Wölfle, “Homogeneous dynamical conductivity of simple metals,” *Phys. Rev. B*, vol. 6, pp. 1226–1238, Aug 1972.
- [18] U. Nagel, T. Uleksin, T. Rööm, R. P. S. M. Lobo, P. Lejay, C. C. Homes, J. S. Hall, A. W. Kinross, S. K. Purdy, T. Munsie, T. J. Williams, G. M. Luke, and T. Timusk, “Optical spectroscopy shows that the normal state of URu_2Si_2 is an anomalous Fermi liquid,” *Proceedings of the National Academy of Sciences*, vol. 109, no. 47, pp. 19161–19165, 2012.
- [19] D. L. Maslov and A. V. Chubukov, “First-Matsubara-frequency rule in a Fermi liquid. II. optical conductivity and comparison to experiment,” *Phys. Rev. B*, vol. 86, p. 155137, Oct 2012.
- [20] J. S. Lee, Y. S. Lee, T. W. Noh, S.-J. Oh, J. Yu, S. Nakatsuji, H. Fukazawa, and Y. Maeno, “Electron and orbital correlations in $\text{Ca}_{2-x}\text{Sr}_x\text{RuO}_4$ probed by optical spectroscopy,” *Phys. Rev. Lett.*, vol. 89, p. 257402, Dec 2002.
- [21] P. V. Rysselberghe, “Remarks concerning the Clausius-Mossotti law,” *The Journal of Physical Chemistry*, vol. 36, no. 4, pp. 1152–1155, 1931.
- [22] E. van Heumen, R. Lortz, A. B. Kuzmenko, F. Carbone, D. van der Marel, X. Zhao, G. Yu, Y. Cho, N. Barisic, M. Greven, C. C. Homes, and S. V. Dordevic, “Optical and thermodynamic properties of the high-temperature superconductor $\text{HgBa}_2\text{CuO}_{4+\delta}$,” *Phys. Rev. B*, vol. 75, p. 054522, Feb 2007.

BIBLIOGRAPHY

- [23] L. Pauling, "The theoretical prediction of the physical properties of many-electron atoms and ions. mole refraction, diamagnetic susceptibility, and extension in space," *Proceedings of the Royal Society of London A: Mathematical, Physical and Engineering Sciences*, vol. 114, no. 767, pp. 181–211, 1927.
- [24] Q. Huang, J. Soubeyroux, O. Chmaissem, I. Sora, A. Santoro, R. Cava, J. Krajewski, and W. P. Jr., "Neutron powder diffraction study of the crystal structures of Sr_2RuO_4 and Sr_2IrO_4 at room temperature and at 10 K," *Journal of Solid State Chemistry*, vol. 112, no. 2, pp. 355 – 361, 1994.
- [25] R. Shaheen, M. Akhtar, M. Nadeem, and M. Haque, "Atomistic computer simulation studies of Sr_2RuO_4 and Ca_2RuO_4 ," *Journal of Physics and Chemistry of Solids*, vol. 64, no. 2, pp. 237 – 245, 2003.
- [26] F. Wooten, *Optical Properties of Solids*. Academic-Press, New-York, 1972.
- [27] R. Kiebooms, R. Menon, and K. Lee, "Chapter 1 - synthesis, electrical, and optical properties of conjugated polymers," in *Handbook of Advanced Electronic and Photonic Materials and Devices* (H. S. Nalwa, ed.), pp. 1 – 102, Burlington: Academic Press, 2001.
- [28] A. B. Kuzmenko, "Kramers–Kronig constrained variational analysis of optical spectra," *Review of Scientific Instruments*, vol. 76, no. 8, pp. –, 2005.
- [29] D. B. Tanner, "Use of X-ray scattering functions in Kramers-Kronig analysis of reflectance," *Physical Review B*, vol. 91, p. 035123, Jan. 2015.
- [30] B. Henke, E. Gullikson, and J. Davis, "X-ray interactions: Photoabsorption, scattering, transmission, and reflection at $e = 50\text{--}30,000$ eV, $z = 1\text{--}92$," *Atomic Data and Nuclear Data Tables*, vol. 54, no. 2, pp. 181 – 342, 1993.
- [31] C. Berthod, *Applications of the Many-Body Formalism in Condensed-Matter Physics*. University of Geneva, 2014.
- [32] P. Allen, "Chapter 6 electron transport," in *Conceptual Foundations of Materials A Standard Model for Ground- and Excited-State Properties* (S. G. Louie and M. L. Cohen, eds.), vol. 2 of *Contemporary Concepts of Condensed Matter Science*, pp. 165 – 218, Elsevier, 2006.
- [33] P. B. Allen, "Electron self-energy and generalized Drude formula for infrared conductivity of metals," *Phys. Rev. B*, vol. 92, p. 054305, Aug 2015.
- [34] G. D. Mahan, *Many-Particle Physics*. Physics of Solids and Liquids, Springer, 2000.
- [35] E. V. Heumen, *Towards a quantitative understanding of the high T_c phenomenon*. PhD thesis, Université de Genève, 2009.
- [36] A. Migdal, "Interaction between electrons and lattice vibrations in a normal metal," *Sov. Phys. JETP*, vol. 7, no. 6, pp. 996–1001, 1958.
- [37] A. Khurana, "Electrical conductivity in the infinite-dimensional Hubbard model," *Physical Review Letters*, vol. 64, pp. 1990–1990, Apr. 1990.
- [38] C. Berthod, J. Mravlje, X. Deng, R. Žitko, D. van der Marel, and A. Georges, "Non-Drude universal scaling laws for the optical response of local Fermi liquids," *Phys. Rev. B*, vol. 87, p. 115109, Mar 2013.
- [39] P. B. Allen, "Electron-phonon effects in the infrared properties of metals," *Phys. Rev. B*, vol. 3, pp. 305–320, Jan 1971.
- [40] J. M. Ziman, *Electrons And Phonons. The Theory of Transport Phenomena in Solids*. Clarendon Press, Oxford, 1960.
- [41] S. I. Mirzaei, D. Stricker, J. N. Hancock, C. Berthod, A. Georges, E. van Heumen, M. K. Chan, X. Zhao, Y. Li, M. Greven, N. Barišić, and D. van der Marel, "Spectroscopic evidence for Fermi liquid-like energy and temperature dependence of the relaxation rate in the pseudogap phase of the cuprates," *Proceedings of the National Academy of Sciences*, vol. 110, no. 15, pp. 5774–5778, 2013.
- [42] F. Marsiglio, "Electron-phonon mass enhancement and lifetime at finite temperature," *Phys. Rev. B*, vol. 55, pp. 6674–6677, Mar 1997.
- [43] C. Berthod, "Private communication."
- [44] P. B. Allen and B. Mitrović, "Theory of superconducting T_c ," in *Solid State Physics* (F. S. Henry Ehrenreich and D. Turnbull, eds.), vol. 37 of *Solid State Physics*, pp. 1 – 92, Academic Press, 1983.
- [45] E. Maxwell, "Isotope effect in the superconductivity of mercury," *Physical Review*, vol. 78, pp. 477–477, May 1950.
- [46] C. A. Reynolds, B. Serin, W. H. Wright, and L. B. Nesbitt, "Superconductivity of isotopes of mercury," *Physical Review*, vol. 78, pp. 487–487, May 1950.
- [47] J. Bardeen, L. N. Cooper, and J. R. Schrieffer, "Microscopic theory of superconductivity," *Phys. Rev.*, vol. 106, pp. 162–164, Apr 1957.
- [48] P. W. Anderson, *The theory of superconductivity in the high- T_c cuprates*. Princeton University Press, 1997.

- [49] L. Landau, "Theory of Fermi-liquids," *Zh. Eksp. Teor. Fiz.*, vol. 30, p. 1058, 1956.
- [50] P. Misra, *Heavy-Fermion Systems*. Handbook of Metal Physics, Elsevier Science, 1st ed., 2008.
- [51] J. M. Luttinger, "Analytic properties of single-particle propagators for many-fermion systems," *Phys. Rev.*, vol. 121, pp. 942–949, Feb 1961.
- [52] A. H. MacDonald, R. Taylor, and D. J. W. Geldart, "Umklapp electron-electron scattering and the low-temperature electrical resistivity of the alkali metals," *Phys. Rev. B*, vol. 23, pp. 2718–2730, Mar 1981.
- [53] A. Ioffe and A. Regel *Prog. Semicond.*, vol. 4, no. 247, 1960.
- [54] M. Gurvitch, "Ioffe-Regel criterion and resistivity of metals," *Phys. Rev. B*, vol. 24, pp. 7404–7407, Dec 1981.
- [55] N. F. Mott and L. Friedman, "Metal-insulator transitions in VO_2 , Ti_2O_3 and $\text{Ti}_{2-x}\text{V}_x\text{O}_3$," *Philosophical Magazine*, vol. 30, no. 2, pp. 389–402, 1974.
- [56] R. N. Gurzhi, "Mutual electron correlations in metal optics," *Sov. Phys. JETP*, vol. 35, no. 4, p. 673, 1959.
- [57] N. E. Hussey, "Non-generality of the Kadowaki-Woods ratio in correlated oxides," *Journal of the Physical Society of Japan*, vol. 74, no. 4, pp. 1107–1110, 2005.
- [58] A. C. Jacko, J. O. Fjaerestad, and B. J. Powell, "A unified explanation of the Kadowaki-Woods ratio in strongly correlated metals," *Nat Phys*, vol. 5, pp. 422–425, 06 2009.
- [59] E. van Heumen, W. Meevasana, A. B. Kuzmenko, H. Eisaki, and D. van der Marel, "Doping-dependent optical properties of Bi2201 ," *New Journal of Physics*, vol. 11, p. 055067, May 2009.
- [60] C. M. Varma, P. B. Littlewood, S. Schmitt-Rink, E. Abrahams, and A. E. Ruckenstein, "Phenomenology of the normal state of Cu-O high-temperature superconductors," *Phys. Rev. Lett.*, vol. 63, pp. 1996–1999, Oct 1989.
- [61] A. J. Millis, H. Monien, and D. Pines, "Phenomenological model of nuclear relaxation in the normal state of $\text{YBa}_2\text{Cu}_3\text{O}_7$," *Phys. Rev. B*, vol. 42, pp. 167–178, Jul 1990.
- [62] A. Abrikosov, L. Gor'kov, I. Dzyaloshinski, and D. Zwigorski, *Methods of Quantum Field Theory in Statistical Physics*. Prentice-Hall, Englewood Cliffs, NJ, 1975.
- [63] C. Varma, Z. Nussinov, and W. van Saarloos, "Singular or non-Fermi liquids," *Physics Reports*, vol. 361, no. 5–6, pp. 267 – 417, 2002.
- [64] M. Čubrović, J. Zaanen, and K. Schalm, "String theory, quantum phase transitions, and the emergent Fermi liquid," *Science*, vol. 325, no. 5939, p. 439, 2009.
- [65] N. Luo and G. H. Miley, "An alternative theory on relaxation rates in cuprate superconductors," *Journal of Physics: Condensed Matter*, vol. 21, no. 2, p. 025701, 2009.
- [66] S. Uchida, T. Ido, H. Takagi, T. Arima, Y. Tokura, and S. Tajima, "Optical spectra of $\text{La}_{2-x}\text{Sr}_x\text{CuO}_4$: Effect of carrier doping on the electronic structure of the CuO_2 plane," *Phys. Rev. B*, vol. 43, pp. 7942–7954, Apr 1991.
- [67] D. N. Basov and T. Timusk, "Electrodynamics of high- T_c superconductors," *Rev. Mod. Phys.*, vol. 77, pp. 721–779, Aug 2005.
- [68] D. N. Basov, R. D. Averitt, D. van der Marel, M. Dressel, and K. Haule, "Electrodynamics of correlated electron materials," *Rev. Mod. Phys.*, vol. 83, pp. 471–541, Jun 2011.
- [69] J. C. Slater, "Microwave electronics," *Rev. Mod. Phys.*, vol. 18, pp. 441–512, Oct 1946.
- [70] M. Scheffler, M. Dressel, M. Jourdan, and H. Adrian, "Extremely slow Drude relaxation of correlated electrons," *Nature*, vol. 438, pp. 1135–1137, 12 2005.
- [71] M. G. Hildebrand, M. Reedyk, T. Katsufuji, and Y. Tokura, "Far-infrared resonance in Sr_2RuO_4 ," *Phys. Rev. Lett.*, vol. 87, p. 227002, 2001.
- [72] P. R. Griffiths and C. C. Homes, "Instrumentation for far-infrared spectroscopy," in *Handbook of Vibrational Spectroscopy*, John Wiley & Sons, Ltd, 2006.
- [73] "Guide for infrared spectroscopy," tech. rep., Bruker Optics, 2011.
- [74] J. Woolam, "A short course in ellipsometry."
- [75] H. Fujiwara, *Spectroscopic Ellipsometry: Principles and Applications*. Wiley, 1st ed., March 2007.
- [76] D. Aspnes, "Interface ellipsometry: An overview," *Surface Science*, vol. 101, no. 1–3, pp. 84 – 98, 1980.
- [77] T. Katsufuji, M. Kasai, and Y. Tokura, "In-plane and out-of-plane optical spectra of Sr_2RuO_4 ," *Phys. Rev. Lett.*, vol. 76, pp. 126–129, Jan 1996.

BIBLIOGRAPHY

- [78] C. Proust, E. Boaknin, R. W. Hill, L. Taillefer, and A. P. Mackenzie, "Heat transport in a strongly overdoped cuprate: Fermi liquid and a pure d -wave BCS superconductor," *Phys. Rev. Lett.*, vol. 89, p. 147003, Sep 2002.
- [79] B. Vignolle, a. Carrington, R. a. Cooper, M. M. J. French, a. P. Mackenzie, C. Jaudet, D. Vignolles, C. Proust, and N. E. Hussey, "Quantum oscillations in an overdoped high- T_c superconductor," *Nature*, vol. 455, pp. 952–955, Oct. 2008.
- [80] M. Platé, J. D. F. Mottershead, I. S. Elfimov, D. C. Peets, R. Liang, D. A. Bonn, W. N. Hardy, S. Chizbaian, M. Falub, M. Shi, L. Patthey, and A. Damascelli, "Fermi surface and quasiparticle excitations of overdoped $Tl_2Ba_2CuO_{6+\delta}$," *Phys. Rev. Lett.*, vol. 95, p. 077001, Aug 2005.
- [81] N. Barišić, Y. Li, X. Zhao, Y.-C. Cho, G. Chabot-Couture, G. Yu, and M. Greven, "Demonstrating the model nature of the high-temperature superconductor $HgBa_2CuO_{4+\delta}$," *Physical Review B*, vol. 78, pp. 1–7, Aug. 2008.
- [82] A. Mann, *High-temperature at 25: Still in suspense*, vol. 475. Nature Publishing Group, 2011.
- [83] O. Fischer, M. Kugler, I. Maggio-Aprile, C. Berthod, and C. Renner, "Scanning tunneling spectroscopy of high-temperature superconductors," *Rev. Mod. Phys.*, vol. 79, pp. 353–419, Mar 2007.
- [84] W. E. Pickett, "Electronic structure of the high-temperature oxide superconductors," *Rev. Mod. Phys.*, vol. 61, pp. 433–512, Apr 1989.
- [85] T. Timusk and B. Statt, "The pseudogap in high-temperature superconductors: an experimental survey," *Reports on Progress in Physics*, vol. 62, pp. 61–122, Jan. 1999.
- [86] E. Uykur, *Pseudogap and Precursor Superconductivity Study of Zn doped YBCO*. Springer Theses, Springer Japan, 2015.
- [87] E. Pavarini, I. Dasgupta, T. Saha-Dasgupta, O. Jepsen, and O. K. Andersen, "Band-structure trend in hole-doped cuprates and correlation with $T_{c,max}$," *Phys. Rev. Lett.*, vol. 87, p. 047003, Jul 2001.
- [88] P. A. Lee, N. Nagaosa, and X.-G. Wen, "Doping a Mott insulator: Physics of high-temperature superconductivity," *Rev. Mod. Phys.*, vol. 78, pp. 17–85, Jan 2006.
- [89] K. Segawa, M. Kofu, S.-H. Lee, I. Tsukada, H. Hiraka, M. Fujita, S. Chang, K. Yamada, and Y. Ando, "Zero-doping state and electron-hole asymmetry in an ambipolar cuprate," *Nat Phys*, vol. 6, pp. 579–583, 08 2010.
- [90] F. C. Zhang and T. M. Rice, "Effective hamiltonian for the superconducting Cu oxides," *Phys. Rev. B*, vol. 37, pp. 3759–3761, Mar 1988.
- [91] C. C. Tsuei and J. R. Kirtley, "Pairing symmetry in cuprate superconductors," *Rev. Mod. Phys.*, vol. 72, pp. 969–1016, Oct 2000.
- [92] E. Uykur, K. Tanaka, T. Masui, S. Miyasaka, and S. Tajima, "Persistence of the superconducting condensate far above the critical temperature of $YBa_2(Cu,Zn)_3O_y$ revealed by c -axis optical conductivity measurements for several Zn concentrations and carrier doping levels," *Phys. Rev. Lett.*, vol. 112, p. 127003, Mar 2014.
- [93] D. A. Wollman, D. J. Van Harlingen, W. C. Lee, D. M. Ginsberg, and A. J. Leggett, "Experimental determination of the superconducting pairing state in YBCO from the phase coherence of YBCO-Pb dc SQUIDs," *Phys. Rev. Lett.*, vol. 71, pp. 2134–2137, Sep 1993.
- [94] C. C. Tsuei, J. R. Kirtley, M. Rupp, J. Z. Sun, A. Gupta, M. B. Ketchen, C. A. Wang, Z. F. Ren, J. H. Wang, and M. Bhushan, "Pairing symmetry in single-layer tetragonal $Tl_2Ba_2CuO_+$ superconductors," *Science*, vol. 271, no. 5247, pp. 329–332, 1996.
- [95] A. J. Leggett, "What DO we know about high T_c ?," *Nat Phys*, vol. 2, pp. 134–136, 03 2006.
- [96] D. B. Romero, C. D. Porter, D. B. Tanner, L. Forro, D. Mandrus, L. Mihaly, G. L. Carr, and G. P. Williams, "Quasiparticle damping in $Bi_2Sr_2CaCu_2O_8$ and $Bi_2Sr_2CuO_6$," *Phys. Rev. Lett.*, vol. 68, pp. 1590–1593, Mar 1992.
- [97] C. Renner, B. Revaz, J.-Y. Genoud, K. Kadowaki, and O. Fischer, "Pseudogap precursor of the superconducting gap in under- and overdoped $Bi_2Sr_2CaCu_2O_{8+\delta}$," *Phys. Rev. Lett.*, vol. 80, pp. 149–152, Jan 1998.
- [98] J. E. Hoffman, "High-temperature superconductivity: To pair or not to pair?," *Nat Phys*, vol. 6, pp. 404–405, 06 2010.
- [99] T. Kondo, R. Khasanov, T. Takeuchi, J. Schmalian, and A. Kaminski, "Competition between the pseudogap and superconductivity in the high- T_c copper oxides," *Nature*, vol. 457, pp. 296–300, 01 2009.
- [100] A. Sacuto, Y. Gallais, M. Cazayous, M.-A. Méason, G. D. Gu, and D. Colson, "New insights into the phase diagram of the copper oxide superconductors from electronic Raman scattering," *Reports on Progress in Physics*, vol. 76, no. 2, p. 022502, 2013.

- [101] J. W. Loram, K. A. Mirza, J. R. Cooper, W. Y. Liang, and J. M. Wade, “Electronic specific heat of $\text{YBa}_2\text{Cu}_3\text{O}_{6+x}$ from 1.8 to 300 K,” *Journal of Superconductivity*, vol. 7, no. 1, pp. 243–249, 1994.
- [102] J. Tallon and J. Loram, “The doping dependence of T^* - what is the real high- T_c phase diagram?,” *Physica C: Superconductivity*, vol. 349, pp. 53–68, Jan. 2001.
- [103] L. Taillefer, “Scattering and pairing in cuprate superconductors,” *Annual Review of Condensed Matter Physics*, vol. 1, no. 1, pp. 51–70, 2010.
- [104] N. Barišić, M. K. Chan, Y. Li, G. Yu, X. Zhao, M. Dressel, A. Smontara, and M. Greven, “Universal sheet resistance and revised phase diagram of the cuprate high-temperature superconductors,” *Proceedings of the National Academy of Sciences*, vol. 110, pp. 12235–12240, 07 2013.
- [105] Y. Ando, S. Komiyama, K. Segawa, S. Ono, and Y. Kurita, “Electronic phase diagram of high- T_c cuprate superconductors from a mapping of the in-plane resistivity curvature,” *Phys. Rev. Lett.*, vol. 93, p. 267001, Dec 2004.
- [106] T. Sato, H. Matsui, S. Nishina, T. Takahashi, T. Fujii, T. Watanabe, and A. Matsuda, “Low energy excitation and scaling in $\text{Bi}_2\text{Sr}_2\text{Ca}_{n-1}\text{Cu}_n\text{O}_{2n+4}$ ($n = 1 - 3$): Angle-resolved photoemission spectroscopy,” *Phys. Rev. Lett.*, vol. 89, p. 067005, Jul 2002.
- [107] H. Alloul, T. Ohno, and P. Mendels, “ ^{89}Y NMR evidence for a Fermi-Liquid behavior in $\text{YBa}_2\text{Cu}_3\text{O}_{6+x}$,” *Phys. Rev. Lett.*, vol. 63, pp. 1700–1703, Oct 1989.
- [108] N. Hussey, “What drives pseudogap physics in high- T_c cuprates? a view from the (resistance) bridge,” *Journal of Physics and Chemistry of Solids*, vol. 72, pp. 529–532, May 2011.
- [109] H. Ding, T. Yokoya, J. C. Campuzano, T. Takahashi, M. Randeria, M. R. Norman, T. Mochiku, K. Kadowaki, and J. Giapintzakis, “Spectroscopic evidence for a pseudogap in the normal state of underdoped high- T_c superconductors,” *Nature*, vol. 382, pp. 51–54, July 1996.
- [110] S. E. Sebastian, N. Harrison, and G. G. Lonzarich, “Quantum oscillations in the high- T_c cuprates,” *Philosophical Transactions of the Royal Society of London A: Mathematical, Physical and Engineering Sciences*, vol. 369, no. 1941, pp. 1687–1711, 2011.
- [111] K. M. Shen, F. Ronning, D. H. Lu, F. Baumberger, N. J. C. Ingle, W. S. Lee, W. Meevasana, Y. Kohsaka, M. Azuma, M. Takano, H. Takagi, and Z.-X. Shen, “Nodal quasiparticles and antinodal charge ordering in $\text{Ca}_{2-x}\text{Na}_x\text{CuO}_2\text{Cl}_2$,” *Science*, vol. 307, no. 5711, pp. 901–904, 2005.
- [112] N. Doiron-Leyraud, C. Proust, D. LeBoeuf, J. Levallois, J.-B. Bonnemaïson, R. Liang, D. A. Bonn, W. N. Hardy, and L. Taillefer, “Quantum oscillations and the Fermi surface in an underdoped high- T_c superconductor,” *Nature*, vol. 447, pp. 565–568, 05 2007.
- [113] D. LeBoeuf, N. Doiron-Leyraud, J. Levallois, R. Daou, J. B. Bonnemaïson, N. E. Hussey, L. Balicas, B. J. Ramshaw, R. Liang, D. A. Bonn, W. N. Hardy, S. Adachi, C. Proust, and L. Taillefer, “Electron pockets in the Fermi surface of hole-doped high- T_c superconductors,” *Nature*, vol. 450, pp. 533–536, 11 2007.
- [114] J. Orenstein, G. A. Thomas, A. J. Millis, S. L. Cooper, D. H. Rapkine, T. Timusk, L. F. Schneemeyer, and J. V. Waszczak, “Frequency- and temperature-dependent conductivity in $\text{YBa}_2\text{Cu}_3\text{O}_{6+x}$ crystals,” *Phys. Rev. B*, vol. 42, pp. 6342–6362, Oct 1990.
- [115] I. M. Vishik, W. S. Lee, R.-H. He, M. Hashimoto, Z. Hussain, T. P. Devereaux, and Z.-X. Shen, “ARPES studies of cuprate fermiology: superconductivity, pseudogap and quasiparticle dynamics,” *New Journal of Physics*, vol. 12, no. 10, p. 105008, 2010.
- [116] S. Hufner, M. A. Hossain, A. Damascelli, and G. A. Sawatzky, “Two gaps make a high-temperature superconductor?,” *Reports on Progress in Physics*, vol. 71, no. 6, p. 062501, 2008.
- [117] W. F. Brinkman and T. M. Rice, “Application of gutzwiller’s variational method to the metal-insulator transition,” *Phys. Rev. B*, vol. 2, pp. 4302–4304, Nov 1970.
- [118] B. Edegger, V. N. Muthukumar, and C. Gros, “Gutzwiller–RVB theory of high-temperature superconductivity: Results from renormalized mean-field theory and variational Monte Carlo calculations,” *Advances in Physics*, vol. 56, no. 6, pp. 927–1033, 2007.
- [119] M. Ogata and H. Fukuyama, “The $t - j$ model for the oxide high- T_c superconductors,” *Reports on Progress in Physics*, vol. 71, no. 3, p. 036501, 2008.
- [120] C. M. Varma, “Pseudogap phase and the quantum-critical point in copper-oxide metals,” *Phys. Rev. Lett.*, vol. 83, pp. 3538–3541, Oct 1999.
- [121] C. M. Varma, “Theory of the pseudogap state of the cuprates,” *Phys. Rev. B*, vol. 73, p. 155113, Apr 2006.

BIBLIOGRAPHY

- [122] J. Xia, E. Schemm, G. Deutscher, S. A. Kivelson, D. A. Bonn, W. N. Hardy, R. Liang, W. Siemons, G. Koster, M. M. Fejer, and A. Kapitulnik, “Polar kerr-effect measurements of the high-temperature $\text{YBa}_2\text{Cu}_3\text{O}_{6+x}$ superconductor: Evidence for broken symmetry near the pseudogap temperature,” *Phys. Rev. Lett.*, vol. 100, p. 127002, Mar 2008.
- [123] H. Karapetyan, J. Xia, M. Hücker, G. D. Gu, J. M. Tranquada, M. M. Fejer, and A. Kapitulnik, “Evidence of chiral order in the charge-ordered phase of superconducting $\text{La}_{1.875}\text{Ba}_{0.125}\text{CuO}_4$ single crystals using polar Kerr-effect measurements,” *Phys. Rev. Lett.*, vol. 112, p. 047003, Jan 2014.
- [124] Y. Li, V. Baledent, G. Yu, N. Barisic, K. Hradil, R. A. Mole, Y. Sidis, P. Steffens, X. Zhao, P. Bourges, and M. Greven, “Hidden magnetic excitation in the pseudogap phase of a high-Tc superconductor,” *Nature*, vol. 468, pp. 283–285, 11 2010.
- [125] T. M. Rice, K.-Y. Yang, and F. C. Zhang, “A phenomenological theory of the anomalous pseudogap phase in underdoped cuprates,” *Reports on Progress in Physics*, vol. 75, no. 1, p. 016502, 2012.
- [126] T. Wu, H. Mayaffre, S. Kramer, M. Horvatic, C. Berthier, W. N. Hardy, R. Liang, D. A. Bonn, and M.-H. Julien, “Magnetic-field-induced charge-stripe order in the high-temperature superconductor $\text{YBa}_2\text{Cu}_3\text{O}_y$,” *Nature*, vol. 477, pp. 191–194, 09 2011.
- [127] T. Wu, H. Mayaffre, S. Krämer, M. Horvatic, C. Berthier, P. L. Kuhns, A. P. Reyes, R. Liang, W. N. Hardy, D. A. Bonn, and M.-H. Julien, “Emergence of charge order from the vortex state of a high-temperature superconductor,” *Nat Commun*, vol. 4, 07 2013.
- [128] T. Wu, H. Mayaffre, S. Krämer, M. Horvatic, C. Berthier, W. N. Hardy, R. Liang, D. A. Bonn, and M.-H. Julien, “Incipient charge order observed by NMR in the normal state of $\text{YBa}_2\text{Cu}_3\text{O}_y$,” *Nat Commun*, vol. 6, 03 2015.
- [129] E. Fradkin and S. A. Kivelson, “High-temperature superconductivity: Ineluctable complexity,” *Nat Phys*, vol. 8, pp. 864–866, 12 2012.
- [130] X. Zhao, G. Yu, Y.-C. Cho, G. Chabot-Couture, N. Barišić, P. Bourges, N. Kaneko, Y. Li, L. Lu, E. Motoyama, O. Vajk, and M. Greven, “Crystal growth and characterization of the model high-temperature superconductor $\text{HgBa}_2\text{CuO}_{4+}$,” *Advanced Materials*, vol. 18, no. 24, pp. 3243–3247, 2006.
- [131] S. I. Mirzaei, *Low energy electrodynamics of high temperature superconductors*. PhD thesis, Université de Genève, 2013.
- [132] N. Barišić, M. K. Chan, M. J. Veit, C. J. Dorow, Y. Ge, Y. Tang, W. Tabis, G. Yu, X. Zhao, and M. Greven, “Hidden Fermi-liquid behavior throughout the phase diagram of the cuprates,” *ArXiv e-prints*, July 2015.
- [133] S. Tajima, T. Ido, S. Ishibashi, T. Itoh, H. Eisaki, Y. Mizuo, T. Arima, H. Takagi, and S. Uchida, “Optical-phonon study of single crystals of various layered cuprates and related materials: Evidence of unique electron-phonon coupling in the CuO_2 plane,” *Phys. Rev. B*, vol. 43, pp. 10496–10507, May 1991.
- [134] D. van der Marel and A. Tsvetkov, “Transverse optical plasmons in layered superconductors,” *Czechoslovak Journal of Physics*, vol. 46, no. 6, pp. 3165–3168, 1996.
- [135] D. van der Marel, “Anisotropy of the optical conductivity of high-Tc cuprates,” *Phys. Rev. B*, vol. 60, pp. R765–R768, Jul 1999.
- [136] L. Lu, G. Chabot-Couture, X. Zhao, J. N. Hancock, N. Kaneko, O. P. Vajk, G. Yu, S. Grenier, Y. J. Kim, D. Casa, T. Gog, and M. Greven, “Charge-transfer excitations in the model superconductor $\text{HgBa}_2\text{CuO}_{4+\delta}$,” *Phys. Rev. Lett.*, vol. 95, p. 217003, Nov 2005.
- [137] M. Holcomb, J. Collman, and W. Little, “Optical evidence of an electronic contribution to the pairing interaction in superconducting $\text{Tl}_2\text{Ba}_2\text{Ca}_2\text{Cu}_3\text{O}_{10}$,” *Physical Review Letters*, pp. 2360–2363, Oct.
- [138] M. Rübhausen, A. Gozar, M. V. Klein, P. Gopatasarma, and D. G. Hinks, “Superconductivity-induced optical changes for energies of 100Δ in the cuprates,” *Physical Review B*, vol. 63, p. 224514, May 2001.
- [139] H. J. A. Molegraaf, C. Presura, D. van der Marel, P. H. Kes, and M. Li, “Superconductivity-induced transfer of in-plane spectral weight in $\text{Bi}_2\text{Sr}_2\text{CaCu}_2\text{O}_{8+}$,” *Science*, vol. 295, no. 5563, pp. 2239–2241, 2002.
- [140] a. V. Boris, N. N. Kovaleva, O. V. Dolgov, T. Holden, C. T. Lin, B. Keimer, and C. Bernhard, “In-plane spectral weight shift of charge carriers in $\text{YBa}_2\text{Cu}_3\text{O}_{6.9}$,” *Science (New York, N.Y.)*, vol. 304, pp. 708–10, Apr. 2004.
- [141] A. Santander-Syro, R. Lobo, N. Bontemps, W. Lopera, D. Giratá, Z. Konstantinovic, Z. Li, and H. Raffy, “In-plane electrodynamics of the

- superconductivity in $\text{Bi}_2\text{Sr}_2\text{CaCu}_2\text{O}_{8+\delta}$: Energy scales and spectral weight distribution,” *Physical Review B*, vol. 70, p. 134504, Oct. 2004.
- [142] F. Marsiglio, “Optical sum rule anomalies in the high- T_c cuprates,” *Journal of Superconductivity and Novel Magnetism*, vol. 22, pp. 269–273, Jan. 2009.
- [143] C. Giannetti, F. Cilento, S. Dal Conte, G. Coslovich, G. Ferrini, H. J. A. Molegraaf, M. Raichle, R. Liang, H. Eisaki, M. Greven, Others, A. Damascelli, D. van der Marel, and F. Parmigiani, “Revealing the high-energy electronic excitations underlying the onset of high-temperature superconductivity in cuprates,” *Nature communications*, vol. 2, p. 353, Jan. 2011.
- [144] J. M. WHEATLEY, T. C. HSU, and P. W. ANDERSON, “Interlayer effects in high- T_c superconductors,” *Nature*, vol. 333, pp. 121–121, May 1988.
- [145] J. Hirsch and F. Marsiglio, “Hole superconductivity: Review and some new results,” *Physica C: Superconductivity*, vol. 162-164, pp. 591–598, Dec. 1989.
- [146] F. Marsiglio and J. Hirsch, “Hole superconductivity and the high- T_c oxides,” *Physical Review B*, vol. 41, pp. 6435–6456, Apr. 1990.
- [147] J. Hirsch, “Apparent violation of the conductivity sum rule in certain superconductors,” *Physica C: Superconductivity*, vol. 199, pp. 305–310, Sept. 1992.
- [148] J. Hirsch, “Superconductors that change color when they become superconducting,” *Physica C: Superconductivity*, vol. 201, pp. 347–361, Oct. 1992.
- [149] M. A. Quijada, D. B. Tanner, R. J. Kelley, M. Onellion, H. Berger, and G. Margaritondo, “Anisotropy in the ab -plane optical properties of $\text{Bi}_2\text{Sr}_2\text{CaCu}_2\text{O}_8$ single-domain crystals,” *Phys. Rev. B*, vol. 60, pp. 14917–14934, Dec 1999.
- [150] D. van der Marel, H. J. A. Molegraaf, J. Zaanen, Z. Nussinov, F. Carbone, A. Damascelli, H. Eisaki, M. Greven, P. H. Kes, and M. Li, “Quantum critical behaviour in a high- T_c superconductor,” *Nature*, vol. 425, pp. 271–4, Sept. 2003.
- [151] F. Carbone, A. B. Kuzmenko, H. J. A. Molegraaf, E. van Heumen, E. Giannini, and D. van der Marel, “In-plane optical spectral weight transfer in optimally doped $\text{Bi}_2\text{Sr}_2\text{Ca}_2\text{Cu}_3\text{O}_{10}$,” *Phys. Rev. B*, vol. 74, p. 024502, Jul 2006.
- [152] Y. J. Uemura, G. M. Luke, B. J. Sternlieb, J. H. Brewer, J. F. Carolan, W. N. Hardy, R. Kadono, J. R. Kempton, R. F. Kiefl, S. R. Kreitzman, P. Mulhern, T. M. Riseman, D. L. Williams, B. X. Yang, S. Uchida, H. Takagi, J. Gopalakrishnan, A. W. Sleight, M. A. Subramanian, C. L. Chien, M. Z. Cieplak, G. Xiao, V. Y. Lee, B. W. Statt, C. E. Stronach, W. J. Kossler, and X. H. Yu, “Universal correlations between T_c and $\frac{n_s}{m^*}$ (carrier density over effective mass) in high- T_c cuprate superconductors,” *Phys. Rev. Lett.*, vol. 62, pp. 2317–2320, May 1989.
- [153] C. C. Homes, S. V. Dordevic, M. Strongin, D. A. Bonn, R. Liang, W. N. Hardy, S. Komiyama, Y. Ando, G. Yu, N. Kaneko, X. Zhao, M. Greven, D. N. Basov, and T. Timusk, “A universal scaling relation in high-temperature superconductors,” *Nature*, vol. 430, pp. 539–541, 07 2004.
- [154] E. van Heumen, E. Muhlethaler, A. B. Kuzmenko, H. Eisaki, W. Meevasana, M. Greven, and D. van der Marel, “Optical determination of the relation between the electron-boson coupling function and the critical temperature in high- T_c cuprates,” *Phys. Rev. B*, vol. 79, p. 184512, May 2009.
- [155] F. Carbone, A. B. Kuzmenko, H. J. A. Molegraaf, E. van Heumen, V. Lukovac, F. Marsiglio, D. van der Marel, K. Haule, G. Kotliar, H. Berger, S. Courjault, P. H. Kes, and M. Li, “Doping dependence of the redistribution of optical spectral weight in $\text{Bi}_2\text{Sr}_2\text{CaCu}_2\text{O}_{8+\delta}$,” *Phys. Rev. B*, vol. 74, p. 064510, Aug 2006.
- [156] G. A. Thomas, J. Orenstein, D. H. Rapkine, M. Capizzi, A. J. Millis, R. N. Bhatt, L. F. Schneemeyer, and J. V. Waszczak, “ $\text{Ba}_2\text{YCu}_3\text{O}_{7-\delta}$: Electrodynamics of crystals with high reflectivity,” *Phys. Rev. Lett.*, vol. 61, pp. 1313–1316, Sep 1988.
- [157] A. Comanac, L. de’ Medici, M. Capone, and A. J. Millis, “Optical conductivity and the correlation strength of high-temperature copper-oxide superconductors,” *Nature Physics*, vol. 4, pp. 287–290, 04 2008.
- [158] W. J. Padilla, Y. S. Lee, M. Dumm, G. Blumberg, S. Ono, K. Segawa, S. Komiyama, Y. Ando, and D. N. Basov, “Constant effective mass across the phase diagram of high- T_c cuprates,” *Phys. Rev. B*, vol. 72, p. 060511, Aug 2005.
- [159] D. Fournier, G. Levy, Y. Pennec, J. L. McChesney, A. Bostwick, E. Rotenberg, R. Liang, W. N. Hardy, D. A. Bonn, I. S. Elfimov, and A. Damascelli, “Loss of nodal quasiparticle integrity in underdoped $\text{YBa}_2\text{Cu}_3\text{O}_{6+x}$,” *Nat Phys*, vol. 6, pp. 905–911, 11 2010.

BIBLIOGRAPHY

- [160] A. Kanigel, M. R. Norman, M. Randeria, U. Chatterjee, S. Souma, A. Kaminski, H. M. Fretwell, S. Rosenkranz, M. Shi, T. Sato, T. Takahashi, Z. Z. Li, H. Raffy, K. Kadowaki, D. Hinks, L. Ozyuzer, and J. C. Campuzano, “Evolution of the pseudogap from Fermi arcs to the nodal liquid,” *Nat Phys*, vol. 2, pp. 447–451, 07 2006.
- [161] M. Norman, A. Chubukov, E. van Heumen, A. B. Kuzmenko, and D. van der Marel, “Optical integral in the cuprates and the question of sum-rule violation,” *Physical Review B*, vol. 76, Dec. 2007.
- [162] F. Marsiglio, F. Carbone, A. B. Kuzmenko, and D. van der Marel, “Intraband optical spectral weight in the presence of a van hove singularity: Application to $\text{Bi}_2\text{Sr}_2\text{CaCu}_2\text{O}_{8+\delta}$,” *Phys. Rev. B*, vol. 74, p. 174516, Nov 2006.
- [163] M. J. Rozenberg, G. Kotliar, H. Kajueter, G. A. Thomas, D. H. Rapkine, J. M. Honig, and P. Metcalf, “Optical conductivity in Mott-Hubbard systems,” *Phys. Rev. Lett.*, vol. 75, pp. 105–108, Jul 1995.
- [164] A. F. Santander-Syro, R. P. S. M. Lobo, N. Bonemps, Z. Konstantinovic, Z. Li, and H. Raffy, “Absence of a loss of in-plane infrared spectral weight in the pseudogap regime of $\text{Bi}_2\text{Sr}_2\text{CaCu}_2\text{O}_{8+\delta}$,” *Phys. Rev. Lett.*, vol. 88, p. 097005, Feb 2002.
- [165] Y. Li, G. Yu, M. K. Chan, V. Baledent, Y. Li, N. Barisic, X. Zhao, K. Hradil, R. A. Mole, Y. Sidis, P. Steffens, P. Bourges, and M. Greven, “Two Ising-like magnetic excitations in a single-layer cuprate superconductor,” *Nature Physics*, vol. 8, pp. 404–410, 05 2012.
- [166] I. M. Vishik, N. Barišić, M. K. Chan, Y. Li, D. D. Xia, G. Yu, X. Zhao, W. S. Lee, W. Meevasana, T. P. Devereaux, M. Greven, and Z.-X. Shen, “Angle-resolved photoemission spectroscopy study of $\text{HgBa}_2\text{CuO}_{4+\delta}$,” *Phys. Rev. B*, vol. 89, p. 195141, May 2014.
- [167] J. Hwang, J. Yang, T. Timusk, S. G. Sharapov, J. P. Carbotte, D. A. Bonn, R. Liang, and W. N. Hardy, “*a*-axis optical conductivity of detwinned ortho-II $\text{YBa}_2\text{Cu}_3\text{O}_{6.50}$,” *Phys. Rev. B*, vol. 73, p. 014508, Jan 2006.
- [168] H. Eisaki, N. Kaneko, D. Feng, a. Damascelli, P. Mang, K. Shen, Z.-X. Shen, and M. Greven, “Effect of chemical inhomogeneity in bismuth-based copper oxide superconductors,” *Physical Review B*, vol. 69, p. 064512, Feb. 2004.
- [169] C. Varma, “High-temperature superconductivity: Mind the pseudogap,” *Nature*, vol. 468, pp. 184–5, Nov. 2010.
- [170] V. Barzykin and D. Pines, “Universal behaviour and the two-component character of magnetically underdoped cuprate superconductors,” *Advances in Physics*, vol. 58, no. 1, pp. 1–65, 2009.
- [171] A. V. Chubukov and D. L. Maslov, “Singular corrections to the Fermi-liquid theory,” *Phys. Rev. B*, vol. 69, p. 121102, Mar 2004.
- [172] D. Tanner and T. Timusk, “Physical properties of high temperature superconductors iii,” 1992.
- [173] D. N. Basov, C. C. Homes, E. J. Singley, M. Strongin, T. Timusk, G. Blumberg, and D. van der Marel, “Unconventional energetics of the pseudogap state and superconducting state in high- T_c cuprates,” *Phys. Rev. B*, vol. 63, p. 134514, Mar 2001.
- [174] K. Haule and G. Kotliar, “Strongly correlated superconductivity: A plaquette dynamical mean-field theory study,” *Phys. Rev. B*, vol. 76, p. 104509, Sep 2007.
- [175] J. A. Nelder and R. Mead, “A simplex method for function minimization,” *The Computer Journal*, vol. 7, no. 4, pp. 308–313, 1965.
- [176] M. Alan, *Least-squares computations*, ch. 2, p. 11. Chapman and Hall/CRC, 2015/10/11 2002.
- [177] S. V. Dordevic, C. C. Homes, J. J. Tu, T. Valla, M. Strongin, P. D. Johnson, G. D. Gu, and D. N. Basov, “Extracting the electron-boson spectral function $\alpha^2F(\omega)$ from infrared and photoemission data using inverse theory,” *Phys. Rev. B*, vol. 71, p. 104529, Mar 2005.
- [178] N. Plakida, *High-Temperature Cuprate Superconductors: Experiment, Theory, and Applications*. Springer Series in Solid-State Sciences, Springer Berlin Heidelberg, 2010.
- [179] E. Gull, M. Ferrero, O. Parcollet, A. Georges, and A. J. Millis, “Momentum-space anisotropy and pseudogaps: A comparative cluster dynamical mean-field analysis of the doping-driven metal-insulator transition in the two-dimensional Hubbard model,” *Phys. Rev. B*, vol. 82, p. 155101, Oct 2010.
- [180] B. S. Shastry, “Extremely correlated Fermi liquids,” *Phys. Rev. Lett.*, vol. 107, p. 056403, Jul 2011.
- [181] D. Bergeron, V. Hankevych, B. Kyung, and A.-M. S. Tremblay, “Optical and dc conductivity of the two-dimensional Hubbard model in the pseudogap regime and across the antiferromagnetic quantum critical point including vertex corrections,” *Phys. Rev. B*, vol. 84, p. 085128, Aug 2011.

- [182] P. W. Anderson, "Hidden Fermi liquid: The secret of high- T_c cuprates," *Phys. Rev. B*, vol. 78, p. 174505, Nov 2008.
- [183] L. B. Ioffe and A. J. Millis, "Zone-diagonal-dominated transport in high- T_c cuprates," *Phys. Rev. B*, vol. 58, pp. 11631–11637, Nov 1998.
- [184] B. P. Stojkovic-acute and D. Pines, "Theory of the longitudinal and Hall conductivities of the cuprate superconductors," *Phys. Rev. B*, vol. 55, pp. 8576–8595, Apr 1997.
- [185] S. Nakamae, K. Behnia, N. Mangkorntong, M. Nohara, H. Takagi, S. J. C. Yates, and N. E. Hussey, "Electronic ground state of heavily overdoped nonsuperconducting $\text{La}_{2-x}\text{Sr}_x\text{CuO}_4$," *Phys. Rev. B*, vol. 68, p. 100502, Sep 2003.
- [186] N. E. Hussey, A. P. Mackenzie, J. R. Cooper, Y. Maeno, S. Nishizaki, and T. Fujita, "Normal-state magnetoresistance of Sr_2RuO_4 ," *Phys. Rev. B*, vol. 57, pp. 5505–5511, Mar 1998.
- [187] A. P. Mackenzie and Y. Maeno, "The superconductivity of Sr_2RuO_4 and the physics of spin-triplet pairing," *Rev. Mod. Phys.*, vol. 75, no. 2, pp. 657–725, 2003.
- [188] C. Kallin, "Chiral p -wave order in Sr_2RuO_4 ," *Rep. Prog. Phys.*, vol. 75, no. 4, p. 042501, 2012.
- [189] X. Deng, J. Mravlje, R. Zitko, M. Ferrero, G. Kotliar, and A. Georges, "How bad metals turn good: Spectroscopic signatures of resilient quasiparticles," *Phys. Rev. Lett.*, vol. 110, p. 086401, Feb 2013.
- [190] D. Stricker, J. Mravlje, C. Berthod, R. Fittipaldi, A. Vecchione, A. Georges, and D. van der Marel, "Optical response of Sr_2RuO_4 reveals universal Fermi-Liquid scaling and quasiparticles beyond Landau theory," *Phys. Rev. Lett.*, vol. 113, p. 087404, Aug 2014.
- [191] S. N. Ruddlesden and P. Popper, "New compounds of the K_2NiF_4 type," *Acta Crystallographica*, pp. 538–539, Aug.
- [192] M. K. Crawford, R. L. Harlow, W. Marshall, Z. Li, G. Cao, R. L. Lindstrom, Q. Huang, and J. W. Lynn, "Structure and magnetism of single crystal $\text{Sr}_4\text{Ru}_3\text{O}_{10}$: A ferromagnetic triple-layer ruthenate," *Phys. Rev. B*, vol. 65, p. 214412, May 2002.
- [193] B. Hu, G. T. McCandless, M. Menard, V. B. Nascimento, J. Y. Chan, E. W. Plummer, and R. Jin, "Surface and bulk structural properties of single-crystalline $\text{Sr}_3\text{Ru}_2\text{O}_7$," *Phys. Rev. B*, vol. 81, p. 184104, May 2010.
- [194] S. S. Kim, T. S. Kang, and J. H. Je, "Structural evolution of epitaxial SrRuO_3 thin films grown on $\text{SrTiO}_3(001)$," *Journal of Applied Physics*, vol. 90, no. 9, p. 4407, 2001.
- [195] S. Nakatsuji and Y. Maeno, "Switching of magnetic coupling by a structural symmetry change near the mott transition in $\text{Ca}_{2-x}\text{Sr}_x\text{RuO}_4$," *Phys. Rev. B*, vol. 62, pp. 6458–6466, Sep 2000.
- [196] Z. Fang and K. Terakura, "Magnetic phase diagram of $\text{Ca}_{2-x}\text{Sr}_x\text{RuO}_4$ governed by structural distortions," *Phys. Rev. B*, vol. 64, p. 020509, Jun 2001.
- [197] H. Shaked, J. Jorgensen, O. Chmaissem, S. Ikeda, and Y. Maeno, "Neutron diffraction study of the structural distortions in $\text{Sr}_3\text{Ru}_2\text{O}_7$," *Journal of Solid State Chemistry*, vol. 154, no. 2, pp. 361–367, 2000.
- [198] R. S. Perry, L. M. Galvin, S. A. Grigera, L. Capogna, A. J. Schofield, A. P. Mackenzie, M. Chiao, S. R. Julian, S. I. Ikeda, S. Nakatsuji, Y. Maeno, and C. Pfleiderer, "Metamagnetism and critical fluctuations in high quality single crystals of the bilayer ruthenate $\text{Sr}_3\text{Ru}_2\text{O}_7$," *Phys. Rev. Lett.*, vol. 86, pp. 2661–2664, Mar 2001.
- [199] R. S. Perry, K. Kitagawa, S. A. Grigera, R. A. Borzi, A. P. Mackenzie, K. Ishida, and Y. Maeno, "Multiple first-order metamagnetic transitions and quantum oscillations in ultrapure $\text{Sr}_3\text{Ru}_2\text{O}_7$," *Phys. Rev. Lett.*, vol. 92, p. 166602, Apr 2004.
- [200] A. Damascelli, K. Shen, D. Lu, N. Armitage, F. Ronning, D. Feng, C. Kim, Z.-X. Shen, T. Kimura, Y. Tokura, Z. Mao, and Y. Maeno, "Fermi surface of Sr_2RuO_4 from angle resolved photoemission," *Journal of Electron Spectroscopy and Related Phenomena*, vol. 114–116, pp. 641–646, 2001. Proceeding of the Eight International Conference on Electronic Spectroscopy and Structure,.
- [201] D. Belitz, T. R. Kirkpatrick, and J. Rollbühler, "Tri-critical behavior in itinerant quantum ferromagnets," *Phys. Rev. Lett.*, vol. 94, p. 247205, Jun 2005.
- [202] Y. Maeno, T. M. Rice, and M. Sigrist, "The intriguing superconductivity of strontium ruthenate," *Physics Today*, vol. 54, no. 1, pp. 42–47, 2001.
- [203] C. Honerkamp and T. M. Rice, "Cuprates and ruthenates: Similarities and differences," *Journal of Low Temperature Physics*, vol. 131, no. 3-4, pp. 159–167, 2003.
- [204] C. Bergemann, A. P. Mackenzie, S. R. Julian, D. Forsythe, and E. Ohmichi, "Quasi-two-dimensional Fermi liquid properties of the unconventional superconductor Sr_2RuO_4 ," *Advances in Physics*, vol. 52, no. 7, pp. 639–725, 2003.

BIBLIOGRAPHY

- [205] C. N. Veenstra, Z.-H. Zhu, M. Raichle, B. M. Ludbrook, A. Nicolaou, B. Slomski, G. Landolt, S. Kitaka, Y. Maeno, J. H. Dil, I. S. Elfimov, M. W. Haverkort, and A. Damascelli, “Spin-orbital entanglement and the breakdown of singlets and triplets in Sr_2RuO_4 revealed by spin- and angle-resolved photoemission spectroscopy,” *Phys. Rev. Lett.*, vol. 112, p. 127002, Mar 2014.
- [206] Y. Maeno, H. Hashimoto, K. Yoshida, S. Nishizaki, T. Fujita, J. G. Bednorz, and F. Lichtenberg, “Superconductivity in a layered perovskite without copper,” *Nature*, vol. 372, pp. 532–534, Dec. 1994.
- [207] C. W. Chu, L. Gao, F. Chen, Z. J. Huang, R. L. Meng, and Y. Y. Xue, “Superconductivity above 150 K in $\text{HgBa}_2\text{Ca}_2\text{Cu}_3\text{O}_{8+\delta}$ at high pressures,” *Nature*, vol. 365, pp. 323–325, 09 1993.
- [208] A. P. Mackenzie, R. K. W. Haselwimmer, A. W. Tyler, G. G. Lonzarich, Y. Mori, S. Nishizaki, and Y. Maeno, “Extremely strong dependence of superconductivity on disorder in Sr_2RuO_4 ,” *Phys. Rev. Lett.*, vol. 80, pp. 161–164, Jan 1998.
- [209] M. Eschrig, T. Löfwander, T. Champel, J. C. Cuevas, J. Kopu, and G. Schön, “Symmetries of pairing correlations in superconductor–ferromagnet nanostructures,” *Journal of Low Temperature Physics*, vol. 147, no. 3-4, pp. 457–476, 2007.
- [210] Y. Tanaka and A. A. Golubov, “Theory of the proximity effect in junctions with unconventional superconductors,” *Phys. Rev. Lett.*, vol. 98, p. 037003, Jan 2007.
- [211] F. S. Bergeret, A. F. Volkov, and K. B. Efetov, “Long-range proximity effects in superconductor–ferromagnet structures,” *Phys. Rev. Lett.*, vol. 86, pp. 4096–4099, Apr 2001.
- [212] P. Anderson, “Theory of dirty superconductors,” *Journal of Physics and Chemistry of Solids*, vol. 11, no. 1, pp. 26 – 30, 1959.
- [213] S. NishiZaki, Y. Maeno, and Z. Mao, “Changes in the superconducting state of Sr_2RuO_4 under magnetic fields probed by specific heat,” *Journal of the Physical Society of Japan*, vol. 69, no. 2, pp. 572–578, 2000.
- [214] K. D. Nelson, Z. Q. Mao, Y. Maeno, and Y. Liu, “Odd-parity superconductivity in Sr_2RuO_4 ,” *Science*, vol. 306, no. 5699, pp. 1151–1154, 2004.
- [215] K. Ishida, H. Mukuda, Y. Kitaoka, K. Asayama, Z. Q. Mao, Y. Mori, and Y. Maeno, “Spin-triplet superconductivity in Sr_2RuO_4 identified by 170 Knight shift,” *Nature*, vol. 396, pp. 658–660, 12 1998.
- [216] J. Xia, Y. Maeno, P. T. Beyersdorf, M. M. Fejer, and A. Kapitulnik, “High resolution polar Kerr effect measurements of Sr_2RuO_4 : Evidence for broken time-reversal symmetry in the superconducting state,” *Phys. Rev. Lett.*, vol. 97, p. 167002, Oct 2006.
- [217] G. M. Luke, Y. Fudamoto, K. M. Kojima, M. I. Larkin, J. Merrin, B. Nachumi, Y. J. Uemura, Y. Maeno, Z. Q. Mao, Y. Mori, H. Nakamura, and M. Sigrist, “Time-reversal symmetry-breaking superconductivity in Sr_2RuO_4 ,” *Nature*, vol. 394, pp. 558–561, 08 1998.
- [218] A. Bouhon and M. Sigrist, “Influence of the domain walls on the josephson effect in Sr_2RuO_4 ,” *New Journal of Physics*, vol. 12, no. 4, p. 043031, 2010.
- [219] A. Bouhon, *Electronic Properties of Domain Walls in Sr_2RuO_4* . PhD thesis, ETH Zurich, 2014.
- [220] J. A. Duffy, S. M. Hayden, Y. Maeno, Z. Mao, J. Kulda, and G. J. McIntyre, “Polarized-neutron scattering study of the Cooper-pair moment in Sr_2RuO_4 ,” *Phys. Rev. Lett.*, vol. 85, pp. 5412–5415, Dec 2000.
- [221] D. J. Scalapino, “A common thread: The pairing interaction for unconventional superconductors,” *Rev. Mod. Phys.*, vol. 84, pp. 1383–1417, Oct 2012.
- [222] I. A. Firmo, S. Lederer, C. Lupien, A. P. Mackenzie, J. C. Davis, and S. A. Kivelson, “Evidence from tunneling spectroscopy for a quasi-one-dimensional origin of superconductivity in Sr_2RuO_4 ,” *Phys. Rev. B*, vol. 88, p. 134521, Oct 2013.
- [223] S. Raghu, A. Kapitulnik, and S. A. Kivelson, “Hidden quasi-one-dimensional superconductivity in Sr_2RuO_4 ,” *Phys. Rev. Lett.*, vol. 105, p. 136401, Sep 2010.
- [224] S. Raghu, S. B. Chung, and S. Lederer, “Theory of ‘hidden’ quasi-1D superconductivity in Sr_2RuO_4 ,” *Journal of Physics: Conference Series*, vol. 449, no. 1, p. 012031, 2013.
- [225] T. Scaffidi, J. C. Romers, and S. H. Simon, “Pairing symmetry and dominant band in Sr_2RuO_4 ,” *Phys. Rev. B*, vol. 89, p. 220510, Jun 2014.
- [226] J. Jang, D. G. Ferguson, V. Vakaryuk, R. Budakian, S. B. Chung, P. M. Goldbart, and Y. Maeno, “Observation of half-height magnetization steps in Sr_2RuO_4 ,” *Science*, vol. 331, no. 6014, pp. 186–188, 2011.
- [227] D. A. Ivanov, “Non-abelian statistics of half-quantum vortices in p -wave superconductors,” *Phys. Rev. Lett.*, vol. 86, pp. 268–271, Jan 2001.

- [228] C. W. Hicks, D. O. Brodsky, E. A. Yelland, A. S. Gibbs, J. A. N. Bruin, M. E. Barber, S. D. Edkins, K. Nishimura, S. Yonezawa, Y. Maeno, and A. P. Mackenzie, "Strong increase of T_c of Sr_2RuO_4 under both tensile and compressive strain," *Science*, vol. 344, no. 6181, pp. 283–285, 2014.
- [229] S. Kittaka, H. Taniguchi, S. Yonezawa, H. Yaguchi, and Y. Maeno, "Higher- T_c superconducting phase in Sr_2RuO_4 induced by uniaxial pressure," *Phys. Rev. B*, vol. 81, p. 180510, May 2010.
- [230] R. Fittipaldi, A. Vecchione, S. Fusanobori, K. Takizawa, H. Yaguchi, J. Hooper, R. Perry, and Y. Maeno, "Crystal growth of the new Sr_2RuO_4 - $Sr_3Ru_2O_7$ eutectic system by a floating-zone method," *J. Cryst. Growth*, vol. 282, no. 1-2, pp. 152–159, 2005.
- [231] K. Jacob, K. T. Lwin, and Y. Waseda, "Strontium ruthenates: determination of Gibbs energies of formation using electrochemical cells," *Materials Science and Engineering: B*, vol. 103, no. 2, pp. 152 – 161, 2003.
- [232] Y. Maeno, T. Ando, Y. Mori, E. Ohmichi, S. Ikeda, S. NishiZaki, and S. Nakatsuji, "Enhancement of superconductivity of Sr_2RuO_4 to 3 K by embedded metallic microdomains," *Phys. Rev. Lett.*, vol. 81, pp. 3765–3768, Oct 1998.
- [233] R. Perry and Y. Maeno, "Systematic approach to the growth of high-quality single crystals of $Sr_3Ru_2O_7$," *Journal of Crystal Growth*, vol. 271, no. 1–2, pp. 134 – 141, 2004.
- [234] Z. Mao, Y. Maeno, and H. Fukazawa, "Crystal growth of Sr_2RuO_4 ," *Materials Research Bulletin*, vol. 35, no. 11, pp. 1813 – 1824, 2000.
- [235] A. P. Mackenzie, S. R. Julian, A. J. Diver, G. J. McMullan, M. P. Ray, G. G. Lonzarich, Y. Maeno, S. Nishizaki, and T. Fujita, "Quantum oscillations in the layered perovskite superconductor Sr_2RuO_4 ," *Phys. Rev. Lett.*, vol. 76, pp. 3786–3789, May 1996.
- [236] C. Bergemann, A. P. Mackenzie, S. R. Julian, D. Forsythe, and E. Ohmichi, "Quasi-two-dimensional Fermi liquid properties of the unconventional superconductor Sr_2RuO_4 ," *Advances in Physics*, vol. 52, no. 7, pp. 639–725, 2003.
- [237] K. Olivier, *Comments on Modern Physics: Comments on condensed matter physics*. No. vol. 17 in *Comments on modern physics*, Gordon & Breach, 1994.
- [238] T. E. Kidd, T. Valla, A. V. Fedorov, P. D. Johnson, R. J. Cava, and M. K. Haas, "Orbital dependence of the Fermi liquid state in Sr_2RuO_4 ," *Phys. Rev. Lett.*, vol. 94, p. 107003, Mar 2005.
- [239] K. Pucher, J. Hemberger, F. Mayr, V. Fritsch, A. Loidl, E.-W. Scheidt, S. Klimm, R. Horny, S. Horn, S. G. Ebbinghaus, A. Reller, and R. J. Cava, "Transport, magnetic, thermodynamic, and optical properties in Ti-doped Sr_2RuO_4 ," *Phys. Rev. B*, vol. 65, p. 104523, Mar 2002.
- [240] N. Hussey, A. Mackenzie, J. Cooper, Y. Maeno, S. Nishizaki, and T. Fujita, "The out-of-plane magnetoresistance of Sr_2RuO_4 ," *Physica C: Superconductivity*, vol. 282–287, Part 3, pp. 1229 – 1230, 1997. Proceedings of the International Conference on Materials and Mechanisms of Superconductivity High Temperature Superconductors V.
- [241] D. Forsythe, S. R. Julian, C. Bergemann, E. Pugh, M. J. Steiner, P. L. Alireza, G. J. McMullan, F. Nakamura, R. K. W. Haselwimmer, I. R. Walker, S. S. Saxena, G. G. Lonzarich, A. P. Mackenzie, Z. Q. Mao, and Y. Maeno, "Evolution of Fermi-Liquid interactions in Sr_2RuO_4 under pressure," *Phys. Rev. Lett.*, vol. 89, p. 166402, Sep 2002.
- [242] A. W. Tyler, A. P. Mackenzie, S. NishiZaki, and Y. Maeno, "High-temperature resistivity of Sr_2RuO_4 : bad metallic transport in a good metal," *Phys. Rev. B*, vol. 58, pp. R10107–R10110, Oct 1998.
- [243] T. Yokoya, A. Chainani, T. Takahashi, H. Katayama-Yoshida, M. Kasai, and Y. Tokura, "Extended van-Hove singularity in Sr_2RuO_4 observed by angle-resolved photoemission," *Physica C: Superconductivity*, vol. 263, no. 1–4, pp. 505 – 509, 1996. Proceedings of the International Symposium on Frontiers of High - T_c Superconductivity.
- [244] D. Newns, H. Krishnamurthy, P. Pattnaik, C. Tsuei, C. Chi, and C. Kane, "Van Hove scenario for cuprate superconductivity," *Physica B: Condensed Matter*, vol. 186–188, pp. 801 – 807, 1993.
- [245] K.-S. Chen, S. Pathak, S.-X. Yang, S.-Q. Su, D. Galanakis, K. Mikelsons, M. Jarrell, and J. Moreno, "Role of the van Hove singularity in the quantum criticality of the Hubbard model," *Phys. Rev. B*, vol. 84, p. 245107, Dec 2011.
- [246] A. Liebsch and A. Lichtenstein, "Photoemission quasiparticle spectra of Sr_2RuO_4 ," *Phys. Rev. Lett.*, vol. 84, pp. 1591–1594, Feb 2000.
- [247] A. Damascelli, D. H. Lu, K. M. Shen, N. P. Armitage, F. Ronning, D. L. Feng, C. Kim, Z.-X. Shen, T. Kimura, Y. Tokura, Z. Q. Mao, and Y. Maeno, "Fermi surface, surface states, and surface reconstruction in Sr_2RuO_4 ," *Phys. Rev. Lett.*, vol. 85, pp. 5194–5197, Dec 2000.
- [248] D. van der Marel, "Private communication."

BIBLIOGRAPHY

- [249] I. I. Mazin and D. J. Singh, “Ferromagnetic spin fluctuation induced superconductivity in Sr_2RuO_4 ,” *Phys. Rev. Lett.*, vol. 79, pp. 733–736, Jul 1997.
- [250] T. Oguchi, “Electronic band structure of the superconductor Sr_2RuO_4 ,” *Phys. Rev. B*, vol. 51, pp. 1385–1388, 1995.
- [251] D. J. Singh, “Relationship of Sr_2RuO_4 to the superconducting layered cuprates,” *Phys. Rev. B*, vol. 52, no. 2, pp. 1358–1361, 1995.
- [252] V. J. Emery and S. A. Kivelson, “Superconductivity in bad metals,” *Phys. Rev. Lett.*, vol. 74, pp. 3253–3256, Apr 1995.
- [253] V. Emery and S. Kivelson, “Collective charge transport in high temperature superconductors,” *Physica C: Superconductivity*, vol. 235, pp. 189 – 192, 1994.
- [254] M. H. Fischer and M. Sigrist, “Dimensional crossover in Sr_2RuO_4 within a slave-boson mean-field theory,” *EPL (Europhysics Letters)*, vol. 85, no. 2, p. 27011, 2009.
- [255] A. F. Ho and A. J. Schofield, “c-axis transport in highly anisotropic metals: Role of small polarons,” *Phys. Rev. B*, vol. 71, p. 045101, Jan 2005.
- [256] N. E. H. ÅrÅ, K. Takenaka, and H. Takagi, “Universality of the Mott–Ioffe–Regel limit in metals,” *Philosophical Magazine*, vol. 84, no. 27, pp. 2847–2864, 2004.
- [257] N. J. C. Ingle, K. M. Shen, F. Baumberger, W. Meevasana, D. H. Lu, Z.-X. Shen, A. Damascelli, S. Nakatsuji, Z. Q. Mao, Y. Maeno, T. Kimura, and Y. Tokura, “Quantitative analysis of Sr_2RuO_4 angle-resolved photoemission spectra: Many-body interactions in a model Fermi liquid,” *Phys. Rev. B*, vol. 72, p. 205114, Nov 2005.
- [258] J. S. Lee, S. J. Moon, T. W. Noh, S. Nakatsuji, and Y. Maeno, “Orbital-selective mass enhancements in multiband $\text{Ca}_{2-x}\text{Sr}_x\text{RuO}_4$ systems analyzed by the extended Drude model,” *Phys. Rev. Lett.*, vol. 96, p. 057401, 2006.
- [259] P. E. Sulewski, A. J. Sievers, M. B. Maple, M. S. Torikachvili, J. L. Smith, and Z. Fisk, “Far-infrared absorptivity of UPt_3 ,” *Phys. Rev. B*, vol. 38, pp. 5338–5352, Sep 1988.
- [260] T. Katsufuji and Y. Tokura, “Frequency and temperature dependence of conductivity for perovskite titanates,” *Physical Review B*, vol. 60, pp. 7673–7676, Sept. 1999.
- [261] J. Yang, J. Hwang, T. Timusk, A. S. Sefat, and J. E. Greedan, “Temperature-dependent optical spectroscopy studies of $\text{Nd}_{1-x}\text{TiO}_3$,” *Phys. Rev. B*, vol. 73, p. 195125, May 2006.
- [262] D. N. Basov, E. J. Singley, and S. V. Dordevic, “Sum rules and electrodynamics of high- T_c cuprates in the pseudogap state,” *Phys. Rev. B*, vol. 65, p. 054516, Jan 2002.
- [263] P. Blaha, K. Schwarz, G. Madsen, D. Kvasnicka, and J. Luitz, *WIEN2k, An augmented Plane Wave + Local Orbitals Program for Calculating Crystal Properties*. Techn. Universitat Wien, Austria, ISBN 3-9501031-1-2., 2001.
- [264] A. Georges, G. Kotliar, W. Krauth, and M. J. Rozenberg, “Dynamical mean-field theory of strongly correlated fermion systems and the limit of infinite dimensions,” *Rev. Mod. Phys.*, vol. 68, pp. 13–125, Jan 1996.
- [265] M. Aichhorn, L. Pourovskii, V. Vildosola, M. Ferrero, O. Parcollet, T. Miyake, A. Georges, and S. Biermann, “Dynamical mean-field theory within an augmented plane-wave framework: Assessing electronic correlations in the iron pnictide LaFeAsO ,” *Phys. Rev. B*, vol. 80, p. 085101, Aug 2009.
- [266] M. Ferrero, O. Parcollet, and L. Pourovskii, “TRIQS: a Toolbox for Research on Interacting Quantum Systems.”
- [267] C. Ambrosch-Draxl and J. O. Sofo, “Linear optical properties of solids within the full-potential linearized augmented planewave method,” *Computer Physics Communications*, vol. 175, no. 1, pp. 1 – 14, 2006.
- [268] J. Mravlje, M. Aichhorn, T. Miyake, K. Haule, G. Kotliar, and A. Georges, “Coherence-incoherence crossover and the mass-renormalization puzzles in Sr_2RuO_4 ,” *Phys. Rev. Lett.*, vol. 106, p. 096401, Mar 2011.
- [269] H. Iwasawa, Y. Yoshida, I. Hase, K. Shimada, H. Namatame, M. Taniguchi, and Y. Aiura, “True bosonic coupling strength in strongly correlated superconductors,” *Sci. Rep.*, vol. 3, p. 1930, 2013.
- [270] J. A. Sobota, S.-L. Yang, A. F. Kemper, J. J. Lee, F. T. Schmitt, W. Li, R. G. Moore, J. G. Analytis, I. R. Fisher, P. S. Kirchmann, T. P. Devereaux, and Z.-X. Shen, “Direct optical coupling to an unoccupied dirac surface state in the topological insulator Bi_2Se_3 ,” *Phys. Rev. Lett.*, vol. 111, p. 136802, 2013.
- [271] M. Braden, W. Reichardt, Y. Sidis, Z. Mao, and Y. Maeno, “Lattice dynamics and electron-phonon

- coupling in Sr_2RuO_4 : Inelastic neutron scattering and shell-model calculations,” *Phys. Rev. B*, vol. 76, p. 014505, Jul 2007.
- [272] M. Braden, W. Reichardt, S. Nishizaki, Y. Mori, and Y. Maeno, “Structural stability of Sr_2RuO_4 ,” *Phys. Rev. B*, vol. 57, pp. 1236–1240, Jan 1998.
- [273] K. Pucher, A. Loidl, N. Kikugawa, and Y. Maeno, “Gaplike behavior of the c-axis dynamic conductivity in pure and Ti-doped Sr_2RuO_4 ,” *Phys. Rev. B*, vol. 68, p. 214502, 2003.
- [274] M. Udagawa, T. Minami, N. Ogita, Y. Maeno, F. Nakamura, T. Fujita, J. Bednorz, and F. Lichtenberg, “Phonon Raman scattering of Sr_2RuO_4 ,” *Physica B: Condensed Matter*, vol. 219–220, pp. 222 – 224, 1996. Proceedings of the Combined Conference of the 4th International Conference on Phonon Physics and the 8th International Conference on Phonon Scattering in Condensed Matter.
- [275] L. Pintschovius, J. M. Bassat, P. Odier, F. Gervais, G. Chevrier, W. Reichardt, and F. Gompf, “Lattice dynamics of La_2NiO_4 ,” *Phys. Rev. B*, vol. 40, pp. 2229–2238, Aug 1989.
- [276] U. Fano, “Effects of configuration interaction on intensities and phase shifts,” *Phys. Rev.*, vol. 124, pp. 1866–1878, Dec 1961.
- [277] A. Damascelli, K. Schulte, D. van der Marel, and A. A. Menovsky, “Infrared spectroscopic study of phonons coupled to charge excitations in FeSi ,” *Phys. Rev. B*, vol. 55, pp. R4863–R4866, Feb 1997.
- [278] A. Damascelli, *Optical Spectroscopy of Quantum Spin Systems*. PhD thesis, University of Groningen, 1999.
- [279] K. Pucher, *Die Farbe der Ruthenate: Optische Spektroskopie an $\text{Sr}_2\text{Ru}_{1-x}\text{Ti}_x\text{O}_4$* . PhD thesis, Universität Augsburg, 2003.
- [280] A. Chaves and S. Porto, “Generalized Lyddane-Sachs-Teller relation,” *Solid State Communications*, vol. 13, no. 7, pp. 865 – 868, 1973.
- [281] V. Goian, S. Kamba, O. Pacherová, J. Drahokoupil, L. Palatinus, M. Dušek, J. Rohlíček, M. Savinov, F. Laufek, W. Schranz, A. Fuith, M. Kachlík, K. Maca, A. Shkabko, L. Sagarna, A. Weidenkaff, and A. A. Belik, “Antiferrodistortive phase transition in EuTiO_3 ,” *Phys. Rev. B*, vol. 86, p. 054112, Aug 2012.
- [282] S. Liu, H. Weng, D. Mou, W. Zhang, Q. Wu, J. He, G. Liu, L. Zhao, H. Liu, X. Jia, Y. Peng, S. He, X. Dong, J. Zhang, Z. Q. Mao, C. Chen, Z. Xu, X. Dai, Z. Fang, and X. J. Zhou, “Fermi surface sheet-dependent band splitting in Sr_2RuO_4 revealed by high-resolution angle-resolved photoemission spectroscopy,” *Phys. Rev. B*, vol. 86, p. 165112, Oct 2012.
- [283] M. Iliev, V. Popov, A. Litvinchuk, M. Abrashev, J. Bäckström, Y. Sun, R. Meng, and C. Chu, “Comparative Raman studies of Sr_2RuO_4 , $\text{Sr}_3\text{Ru}_2\text{O}_7$ and $\text{Sr}_4\text{Ru}_3\text{O}_{10}$,” *Physica B: Condensed Matter*, vol. 358, no. 1–4, pp. 138 – 152, 2005.
- [284] S. Sakita, S. Nimori, Z. Q. Mao, Y. Maeno, N. Ogita, and M. Udagawa, “Anisotropic properties of the excitation spectrum of Sr_2RuO_4 crystals ($T_c = 1.4\text{K}$) in the normal state investigated by Raman scattering,” *Phys. Rev. B*, vol. 63, p. 134520, Mar 2001.
- [285] S. I. Ikeda, U. Azuma, N. Shirakawa, Y. Nishihara, and Y. Maeno, “Bulk single-crystal growth of strontium ruthenates by a floating-zone method,” *Journal of Crystal Growth*, vol. 237–239, Part 1, pp. 787–791, 4 2002.
- [286] M. S., S. D. G., D. A., D. H. A., and Y. Liu, “Growth of epitaxial $a\text{-}\hat{a}$ and $c\text{-}\hat{a}$ oriented Sr_2RuO_4 films,” *Appl. Phys. Lett.*, vol. 68, no. 559, 1996.
- [287] L. Walz and F. Lichtenberg, “Refinement of the structure of Sr_2RuO_4 with 100 and 295 K X-ray data,” *Acta Crystallographica Section C*, vol. 49, pp. 1268–1270, Jul 1993.
- [288] O. Chmaissem, J. D. Jorgensen, H. Shaked, S. Ikeda, and Y. Maeno, “Thermal expansion and compressibility of Sr_2RuO_4 ,” *Phys. Rev. B*, vol. 57, pp. 5067–5070, Mar 1998.
- [289] A. L. Patterson, “The Scherrer formula for X-ray particle size determination,” *Phys. Rev.*, vol. 56, pp. 978–982, Nov 1939.
- [290] Y. Maeno, K. Yoshida, H. Hashimoto, S. Nishizaki, S. ichi Ikeda, M. Nohara, T. Fujita, A. P. Mackenzie, N. E. Hussey, J. G. Bednorz, and F. Lichtenberg, “Two-dimensional Fermi liquid behavior of the superconductor Sr_2RuO_4 ,” *Journal of the Physical Society of Japan*, vol. 66, no. 5, pp. 1405–1408, 1997.
- [291] S.-I. Ikeda, Y. Maeno, S. Nakatsuji, M. Kosaka, and Y. Uwatoko, “Ground state in $\text{Sr}_3\text{Ru}_2\text{O}_7$: Fermi liquid close to a ferromagnetic instability,” *Phys. Rev. B*, vol. 62, pp. R6089–R6092, Sep 2000.
- [292] Z. Xu, X. Xu, R. S. Freitas, Z. Long, M. Zhou, D. Fobes, M. Fang, P. Schiffer, Z. Mao, and Y. Liu,

BIBLIOGRAPHY

- “Magnetic, electrical transport, and thermoelectric properties of $\text{Sr}_4\text{Ru}_3\text{O}_{10}$: Evidence for a field-induced electronic phase transition at low temperatures,” *Phys. Rev. B*, vol. 76, p. 094405, Sep 2007.
- [293] P. A. Joy, P. S. A. Kumar, and S. K. Date, “The relationship between field-cooled and zero-field-cooled susceptibilities of some ordered magnetic systems,” *Journal of Physics: Condensed Matter*, vol. 10, no. 48, p. 11049, 1998.
- [294] R. Dirsyte, J. Schwarzkopf, M. Schmidbauer, G. Wagner, K. Irmscher, S. B. Anooz, and R. Fornari, “Impact of epitaxial strain on the ferromagnetic transition temperature of SrRuO_3 thin films,” *Thin Solid Films*, vol. 519, no. 19, pp. 6264 – 6268, 2011.
- [295] A. Vailionis, W. Siemons, and G. Koster, “Room temperature epitaxial stabilization of a tetragonal phase in ARuO_3 (A=Ca and Sr) thin films,” *Applied Physics Letters*, vol. 93, no. 5, pp. –, 2008.

Publication list

- [1] D. Stricker, J. Mravlje, C. Berthod, R. Fittipaldi, A. Vecchione, A. Georges, and D. van der Marel, “Optical response of Sr_2RuO_4 reveals universal Fermi-Liquid scaling and quasiparticles beyond Landau theory,” *Phys. Rev. Lett.*, vol. 113, p. 087404, Aug 2014.
- [2] S. I. Mirzaei, D. Stricker, J. N. Hancock, C. Berthod, A. Georges, E. van Heumen, M. K. Chan, X. Zhao, Y. Li, M. Greven, N. Barišić, and D. van der Marel, “Spectroscopic evidence for Fermi liquid-like energy and temperature dependence of the relaxation rate in the pseudogap phase of the cuprates,” *Proceedings of the National Academy of Sciences*, vol. 110, no. 15, pp. 5774–5778, 2013.
- [3] R. Comin, G. Levy, B. Ludbrook, Z.-H. Zhu, C. N. Veenstra, J. A. Rosen, Y. Singh, P. Gegenwart, D. Stricker, J. N. Hancock, D. van der Marel, I. S. Elfimov, and A. Damascelli, “ Na_2IrO_3 as a novel relativistic mott insulator with a 340-meV gap,” *Phys. Rev. Lett.*, vol. 109, p. 266406, Dec 2012.
- [4] J. Levallois, F. Lévy-Bertrand, M. K. Tran, D. Stricker, J. A. Mydosh, Y.-K. Huang, and D. van der Marel, “Hybridization gap and anisotropic far-infrared optical conductivity of URu_2Si_2 ,” *Phys. Rev. B*, vol. 84, p. 184420, Nov 2011.

Acknowledgements

Merci à toi Dirk de m'avoir fait confiance durant toutes ces années. Tout en me guidant, tu m'as permis de garder mon indépendance et mes idées, me permettant de tracer mon propre chemin pour la réalisation de ce travail. Comme dans toute recherche, il y a eu de belles découvertes mais aussi des moments difficiles, mais grâce à tes encouragements et à ta persévérance, nous avons pu tourner à notre avantage la plupart de ces situations. Sans la défaillance de ce fameux Oxford ITC 503, nous ne nous serions jamais intéressés à la caractérisation des échantillons et serions probablement passé à côté de beaucoup de choses. Aussi personnelle que puisse paraître une thèse, elle est aussi un formidable projet collaboratif. De la fabrication de la bobine supraconductrice aux corrections syntaxiques de ce document, il y a tant de choses pour lesquelles j'aimerais remercier toutes les personnes avec qui j'ai travaillé ou simplement pris une pause café. Vous avez tous apporté une brique à l'édifice et je vous en remercie plus que jamais ! Un grand *thumbs up* pour vous tous ! Et puis il y a toi Nadège, pour qui je dédie cette thèse. Toujours présente et dévouée, tu as toujours su me redonner le moral pour aller de l'avant, je ne l'oublierai jamais.

Adriana
Adrien
Alberto
Alberto
Alexandre
Alexey Ana
Anaïs Antoine
Antonio Bene-
dict Bernard Carmine Céline
Charly Christian Christophe Damien Daniel Davide
Davide Denise Didier Dirk Dominique Dook Enrico Erik
Fabienne Florence Géraldine Gernot Grégory Guillaume
Iaroslav Ievgeniia Iman Iris Ivan Jacim Jason Javier
Jean-Gabriel Jean-Marc Jean-Marie Jérémie Jernej Johanie
Julien Kai Laurent Lidia Lionel Louis Manisha Marc Marco
Maria Marie-José Marta Mehdi Michaël Michel Miguel
Murielle Nadège Natacha Nathalie Nicolas Nimrod Oleg
Pascal Patrycja Pieter Radovan Régis René Riccardo
Robert Roland Romain Sandro Sarah Sébastien Skirmante
Spiros Stefano Stéphanie Thierry Verner

Glossary

- ^3He Helium isotope with mass number 3 103, 111, 117
- 3K-phase** 109, 110, 143
- a-axis** The crystallographic axis in a tetragonal crystal which is inplane 44, 151
- ab-plane** The crystallographic plane formed by the two lattice parameters $\hat{\mathbf{a}}$ and $\hat{\mathbf{b}}$ in a tetragonal crystal 44, 47, 54, 67, 72, 104, 105, 112–115, 118–122, 125, 142, 199
- ac-plane** The crystallographic plane formed by the two lattice parameters $\hat{\mathbf{a}}$ and $\hat{\mathbf{c}}$ in a tetragonal crystal 44, 47, 71, 119, 120, 140, 149, 151, 158
- Allen formula** 26, 27, 137, 139
- Ampère's law** 2–4
- bad metal** 118
- Bose-Einstein function** 26, 29
- bound-charge** Collective phenomenon due to the polarization of the medium giving rise to a polarization charge. 3, 77
- Bruker**
- Bruker 70v** 42, 71, 72
 - Bruker IFS 113v** 42–45, 68, 120
 - Bruker IFS 66v/S** 42, 51, 68, 120
- Cauchy theorem** 20
- cavity perturbation** 41
- c-axis** The crystallographic axis in a tetragonal crystal which is perpendicular the the *ab*-plane 44, 46, 47, 54, 67, 69–73, 80, 103–105, 111–115, 118–122, 124, 125, 140–143, 147, 148, 150–153, 156–158, 167, 199
- chemical potential** 25
- Clausius-Mossotti relation** 18
- conductivity** 3–5, 8–10, 13, 16, 24, 26, 32, 36
- Cooper pairs** 28
- Corbino spectrometer** 41, 42
- correlation function** 23, 24, 34
- Coulomb** 28
- coupling function** 27
- cryostat** 46, 48, 49, 51, 52, 55, 67, 68, 111, 119, 121
- cuprate** 57–61, 63–65, 70, 71, 73, 80–82, 84, 87, 89–91, 96, 98, 99, 101, 103–105, 107, 108, 114, 116, 117, 119, 126, 128, 130, 131
- $\text{Bi}_2\text{Sr}_2\text{CuO}_{6+x}$** 81, 89, 90, 96, 98
- $\text{Bi}_2\text{Sr}_2\text{CaCu}_2\text{O}_{8+x}$** 63, 81, 89, 90
- $\text{HgBa}_2\text{Ca}_2\text{Cu}_3\text{O}_{8+x}$** 107
- $\text{HgBa}_2\text{CuO}_{4+x}$** The second material studied

- in this thesis ix, xi, 18, 39, 44, 46, 47, 54, 57, 59, 63–67, 69–74, 76–81, 83, 84, 89–92, 96, 121, 128, 161, 198
- $\text{La}_{2-x}\text{Ba}_x\text{CuO}_4$ 104
- $\text{La}_{2-x}\text{Sr}_x\text{CuO}_4$ 64, 75, 80
- $\text{YBa}_2\text{Cu}_3\text{O}_{7-x}$ ybco 62–64, 80, 89, 90
- de Haas-van Alphen effect 107
- dielectric constant 4, 5, 11, 12, 15, 18, 20
- Dirac identities 20
- Drude
- Drude model Phenomenological model describing the electrical conduction in metals 7, 9–11, 15, 16, 26, 30–34, 36, 82
 - Drude peak 16, 32, 62, 75–77, 80, 92, 123, 124, 132
 - Drude-Lorentz model Phenomenological model describing many light-matter interactions 15, 16, 18, 21, 71, 75, 76, 82, 123–125
 - extended Drude model 7, 17, 27, 34–36, 82
- d*-wave 84
- effective mass 17, 30, 80, 84–86, 89, 198
- E_g 140–142, 149–151
- electrical field 5–8, 24
- electron
- electron mass 8
 - electron-boson 39, 197
 - electron-electron 31, 36, 39
 - electron-phonon 28
- ellipsometer 42, 54, 67, 75
- ellipsometry 75, 76
- E_u 121, 122, 140
- external perturbation 19
- Faraday's law A quantum liquid of interacting particles which have Fermi-Dirac statistics 2
- Fermi
- Fermi energy At zero temperature and in a metal this is the energy difference between the Fermi level and lowest occupied single-particle state 30, 31, 37, 38, 59, 81, 91, 101, 106, 116, 135, 139
 - Fermi function The probability function of occupancy for a fermion (eg. electron) energy state at energy ε by a fermion 29
 - Fermi gas 25, 30
 - Fermi level The total chemical potential for electrons. In a metal at zero temperature it is the energy of the highest occupied single particle state 118, 134
 - Fermi surface The abstract interface of constant energy in the momentum space which separates the unfilled orbitals from the filled orbitals, at absolute zero temperature 29, 57, 59, 61, 63, 64, 71, 80, 82, 101
 - Fermi velocity 30
 - Fermi-Dirac function 26
 - Fermi-liquid A quantum liquid of interacting particles which have Fermi-Dirac statistics 1, 22, 29–34, 36–40, 57–59, 61, 86, 87, 91–96, 98–101, 103, 104, 111, 114–119, 123, 125, 126, 128, 130–135, 137–139, 158, 161–166
 - Fermi-liquid model 17, 30, 133
- ferromagnetic 104
- ferromagnetic transition 156, 157
- fluctuation-dissipation theorem 22
- Fourier transform 3, 19
- free electron model 12
- free-charge Conduction (or mobile) electrons

Glossary

- (holes) 77
- Fresnel equations 5
- Gauss' law 2, 4
- Genzel geometry 43
- glue function 27, 38, 98, 100, 197
- Green's function 19, 25
- group velocity 26
- Hagen-Rubens equation Low frequency regime of the reflectivity of metals 12, 35, 66, 68, 124, 125
- harmonic oscillator 14
- high- T_c High critical temperature, related to superconductors 11, 28, 57, 62, 103, 107
- histogram model 36–38, 96, 97, 99
- Homes scaling 79, 80
- homogeneous 19
- Hubbard model 135, 138
- impedance analyzer 41
- index of refraction 5–7, 20
- in-plane See *ab*-plane 34, 44, 47, 51, 68–71, 73, 76, 78, 81, 103, 109, 111–115, 119–122, 124, 130, 140, 141, 150, 198
- interband Describing processes happening between two bands 12, 16, 73, 75–77, 82, 123–125, 134, 145
- interband transition Describing transitions happening between two bands 17, 18, 21, 75, 82
- intraband Describing processes happening within the band xvi, 16, 26, 36, 75–77, 92, 94, 123, 124, 126, 134, 135, 145
- intraband transition Describing transitions happening within the band 17
- isotropic 19
- K_2NiF_4 140
- kinetic energy 80
- knight shift 109
- Kramers-Kronig 21, 76, 138
- Kramers-Kronig relations 7, 18, 20, 21, 51, 75, 76, 123, 124, 135, 136, 138, 141
- Kramers-Kronig transformation 22, 72, 75, 77, 123, 130
- Kubo formalism 1
- Kubo formula 22
- macroscopic at the phenomenological level 1, 31
- magnetic field strength 4
- magnetization 3
- Martin-Puplett interferometer 42
- MATLAB® a multi-paradigm numerical computing environment and fourth-generation programming language 96
- Maxwell equations Set of four equations describing the electromagnetic waves in waves in vacuum 1, 2, 4, 5
- Maxwell-Garnett approximation A model for the effective-medium approximation (EMA) 150
- memory function 17, 35, 80, 82, 83, 87, 96–100, 126, 127, 139, 199
- metamagnetic transition 104
- microscopic at the particule size level 1, 17, 28
- Migdal theorem 25
- Migdal-Eliashberg theory 1
- monochromator 51
- Mott-Ioffe-Regel limit 31, 118
- Ohm's law 3, 5, 8, 20, 23, 24
- optical conductivity 1, 10–12, 14–17, 20, 22, 23, 26, 31–35, 71, 73, 74, 76–79, 81, 92, 93, 95, 101, 103, 104, 119, 123, 125, 130–134, 137, 139, 143, 144, 198

- orthorhombic** A crystal system among the seven lattice point groups which represent a rectangular prism with a rectangular base $a \times b$ and height c such that $a \neq b \neq c$. In addition a , b and c are mutually orthogonal (90° angles) 53
- out-of-plane** 11, 111, 114
- oxygen** 104, 105
- O_{zz}** 140, 141
- Pauli's exclusion principle** 30
- permeability** 4
- perovskite** 104
- perturbation theory** 23
- phonon** A quantum mechanical elementary vibration motion of atoms in a periodic lattice. Considered as a usual quasiparticle in crystals, they play a key role in most of the material by such as for their thermal and electrical conductivity. 14, 28, 38, 44, 46, 47, 61, 67, 69–71, 75–77, 82, 84, 96, 98, 100, 103, 121, 122, 125, 126, 132, 140, 141, 143–147, 149–152, 157, 158
- plasma frequency** 9, 10, 12, 14, 16, 29, 75, 76, 80, 82
- polarization** 3
- polarizer** 43, 44, 46, 52
- p -polarization** An electromagnetic wave with the electrical field vector parallel to the plane of incidence 6, 53
- pseudogap** 57, 58, 60, 62–64, 77, 82, 91, 101
- pseudogap temperature** 58, 62, 65
- p -wave** 103, 108, 109
- quasiparticle** 30, 31, 57, 61, 71, 73, 80, 84, 94, 118, 135, 136, 139
- ReFFIT** 16, 72, 75, 96, 123, 145
- reflectivity** 5, 7, 12, 13, 20, 21, 34, 35, 49, 121, 122, 147, 197
- relaxation regime** 12
- relaxation time** 8
- renormalization** 25
- resilient quasiparticle** 103, 104, 134, 135
- response theory** 18
- retarded correlation function** 23
- Rice-Kadowaki-Woods ratio** 34, 35
- root-mean square** 128–130
- Ruddlesden-Popper series** A crystallographic structure consisting of n unit cells of perovskite ABO_3 alternated with a layer of rocksalt AO along the crystallographic c -axis [191] 104–106, 109, 140, 151–153, 156
- ruthenate** 104–106, 116
- Sr_2RuO_4** The second material studied in this thesis x, xi, 18, 22, 29, 34, 39, 44, 47, 50, 54, 71, 94, 101, 103, 104, 106–109, 111, 113–115, 117–126, 128, 130, 134, 138, 140, 141, 143–145, 147, 148, 150–158, 198, 199
- $Sr_3Ru_2O_7$** 104, 106, 151–158
- Sr_3RuO_{5+x}** An insulating impurity phase presenting oxygen vacancies 148, 152
- $Sr_4Ru_3O_{10}$** 104, 106, 153, 156, 157
- $SrRuO_3$** 104, 106, 156, 157
- ruthenium** 104, 105, 110
- scanning electron microscope** 140
- scattering rate** 8–10, 12, 13, 17, 27, 31, 103, 115, 116, 119, 131, 135, 138, 139, 158
- optical scattering rate** 17, 25, 31, 33, 34, 57, 82, 84–90, 198
- quasiparticle scattering rate** 25, 31, 34
- self-energy** The contribution to the effective mass (or the potential felt by the elec-

Glossary

- tron), due to the surrounding lattice or medium's interactions 17, 22, 25–31, 34, 35, 37, 64, 92, 126, 134–139, 199
- sheet conductance 11, 80
- spectral function 26, 28, 30, 37
- spectral weight 9, 11, 26, 36, 57, 62, 73, 75, 77, 80–82, 84, 94, 116, 123, 124, 126, 134, 138
- coherent spectral weight 75, 77, 80, 81, 94, 100
- quasiparticle spectral weight 30
- spectrometer 67, 68
- spectroscopic Experimental study of the energy dependence of a physical phenomenon 1
- s*-polarization An electromagnetic wave with the electrical field vector perpendicular to the plane of incidence. *s* stands for *senkrecht*, being perpendicular in German 6, 53
- strontium 104, 105
- sum rule 9, 11
- FGT sum rule 11
- f-sum rule 9
- superconductivity 28
- superconductor 11, 104
- superfluid condensate 11
- s*-wave 61, 107, 108
- tetragonal 104
- thermal regime 34
- transmission 5
- transport function 26
- unit cell The primitive and smallest volume repeating the geometry of a crystal structure 1
- Van Hove singularity 116, 134
- vertex correction 25
- Wooten extrapolation 22

Acronyms

- ac** alternating current 111
- ADC** analog to digital converter 48
- ARPES** angle-resolved photoemission spectroscopy
1, 62–64, 106, 107, 111, 120, 139
- BCS** Bardeen-Cooper-Schrieffer 28, 61, 108
- BSED** back-scattered electron detector 152
- C362** Sr_2RuO_4 sample with $T_c = 1.3$ K 111, 120, 143–145, 148–152, 154
- CCD** charge-coupled device 148
- CGS** centimeter-gram-second system of unit 2
- dc** direct current 8–10, 13, 22, 29, 32, 40, 41, 62, 65, 66, 70, 79, 86, 96, 98, 100, 124, 125, 199
- DFT** density functional theory 132, 133, 139, 158
- DMFT** dynamical mean field theory 31, 125, 132–135, 137–139
- DOS** density of states 12, 13, 27, 118, 134
- FC** field cooling 153
- FFFZ** flux feeding floating zone 110, 111
- FIR** far-Infrared 34, 42, 43, 46, 49, 50, 68–70, 120, 121, 161, 199
- FTIR** Fourier transform infrared 34, 41–43, 51, 67, 72, 120, 122, 197
- FZT** Floating-zone technique 110
- HV** high vacuum 51
- IR** infrared 42, 71, 72
- KKR** Kramers-Kronig relations 20, 21, 55
- LDA** local-density approximation 13, 81, 136, 138
- MFL** Marginal Fermi-liquid 96
- MIR** mid-Infrared 43, 46, 73, 75, 77, 92, 94, 118, 121, 125
- MMP** Millis-Monien-Pines 37, 96
- NIR** near-Infrared 12, 43, 44, 46, 51, 68, 70, 120, 121
- NMR** Nuclear magnetic resonance 109
- OFHC** oxygen-free high thermal conductivity 67
- OpD97** optimally doped with $T_c = 97$ K 64, 65, 67, 69–72, 77–79, 84, 89, 162
- PID** proportional integral derivative 46
- RF** radio frequency 41
- RIXS** resonant inelastic X-ray scattering 73
- SI** international system of units 2
- SQUID** superconducting quantum interference device 108
- STM** scanning tunneling microscopy 1, 109
- STS** scanning tunneling spectroscopy 1

Acronyms

- Tc128** Sr₂RuO₄ sample with $T_c = 1.28$ K 111, 119, 120, 143–145, 150, 152–154, 157
- Tc134** Sr₂RuO₄ sample with $T_c = 1.34$ K 111–113, 115, 119–122, 140, 143–145, 147–153, 155–157, 198, 199
- UD45** underdoped with $T_c = 47$ K 64, 65, 68–72, 75, 78, 79, 82, 85–87, 89, 92, 94, 100, 162
- UD55** underdoped with $T_c = 55$ K 64, 65, 68–70, 72, 75, 78, 79, 82, 85–87, 89, 94, 100, 162
- UD67** underdoped with $T_c = 67$ K 64, 65, 68–78, 82, 84, 86–89, 92, 94, 96–100, 161, 198
- UHV** ultra High Vacuum 46, 52, 119
- UV** ultraviolet 12, 42, 43, 51, 67, 75, 120
- VASE** variable Angle Spectroscopic Ellipsometry 42, 51
- VIS** visible 46, 51
- xFIR** extra far infrared 43, 67
- X-ray** X-radiation 1, 120, 140, 152, 153, 155
- ZFC** zero field cooling 153

List of Symbols

- A** vector potential 2
- A_g 140–142, 149–152
- A_u 122, 140–142, 150
- $b(a, a)\bar{b}$ Raman measurement geometry 148–150
- $b(a, c)\bar{b}$ Raman measurement geometry 148, 150, 151
- $b(c, a)\bar{b}$ Raman measurement geometry 148, 150, 151
- $b(c, c)\bar{b}$ Raman measurement geometry 148–150
- $c(a, a)\bar{c}$ Raman measurement geometry 151
- \mathcal{C}_{AB} correlation function of A and B 23
- χ_e electric susceptibility 4
- χ_m magnetic susceptibility 4
- D** electric displacement 4, 6
- d_c average interlayer spacing 11
- D differential operator 19
- $d_{r^2-3z^2}$ ruthenium d orbital 59, 105
- $d_{x^2-y^2}$ ruthenium d orbital 59, 61, 63, 105
- d_{xy} ruthenium d orbital along the xy plane 59, 105–107, 116, 134–137
- d_{xz} ruthenium d orbital along the xz plane 59, 105–107, 116, 135–139
- d_{yz} ruthenium d orbital along the yz plane 59, 105–107, 116, 135, 137–139
- e_g representations of the d -orbitals of transition metals with an FCC-crystal structure 59, 105, 106
- E** electrical field 2, 5, 6
- e electron charge 8
- eV electronvolt 2
- ϵ_b bound charge dielectric function 75, 82
- ϵ dielectric constant 4
- ϵ_{pd} pseudo dielectric function 54, 73
- ϵ_0 free space permittivity 2
- ϵ_F Fermi energy 30
- ϵ_∞ high energy contribution to dielectric constant 75
- η coefficient of the law glue function 38
- \mathcal{G} Green's function 25
- G_0 quantum of conductance 11
- Γ_{imp} impurity scattering rate 34
- H** magnetic field strength 4–6
- J** current density 2
- J_b bound current 3
- J_c conduction current 3
- j^d diamagnetic particle-current 23
- J_f free current 3
- j^p paramagnetic particle-current 23
- J_p polarization current 3
- K spectral weight 11

List of Symbols

- \mathbf{k} wave vector 3, 5, 6
 k_B Boltzmann constant 34
 λ wavelength of light 3
 m bar electron mass 8
 M memory function 17
 \mathbf{M} magnetization 3
 \mathbf{B} magnetic induction field 2, 6
 m^* effective mass 30
 μ permeability 4
 N index of refraction 6
 n charge density 8
 N_L number of CuO_2 layers per uc 11
 \mathbf{p} dipole moment 14
 Φ transport function 26
 ϕ_r phase of the reflectivity 7
 Φ scalar potential 2
 \mathbf{P} polarization 3
 Π glue function 27
 p_x 59
 $p_x + ip_y$ phase of the reflectivity 109
 p_y 59
 q electrical charge 2
 R reflectivity 5
 ρ_b bound-charge 3
 $\rho(\mathbf{r}, t)$ charge density 2
 ρ_f free charge 3
 ϱ s and p reflectivity ratio 52
 r_p p -polarization reflectivity coefficient 6
 r_s s -polarization reflectivity coefficient 6
 \mathcal{S} scaling function 32
 $1/\tau$ scattering rate (γ) 8, 16
 σ optical conductivity, Scm^{-1} 3
 σ_{MIR} MIR band conductivity 77
 ζ spin operator 23
 c speed of light in free space 2
 T transmission 5
 T_0 Fermi-liquid temperature scale 30–32, 34, 35, 94, 131, 162
 t_{2g} representations of the d -orbitals of transition metals with an FCC-crystal structure 59, 105, 106, 135, 136, 138
 τ relaxation time 8
 T_c superconductor critical temperature 11, 28, 57–59, 61–63, 65, 67, 68, 73–75, 77, 79, 82, 84–86, 88–91, 108, 109, 112, 114, 119, 144, 157, 161
 T_{FL} Fermi liquid temperature 31, 32, 114, 115, 118, 131
 T_{max} Maximum temperature in the c -axis resistivity of Sr_2RuO_4 118
 T' superconducting fluctuations temperature 65, 67, 87, 88, 92
 T^* pseudogap temperature 58, 59, 62–67, 70, 82, 84, 86–90, 92–94, 99, 162, 164, 166
 \mathbf{v} speed of particles 2
 \mathbf{v}_F Fermi velocity 30
 \mathbf{v}_k group velocity 26
 ω frequency, rad/sec 3
 ω_0 mode frequency 14, 149, 150
 ω_p plasma frequency 9, 14, 16
 Z quasiparticle spectral weight 30

List of Figures

1.1	Light interaction at the material interface	6
1.2	Classical representation of an electron motion in metal	8
1.3	Dielectric constant and optical conductivity of the Drude model	10
1.4	reflectivity of typical metals	13
1.5	Hagen-Rubens extrapolation	13
1.6	Drude-Lorentz model	15
1.7	Contour integral	19
1.8	Comparison between different extrapolation techniques	22
1.9	Representation of Green's functions model	25
1.10	Fermi liquid electron-boson	31
1.11	Fermi liquid conductivity	33
1.12	Rice-Kadowaki-Woods ratio	35
1.13	Strongly correlated conductivity	36
1.14	Glue function for different models	38
2.1	Typical energy scales	42
2.2	Schematic view of the Bruker FTIR spectrometer	43
2.3	Bruker IFS 113v experimental parameters	45
2.4	Polarizer calibration	47
2.5	Evaporation and drift calibration procedure	48
2.6	Drift Calibration	50
2.7	Typical ellipsometry configuration	52
2.8	Pseudo dielectric function	54
3.1	Schematic phase diagram of the cuprates	58
3.2	Electronic structure of the cuprates	60
3.3	Schematic view of the pseudogap doping dependence	62
3.4	Schematic view of the pseudogap doping dependence	63

LIST OF FIGURES

3.5	Fermi surface of $\text{Ca}_{2-x}\text{Na}_x\text{CuO}_2\text{Cl}_2$ seen by ARPES	64
3.6	Crystal structure of $\text{HgBa}_2\text{CuO}_{4+x}$	65
3.7	Resistivity and susceptibility of $\text{HgBa}_2\text{CuO}_{4+x}$	66
3.8	In-plane optical reflectivity of four different doping of $\text{HgBa}_2\text{CuO}_{4+x}$	69
3.9	Reflectivity of $\text{HgBa}_2\text{CuO}_{4+x}$ UD67	71
3.10	c-axis reflectivity of $\text{HgBa}_2\text{CuO}_{4+x}$	72
3.11	in-plane dielectric function of $\text{HgBa}_2\text{CuO}_{4+x}$ UD67	73
3.12	Ellipsometric (pseudo) optical conductivity of $\text{HgBa}_2\text{CuO}_{4+x}$ UD67	74
3.13	Drude-Lorentz model shown using optical conductivity	76
3.14	Mobile and bound charge contributions to the dielectric function of $\text{HgBa}_2\text{CuO}_{4+x}$	77
3.15	In-plane optical conductivity of four different doping of $\text{HgBa}_2\text{CuO}_{4+x}$	78
3.16	Comparison of the optical conductivity of four different doping of $\text{HgBa}_2\text{CuO}_{4+x}$	79
3.17	Home's scaling relation	80
3.18	Intraband band spectral of different cuprates compounds	81
3.19	Memory function of $\text{HgBa}_2\text{CuO}_{4+x}$	83
3.20	Optical scattering rate of $\text{HgBa}_2\text{CuO}_{4+x}$ UD67	84
3.21	Temperature dependence of the effective mass and optical scattering rate of $\text{HgBa}_2\text{CuO}_{4+x}$	85
3.22	Scaling of the optical scattering of the underdoped sample $\text{HgBa}_2\text{CuO}_{4+x}$	88
3.23	Scaling of the optical scattering rate of different cuprates	90
3.24	Doping analysis of the scattering rate suppression for different cuprates	91
3.25	Fermi-liquid fit (Procedure A) to the low energy optical conductivity of $\text{HgBa}_2\text{CuO}_{4+x}$ UD67 (A)	93
3.26	Fermi-liquid fit (Procedure B) to the low energy optical conductivity of $\text{HgBa}_2\text{CuO}_{4+x}$ UD67 (PB)	95
3.27	Histogram model of the bosonic spectral function	97
3.28	Fermi-liquid model of the bosonic spectral function	98
3.29	Combined model for the Glue function	99
4.1	Crystal structure of Sr_2RuO_4	105
4.2	BandStructure	106
4.3	Phase diagram of the Ruddlesden-Popper series ruthenate	106
4.4	Orbitals of Sr_2RuO_4	107
4.5	T_c dependence under non-magnetic doping.	108
4.6	Oxygen potential diagram for the growing condition of Sr_2RuO_4	110
4.7	SampleTransport	112
4.8	Power law fit to the Sr_2RuO_4 Tc134 resistivity	113
4.9	Resistivity anisotropy of Sr_2RuO_4	114

4.10	<i>ab</i> -plane and <i>c</i> -axis dc resistivity of Sr ₂ RuO ₄	115
4.11	Inplane susceptibility of Sr ₂ RuO ₄	116
4.12	High-temperature fit of the Sr ₂ RuO ₄ in-plane resistivity	117
4.13	Transport function and DOS of Sr ₂ RuO ₄	118
4.14	Picture of the Sr ₂ RuO ₄ Tc134 sample	119
4.15	Back Laue reflection images of Sr ₂ RuO ₄ samples	120
4.16	Reflectivity of Sr ₂ RuO ₄ Tc134 at selected temperatures	122
4.17	in-plane dielectric function of Sr ₂ RuO ₄ Tc134	122
4.18	Drude-Lorentz optical conductivity of Sr ₂ RuO ₄	123
4.19	Intraband dielectric function of Sr ₂ RuO ₄ Tc134	124
4.20	Optical conductivity of Sr ₂ RuO ₄ Tc134 sample	125
4.21	Memory function of Sr ₂ RuO ₄ Tc134	126
4.22	Energy-dependent mass enhancement of Sr ₂ RuO ₄ Tc134	127
4.23	Imaginary part of the memory function	127
4.24	Scaling	129
4.25	In-plane optical conductivity of Sr ₂ RuO ₄ in the Fermi-liquid regime.	130
4.26	Fermi-liquid thermometry.	131
4.27	Optical conductivity of Sr ₂ RuO ₄ from experiment, theory and numerical calculations	133
4.28	Transport function of Sr ₂ RuO ₄	135
4.29	Sr ₂ RuO ₄ k -resolved spectral function	136
4.30	Local self-energies for the <i>d</i> _{xy} and <i>d</i> _{xz} bands	136
4.31	Optical self energy from the damped orbitals	137
4.32	Optical conductivity of Sr ₂ RuO ₄ and self-energy	139
4.33	Memory function: DFT+DMFT and experiment	139
4.34	Phonon dispersion in Sr ₂ RuO ₄	141
4.35	StructurePhonon	142
4.36	Comparison of the phonon for the different samples.	144
4.37	Comparison of the phonon parameters	146
4.38	Drude-Lorentz fit to the Sr ₂ RuO ₄	147
4.39	Verification of the fit quality for the <i>c</i> -axis reflectivity of Sr ₂ RuO ₄ sample Tc134 .	148
4.40	Raman spectra of Sr ₂ RuO ₄	149
4.41	Raman analysis of Sr ₂ RuO ₄ <i>ac</i> -plane of sample C362	151
4.42	Scanning electron surface topography of Sr ₂ RuO ₄	154
4.43	X-ray diffraction pattern	155
4.44	Susceptibility of Sr ₂ RuO ₄	156
A.1	Fermi-liquid fit to the FIR reflectivity	161
A.2	Fermi-liquid fit to the low energy optical conductivity of HgBa ₂ CuO _{4+x} UD55 (PA)	162

LIST OF FIGURES

A.3	Fermi-liquid fit to the low energy optical conductivity of $\text{HgBa}_2\text{CuO}_{4+x}$ UD55 (PB)	163
A.4	Fermi-liquid fit to the low energy optical conductivity of $\text{HgBa}_2\text{CuO}_{4+x}$ UD45 (PA)	164
A.5	Fermi-liquid fit to the low energy optical conductivity of $\text{HgBa}_2\text{CuO}_{4+x}$ UD45 (PB)	165
A.6	Fermi-liquid fit to the low energy optical conductivity of $\text{HgBa}_2\text{CuO}_{4+x}$ OpD97 (PA)	166
B.1	Comparison between Drude-Lorentz fit and Kramers-Kronig transformation	167